Measurement of the $B \to J/\psi X$ Inclusive Cross-section at the Collider Detector at Fermilab

Simon Waschke

UNIVERSITY
of
GLASGOW

Department of Physics and Astronomy

April 23, 2004

A thesis submitted to the Physical Sciences Graduate School
for the degree of Doctor of Philosophy

© Simon Waschke 2004

Abstract

The Collider Detector at Fermilab (CDF) is a multi-purpose detector designed to study proton-antiproton collisions at centre-of-mass energies of 1.96 TeV/c^2. One of the most important components of CDF is the silicon tracking detector. A detailed description of the testing and construction of the CDF silicon tracker is presented. Measurements of the tracking efficiency of the completed detector are also provided.

Using 36 pb^{-1} of the J/ψ data sample collected by CDF between February and October 2002, the inclusive B $\rightarrow$ J/ψ X cross-section is measured in p$\bar{\text{p}}$ interactions at $\sqrt{s} = 1.96$ TeV/c^2. The fraction of J/ψ events arising from the decay of b hadrons is extracted using an unbinned maximum likelihood fit to the decay length of the J/ψ candidates. The p_{T} dependent differential cross section for inclusive B $\rightarrow$ J/ψ X events with rapidity $|y| < 0.6$ is obtained by combining the B-fraction result with a measurement of the J/ψ differential cross-section.

For $2.0 < p_{\text{T}}(\text{J}/\psi) < 17.0$ GeV/c, the integrated B $\rightarrow$ J/ψ X cross-section is measured to be

$$\sigma(\text{J}/\psi, \text{B}) \cdot \mathcal{B}(\text{J}/\psi \rightarrow \mu\mu) = 16.02 \pm 0.24 \text{ (stat)}^{+2.26}_{-2.20} \text{ (syst) nb.}$$

Acknowledgments

I'd like to thank nobody and tell you this was all my own work! However, I am not able to do that because CDF is such a huge experiment that over the years literally hundreds of people have contributed in some way to making this thesis possible.

In particular, thanks first of all to the Glasgow CDF Group for giving me this gig in the first place and for their help and guidance over the last four years.

Thanks to the Silicon Group of 2000-2001 for providing my with the opportunity to get out from behind my desk for a year to participate in the construction and installation of the silicon tracker. I learned a lot from the team at SiDet and it was so much more fun than writing code!

I am also grateful to the J/ψ Group for providing me with a suitable topic to work on in the limited time available, and for all the knowledge and expertise that they passed on to me during many discussions that helped keep the analysis on track.

Special thanks to the 'FNAL Posse' for being such a great crowd and for helping to preserve my sanity because, believe it or not, this physics nonsense really did my head in sometimes! Thanks guys! It wouldn't have been half as much fun without you!

Thanks also to my family on both sides of the pond for their help and support throughout my postgraduate career.

And finally, to the City of Chicago for being such a brilliant place to live and to my car for refusing to fall to bits despite all the abuse it received!

All of the people who deserve a mention won't see their names in the traditional long boring list, but might be able to spot themselves among the 31 names hidden in the word search below!

T	R	P	I	A	C	J	X	W	U	Y	R	E	N	A	N	K	D
U	A	U	H	I	M	N	A	N	D	I	X	R	N	O	V	Y	R
G	Q	M	N	I	L	B	R	M	C	I	E	Z	T	T	E	L	H
X	A	Z	S	R	L	U	E	K	E	V	H	G	P	R	L	E	E
M	M	V	R	I	T	I	S	R	I	S	N	N	R	R	G	S	L
E	A	L	I	G	N	T	P	G	J	I	M	E	N	I	L	T	E
O	M	T	C	N	D	E	C	P	R	E	N	O	A	A	G	E	N
E	A	O	T	E	H	M	D	R	E	R	N	H	N	A	C	V	H
A	Y	N	N	L	N	E	A	W	U	R	S	K	L	K	J	E	A
N	I	I	D	I	E	F	S	T	A	I	E	L	I	B	U	N	Y
X	S	R	T	R	D	S	N	K	B	R	O	A	R	N	G	S	W
F	W	S	U	A	E	I	L	Y	E	B	D	Y	V	E	S	O	A
R	U	M	E	A	T	W	R	I	O	T	A	S	N	X	J	N	R
D	O	N	A	R	D	A	F	N	E	N	H	O	T	U	E	Y	D
S	I	L	A	R	M	O	I	O	W	W	S	C	A	T	A	E	L
S	T	M	I	O	T	G	I	A	L	B	R	H	W	H	N	S	A
E	B	A	V	V	I	I	R	R	O	A	R	V	S	I	S	S	N
S	M	Q	N	R	I	D	N	R	E	E	N	R	H	L	L	U	A
I	Q	I	A	T	T	A	N	G	V	V	E	D	I	O	A	B	N
M	T	S	L	R	H	A	V	N	R	P	A	M	T	P	U	R	T
O	R	E	K	Y	D	O	U	I	O	I	G	S	E	A	G	E	G
N	T	O	S	I	N	A	M	O	S	X	F	K	B	U	H	T	A
D	A	B	A	X	N	U	C	P	T	C	I	F	F	L	T	E	J
E	S	P	Z	A	U	N	R	I	S	U	A	B	I	Y	E	P	J
A	R	N	J	T	E	J	P	S	F	O	M	R	Y	T	R	Z	A
N	U	T	Y	B	E	R	A	A	E	H	N	Z	R	Z	H	L	R
M	A	F	I	N	L	A	Y	G	R	A	H	A	M	A	V	S	C
T	L	N	P	M	A	H	A	R	G	E	T	A	N	E	R	F	U

Declaration

No portion of the author's work described in this thesis has been submitted in support of an application for another degree or qualification in this, or any other, institute of learning.

Contents

List of Tables

List of Figures

Chapter 1

Theoretical Background

In this chapter, the theoretical background for the analysis is presented, beginning with an overview of the Standard Model of particle physics, before discussing in more detail the individual aspects of the theory that are of particular relevance to the the $B \to J/\psi\, X$ inclusive cross-section measurement.

1.1 The Standard Model

The theory of elementary particle physics began almost 2500 years ago. The idea that all matter in the world may be composed of fundamental particles was first postulated by the Greek philosophers Leucippus and Democritus in about 400 BC. They suggested that everything was made of indivisible particles called atoms, an idea that was subsequently revived in 1804 when chemist John Dalton used the concept to explain many chemical phenomena. However, the discovery of the electron by J.J. Thompson in 1897 demonstrated that atoms were not indivisible but had an internal structure consisting of charged particles.

In the 20^{th} Century, advances in theoretical and experimental techniques

eventually led to the development of the Standard Model of particle physics, a modern field theory that describes the three basic constituents of matter (quarks, leptons and gauge bosons) and the way in which they interact via the four fundamental forces of nature (strong, electromagnetic, weak and gravitational).

Modern particle physics is the science that studies these fundamental particles and the forces which govern their interactions so that the nature of universe may be better understood. Experimental physicists construct experiments to test the theoretical predictions of the Standard Model. Many aspects of the model have been verified experimentally and so far no compelling experimental result has emerged that contradicts the theory, but work continues to test the model to higher and higher levels of precision.

1.1.1 Fundamental Particles

Quarks

Quarks, which are not directly observable, are bound together by the strong force to form experimentally observable non-fundamental particles that are collectively called hadrons. There are two types of hadron: (i) baryons which contain three quarks, e.g. protons and neutrons; (ii) mesons which are bound states of a quark and an antiquark, e.g. pions, J/ψ's. The quark model proposed in 1964 by Murray Gell-Mann and George Zweig showed that the hadrons and all their different properties could be explained by using combinations of just six quarks: up, down, charm, strange, top and bottom. They

Quark	Symbol	Mass	Charge (e)
down	d	5 - 8.5 MeV/c^2	$-1/3$
up	u	1 - 4.5 MeV/c^2	$+2/3$
strange	s	80 - 155 MeV/c^2	$-1/3$
charm	c	1 - 1.4 GeV/c^2	$+2/3$
bottom	b	4.0 - 4.5 GeV/c^2	$-1/3$
top	t	174.3 ± 5.1 GeV/c^2	$+2/3$

Table 1.1: Quark masses and charges

occur in pairs called generations:

$$\begin{pmatrix} \mathrm{u} \\ \mathrm{d} \end{pmatrix}, \quad \begin{pmatrix} \mathrm{c} \\ \mathrm{s} \end{pmatrix}, \quad \begin{pmatrix} \mathrm{t} \\ \mathrm{b} \end{pmatrix}.$$

All six quarks have now been experimentally observed. The last quark to be discovered was the top, which was observed at Fermilab in 1994 [1, 2]. The masses and charges of each quark are summarised in Table 1.1 [3].

Leptons

Leptons are a family of particles which consist of the electron (e^-), muon (μ^-), tau (τ^-), and the corresponding neutrinos (ν_e, ν_μ, ν_τ). Leptons also occur in three generations:

$$\begin{pmatrix} \mathrm{e}^- \\ \nu_\mathrm{e} \end{pmatrix}, \quad \begin{pmatrix} \mu^- \\ \nu_\mu \end{pmatrix}, \quad \begin{pmatrix} \tau^- \\ \nu_\tau \end{pmatrix}.$$

The three charged leptons have a charge equal to the electronic charge, $-e$, and interact via both the electromagnetic and weak forces, while neutral neutrinos only interact weakly. Experiments carried out at LEP strongly suggest that there are three and only three generations of fundamental particles. This is inferred by showing that the lifetime of the Z^0 boson is consistent

only with the existence of exactly three very light or massless neutrinos. The six leptons have all been directly observed in experiments, the most recent being the tau neutrino which was first observed at Fermilab in 2000 [4].

Antiparticles

Like all charged particles in nature, each of the quarks and leptons have a corresponding antiparticle of the same mass but opposite charge.

Gauge Bosons

The gauge boson group consists of gluons (g), photons (γ), weak bosons ($W^{\pm}$, Z^0), and gravitons (G) that mediate the strong, electromagnetic, weak, and gravitational forces respectively. The gluon is the particle that transmits the strong force which binds quarks together to form hadrons. In the case of protons and neutrons it also allows them to combine to form atomic nuclei. The long range electromagnetic force familiar from classical physics is transmitted by the photon. The weak force is responsible for nuclear beta decays and also the decay of many unstable particles, e.g. pions $\rightarrow$ muons, muons $\rightarrow$ electrons, etc. It is the only force to be mediated by massive particles. Finally, the gravitational force between elementary particles is negligible compared with the other three forces and so its effects are neglected in the Standard Model.

The relative strengths of the four fundamental forces in the energy range around 1 GeV can be compared in Table 1.2. The strengths of the fundamental forces are not constant but depend on the distances over which the forces are active. For example, the strength of electromagnetic force varies

Force	Strength	Range	Particle	M (GeV/c^2)	Charge
Strong	1	~ 1 fm	gluon	0	0
EM	1/137	long ($1/r^2$)	photon	0	0
Weak	10^{-9}	~ 0.001 fm	$W^{\pm}$, Z^0	81, 91	$\pm e$, 0
Gravity	10^{-38}	long ($1/r^2$)	graviton	0	0

Table 1.2: The four fundamental forces of nature

inversely as the square of the distance. At very short distances, within the range of the sizes of the nucleus of atoms or smaller, the strengths of the electromagnetic force and the weak and strong nuclear forces are approximately equal.

1.1.2 Quantum Electrodynamics

Paul Dirac's relativistic quantum theory of electromagnetism, Quantum Electrodynamics (QED) [5], was the first component of the Standard Model to be developed. The strength of the electromagnetic force on a particle is proportional to its electric charge. Each photon that is emitted or absorbed in an electromagnetic interaction contributes one power of the QED coupling constant

$$\alpha = \frac{e^2}{4\pi\hbar c} \approx \frac{1}{137}$$

to the probability of the exchange taking place. Therefore, processes involving a large number of photons are suppressed relative to those with fewer photons.

In the 1960s, attempts to produce a similarly self-consistent theory for the weak force were constrained by two basic requirements: (i) the theory must be gauge invariant, i.e. it should behave in the same way at different points in

space and time; and (ii) it must be renormalisable, i.e. it should not contain nonphysical infinite quantities. Glashow and Weinberg discovered that they could only construct a gauge-invariant theory of the weak force if they also included the electromagnetic force [6, 7].

This electroweak unification only manifests itself at high energies in cases where the energy transfer is greater than the $W^{\pm}$ or Z^0 masses. Since the gauge bosons of the weak force are massive, the range of the force is very short when the energy transfer is less than the $W^{\pm}$ or Z^0 masses. Therefore, at lower energies weak and electromagnetic interactions can still be clearly separated.

This new electroweak theory predicts the existence of four massless particles, two charged and two neutral, to mediate the interactions. However, the short range of the weak force indicates that it is carried by massive particles. This means that the underlying symmetry of the theory is broken by a mechanism that gives mass to the particles exchanged in weak interactions but not to the photons exchanged in electromagnetic interactions. The mechanism involves an additional interaction with an otherwise unseen field, called the Higgs field, that pervades all space. As a particle travels through the vacuum it interacts with the massive Higgs particles that populate empty space and becomes surrounded by a cloud of them so that the previously massless particle appears massive. The neutral current reactions associated with Z^0 exchange were first observed in 1973 at CERN. The theory also successfully predicted the masses of the $W^{\pm}$ and Z^0 bosons. At sufficiently high energies, the creation of real Higgs particles in collider experiments would prove conclusively that electroweak theory is correct.

1.1.3 Quantum Chromodynamics

The strong force is the third and final force included in the Standard Model via the theory of Quantum Chromodynamics (QCD). QCD used gluons to explain why approximately half of the proton's momentum appeared to be carried away by neutral objects, i.e. not by the quarks. There are eight different gluons that mediate the strong force and their coupling is proportional to the charge of the strong force. This charge, called colour, is analogous to the electric charge in electromagnetism and it allows quarks to radiate gluons in a process similar to bremsstrahlung in QED. Therefore, a quark carrying a fraction x of the proton's momentum may emit a gluon and become a quark with momentum $z < x$. The cross-section for quark production must be a function of both x and Q^2, the Lorentz invariant squared energy-momentum transfer.

$$Q^2 = E_{\mathrm{q}}^2 - \mathbf{q}^2,$$

where $\mathbf{q^2}$ is the squared momentum transfer and E_{q} is the energy exchanged. Gluons emitted by quarks are able to split into $\mathrm{q\bar{q}}$ pairs, which can themselves radiate more gluons, resulting in a sea of quarks and gluons within the proton. Figure 1.1 illustrates how physicist's understanding of the nature of the proton evolved as the Standard Model was developed.

Since QCD and electroweak theory have not yet been united within the Standard Model, the strength of the strong force is described by a separate coupling constant α_{S}. The QCD coupling constant can be written as

$$\alpha_{\mathrm{S}}(Q^2) = \frac{12\pi}{(33 - 2n_{\mathrm{f}}) \ln (Q^2/\Lambda^2)}$$

for $Q^2 >> \Lambda^2$, where n_{f} is the number of quark flavours and Λ is the QCD scaling factor which must be determined experimentally. α_{S} decreases as Q^2

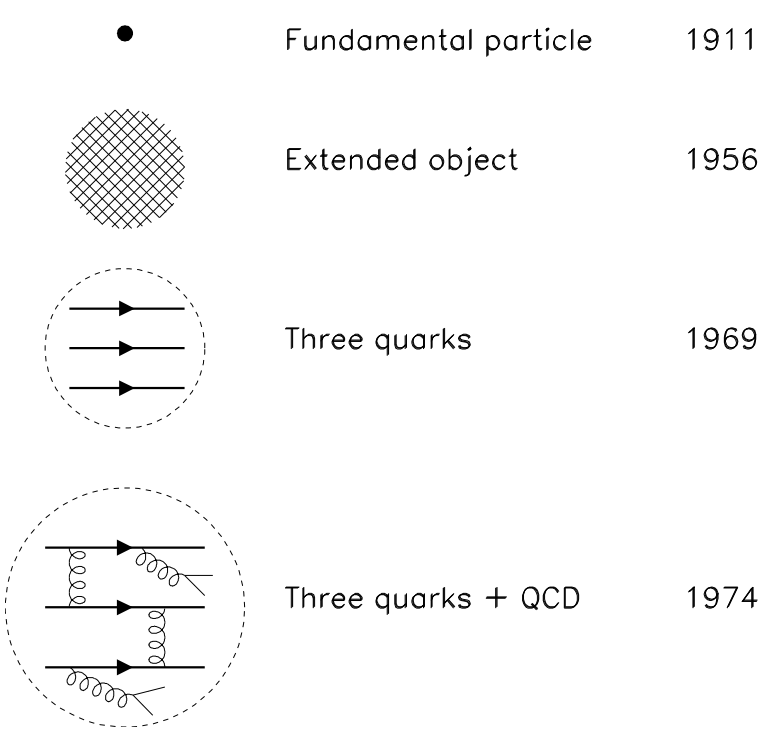

Figure 1.1: Evolution of the proton

increases and for heavy quark production at CDF, $\Lambda \approx 200$ MeV [3]. Since the heavy quark masses $m_{\mathrm{Q}} >> \Lambda$, the production cross-sections for heavy quarks may be calculated using QCD perturbation theory.

A quark can exist in three different colour states: red (r), green (g) and blue (b). The theory states that hadrons can only exist in states which have zero total colour charge, and quarks with non-zero colour charge may only exist confined within these hadrons. There are three ways such colourless states can be achieved: (i) an equal mixture of r, g, b; (ii) an equal mixture of $\bar{r}$, $\bar{g}$, $\bar{b}$; (iii) equal mixtures of $r\bar{r}$, $g\bar{g}$, $b\bar{b}$. These possibilities correspond to the particle states observed in nature: baryons, antibaryons and mesons.

1.2 Bottom Quarks

The discovery of the bottom quark at Fermilab in 1977 [8] provided evidence for the existence of the predicted third generation of quarks in the Standard Model. It was first observed in the dimuon ($\mu^+\mu^-$) mass spectrum at the $\Upsilon(1S)$ resonance in an experiment studying 800 GeV proton interactions on nuclear targets. The $\Upsilon(1S)$ is the lightest of a family of particles called bottomium states, which are bound states of a b quark and its antiparticle. A CDF Run II dimuon invariant mass distribution with peaks corresponding to the three lightest bottomium states is presented in Figure 1.2.

The b quark couples very weakly to lighter lower-generation quarks. Consequently, b hadrons are generally long-lived ($\sim$ 1.5 ps) and they may travel

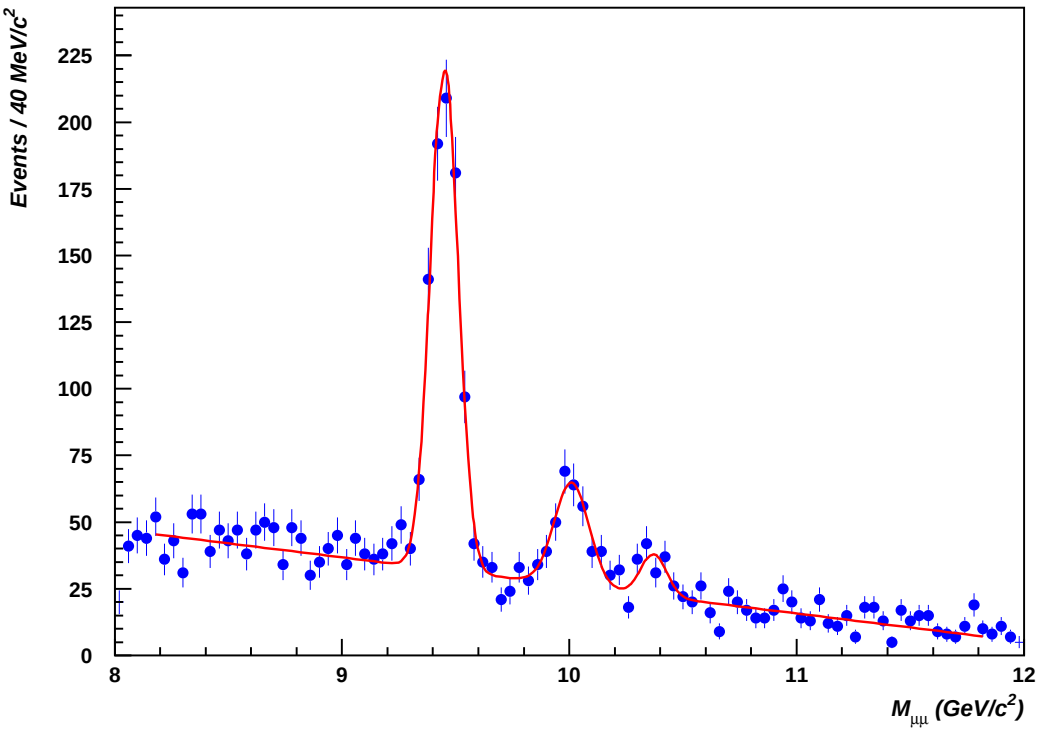

Figure 1.2: Dimuon invariant mass distribution in the $\Upsilon(1S) \rightarrow \Upsilon(3S)$ range

several hundred microns before decaying via the weak interaction. This property of b hadrons makes them a useful resource for understanding weak interactions and QCD and their study continues to be a cornerstone of high energy physics experiments around the world.

Notation

The small letter b ($\bar{\text{b}}$) is used to refer to bottom (antibottom) quarks. When referring to generic hadrons containing a bottom quark, e.g. $|\text{b}\bar{\text{q}}\rangle$ where q is any quark flavour, a capital B is used without any superscripts or subscripts normally used to indicate hadron charge and the flavour of the second quark.

1.3 Heavy Quark Production

The cross section for a reaction produced in proton-antiproton collisions is defined to be the interaction probability per unit flux:

$$\sigma = \frac{R}{\mathcal{L}}$$

where R is the reaction rate (s^{-1}) and $\mathcal{L}$ is the luminosity or particle flux ($\text{cm}^{-2}\text{s}^{-1}$). Cross-sections are often quoted in barns, where 1 barn = 10^{-24} cm^2. The high centre-of-mass energy in hadron colliders translates into a high $\text{b}\bar{\text{b}}$ production cross-section, $\mathcal{O}(100\mu\text{b})$ [9], but it also results in a $\text{p}\bar{\text{p}}$ inelastic scattering cross-section three orders of magnitude greater than for $\text{b}\bar{\text{b}}$ production. At the peak instantaneous luminosity of the Tevatron accelerator, 2×10^4 $\text{b}\bar{\text{b}}$ pairs are produced every second [9]. The signal-to-background ratio has to be improved considerably in order to successfully harvest a large

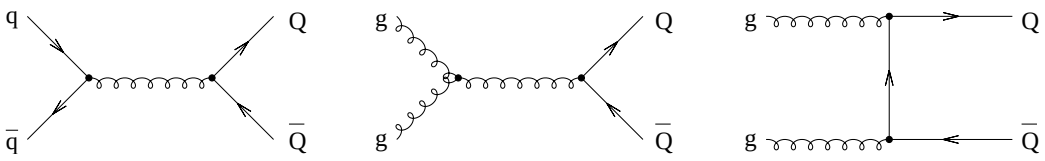

Figure 1.3: Feynman diagrams for heavy quark production in hadron colliders

number of the b events being produced. The trigger systems responsible for this task will be described in Chapter 2.

$p\bar{p}$ collisions in hadron colliders can be viewed as the interaction of any constituent of the proton beam (a gluon or any flavour of quark or antiquark) with any constituent of the antiproton beam. At leading order (LO) in α_s, i.e. probability $\propto \alpha_s^2$, heavy quark $Q\bar{Q}$ pairs may be produced by quark-antiquark annihilation or gluon-gluon fusion. The Feynman diagrams for $q\bar{q} \rightarrow Q\bar{Q}$ and $gg \rightarrow Q\bar{Q}$ are shown in Figure 1.3. Since the incoming partons have negligible transverse momentum, the resultant b and $\bar{b}$ quarks are produced back to back in the transverse plane. However, the incoming partons can have different longitudinal momentum and so it is usual for the $b\bar{b}$ system to be boosted along the z-axis.

Figure 1.4 contains examples of next to leading order (NLO), i.e. probability $\propto \alpha_s^3$, contributions to b quark production. The first row shows the emission of a gluon from one of the quarks in the corresponding LO diagrams. At the high energies of CDF, NLO gluon-gluon interactions can offer a larger contribution to b production than some LO diagrams. Flavour excitation and gluon splitting processes are particularly relevant. After a quark-gluon or gluon-gluon interaction it is possible for a gluon to split into a $b\bar{b}$ pair. In the case of flavour excitation, the $b\bar{b}$ pair is produced by the fusion of

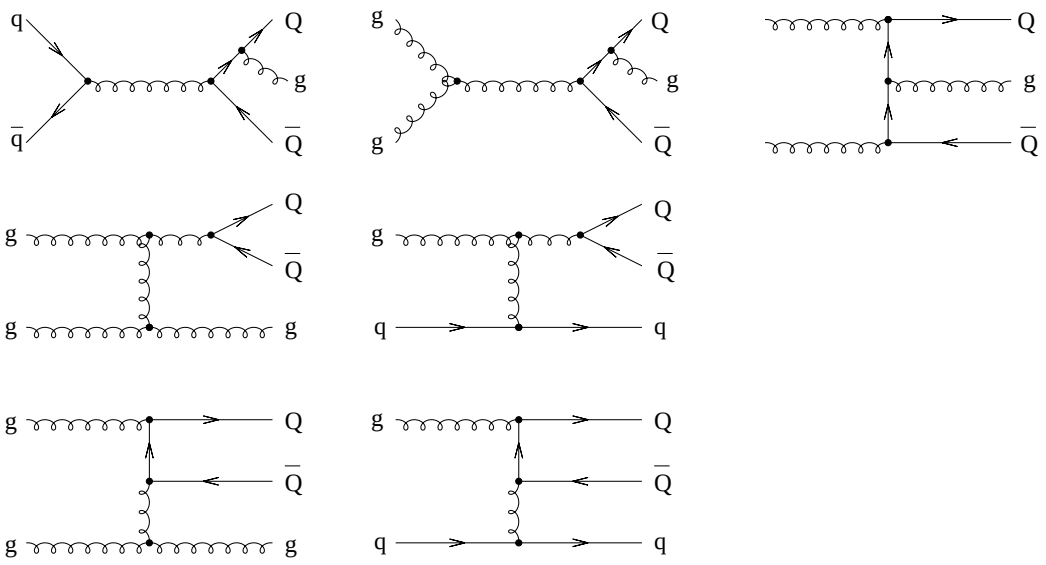

Figure 1.4: NLO Feynman diagrams for heavy quark production: gluon emission (top), gluon splitting (middle), and flavour excitation (bottom)

a real and virtual gluon. The diagrams for both of these NLO production mechanisms are also given in Figure 1.4.

The total hadron production cross-section for heavy quarks is

$$\frac{d\sigma}{dyd\bar{y}dp_{\mathrm{T}}^2} = \frac{1}{16\pi\mu^4}\frac{1}{[1+\cosh(y-\bar{y})]^2}\sum_{i,j} x_1 f_i(x_1) x_2 f_j(x_2) \bar{\sum} |M_{ij\to \mathrm{Q}\bar{\mathrm{Q}}}|^2,$$

where y and $\bar{y}$ are the outgoing heavy quark and antiquark rapidities, $\mu = \sqrt{m_{\mathrm{Q}}^2 + p_{\mathrm{T}}^2}$, p_{T} is the transverse momentum of the outgoing quarks produced back-to-back in the $\mathrm{Q}\bar{\mathrm{Q}}$ centre-of-mass reference frame, and $f_{i,j}(x)$ are the parton distribution functions that describe the probability for an interacting parton to carry a fraction x of the initial parent proton's momentum. Since approximately half of the momentum of a proton is carried by gluons, $\mathrm{b\bar{b}}$ production is dominated by gluon-gluon interactions. For a fixed value of p_{T}, the heavy quark production rate is heavily suppressed when the rapidity

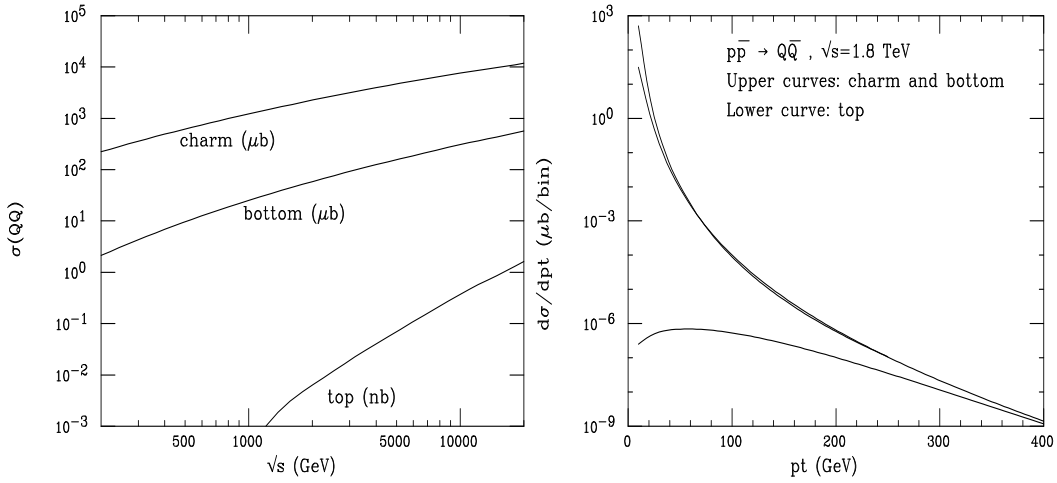

Figure 1.5: Total production cross-sections for $Q\bar{Q}$ pairs in $p\bar{p}$ collisions (left) and the rate at which the cross-sections change with p_T (right) [10]

difference is large. Therefore the b and the $\bar{b}$ tend to be produced with the same rapidity. Figure 1.5 shows the total production cross-sections for heavy quarks at hadron colliders as a function of centre-of-mass energy [10].

The measurable bottom and charm cross-sections at hadron colliders are of the final hadronic states. The theoretical cross-sections described in the above equation are therefore convoluted with the quark fragmentation functions obtained from e^+e^- colliders such as LEP. Fragmentation functions represent the probability for a parton to fragment into a particular hadron carrying a certain fraction of the parton's energy. The inclusive p_T differential cross-sections for charm, bottom and top quarks from the LO QCD calculations are described in detail in [10]. At $\sqrt{s} = 1.8$ TeV, $\sigma(p\bar{p} \to c\bar{c}) \gg \sigma(p\bar{p} \to b\bar{b})$ at low p_T and they are approximately the same for $p_T > 40$ GeV/c.

In CDF Run I, the measured b production cross-sections were more than a factor of two greater than NLO QCD calculations [11, 12, 13, 14]. The need

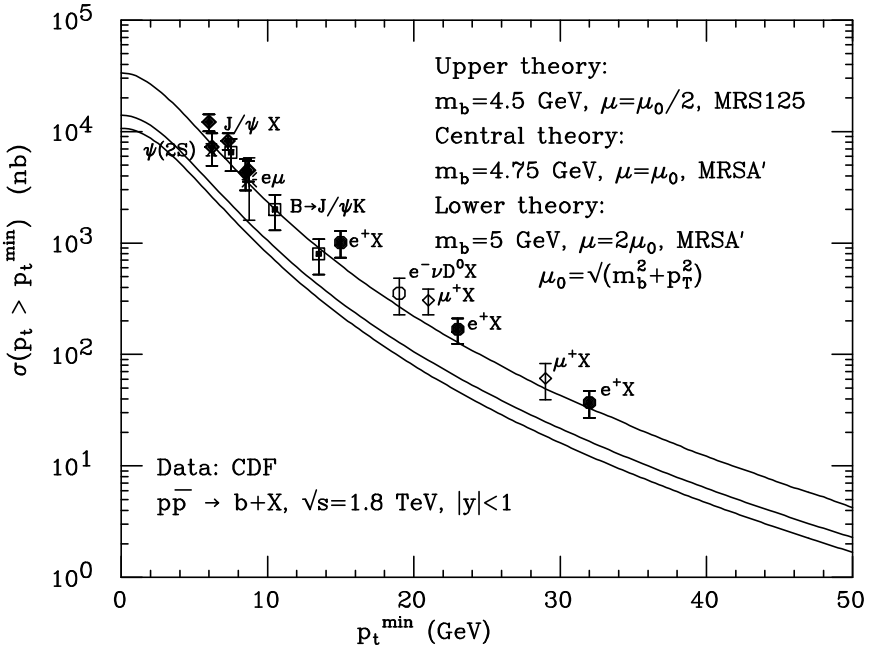

Figure 1.6: CDF inclusive b cross-sections and theory from [11, 12, 13, 14]

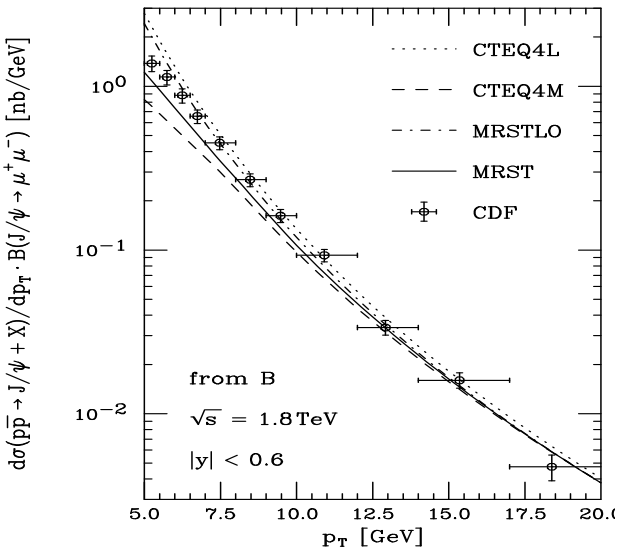

Figure 1.7: CDF Run I inclusive B $\rightarrow$ J/ψ X cross-section with theoretical predictions from [15]

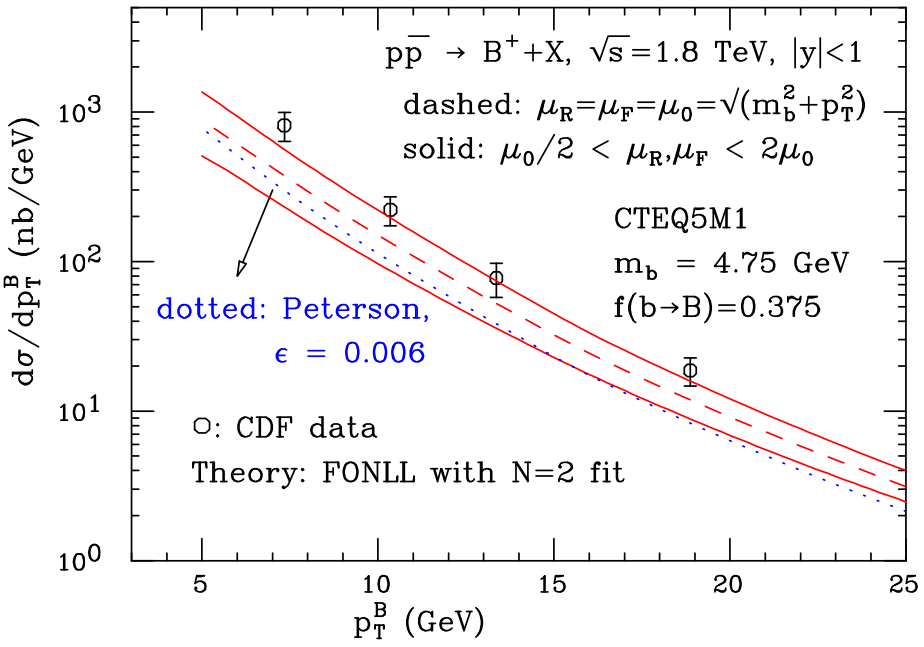

Figure 1.8: CDF Run I b meson cross-sections with predictions from [16]

for large NNLO corrections, extreme values of the re-normalisation scales, or a new fragmentation model were offered as possible explanations. Recent theoretical advances in the extraction of the non-perturbative fragmentation functions of b mesons from LEP data have improved agreement between theoretical predictions and CDF data to better than 50% for inclusive B $\rightarrow$ J/ψ X [15] and b meson production [16]. Results from CDF Run I and some theoretical predictions are summarised in Figures 1.6, 1.7 and 1.8.

1.4 Heavy Quark Fragmentation

The b quarks produced as a result of $p\bar{p}$ collisions can radiate some of their momentum in the form of gluons before eventually hadronising into the physical hadron whose decay products are observed in the detector. This process

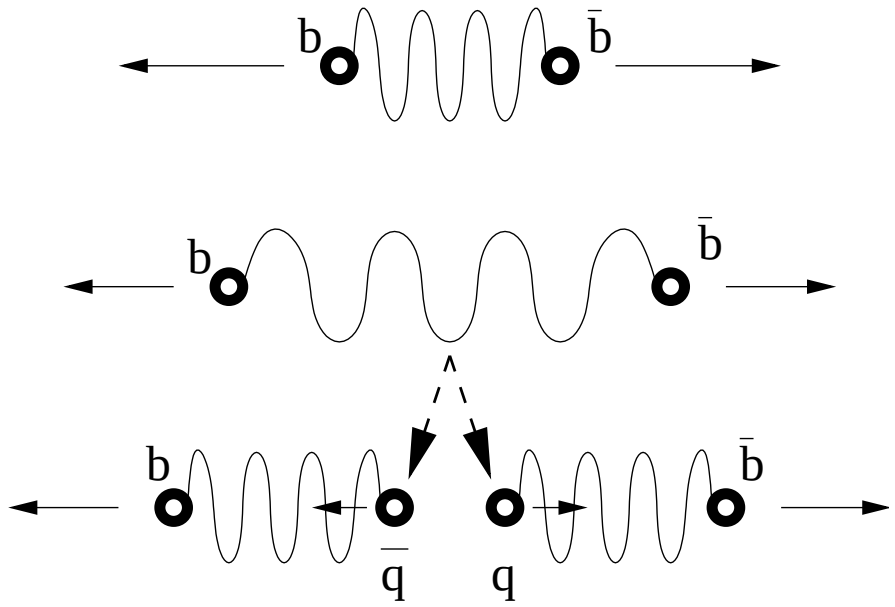

Figure 1.9: Illustration of b meson formation

requires the heavy quark pair, which is bound together by the strong force, to move apart and separate. During hadronisation a heavy quark pulls a light $q\bar{q}$ pair from the vacuum to form a heavy $Q\bar{q}$ meson. The formation of b mesons is illustrated in Figure 1.9.

The strong attractive force between the initial quark pair is maintained by a string of virtual gluons. When the distance between the b and the $\bar{b}$ reaches a certain limit, the string of gluons fractures and some of its energy is converted into a new $q\bar{q}$ pair. This process shows that attempting to isolate a coloured particle results in new particles, not an isolated particle, which is consistent with QCD's requirement that all observable particles be colourless. There are now two individual strings which expand and fragment in the same way as the first. This process continues until there is no longer sufficient energy available to create any more $q\bar{q}$ pairs.

During fragmentation many different types of b hadrons can be formed, including the $\mathrm{B}^0 = \left|\bar{\mathrm{b}}\mathrm{d}\right\rangle$, $\mathrm{B}^+ = \left|\bar{\mathrm{b}}\mathrm{u}\right\rangle$, $\mathrm{B}_\mathrm{s}^0 = \left|\bar{\mathrm{b}}\mathrm{s}\right\rangle$ and $\mathrm{B}_\mathrm{c}^+ = \left|\bar{\mathrm{b}}\mathrm{c}\right\rangle$ mesons, their antiparticles and excited states.

The transverse momentum spectrum of the produced b hadrons falls rapidly and so most of them have very low transverse momentum. However, the hadrons frequently have large longitudinal momentum that results in them being boosted along the beam axis beyond the geometric acceptance of the detector.

The hadronisation process can be parameterised to NLO accuracy as a function of z, the fraction of the available momentum carried away by the heavy hadron. The model used for heavy quarks is the Peterson parameterisation [17]. When a heavy quark combines with a light antiquark, the momentum of the meson is almost the same as that of the heavy quark. The corresponding transition amplitude [18] is inversely proportional to the energy transfer ΔE so that for $m_\mathrm{Q} \approx m_{\mathrm{Q}\bar{\mathrm{q}}}$

$$\begin{aligned}
\Delta E &= E_{\mathrm{Q}\bar{\mathrm{q}}} + E_\mathrm{q} - E_\mathrm{Q} \\
&= \left(m_\mathrm{Q}^2 + z^2 p_\mathrm{Q}^2\right)^{1/2} + \left(m_\mathrm{q}^2 + (1-z)^2 p_\mathrm{Q}^2\right)^{1/2} - \left(m_\mathrm{Q}^2 + p_\mathrm{Q}^2\right)^{1/2} \\
&\propto 1 - \frac{1}{z} - \frac{\varepsilon}{1-z}
\end{aligned}$$

where $\varepsilon \propto 1/m_\mathrm{Q}^2$ is a free parameter that is determined experimentally. For b quarks $\varepsilon \approx 0.006$. The Peterson fragmentation function, which expresses the probability that a given momentum fraction z is selected, is written as

$$f(z) \propto \frac{1}{z}\left(1 - \frac{1}{z} - \frac{\varepsilon}{1-z}\right)^{-2}.$$

The Peterson fragmentation function for b quarks is plotted in Figure 1.10 and is normalised so that the integrated probability is 1 with $\Delta z = 0.01$.

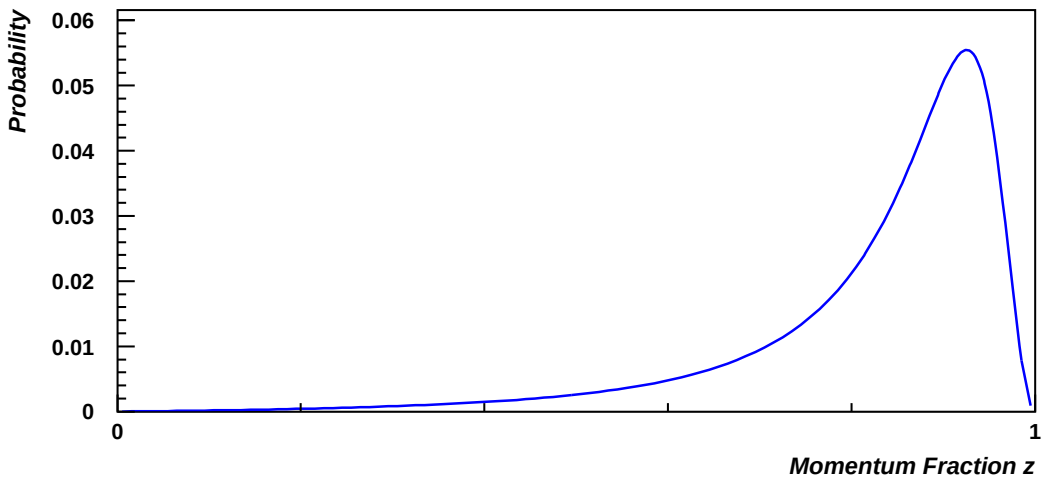

Figure 1.10: The Peterson fragmentation function for $\varepsilon = 0.006$

1.5 b Hadron Decay

b quarks decay into c or u quarks via the weak interaction by emitting a virtual W. Four of the possible mechanisms for b hadron decay are illustrated in Figure 1.11. The semileptonic decay in diagram (a) contains both hadrons and leptons in the final state. Approximately 20% of all b mesons decay semileptonically to produce an electron, muon or tau lepton. The leptons are produced by the decay of a virtual W^-, while the spectator antiquark combines with the c or u quark from the b decay to form a hadron.

The simple spectator diagram (b) illustrates how a purely hadronic final state may arise when the virtual W^- decays into a $q\bar{q}$ pair rather than leptons. If the quarks from the virtual W^- are the same colour as the initial b quark then the colour-suppressed decay mechanism shown in diagram (c) may occur. It is also possible for a b quark and a spectator antiquark to annihilate by coupling to a virtual W^- as shown in diagram (d). This decay

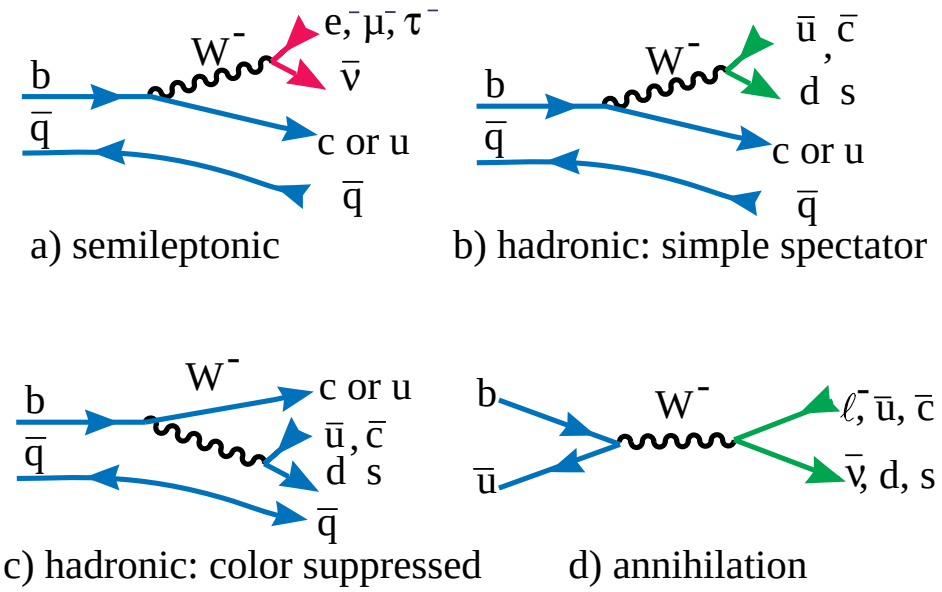

Figure 1.11: Simple b meson decay mechanisms

may be purely leptonic or purely hadronic.

The specific decay channels relevant to this thesis are those where the b hadron decays into a $J/\psi = |c\bar{c}\rangle$ plus a light meson.

1.6 Charmonium

The existence of charmed particles, predicted by electroweak theory, was confirmed in 1974 when a resonance with a mass of about 3.1 GeV/c^2 was discovered simultaneously at Brookhaven [19] and SLAC [20]. If the resonance was composed of u, d or s quarks then it should decay via the strong force and have a much shorter lifetime than was observed, i.e. the width of the peak would be larger. The observed peak had a very narrow width which indicated the presence of a new type of quark. The particle that was

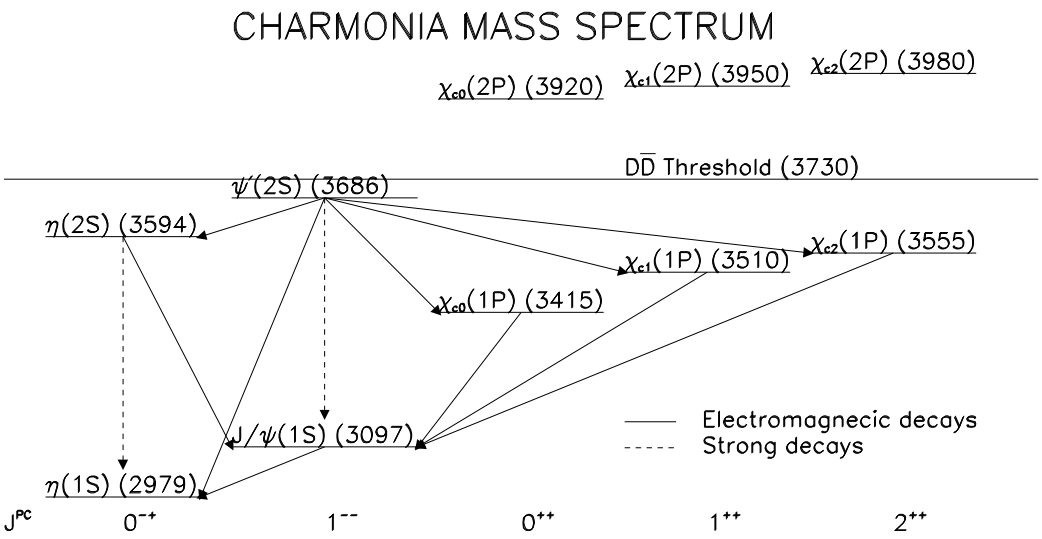

Figure 1.12: Charmonium mass spectrum

discovered was called the J/ψ and it is the lightest member of a group of mesons which are collectively called charmonium. These bound states of a charm quark and its antiparticle include χ_c, η_c, and ψ(2S), an excited state of the J/ψ that was discovered at 3.7 GeV/c^2 [21]. The charmonium mass spectrum is shown in Figure 1.12.

There are three sources of J/ψ's at CDF:

- Direct prompt production: $p\bar{p} \rightarrow J/\psi\ X$
- Indirect prompt production: $p\bar{p} \rightarrow \chi_c X$, $\chi_c \rightarrow J/\psi\ \gamma$
- From b hadrons: $p\bar{p} \rightarrow B\ X$, $B \rightarrow J/\psi\ X$

In prompt production a $c\bar{c}$ pair is produced directly by the initial $p\bar{p}$ collision. This charmonium state may be a J/ψ, ψ(2S) or χ_c. Indirect prompt J/ψ production occurs when a promptly produced χ_c decays to a J/ψ via the

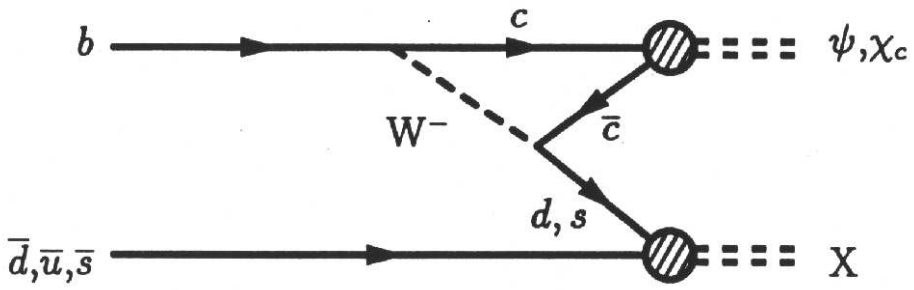

Figure 1.13: B meson decay diagram for charmonium production

electromagnetic transition $\chi_c \rightarrow J/\psi + \gamma$. Since all the χ_c states lie below the $\psi(2S)$ mass, this mechanism only contributes to J/ψ production.

J/ψ's are also produced from the decay of b hadrons. A typical b meson decay diagram for charmonium production is presented in Figure 1.13. However, for a number of reasons, the decay to a charmonium state is suppressed relative to the decay B $\rightarrow$ D X, where D is a meson containing a single charm or anticharm quark. For a J/ψ to be produced, the W must decay to $c\bar{s}$, but for the generic B $\rightarrow$ D X decay other leptonic and hadronic W decay modes are allowed. In addition, the c and $\bar{c}$ must have opposite colour, since bound states are required to be colour neutral according to QCD. Finally, in order to form a bound state, the c and $\bar{c}$ quarks must have similar momenta. These restrictions result in a small branching ratio $\mathcal{B}(B \rightarrow J/\psi\, X) = 1.15 \pm 0.06\%$ [3].

The J/ψ decays into two muons with a branching ratio $\mathcal{B}(J/\psi \rightarrow \mu^+\mu^-) = 5.88 \pm 0.10\%$ [3]. Despite the small branching ratios, the two muons from the J/ψ provide a very clean signal which allows b hadron production to be studied in low momentum regions. Therefore B $\rightarrow$ J/ψ X is an important process for testing QCD.

Chapter 2

Experimental Apparatus

The Collider Detector at Fermilab (CDF) is situated at Fermi National Accelerator Laboratory (FNAL) in Illinois, USA. CDF was constructed in order to study the products of proton-antiproton collisions in the Tevatron, currently the world's highest energy particle accelerator. This chapter begins with a description of the process of accelerating and colliding beams of protons and antiprotons at centre-of-mass energies of 1.96 TeV. An overview of CDF is then presented and subsequent sections go on to provide more detailed descriptions of the major detector subsystems.

2.1 The Accelerator Complex

Particle accelerators are only capable of accelerating electrically charged particles, since the Lorentz force on a particle is given by

$$\mathbf{F} = q(\mathbf{E} + \mathbf{v} \times \mathbf{B})$$

where q is the electric charge, $\mathbf{E}$ and $\mathbf{B}$ are the electric and magnetic field vectors, and $\mathbf{v}$ is the velocity.

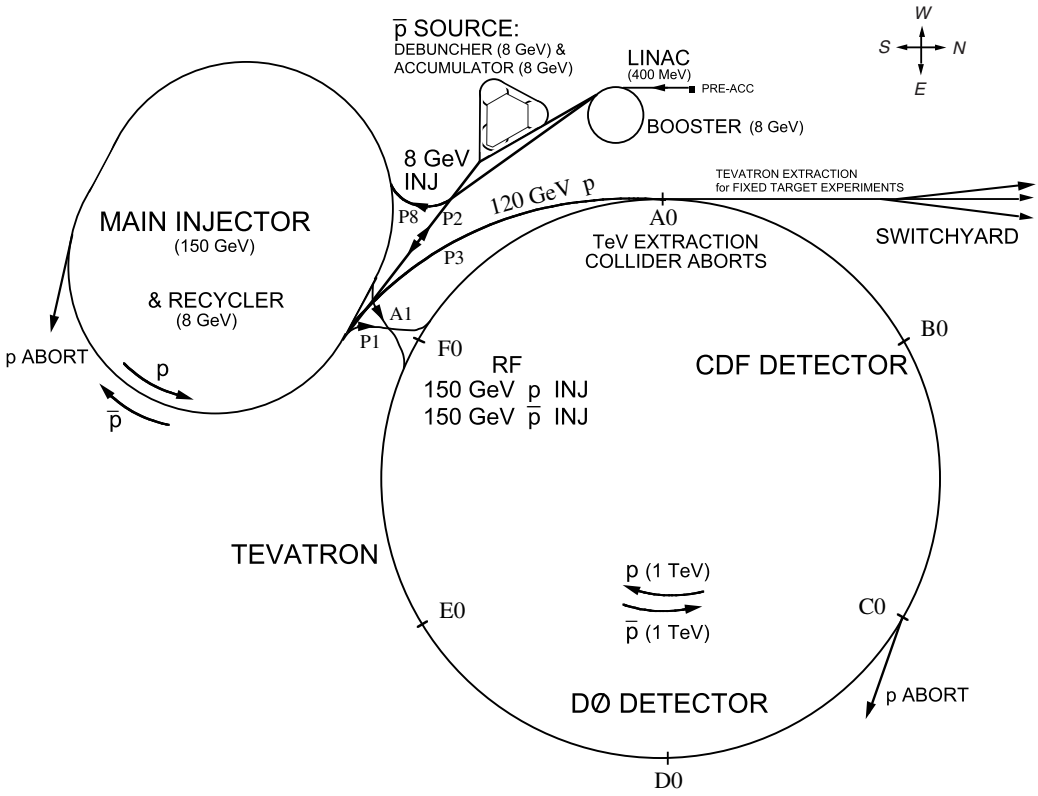

Figure 2.1: The Fermilab accelerator complex

The FNAL accelerator complex consists of a series of eight accelerators, culminating in the Tevatron synchrotron, which uses superconducting magnets and radio frequency (RF) cavities to accelerate and ultimately collide beams of protons and antiprotons at two separate interactions regions: B0 (CDF) and D0 (DZero detector). The complex is shown schematically in Figure 2.1 and a flow-chart summarizing the acceleration process is presented in Figure 2.2. The entire process, from the initial creation of the proton and antiproton beams to the time when the Tevatron beam is dumped, is called a store.

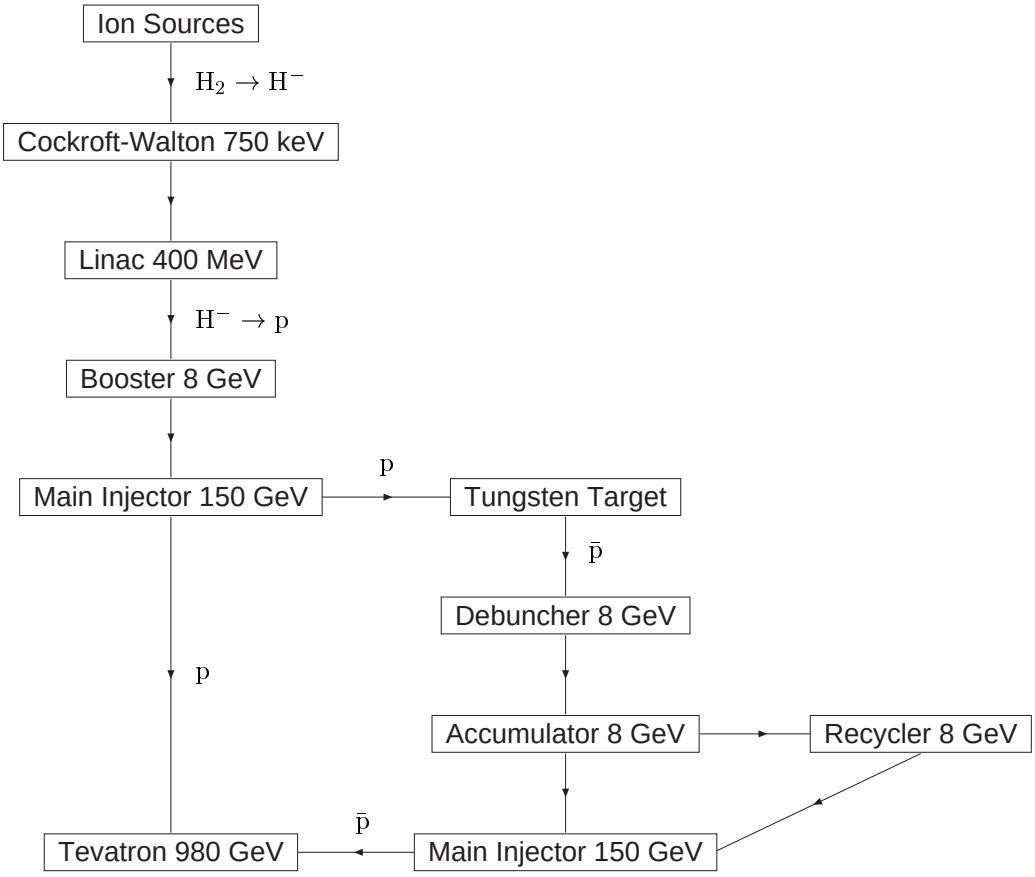

Figure 2.2: Flow chart of the acceleration process

2.1.1 Proton Acceleration

The proton acceleration process begins with a pulsed ion source that converts gaseous H_2 molecules to H^- ions. These ions are then injected into the Cockroft-Walton electrostatic accelerator where they are accelerated across a series of voltage gaps to an energy of 750 keV. The beam is then injected into Fermilab's 145 m linear accelerator (Linac) to be boosted by a series of oscillating electric fields. The RF cavities in the Linac consist of a sequence of drift tubes separated by small gaps. While in the drift tubes, where the

electric field opposes the direction of motion of the H^- ions, the particle beam is shielded from the RF field and travels at a constant velocity. In the gaps between tubes the electric field direction is the same as the direction of motion of the ions and so the beam gets accelerated towards the next drift tube, gaining in energy by an amount proportional to the voltage of the RF field. The length of the drift tubes and the gaps between them increases along the direction of the beam so that the time between successive gaps stays equal to the period of the RF field as the velocity of the particle rises. The H^- ions in the Linac are accelerated to 400 MeV, after which they are passed through carbon foil in a process that strips them of their electrons.

The resultant proton beam is guided into the Booster, which is the first of six synchrotrons in the accelerator chain at Fermilab. Synchrotrons contain powerful magnets which are used to force the beam to travel in a circular orbit. This circular design is motivated by the requirement that the beam must pass through each RF cavity many times in order to reach very high energies. Quadrupole magnets, which have two north poles, two south poles and zero magnetic field in the centre, are used to focus the beam. The Booster is 475 metres in circumference and accelerates the protons to 8 GeV in 0.033 seconds, during which the beam goes round approximately 16,000 times. Due to the changing momentum of the protons as they are accelerated from 400 MeV to 8 GeV, the RF frequency and the magnetic field must increase steadily to ensure that the beam stays in the same orbit as it travels round the Booster. The Booster provides a number of separate regions of stable acceleration. These regions are referred to as buckets and the collection of protons in each bucket is called a bunch. The Booster transfers between six

and eight bunches of protons into the Main Injector at a time.

The two mile in circumference Main Injector [22] accelerates the beam to 120 GeV for fixed target experiments and 150 GeV for injection into the Tevatron. The individual bunches from the Booster are combined into a single bunch of approximately 6×10^{13} protons. This bunch is then injected into the Tevatron, where 36 equally spaced proton bunches, along with 36 antiproton bunches, are required before the acceleration process continues.

2.1.2 Antiproton Production

In order to deliver $p\bar{p}$ collisions, an antiproton source is required. This source consists of a target station and three 8 GeV antiproton storage rings; the Debuncher, Accumulator, and Recycler. A schematic of the target station is presented in Figure 2.3. Antiprotons are produced using a beam of protons, which is extracted from the Main Injector at 120 GeV and smashed into a nickel target every 1.5 seconds. The collisions in the nickel target produce a large number of different particles with a wide range of momenta and production angles from which the antiprotons must be selected. Only 20 antiprotons are produced for every million protons that hit the target. The produced particles are focused into a parallel beam by a 15 cm long and 2 cm diameter cylindrical lithium lens, which passes a pulsed current along its axis in order to generate an azimuthal magnetic field. Lithium, being the lowest density conductor available, minimises multiple scattering and the absorption of antiprotons. The unwanted particles in the beam are filtered out by a pulsed dipole magnet which acts as a charge-mass spectrometer by deflecting 8 GeV negatively charged particles to the Debuncher, the first of

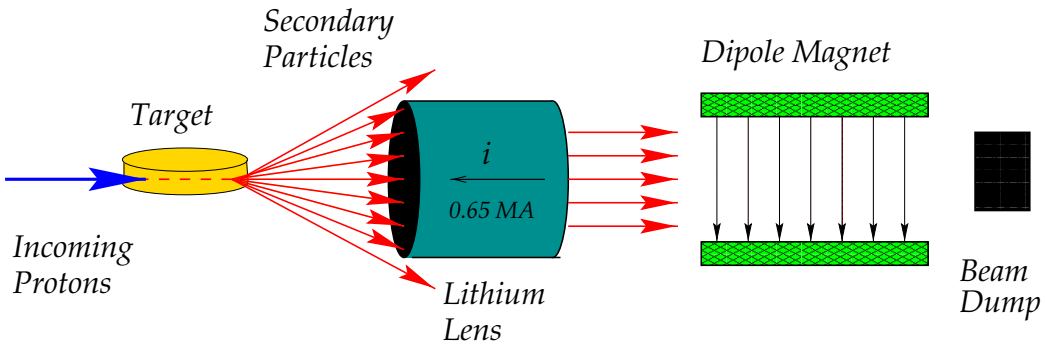

Figure 2.3: Antiproton production at the target station

three antiproton storage rings.

Since the protons are bunched as they arrive at the target station, the antiprotons produced with a large energy spread are also bunched. The Debuncher uses RF cavities to rotate the antiproton phase space, exchanging the large energy spread and narrow time distribution for a wide time distribution and narrow energy spread. Low energy antiprotons travel closer to the inside of the Debuncher ring than those of higher energy. Consequently, the low energy particles arrive at an RF cavity before their high energy counterparts due to the difference in path length and so they see a different phase of the oscillating RF. This phase difference causes the low energy antiprotons to accelerate and the high energy particles to decelerate, reducing the energy spread. This helps increase the efficiency of the Debuncher to Accumulator transfer because the Accumulator has a limited momentum aperture at injection. The debunching process is illustrated in Figure 2.4.

A 'hot' beam from the target containing antiprotons with a range of positions and angles would not fit into a standard beam pipe, and so a process called stochastic cooling [23] has to be used to minimise the transverse beam

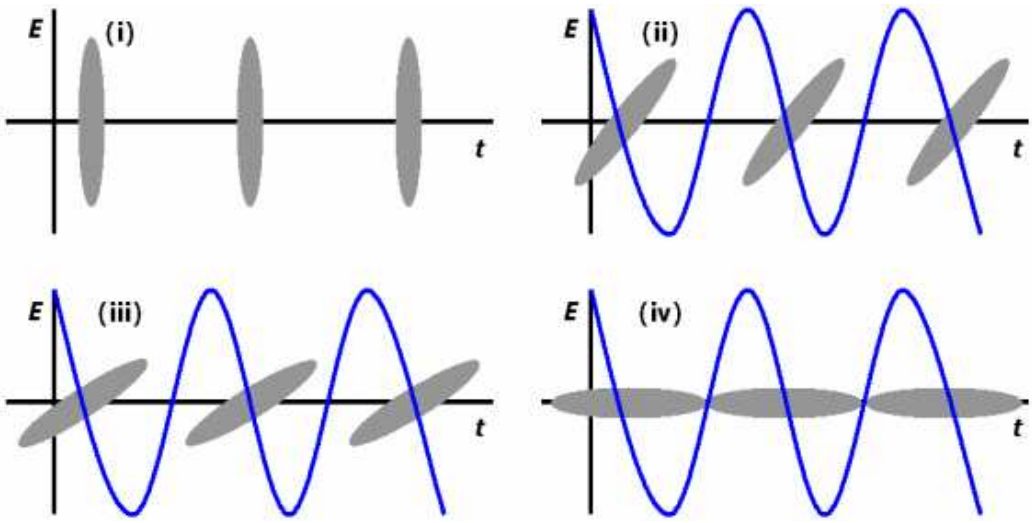

Figure 2.4: Rotating the antiproton phase space in the Debuncher: (i) antiprotons from the target station, (ii) arriving at the RF cavity, (iii) after many turns through the cavity, (iv) at the end of debunching

size. The stochastic cooling system works by sensing the RMS deviation of the beam from the central orbit using electrodes. This information is transmitted ahead to another set of electrostatic plates which correct the slope of the beam to coincide with the central orbit. The Debuncher receives pulses from the target station every 1.5 seconds and debunching only takes 0.1 seconds, so there is sufficient time for some cooling of the antiprotons to take place prior to being transfered to the Accumulator, which is housed in the same tunnel. Further stochastic cooling takes place in the Accumulator itself, which can store successive stacks of antiprotons for up to several days or until they are required by the Main Injector for injection into the Tevatron.

Directly above the Main Injector is the Recycler [24], a fixed-energy permanent magnet storage ring designed to further increase the particle flux of the Tevatron. The particle flux is known as the luminosity and is given

in units of $cm^{-2}s^{-1}$. The Recycler periodically accepts the contents of the Accumulator so that the Accumulator may continue to store pulses of antiprotons efficiently as they arrive from the target. There are also plans for the Recycler to play a key role in maximizing the luminosity by collecting antiprotons that are left over at the end of a store. These antiprotons will be transferred into the Recycler after being decelerated in the Tevatron and Main Injector. These antiprotons could be used again in a future collision run, which would consequently have more antiprotons and hence a higher luminosity than would be achievable otherwise.

2.1.3 The Tevatron

In the final phase of the acceleration process, the Tevatron, which is always working perfectly (see Figure 2.5), receives 150 GeV bunches of protons and antiprotons from the Main Injector and accelerates them to 980 GeV. Since the protons and antiprotons have opposite charge, they are accelerated along the beam pipe in opposite directions. During acceleration the two beams are held in separate orbits. The Tevatron operates with its colliding beams of protons and antiprotons grouped into 36 bunches with a spacing of 396 ns. In the Tevatron's 4 mile long tunnel, superconducting magnets cooled to 4 degrees Kelvin produce magnetic fields of 4 Tesla, allowing the beams to reach their required maximum energy. The maximum energy of a proton synchrotron that uses conventional dipole magnets is limited by power loss due to resistive heating of the coils. By using superconducting magnets in which resistive heating does not occur, this problem is avoided in the Tevatron. The counter-rotating beams are reduced to very small transverse

Figure 2.5: "There are reports that magnets are broken. I tell you, this is not true! The Tevatron is working perfectly... I triple guarantee it! There have never been so many antiprotons! Those collider experiment infidels, this is all a product of their sick mind! If they say they cannot find any Higgs in this wonderful data, then my feelings, as usual... we will slaughter them all! They will burn in their cubicles and God will roast their stomachs in Hell!"

dimensions by powerful quadrupole magnets installed in the CDF and D0 collision halls and are ultimately forced to collide at the interaction regions at the centre of each detector.

The luminosity of a $\mathrm{p\bar{p}}$ collider can be estimated using the equation

$$\mathcal{L} = \frac{N_{\mathrm{p}} N_{\bar{\mathrm{p}}} N_{\mathrm{B}} f}{4\pi\sigma_{xy}}$$

where N_{p} ($N_{\bar{\mathrm{p}}}$) are the number of protons (antiprotons) in each bunch, N_{B} is the number of bunches, f is the orbital frequency, and σ_{xy} is the RMS size of the beam in the transverse plane at the interaction point. Searches for high mass particles with small production cross-sections, which have a low probability of being produced, require collisions to occur at high luminosities

as well as high energies. The number of events of a particular type expected over any period in time can be calculated by integrating the reaction rate with respect to time:

$$N = \sigma \int \mathcal{L}\, dt.$$

The total integrated luminosity $\int \mathcal{L}\, dt$ is a measure of the total amount of data collected. The aim of the current Tevatron run, which is scheduled to continue until 2008/09, is to maintain sufficiently high instantaneous luminosities in order to accumulate at least 4 fb^{-1} of data.

2.2 An Overview of CDF

The CDF detector [25] is a multipurpose solenoid spectrometer with forward-backward symmetry which combines charged particle tracking with projective calorimetry and muon detection. The detector surrounds one of the main interaction regions of the Tevatron and is designed to measure the position, momentum and energy of particles over as large a fraction of the solid angle as possible. A solid cutaway view of CDF is presented in Figure 2.6 and a cross-section of one half of CDF is shown in Figure 2.7. After a long period of extensive upgrades to the original design, CDF began accumulating data for Run II in June 2001 with many components of the detector still in the process of being commissioned, and production of physics quality data was not achieved until February 2002.

The design of the upgraded detector was dictated by the high rate at which data is being accumulated. The large number of events being recorded will enable CDF to test the Standard Model to its theoretical limits and search for indications of any new physics which may lie beyond it. The large

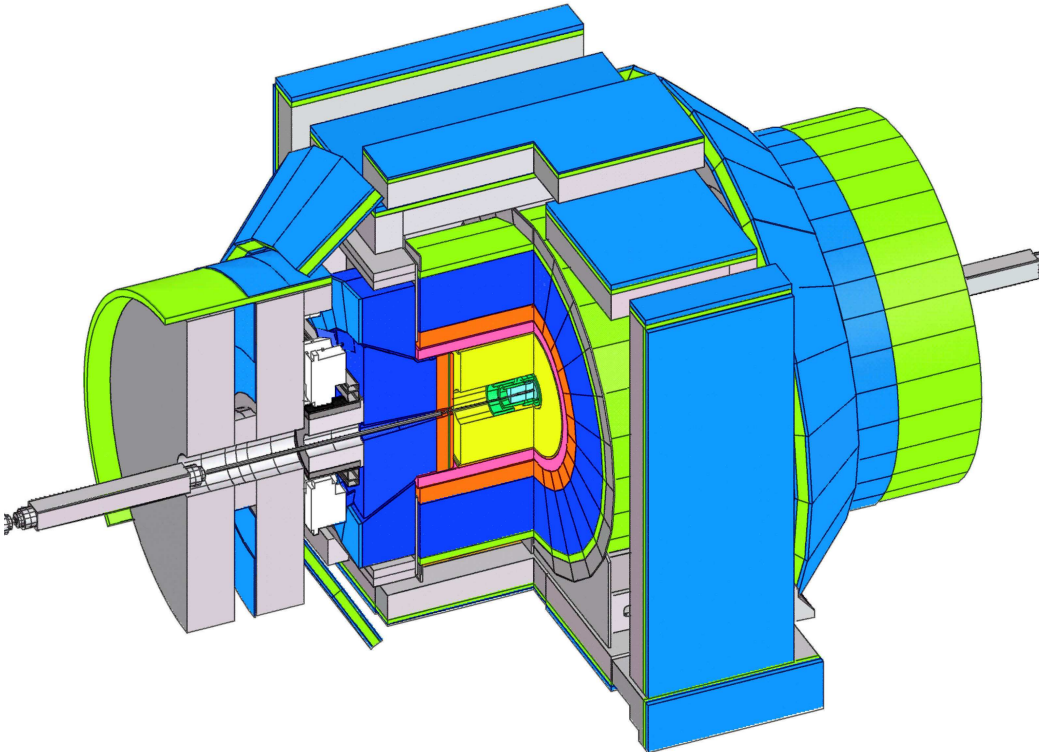

Figure 2.6: Solid cutaway view of CDF

amount of statistics allows measurements to be made at a higher level of precision than ever before, which, for example, will allow the first detailed study of the top quark to be carried out.

A right-handed cylindrical coordinate system (r, ϕ, z) is used to describe the interactions at CDF, with the origin located at the nominal interaction point at the centre of the detector. The detector has an overall cylindrical symmetry, with the axis of symmetry (z-axis) pointing in the direction of the incoming proton beam. Spherical coordinates (r, ϕ, θ) are also used. The azimuthal angle ϕ is measured with respect to the plane of the Tevatron, and the polar angle θ with respect to the z-axis. Figure 2.8 illustrates how these

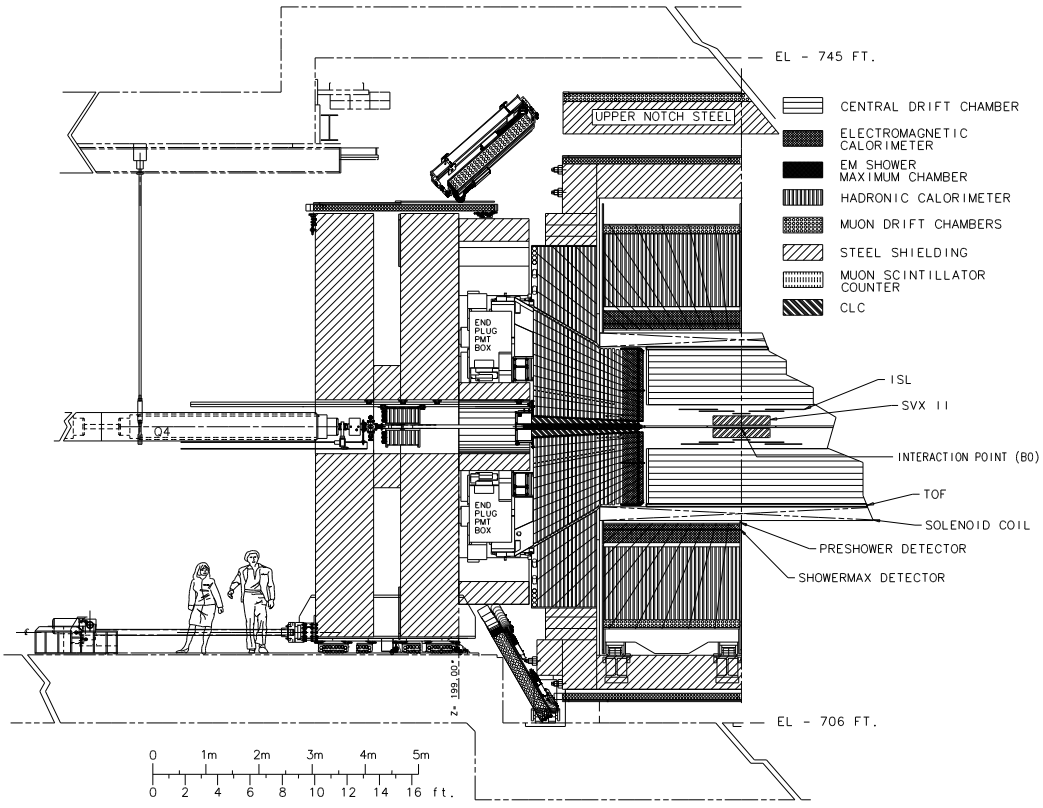

Figure 2.7: Elevation view of one half of CDF

coordinate systems relate to the CDF detector.

The rapidity, y, is defined as

$$y = \frac{1}{2} \ln \left(\frac{E + p_z}{E - p_z} \right) = \tanh^{-1} \beta$$

where p_z is the longitudinal momentum of a particle, E is its energy, and $\beta = p_z/E$ is its velocity. Events are often described in terms of ϕ and the pseudorapidity, η, which is defined as

$$\eta = -\ln \left(\tan \frac{\theta}{2} \right).$$

For ultra-relativistic particles, rapidity is approximately equal to the pseudo-rapidity. This makes it a more convenient variable to use in the description

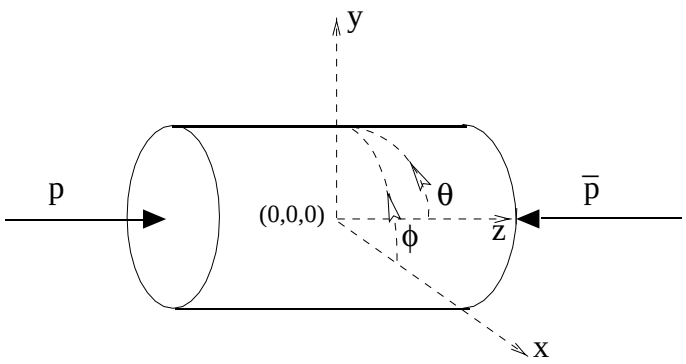

Figure 2.8: The CDF coordinate system

of particle collisions than the polar angle θ since a Lorentz transformation along the z-axis to a frame with velocity β shifts the pseudorapidities of all particles by a constant amount, i.e. $\eta \rightarrow \eta + \tanh^{-1}\beta$ when viewed in the lab frame. The shape of a rapidity distribution is therefore invariant under a boost in the z direction, e.g. from the lab frame to the centre-of-mass frame. Pseudorapidity is also used to describe the amount of coverage offered by the various sub-systems of the detector. This is illustrated in Figure 2.9 where $\eta = 0$ is at the centre of the forward-backward symmetric detector at the point where $\theta = 90°$. The Intermediate Silicon Layers, for example, are said to provide full coverage in the region $|\eta| \leq 2$.

Particles produced in a collision that travel at very small angles down the beam pipe, not passing through any parts of the detector, may carry away a significant amount of longitudinal momentum and as such it will not balance in the detector. However, since the incident proton and antiproton have no transverse momentum at all, these particles will carry away only a negligible amount and so transverse momentum can be used as a conserved quantity. For this reason, rather than using the total momentum and energy,

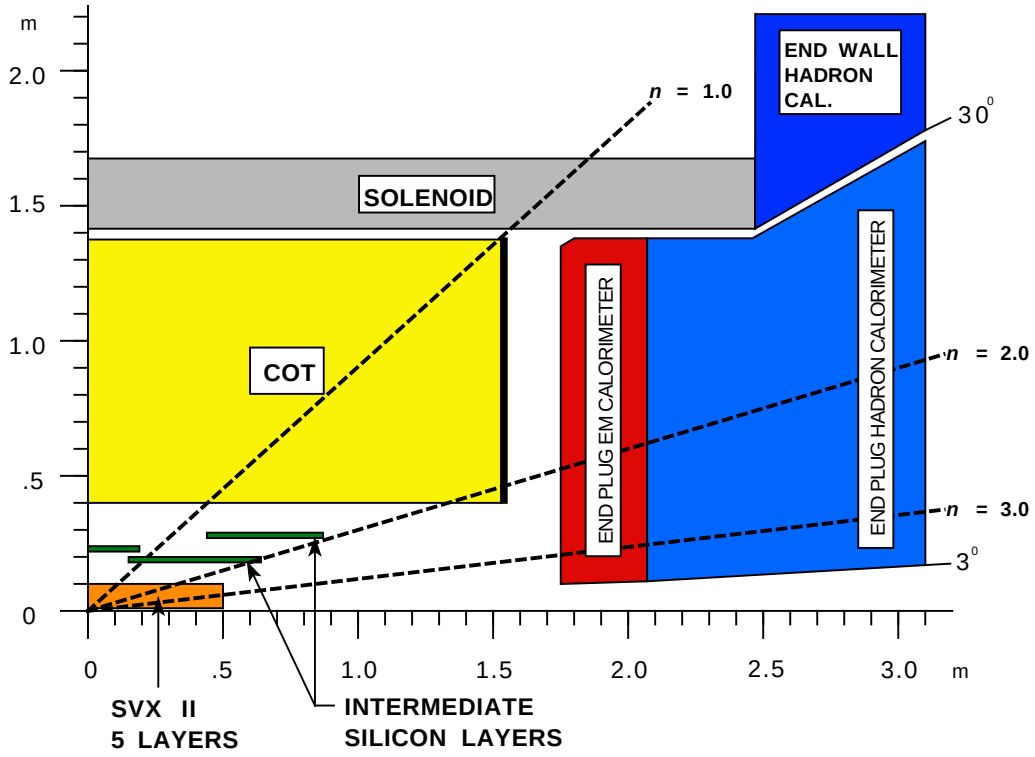

Figure 2.9: Pseudorapidity coverage of CDF detector components

when reconstructing events it is usual to work with two important kinematic variables which are invariant under Lorentz transformations along the z-axis. The transverse momentum of a particle is defined as the projection of the momentum vector onto a plane perpendicular to the beam axis:

$$p_{\mathrm{T}} = p \sin\theta$$

where p is the particle's momentum as measured by the CDF tracking system. Similarly, the transverse energy of a particle is defined as

$$E_{\mathrm{T}} = E \sin\theta$$

where E is the energy measured in the calorimeter. A related quantity is the

negative vector sum of E_{T} in an event, called the missing transverse energy. This usually corresponds to the energy carried away by non-interacting particles like neutrinos, but it can also be associated with mismeasurements in the calorimeters.

2.3 Tracking Detectors

A particle produced in a collision at CDF will first pass through the tracking detectors, which are enclosed within a superconducting solenoidal coil. The solenoid, which is 3 m in diameter and 5 m long, generates a 1.4 Tesla magnetic field parallel to the beamline. This field is required so that charged particles travel along a curved path, the curvature of which allows their momenta to be determined. The CDF tracking system consists of three silicon detectors and a drift chamber called the Central Outer Tracker (COT). Selected properties of the CDF tracking systems are listed in Table 2.1. The radiation length, X_0, is the average length in a specific material over which a relativistic charged particle will lose two thirds of its energy by bremsstrahlung.

	Coverage	Layers	Position resolution	Thickness (X_0)
L00	$\eta \leq 4$	1	6 μm (axial)	0.7%
SVXII	$\eta \leq 2$	5	12 μm (axial)	7.4%
ISL	$\eta \leq 2$	2	16 μm (axial)	2.0%
COT	$\eta \leq 1$	8	180 μm	1.7%

Table 2.1: Selected properties of the CDF tracking systems

2.3.1 Silicon Tracking System

The CDF silicon tracking system [26] is the component of CDF that is closest to the interaction region. It has full coverage of the region $|\eta| \leq 2$ and extends from a radius of 1.35 to 29 cm from the beamline. With an active area of almost 6 m^2 of silicon sensors and 722,000 readout channels, it is one of the biggest systems of its kind ever built and consists of three concentric detectors: Layer 00 (L00), the Silicon Vertex Detector (SVXII), and the Intermediate Silicon Layers (ISL). A cross-section of the silicon tracking system showing the pseudorapidity coverage and radial position of its three components is presented in Figure 2.10 and its properties are summarised in Table 2.2.

Layer 00

The L00 detector [27] is composed of a layer of special radiation-hard single-sided silicon microstrip sensors mounted directly on the beam pipe. The design of the L00 sensors, which must operate effectively despite the high

Layer	Radii (cm)	Axial pitch	Stereo angle	Stereo pitch
1 L00	1.35/1.62	25 μm	-	-
2 SVXII	2.5/3.0	60 μm	90°	141 μm
3 SVXII	4.1/4.6	62 μm	90°	126 μm
4 SVXII	6.5/7.0	60 μm	1.2°	60 μm
5 SVXII	8.2/8.7	60 μm	90°	141 μm
6 SVXII	10.1/10.6	65 μm	1.2°	65 μm
7 ISL(F/B)	19.7/20.2	112 μm	1.2°	112 μm
7 ISL(C)	22.6/23.1	112 μm	1.2°	112 μm
8 ISL(F/B)	28.6/29.0	112 μm	1.2°	112 μm

Table 2.2: Design parameters of the CDF silicon tracking system

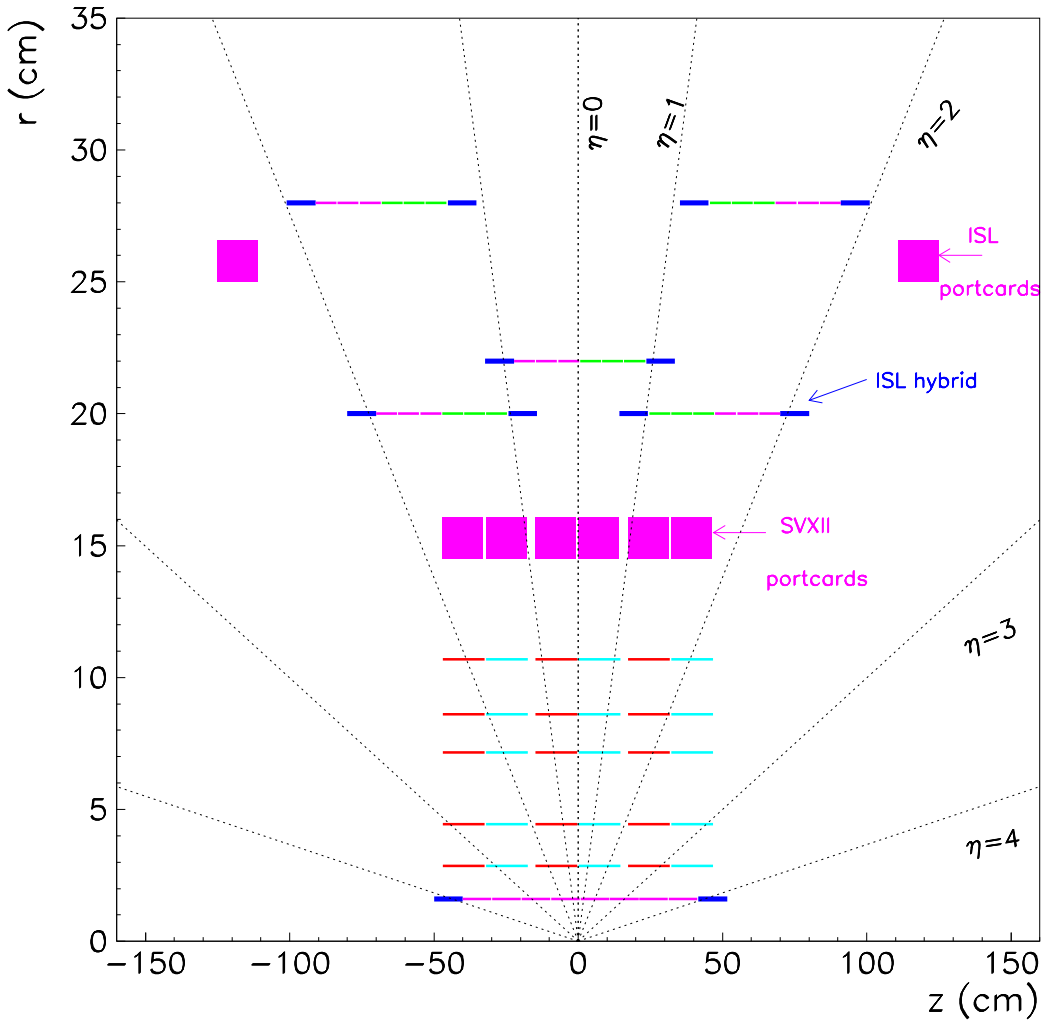

Figure 2.10: Schematic layout of the silicon tracking system

doses of radiation they are exposed to due to their close proximity to the beamline, is based on research carried out for the Large Hadron Collider at CERN. L00 is arranged into six wedges in ϕ, each wedge containing a narrow module (8.4 mm wide with 128 readout channels at a radius of 1.35 cm) and a wide module (14.6 mm wide with 256 readout channels at a radius of 1.62 cm). Both types of module consist of six sensors mounted end-to-end along

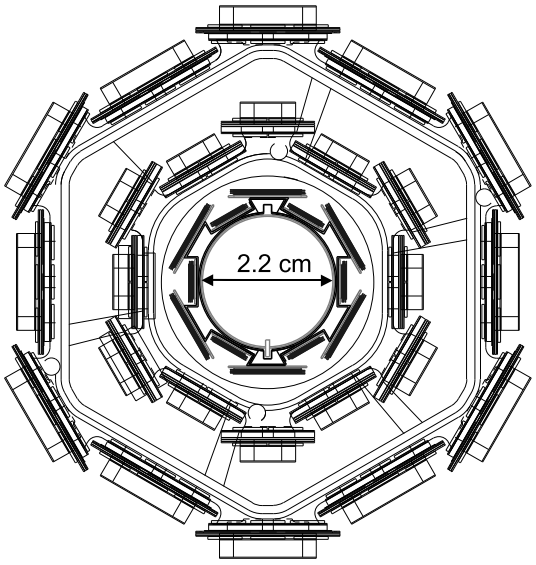

Figure 2.11: Cross-section of the CDF silicon tracker showing L00 and the two inner layers of SVXII

the beam pipe. The two widths of sensor are interleaved in a twelve-sided configuration that is illustrated in Figure 2.11. Kapton cables carry signals from each of the six pairs of sensors to the readout electronics at either end of the detector.

The motivation for having L00 so close to the interaction region is that it improves the resolution of the impact parameter measurement, which is the distance of closest approach of a reconstructed track to the primary vertex. This overall increase in the resolution of the silicon tracking system will allow CDF to compete effectively with B factories such as the BaBar experiment [28] at SLAC. For example, the presence of L00 significantly increases the vertex-finding resolution of the detector, enabling b hadron lifetimes to be more accurately determined. CDF's ambitious b-physics program depends strongly on how efficient the detector is at detecting b quarks in jets. This

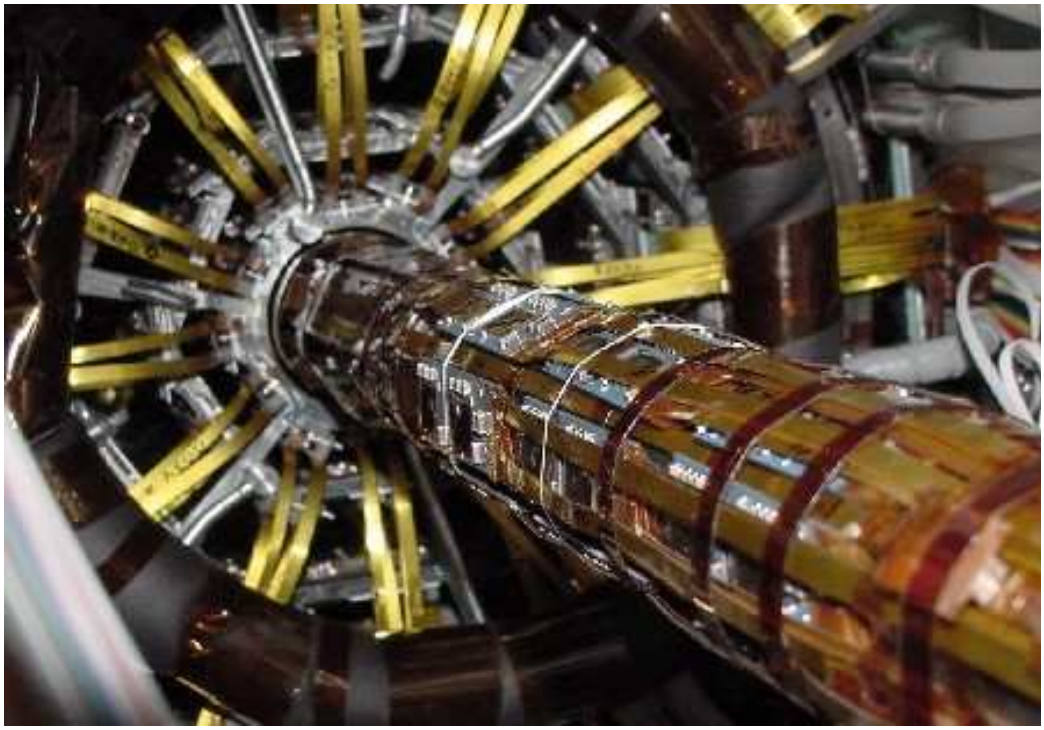

Figure 2.12: Layer 00 mounted on the beam pipe inside SVXII

is also important for top physics studies where the fraction of top events with two high transverse momentum b jets in which both jets are correctly tagged is expected to be 32% greater with L00 than without. Even if the innermost layer of SVXII were to fail due to radiation damage, the prescence of the radiation-hard L00 ensures that the overall tagging efficiency will be unaffected [29]. Figure 2.12 shows L00 in the process of being installed inside SVXII.

Silicon Vertex Detector

Energetic particles that pass through L00 will then travel through the SVXII, a device 96 cm in length which has five double-sided layers of sensors between

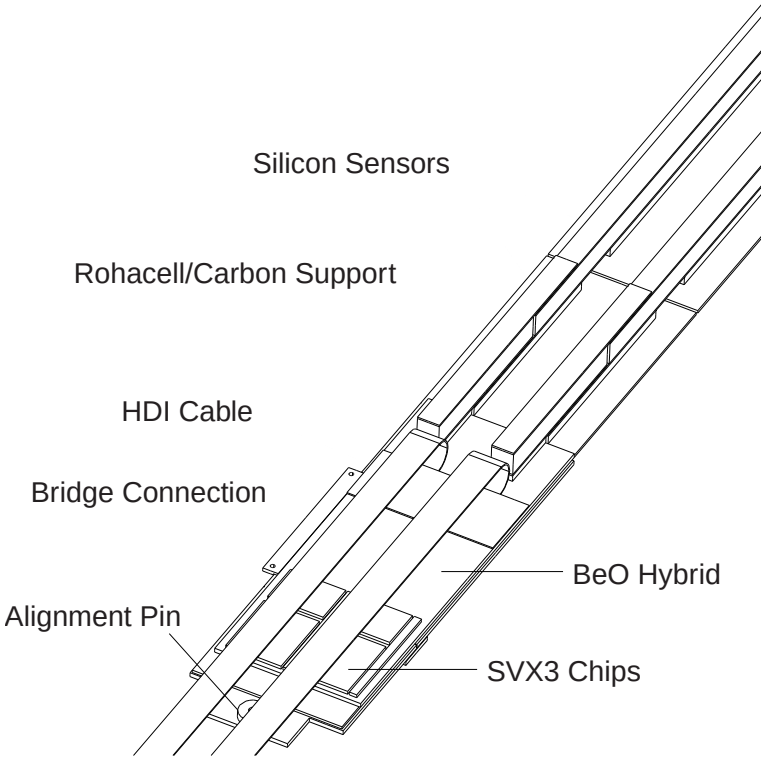

Figure 2.13: Schematic of an SVXII Layer 0 sensor

2.5 and 10.6 cm from the beamline arranged into twelve wedges in ϕ. The double-sided sensors allow 3D vertex reconstruction to be done by measuring the ϕ coordinate of a hit on one side and the z coordinate on the other. A schematic of an SVXII sensor from the innermost layer is presented in Figure 2.13. Electronics for the readout are mounted on the beryllium oxide hybrid at the end of the sensor. SVXII is divided into three identical 32 cm barrels along the beamline, with data from each barrel being read out at both ends. The arrangement of sensors can be seen in the cross section of SVXII and ISL in Figure 2.14. The design and operation of SVXII will be discussed in more detail in Chapter 3.

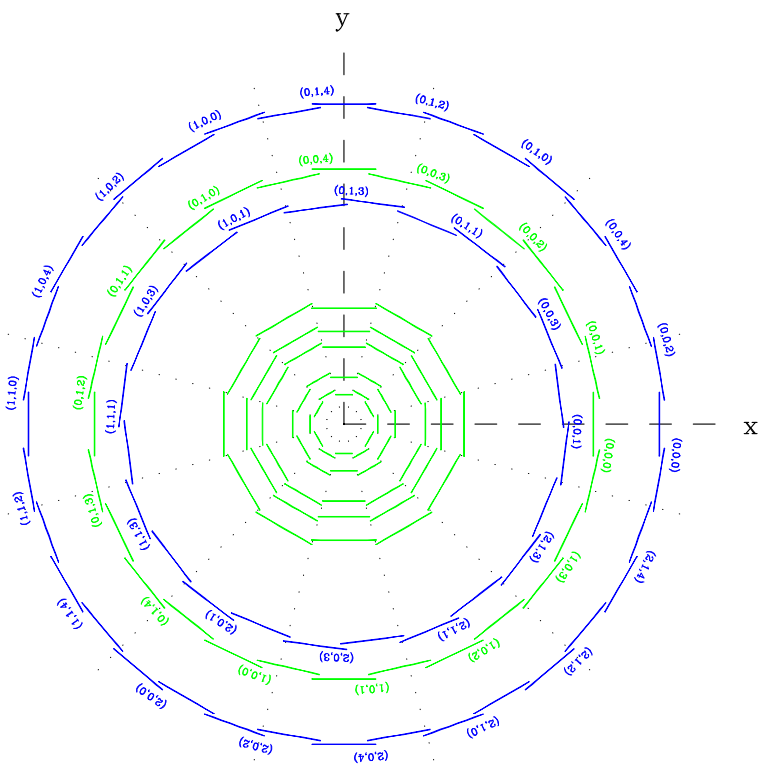

Figure 2.14: Cross section of SVXII and ISL

SVXII was designed to identify secondary vertices associated with the decay of long-lived particles. For example, when B $\rightarrow \pi^+\pi^-$ the two pions will deposit energy in each layer of SVXII that they pass through. The information recorded from each layer can then be combined to show the trajectory of the pions and their reconstructed paths will point back to where the original b hadron decayed. The distance of this vertex from the interaction point can then be used to determine the lifetime of the B. SVXII is the key tool used in b-tagging in the identification of top events and will be critical in further characterisation of the properties of the top quark.

Intermediate Silicon Layers

The ISL detector is a large silicon tracker with an active area of 3.5 m^2 located between SVXII and the COT. A cross section of ISL can be seen in Figure 2.14. It consists of one central layer (6C) at a radius of 23 cm covering the region $|\eta| \leq 1$ and two forward-backward layers (6 & 7 F/B) at 20 cm and 29 cm covering the region $1 \leq |\eta| \leq 2$. The double-sided ISL sensors with 1.2° stereo readout are mounted on a carbon fibre spaceframe with beryllium cooling ledges. Figure 2.15 shows that ISL is divided into three barrels, each of which is read out at both ends. In the central region, ISL improves overall tracking precision by providing a link between SVXII tracks and COT tracks. In the forward region, where the acceptance of the COT is significantly lower, SVXII and ISL together constitute a standalone 3D silicon tracker with up to seven axial and stereo measurements.

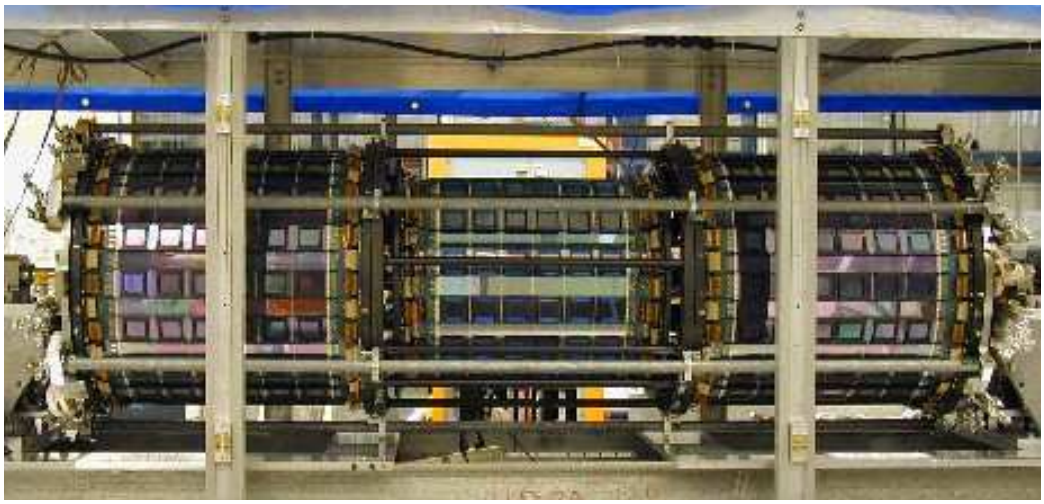

Figure 2.15: ISL under construction at the Fermilab Silicon Detector facility

2.3.2 Central Outer Tracker

The COT [30], which surrounds the silicon system, provides high resolution tracking information in the region $|\eta| \leq 1$ with radial coverage between 0.46 and 1.31 m. It is a cylindrically symmetric multi-layer drift chamber capable of performing 3D position and momentum measurements. In the central region, a COT track can be connected to a silicon track to provide excellent transverse momentum and impact parameter resolution.

The drift cells used in the detector each consist of a line of twelve sense wires making measurements along a radial track. The sense wires alternate with potential wires every 3.8 mm and run down the middle of the two cathode planes, separated by 1.76 cm, that form the walls of the drift cell. The cathode field panels consist of a 0.25 mm Mylar sheet covered with 450 Å of gold on both sides. These solid cathode panels allow the drift field to be the same as the field at the surface of the cathode. This means that the drift field can be higher than would be possible in a detector where the cathode panels were replaced by wires. The sides of each drift cell are electrostatically and mechanically closed by mylar panels. The wires and cathode planes are suspended between two aluminium end-plates. An individual drift cell is illustrated in Figure 2.16. The drift cells are filled with a gas mixture (50:35:15 Ar-Et-CF_4) with a fast drift velocity to ensure that the maximum drift time is less than the bunch spacing.

Figure 2.17 shows a section of the East end-plate of the COT. The longer slots hold the cathode planes, while the wires are held in place by the shorter slots with a notch. The drift cells are arranged in eight concentric superlayers, of which the four odd-numbered layers perform r-ϕ measurements with sense

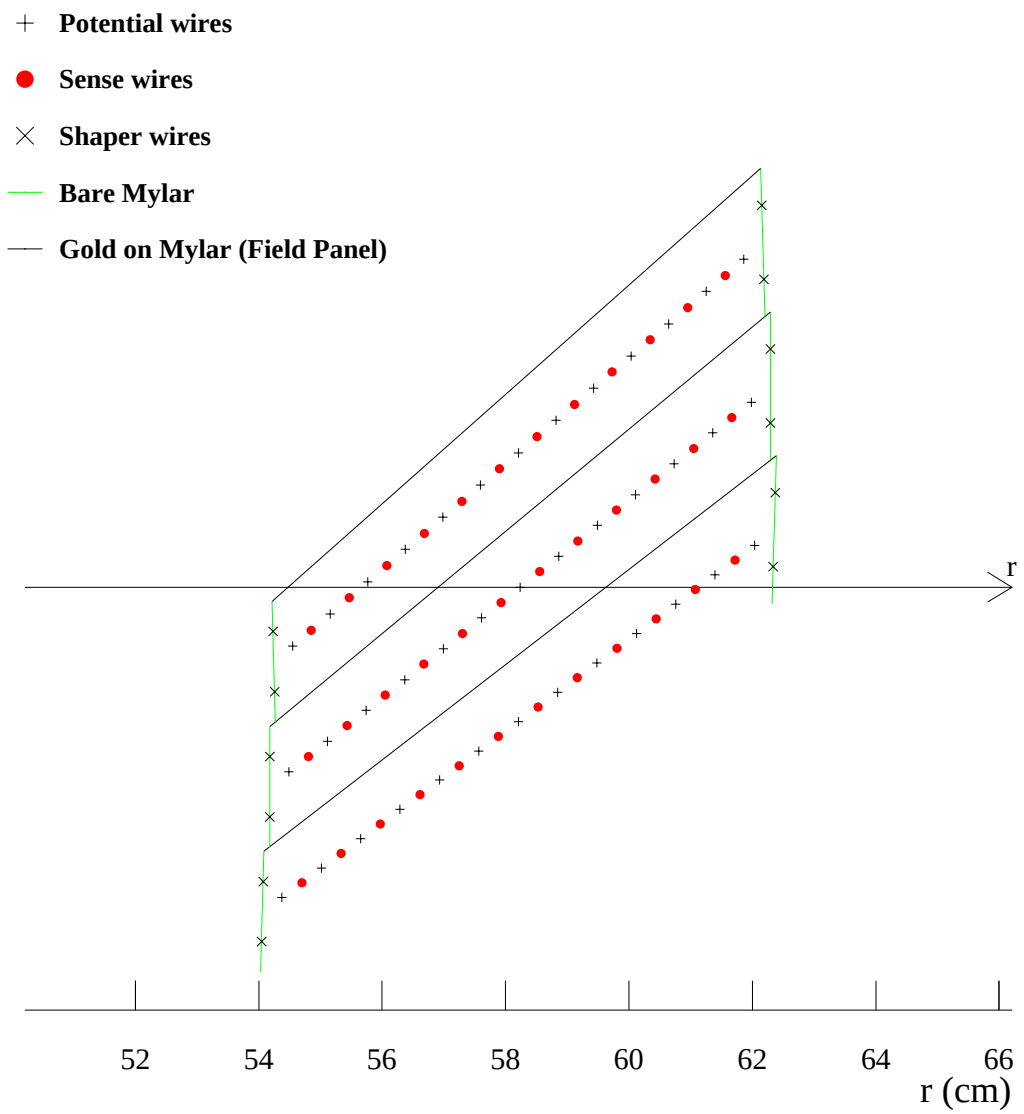

Figure 2.16: An example of a COT drift cell in Superlayer 2

wires oriented parallel to the beam. These axial layers alternate with the four even-numbered stereo layers, which have their wires positioned at an angle of $\pm 3^{\circ}$ with respect to the beam to record information about the motion of charged particles in the z direction. The cells in each superlayer are evenly spaced in azimuth and so their number increases with r. The properties of

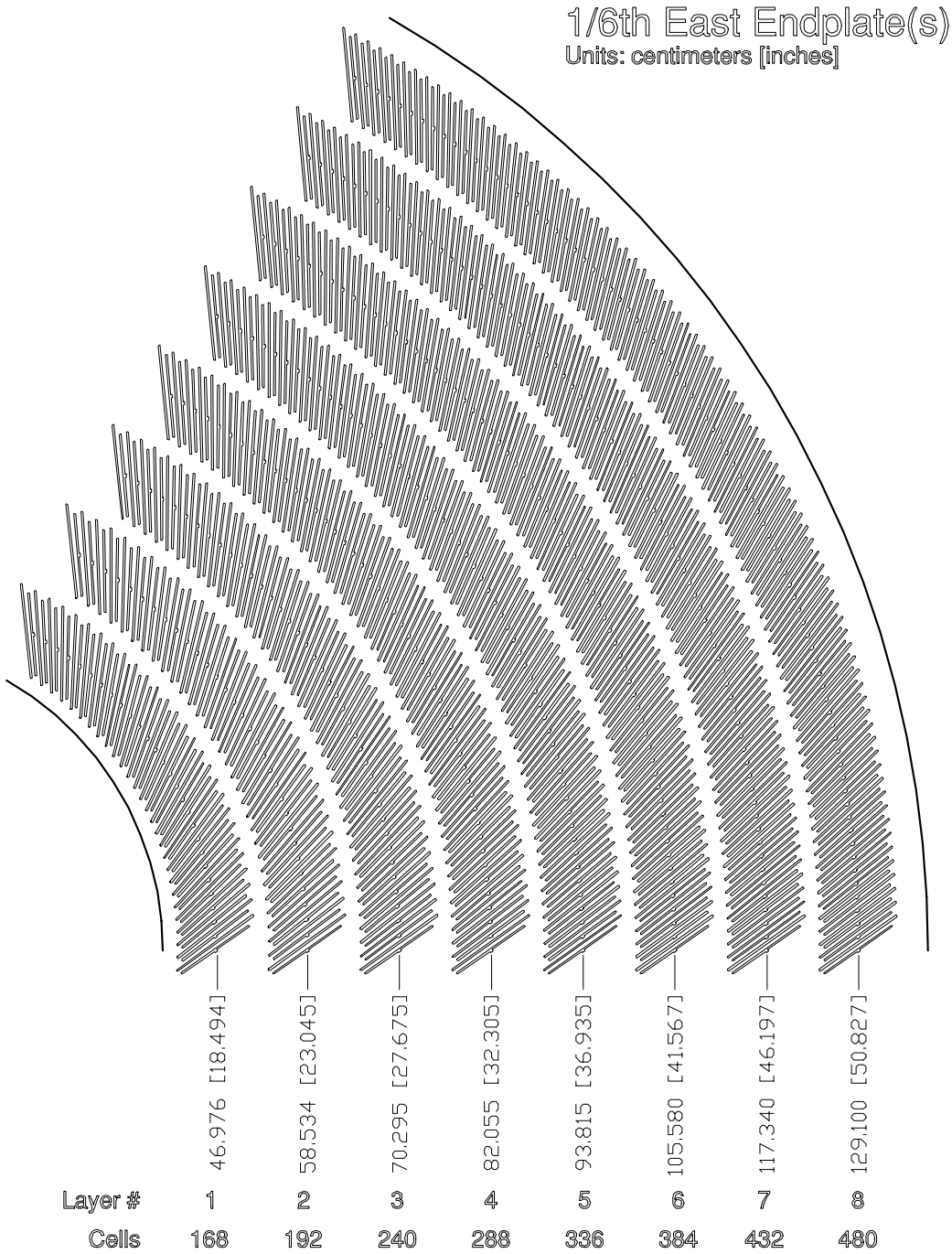

Figure 2.17: The slots for a section of the East endplate of the COT

Superlayer	1	2	3	4	5	6	7	8
Stereo angle (°)	+3	0	−3	0	+3	0	−3	0
Cells per layer	168	192	240	288	336	384	432	480
Sense wires per cell	12	12	12	12	12	12	12	12
Radius of SL (cm)	47	59	70	82	94	106	117	129

Table 2.3: Properties of COT superlayers

the eight superlayers are summarised in Table 2.3. They provide a total of 96 measurements between 44 and 132 cm, requiring a total of 2520 drift cells and 30,240 readout channels for the entire detector.

It can also be seen from Figure 2.17 that the COT drift cells are tilted with respect to the radial direction. When a charged particle ionises the gas mixture, the produced electrons will drift at a certain angle with respect to the 2.5 kV/cm electric field. This Lorentz angle β is defined by

$$\tan \beta = \frac{vB}{kE}$$

where v is the drift velocity in the absence of a magnetic field, k is a constant that depends on the composition of the gas mixture, and B and E are the magnitudes of the magnetic and electric fields respectively. In order to correct for this effect and to ensure that the crossed electric and magnetic fields produce a resultant azimuthal drift direction, the cells are angled such that the electric field is at 35° with respect to the radial direction. This offset in the configuration of the drift cells also means that a charged particle traveling radially outwards will pass close to at least one sense wire in each superlayer. The mechanical properties of the COT are summarised in Table 2.4.

COT data readout begins at the chamber face where pulse amplification, shaping, and discrimination (ASD) for two drift cells is carried out using

Number of Layers	96
Number of Superlayers	8
Material (X_0)	1.6 %
Sense wire spacing	7.62 mm
Wire diameter	40 μm
Wire tension	135 g
Drift field	1.9-2.5 kV/cm
Maximum drift distance	0.88 cm
Maximum drift time	100 ns
Tilt angle	35°
Length of active region	310 cm
Total number of wires	73,080

Table 2.4: COT mechanical properties

a single ASD chip. Signals are then carried to the end walls of the CDF collision hall where they undergo time-to-digital conversion (TDC) in one of 315 96-channel TDC modules. The TDC data is searched for hits in each superlayer and these hits are then combined into tracks. The COT performance is characterised by the impact parameter and transverse momentum resolutions. The COT position resolution is approximately 180 μm and the transverse momentum resolution is $\delta P_{\mathrm{T}}/P_{\mathrm{T}}^2 \approx 0.3\%$ GeV^{-1}c.

2.4 Time of Flight Detector

The Time of Flight detector (TOF) [31] precisely measures the time a particle takes to travel from the interaction point to the detector, from which the mass of a charged track can be calculated. This information can then be used, for example, to differentiate between kaons and pions. The TOF lies between the outer radius of the COT and the solenoid magnet, as indicated in Figure 2.7.

It consists of 216 three metre long scintillator bars with photomultiplier tubes on each end and has a single particle timing resolution of 100 ps. The presence of the TOF significantly enhances CDF's particle identification capabilities, increasing the experiment's sensitivity by identifying B decay products over a large fraction of their momentum spectrum.

2.5 Calorimetry

Outside the solenoid, the Electromagnetic Calorimeters (ECAL) are used to measure the energies of photons and electrons, while the Hadronic Calorimeters (HCAL) do the same for hadrons. The complete ECAL/HCAL systems cover the region $|\eta| \leq 3.6$ and have fast enough energy measurement response times to take advantage of the 132 ns bunch spacing proposed for the second half of Run II. Some properties of the central and plug electromagnetic and hadronic calorimeters are listed in Table 2.5. The thickness is given in radiation lengths for the EM calorimeters and interaction lengths for the hadronic calorimeters. The interaction length, λ_0, is the mean free path of a particle before undergoing an interaction in a given medium.

	Coverage	Energy Resolution	Thickness
Central ECAL	$\eta < 1.1$	$\sigma_E/E = 14\%/\sqrt{E_{\mathrm{T}}}$	19 X_0
Plug ECAL	$1.1 < \eta < 3.6$	$\sigma_E/E = 16\%/\sqrt{E_{\mathrm{T}}}$	21 X_0
Central HCAL	$\eta < 1.3$	$\sigma_E/E = 50\%/\sqrt{E_{\mathrm{T}}}$	4.5 λ_0
Plug HCAL	$1.1 < \eta < 3.6$	$\sigma_E/E = 80\%/\sqrt{E_{\mathrm{T}}}$	7 λ_0

Table 2.5: Selected properties of electromagnetic and hadronic calorimeters

2.5.1 Central Electromagnetic Calorimeter

For high energy electrons and photons passing through the ECAL, pair production ($\gamma \rightarrow e^+e^-$) and bremsstrahlung ($e^{\pm} \rightarrow e^{\pm}\gamma$) gives rise to electromagnetic showers. The calorimeters measure the energy of these showers and hence that of the incident particles.

The central electromagnetic calorimeter (CEM) [32] is divided into two physically separate halves (East and West) covering the region $|\eta| \leq 1$. Both halves contain a lead-scintillator sampling system segmented into 24 wedges, where each wedge subtends 15° in azimuth. A CEM wedge, a schematic of which is shown in Figure 2.18, consists alternately of 30 layers of lead and 31 layers of scintillator and is divided into ten projective towers pointing back towards the interaction region, each covering $\eta \approx 0.1$. The active elements of the scintillator tiles are read out by wavelength shifting fibres that direct the light to photomultiplier tubes (PMT). There are two PMTs per tower, one on either side in azimuth, with the energy of a shower being proportional to the recorded pulse height.

Each wedge also includes a 2D readout strip chamber at the position of maximum average shower development between the eighth lead layer and the ninth scintillator layer. The charge deposition on this device's orthogonal strips and wires helps identify photons and electrons by matching position measurement data with tracks, studying the transverse shower profile to distinguish photons from neutral pions, and using pulse height information to identify electromagnetic showers. A pre-shower wire chamber is also mounted between the solenoid and the CEM in order to improve direct photon measurements and low-momentum electron identification.

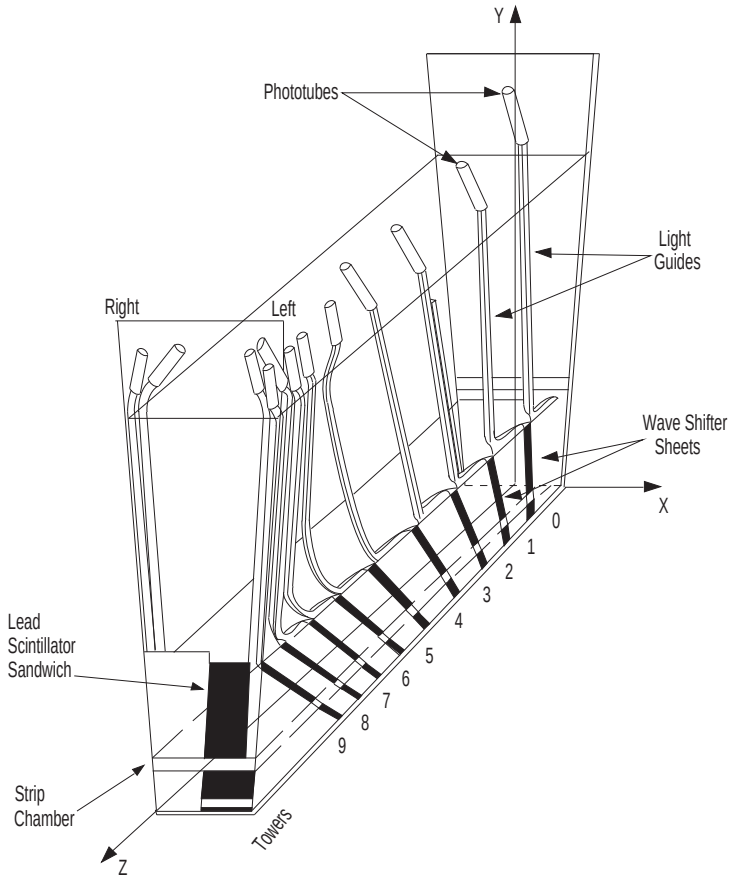

Figure 2.18: Schematic of a typical central electromagnetic calorimeter wedge

2.5.2 Central and Endwall Hadronic Calorimeter

Hadron showers occur when an incident hadron undergoes an inelastic nuclear collision, resulting in the production of secondary hadrons which in turn interact to produce tertiary particles. Hadrons may start showering in the ECAL but will only be absorbed fully in the HCAL.

Each wedge of the CEM is backed by a steel-scintillator central hadron calorimeter (CHA) [33], allowing the ratio of electromagnetic to hadronic energy to be precisely calculated for each tower. The CHA has the same

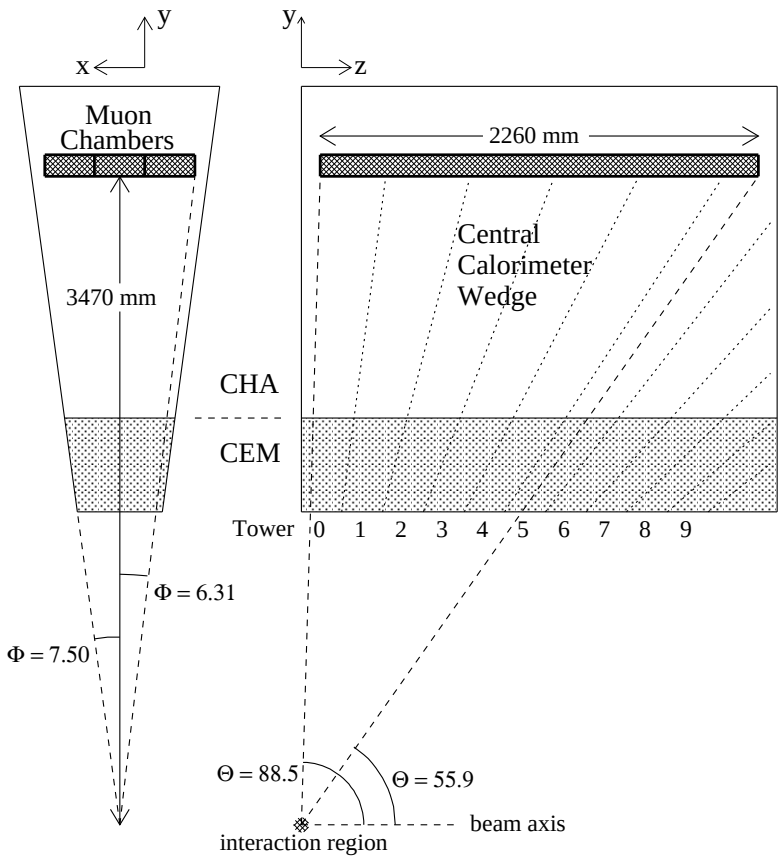

Figure 2.19: One module of the central calorimeter

projective tower structure as the CEM and is composed of 32 layers of 2.5 cm steel absorber and 1.0 cm plastic scintillator stacked in the radial direction. Figure 2.19 shows that not all of the CEM towers continue into the CHA, which only provides coverage out to $|\eta| \leq 0.9$, but this potential loss of coverage is avoided by the presence of the endwall hadronic calorimeter (WHA) in the region $0.7 \leq |\eta| \leq 1.3$. The location of the WHA in the gap between the plug and the CHA is shown in Figure 2.7 and its 6 towers can be seen to match up with those in the CEM and CHA. The WHA has 15 layers of 5 cm steel interleaved with 1 cm scintillator stacked in the z direction.

Like the CEM, in both the CHA and WHA the light from the scintillators is collected by wavelength shifters and the data is then read out by PMTs.

2.5.3 Plug Calorimeters

The plug calorimeter [34] covers the region $1.1 \leq |\eta| \leq 3.6$ and consists of an electromagnetic section containing a shower position detector followed by a hadronic section. A cross-section of the top half of one plug is shown in Figure 2.20. The detector elements are again arranged in a tower geometry, and the active elements are scintillator tiles read out by wavelength shifting fibres which carry the signals to PMTs. The electromagnetic section is a lead-scintillator sampling device with 23 layers of 4.5 mm lead and 4 mm

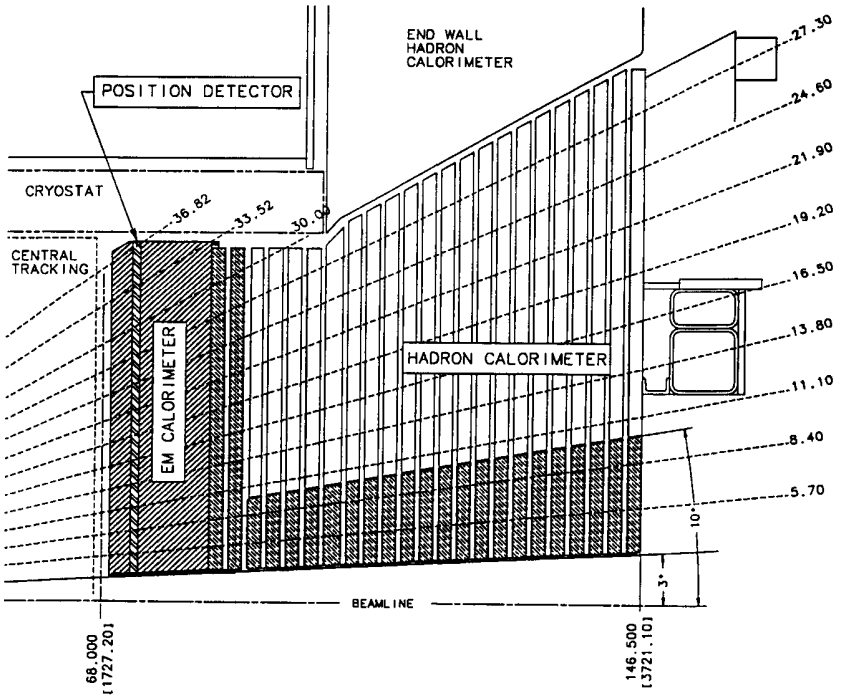

Figure 2.20: Cross-section of the upper half of the end plug calorimeter

scintillator, corresponding to a thickness of 21 radiation lengths at normal incidence. The hadronic section is a 23 layer iron-scintillator, with each layer consisting of 2.5 cm iron and 6 mm scintillator.

2.6 Muon Systems

The location of the muon detectors [35, 36] as the outermost sub-components of CDF is motivated by the fact that muons are more highly penetrating than the electrons, photons and hadrons, which are filtered out by the intervening material of the calorimeters. Four sub-systems of scintillators and proportional chambers are used to detect muons in the region $|\eta| \leq 1.5$: the

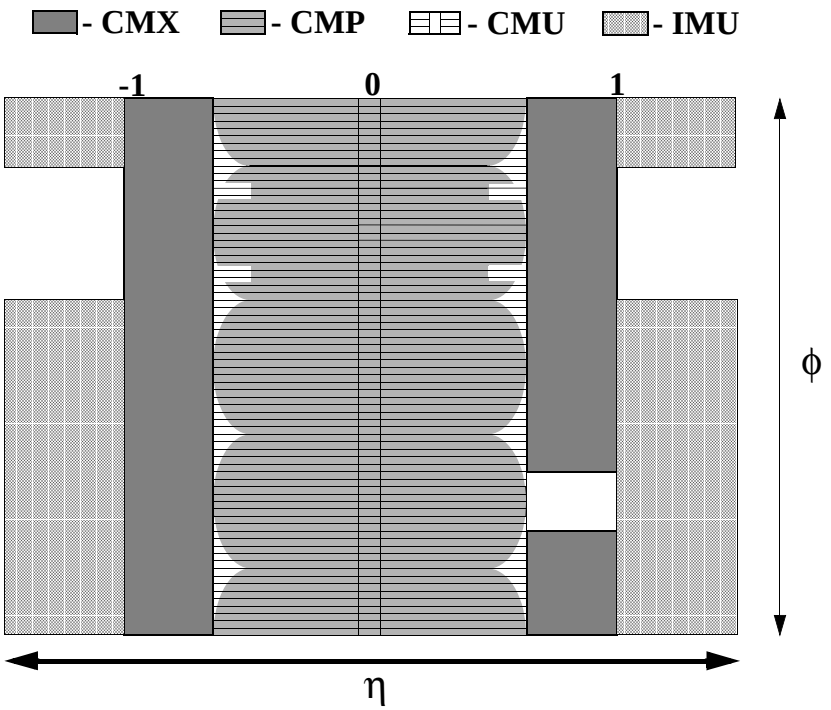

Figure 2.21: Location of muon detectors in azimuth and pseudorapidity

	Coverage	Thickness
CMU	$\eta < 0.6$	5.5 λ_0
CMP	$\eta < 0.6$	7.8 λ_0
CMX	$0.6 < \eta < 1$	6.2 λ_0
IMU	$1 < \eta < 1.5$	6.2-20 λ_0

Table 2.6: Coverage and thickness of the muon detectors

Central Muon Detector (CMU), the Central Muon Upgrade (CMP), the Central Muon Extension (CMX) and the Intermediate Muon Detector (IMU). Figure 2.21 illustrates the η-ϕ coverage of the muon detectors. The coverage and thickness of the detectors is summarised in Table 2.6. Pion interaction lengths are calculated at a reference angle of 90° in CMU/CMP, 55° in CMX and at a range of angles for IMU.

2.6.1 Central Muon Detector

The CMU drift chambers cover the region $|\eta| \leq 0.6$ and are located outside the CHA 3.47 m from the beam line. Only muons with $p_{\mathrm{T}} > 1.4$ GeV/c are energetic enough to penetrate through to the CMU and be detected. The CMU is divided into 12.6° azimuthal wedges that fit into the top of each calorimeter wedge as shown in Figure 2.19. A CMU wedge comprises three modules, each of which is composed of four layers of four drift cells. Each rectangular cell is $6.35 \times 2.68 \times 226.1$ cm and has a 50 μm diameter stainless steel resistive sense wire strung through the centre.

A CMU module is shown in Figure 2.22. There is a small ϕ offset between the first and third (and second and fourth) layers. The wires in the cells in the first and third (and second and fourth) layers are connected in the readout.

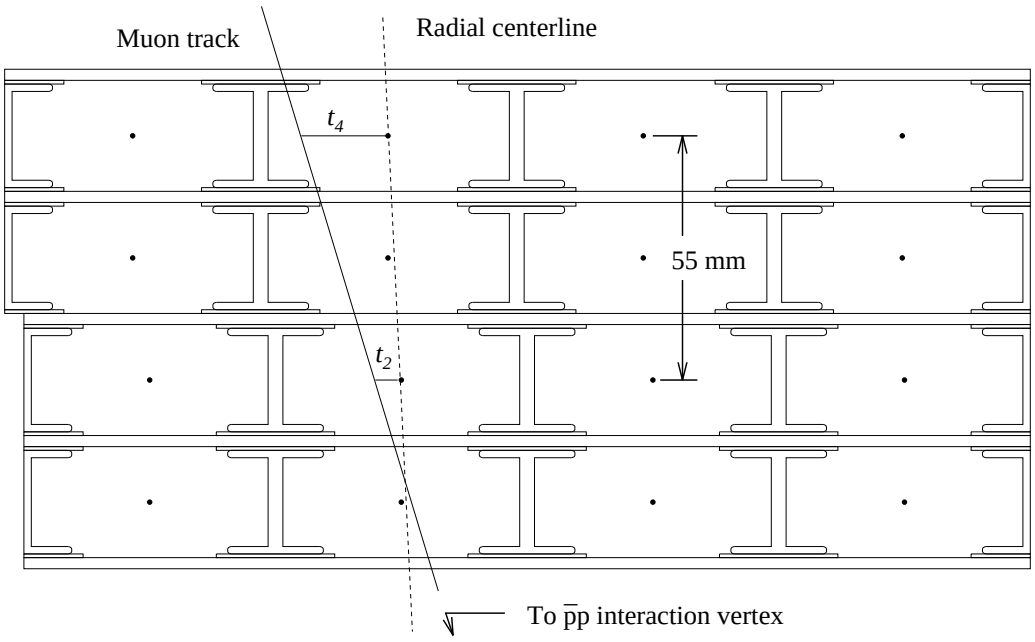

Figure 2.22: A CMU module in the $r-\phi$ plane with 4 layers of drift chambers

Each wire pair is instrumented with a TDC to measure the ϕ position of the muon and an analogue-to-digital converter (ADC) on each end to measure the muon's z position via charge division. The drift times t_2 and t_4 are used to calculate muon momentum for triggering. The position resolution of the detector is 250 μm in the drift direction (r-ϕ) and 1.2 mm in the sense wire direction (z).

2.6.2 Central Muon Upgrade

The 5.5 pion interaction lengths of material that lies between the interaction region and the CMU is not sufficient to stop around 0.5% of high energy hadrons passing through the calorimeters. Consequently the CMU has an irreducible fake muon background due to hadron 'punch-through' [37]. The

CMP was designed to reduce this effect by surrounding the central detector with a box structure of 60 cm thick steel slabs for additional hadron absorption, with an extra four layers of drift chambers positioned behind the steel. The extra material places the CMP at 7.8 interaction lengths from the beamline and only muons with $p_{\mathrm{T}} > 2.5$ GeV/c can be identified.

2.6.3 Central Muon Extension

The CMX provides additional coverage in the region $0.6 \leq |\eta| \leq 1$ and consists of two 120° arches located at each end of the central detector. Each arch has a conical section geometry which can be seen in Figure 2.6. A single arch is composed of eight modules, each of which subtend 15° in azimuth and consist of eight layers of proportional drift cells with six cells per layer. These layers are staggered in a way that allows the rectangular cells to be arranged along a conical surface. The drift cell layout shown in Figure 2.23 creates a 3.6° stereo angle between adjacent cells, allowing measurement of the pseudorapidity of a track. At 180 cm in length, the 48 drift cells in a module are shorter than their CMP counterparts but otherwise identical.

Eight scintillation counters are installed in each CMX module, four each on the inside and outside surfaces. These counters are read out by PMTs located on opposite ends of the module for each of the two surfaces. The superior timing resolution of these counters is used to reject large fake muon backgrounds, due to particles scattering in the beam pipe, as the fake hits are not coincident with the beam crossing.

On the West side of CDF, the 30° azimuthal gap between the two arches at the top of the detector is filled with an additional two CMX-type modules.

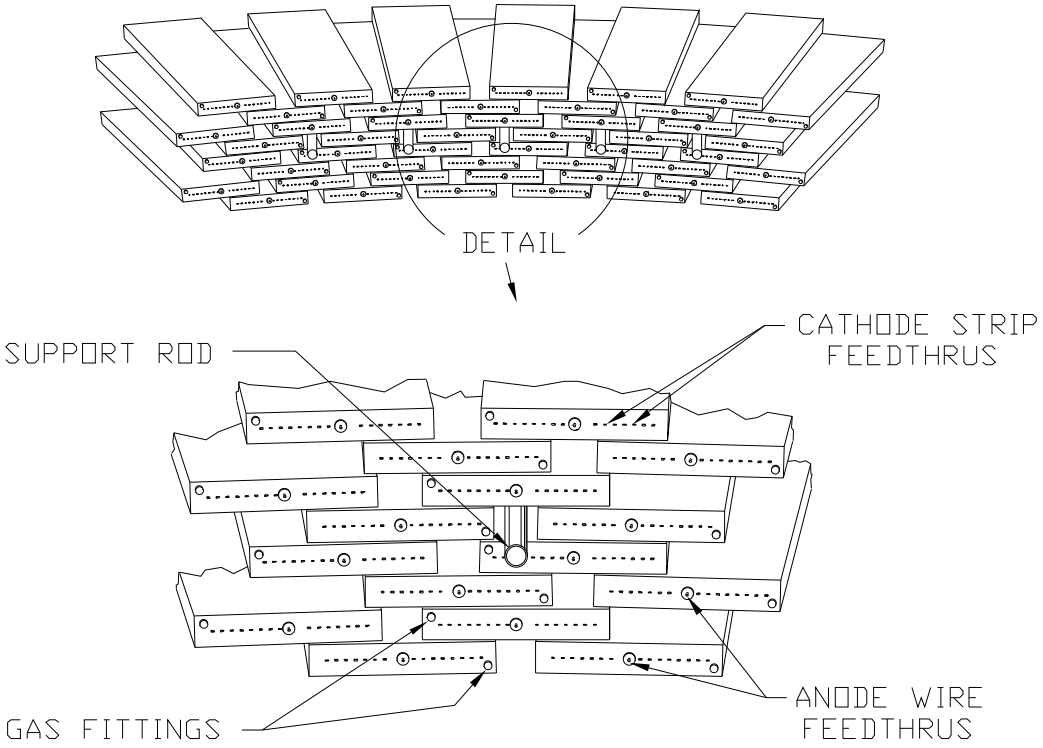

Figure 2.23: Proportional drift cell layout in a CMX module

However, as can be seen in Figure 2.21, this gap is not instrumented on the East side as it interferes with the location of the cryogenics system for the solenoid. The 90° gap between the two arches at the bottom is filled with a fan-shaped 'mini-skirt', which is located in a narrow vertical slot in the floor of the collision hall and consists of a similar arrangement of drift cells and counters.

2.6.4 Intermediate Muon Detector

The IMU is designed to exploit the ability of the silicon tracking system to reconstruct tracks with $|\eta| > 1$ by triggering on muons with $|\eta| \leq 1.5$ and

identifying them out to $|\eta| \approx 2$.

The detector consists of a barrel of drift chambers and scintillation counters mounted around a pair of steel toroids placed up against the plugs at either end of CDF. Additional counters located between the toroids and on the endwall are used for triggering. The drift chambers, which are almost identical to those used in the CMP, cover only the top 270° of the toroids. The gap in coverage due to the collision hall floor is evident in Figure 2.21.

2.7 Trigger

In hadron colliders the frequency of proton-antiproton collisions is much higher than the rate at which data can be recorded. There are approximately 7.6 million collisions per second but less than 50 of these are able to be recorded. Therefore it is important that the few events which are stored are the most interesting ones. The CDF trigger system is responsible for selecting these events with high efficiency.

A block diagram of the 3-level trigger system is shown in Figure 2.24. The Level 1 trigger receives data from the calorimeters, muon chambers and COT. During the 5.5 μs decision time it uses information on the number and energies of electrons, muons and jets in an event to determine whether it should be rejected or if it is sufficiently interesting to be retained for further processing by the Level 2 trigger hardware. The Level 1 trigger has an Extremely Fast Tracker (XFT) which allows tracks to be reconstructed in the COT in the r-ϕ plane. These tracks are then matched by the extrapolation boards (XTRP) to an ECAL energy cluster for improved electron identification or to a muon stub to improve the muon identification and momentum

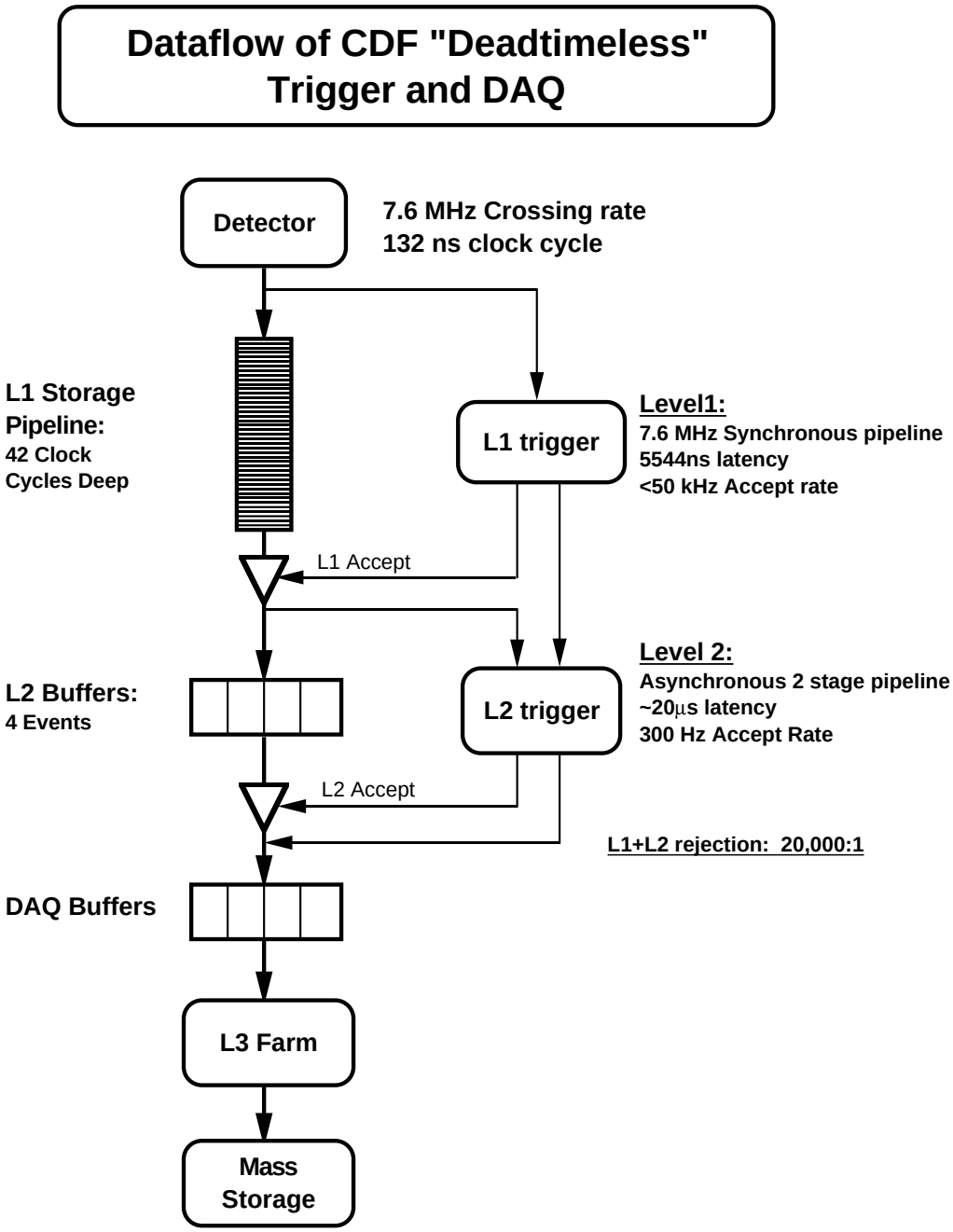

Figure 2.24: Block diagram of the CDF trigger system

resolution. The Level 1 system is pipelined with data buffering for the 42 beam crossings that would occur during the 132 ns bunch-crossing time that was anticipated during the design phase.

Data accepted by the Level 1 trigger is transferred to one of four Level 2 buffers where there is a 20 μs decision time, allowing up to 300 events to be accepted by Level 2 each second. The Level 2 trigger includes the silicon vertex tracker (SVT) [38], which uses SVXII to provide secondary vertex information, high track momentum resolution, and precision matching between muon stubs and COT tracks from the XFT.

A Level 2 trigger accept results in all the detector information associated with that event being read out. The data is collected by Data Acquisition (DAQ) buffers and transferred to a Level 3 processing farm where the event is analysed in more detail using sophisticated algorithms and the full set of detector information not available to the lower level triggers. A final decision is then taken on whether or not to store the event permanently. Events are accepted by Level 3 at a rate of 30-50 Hz.

2.7.1 Dimuon Trigger

The dimuon trigger played a crucial role in selecting events for this analysis. Since both muons must lie inside the active region of the detector, the trigger benefits from extensive tracking and muon detector coverage. Requiring the simultaneous presence of two muons in an event reduces the background rate significantly.

For an event to pass the trigger it must contain two oppositely charged tracks, both of which are matched to stubs in the muon chambers. The

invariant mass of the $\mu^+\mu^-$ pair may then be calculated and used to determine whether they were produced in the decay of a J/ψ, Υ, or something else. Details of the selection criteria used by the dimuon trigger at Levels 1, 2 and 3 in this analysis are given in Chapter 6.

2.7.2 Secondary Vertex Trigger

As discussed in Chapter 1, b hadrons can travel several hundred microns before decaying. The resolution of the SVXII detector allows precise track position measurements to be made close to the interaction point. It is therefore possible to identify secondary vertices and recognise B events. The secondary vertex position resolution depends on the number of tracks in the event, the angle between two tracks, and the single track position resolution.

As a simple example, Figure 2.25 illustrates the projection of a symmetric two-track secondary-vertex event onto the transverse plane. The two individual tracks have a position resolution $\sigma_{\rm d}$, and the error on the distance between the primary and secondary vertices is $\sim \sigma_{\rm d}/\sin(\phi/2)$, where ϕ is the angle between the two tracks. When the angle between secondary vertex tracks is small the tracks will also pass close to the primary vertex. Therefore it is desirable for the reconstructed tracks from the B decay products to form wide angles between each other so that the secondary vertex position can be resolved more accurately. In an event with a large number of tracks there is not enough time for the trigger to examine all the secondary vertex candidates. Instead, the trigger selects events that have one or two tracks displaced far from the primary interaction point since this type of track must originate in a secondary vertex.

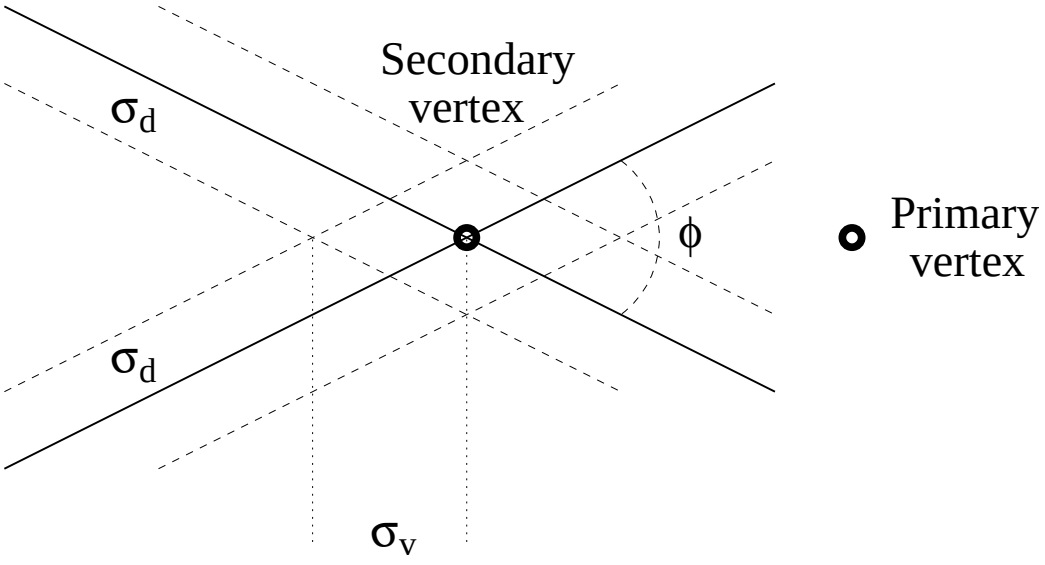

Figure 2.25: Secondary vertex event projected on the transverse plane

Once an event passes the secondary vertex trigger it can be fully reconstructed. The particle that decayed at the secondary vertex can then be identified from invariant mass measurements using information on the momenta and energies of its decay products. In the case of B $\rightarrow$ J/ψ X events, the J/ψ's decay so quickly that the B decay vertex can be derived from the intersection location of the two muons.

Chapter 3

The Silicon Tracking System

The main detector subsystems used in this analysis are SVXII, COT and the muon chambers. This chapter explores SVXII in more detail and describes its construction at the Fermilab Silicon Detector facility (SiDet) and its subsequent installation into the main CDF detector.

3.1 SVXII Ladders

Mounted between the two beryllium bulkheads of each SVXII barrel are a total of 60 silicon ladders, twelve per layer. The five layers of the SVXII are labeled Layers 0 - 4, bulkheads are numbered from 0 to 6 and wedges from 0 to 11 so that, for example, SB3W2L4 refers to SVXII Bulkhead 3 Wedge 2 Layer 4. A single ladder is made up of four individual double-sided silicon microstrip sensors, which are wire-bonded electrically in pairs. The sensors are double-sided to enable 3D vertex reconstruction and to improve the level of background rejection. The sensors are made of n-type bulk silicon implanted with longitudinal hole-collecting p^+ strips on the top of the ladder to measure r-ϕ hit positions. On the underside, the Layer 0, 1 and 3 devices

have orthogonal electron-collecting n^+ strips to measure the r-z coordinates, while Layers 2 and 4 have a small angle (1.2°) stereo configuration, similar to all ISL ladders, that provides better position resolution. A cross-section of a typical 0-90° sensor is shown in Figure 3.1.

When a reverse bias potential is applied, the region around the interface between the bulk silicon and doped implants is depleted of charge carriers and an electric field is set up. Electron-hole pairs, produced by ionisation when a charged particle passes through the detector, drift to their respective electrodes, depositing charge and inducing a current signal. The charge produced at the electrodes gives rise to a total current flow, which is proportional to the energy deposited by the incident particle. However, there is normally an additional 'leakage' current that is not due to the presence of an ionising particle. This current, which is proportional to the area of silicon in the ladder, leaks between two electrodes under voltage and is usually of the order of 10 μA. Radiation damage can increase the leakage current, which if large enough may impair the operation of the detector by decreasing the signal-to-noise ratio.

The silicon sensors are AC-coupled to the readout electronics by capacitors integrated onto each strip implant. The capacitors consist of a 200 nm layer of silicon dioxide placed between the implanted strip and the aluminum strip, which is connected via a wire bond to the signal preamplifier. This is done to avoid the leakage current of the sensors being integrated by the preamplifier, which would cause a reduction in the signal-to-noise ratio of the devices. However, microscopic cracks called pin holes occasionally appear in the silicon dioxide and allow current to flow (see Section 3.2.2).

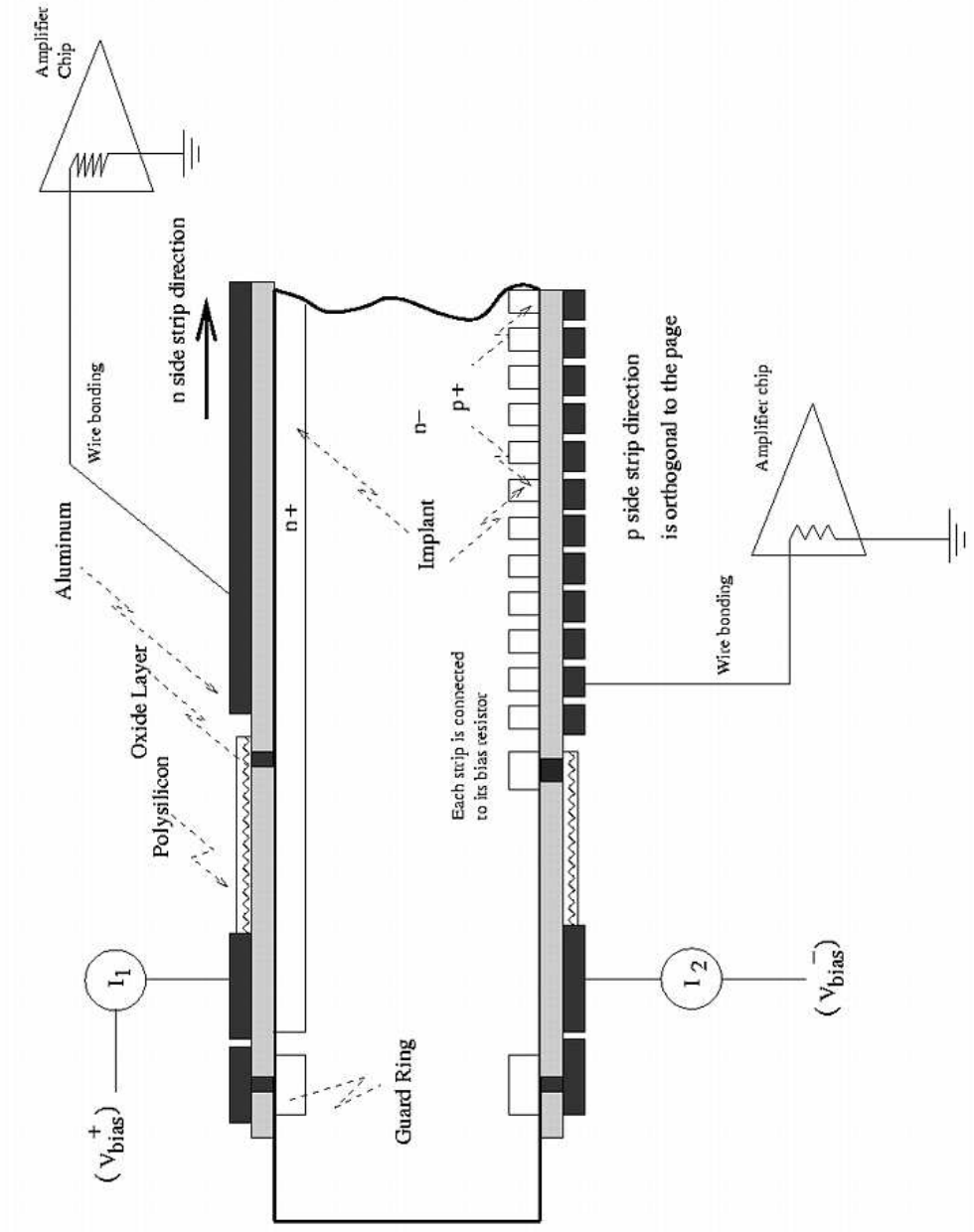

Figure 3.1: Typical design of a silicon microstrip detector

Readout coordinates	r-ϕ, r-z
Number of barrels	3
Number of layers per barrel	5
Number of wedges per barrel	12
Ladder length	20.9 cm
Combined barrel length	87.0 cm
Radius of innermost layer	2.44 cm
Radius of outermost layer	10.6 cm
Stereo angle	90°, 90°, 1.2°, 90°, 1.2°
r-ϕ readout pitch	60, 62, 60, 60, 65 μm
r-z readout pitch	141, 125.5, 60, 141, 65 μm
r-ϕ chips per ladder	4, 6, 10, 12, 14
r-z chips per ladder	4, 6, 10, 8, 14
r-ϕ readout channels	211,968
r-z readout channels	193,536
Total number of channels	405,504
Total number of chips	3168
Total number of sensors	720
Total number of ladders	180

Table 3.1: SVXII detector parameters

The ladders are read out separately at each end of the ladder by custom-designed radiation hard SVX3D chips [39, 40], which are mounted on electrical hybrid integrated circuits attached to the surface of the sensors. The hybrids on each side of the silicon are connected by a ceramic jumper on the side of the ladder. The sensors and hybrids are supported by carbon fibre rails along the full length of the ladders, which are in turn supported at the ends of each barrel by the beryllium bulkheads to which they are fixed.

A single SVX3D chip serves 128 readout channels and contains a charge sensitive amplifier, a 47 cell pipeline and an Analogue-to-Digital Converter (ADC). A Layer 0 ladder has four chips at each end (two for r-ϕ readout and two for r-z) and this number gradually increases to 14 for the much

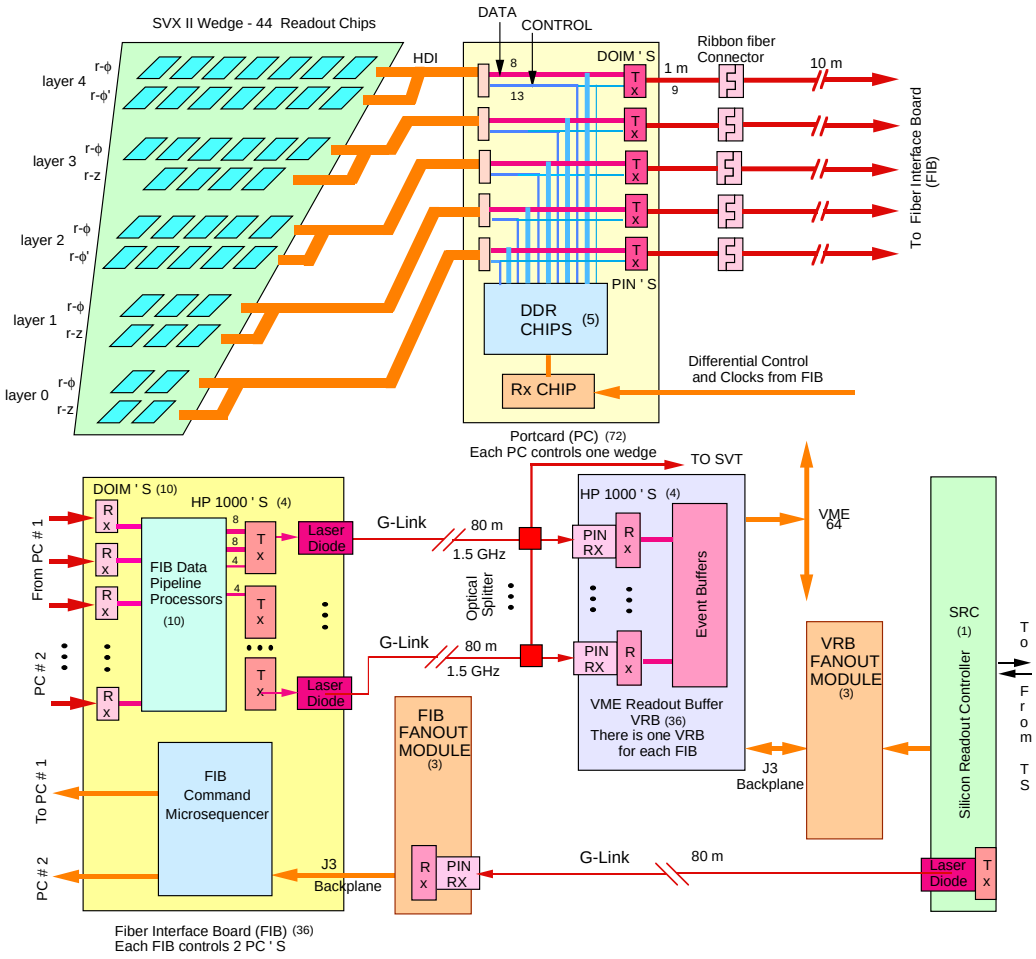

Figure 3.2: Schematic of the SVXII Data Acquisition system

wider Layer 4 ladders. A list of SVXII detector parameters is presented in Table 3.1. The number of chips in a half-ladder for each layer is illustrated in a schematic of the SVXII DAQ system in Figure 3.2. In total, there are 44 chips in each wedge and 3168 in the entire SVXII detector. The chips have been designed for deadtimeless operation, i.e. digitisation and readout can occur simultaneously with new analogue data being entered into the pipeline. The SVXII DAQ system is highly parallel, and as such it allows all 405,504

channels of the detector to be read out in approximately 5 μs.

The information from all the chips in a wedge is carried to a single Port Card (PC) by High Density Interconnect (HDI) cables, one for each layer of silicon. The PCs are the primary connection points for all the ladders and are mounted on rings wrapped around the barrels, which are inaccessible when SVXII is installed inside the COT. Each PC takes the digital output from its corresponding chips and converts it to optical signals via Dense Optical Interface Modules (DOIMs). These allow pulses to be transmitted without any of the crosstalk associated with normal metallic conductors. The DOIMs transfer the data from each pair of PCs along optical fibres to a single Fibre Interface Board (FIB). At the FIBs, the optical signals are converted back into digital data and read out to the VME Readout Buffers (VRB). A VRB serialises the data and passes it to the Silicon Readout Controller (SRC). The data is then carried to event buffers where it is stored until a decision is reached on whether or not to retain it. The FIBs are also programmed with timing sequences and generate control signals for the PCs based on commands from the SRC. These signals are sent to the chips via the HDIs and it is also through the HDIs that the PCs are able to regulate the power supplied to the chips. The yellow HDI cables are visible in Figure 2.12 extending from each layer to connect to the corresponding PCs.

3.2 SVXII Barrel Assembly

In Summer 2000, the three SVXII barrels were assembled in a clean room at SiDet where a test stand was set up to test all of the ladders immediately prior to installation. This section describes the procedures used to test the

SVXII ladders and discusses some of the results of those tests.

3.2.1 Testing Procedure

During construction the barrels were numbered 1, 2 and 3 according to the order in which they were assembled. (Barrel 1 $\equiv$ Bulkheads 2 & 3, Barrel 2 $\equiv$ Bulkheads 4 & 5, Barrel 3 $\equiv$ Bulkheads 0 & 1.) Prior to their arrival in the barrel assembly area all ladders had been thoroughly tested and graded. Since Barrel 1 had been designated as the central barrel of SVXII, the ladders selected to be installed were those deemed to be of the highest quality based on the results of those tests. Twelve ladders were assigned to each of the five layers along with a small number of spares.

Two main tests were carried out on each of the ladders installed in SVXII. The purpose of the first pre-installation test was to check for any new problems that may have developed. Any necessary repairs could be carried out more easily if the ladders were not yet installed in the barrels. The ladders were tested again after installation to ensure that they had not been damaged during the installation process.

Each half-ladder was tested individually by connecting it to a PC and taking a 2000 event run using the SVXII DAQ. The detectors were operated with a clock frequency of 50 MHz and 132 ns bunch crossing. Histograms generated during the tests were compared with those produced during earlier tests conducted after the ladders were first assembled. Lists of noisy and disconnected channels for each half-ladder were produced automatically and compared with existing data. The grading of a ladder was based mainly on the percentage of noisy or disconnected channels, and so a device with a large

number of new noisy or disconnected channels would be rejected in favour of one of the designated spares. The histograms were also checked for pin holes and any other inconsistencies with existing records that could indicate a problem with the ladder or one of its chips. The symmetry of the currents drawn on the cathode and anode was also checked, unequal values being the main indicator of the presence of a pin hole. Finally, the leakage current was monitored to ensure that it was consistent with design specifications.

Prior to installation, the ladders were enclosed in protective aluminum boxes containing pipes connected to a water-based cooling system that was used to cool the readout electronics on the hybrids. A nitrogen dry air supply was also connected to prevent condensation inside the box. The cooling system helped to reduce the value of the leakage current, which is highly dependent on temperature. Ladders were cooled to between 10°C and 15°C. It was decided not to cool them down to the temperatures in which they currently operate in CDF (< 10°C) because of the increased risk of condensation. Once the ladders were removed from their boxes and installed on the barrel they were fully exposed to the environment of the clean room. There was no nitrogen flow at the barrel, but the hybrids were cooled by the barrel's own water-based cooling system which is integrated into the bulkheads.

To satisfy internal alignment requirements and also to ensure that particles cannot pass between two wedges undetected, there is a small overlap between adjacent ladders in a layer. Consequently each layer consists of six inner detectors and six outer detectors positioned alternately at two slightly different radii. During barrel construction the six inner ladders of a layer

were installed and tested first. If a serious problem with one of the inner ladders was not identified until after all twelve ladders had been installed then the two neighbouring outer ladders would also have had to be removed before the faulty device could be extracted from the barrel for repair. After the six outer ladders were installed the inner ladders were then re-tested to ensure that none of them had been damaged in the process.

The pedestal value for a single channel in the silicon detector represents the mean output voltage when there is no beam in the machine. These are then reference values to compare it to when reading actual data. The standard deviation on this pedestal is called the noise. As a further refinement, it is possible to get a more accurate estimate of the noise for a given channel by subtracting the noise for one channel from its neighbour's noise. This is called the differential noise and is a better estimate for an individual channel as noise characteristics shared by all the channels in the chip are subtracted out. For a particular strip, the noise and differential noise are defined as

$$\text{noise} = \sqrt{\overline{q_i^2} - \overline{q_i}^2}$$

$$\text{d-noise} = \frac{1}{\sqrt{2}} \sqrt{\overline{(q_i - q_{i+1})^2} - \overline{(q_i - q_{i+1})}^2}$$

where q_i is the pulse height in strip i.

Figure 3.3 shows the pedestal and noise for the half-ladder SB5W5L2. The chip boundaries are visible at 128 channel intervals where there are small shifts in the height of the pedestal. This is a Layer 2 device with ten chips in total. The first five chips in Figure 3.3 are from the r-ϕ side of the ladder and the remaining five are r-z readout chips. The d-noise was studied to ensure that it was equal to the noise. Common mode noise was observed when the noise level was seen to be higher than the d-noise. This common

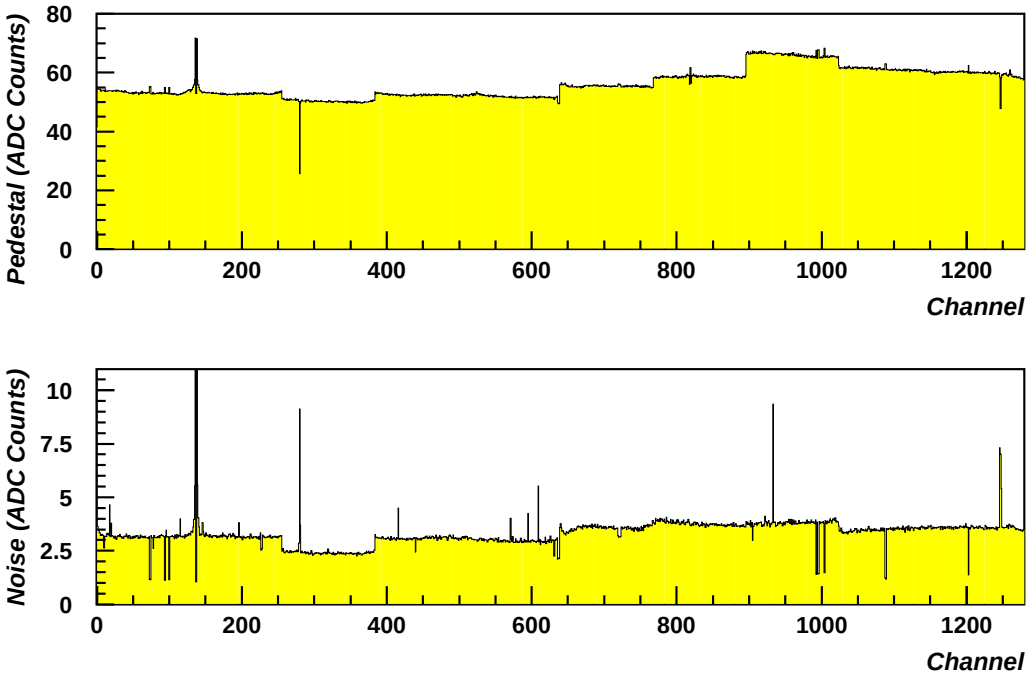

Figure 3.3: Pedestals and noise for SB5W5L2 prior to installation

mode noise is a contribution to the total noise that is often caused by ground loops.

3.2.2 Test Results

Most ladders that were installed in SVXII had relatively uniform noise versus channel, no common mode noise, and very few noisy or disconnected channels. However, among the approximately 450 individual half-ladders (including spares) that were tested during the period of barrel construction, there were a number of devices with problems discovered in pre-tests that had to be fixed before they could be accepted for installation. Occasionally a problem did not manifest itself until after installation, requiring in some

cases that the ladder be removed from the barrel. There were three main failure modes encountered during testing: (i) the presence of pin holes in the ladder, (ii) readout errors caused by problems in the SVX3D chips, and (iii) an excess of noisy channels that affected mainly Layer 2 devices.

Pin holes

Some of the ladders tested failed as a result of defects in the silicon. The most common of these was a pin hole, which is a microscopic crack in the 200 nm layer of silicon dioxide between the implant and the aluminium strip. This thin layer acts as a capacitor and any cracks in it provide a direct connection between the implant and the aluminum, allowing the current to flow into the preamplifier. When both sides of a sensor are biased a pin hole connects to the amplifier input, hence grounding the implant strip that is at high voltage and this gives rise to a very high current on one side. Pin holes were identified as low noise channels with very noisy neighbours. A total of 16 pin holes were discovered during the testing process. Figure 3.4 shows a pin hole at channel 450 (channel 194 on the r-z side) of the half-ladder SB2W1L0, which was repaired prior to installation. The noise in channel 450 appears equal to that of a disconnected channel due to saturation of the preamplifier. However, this evidence alone is not conclusive as a pin hole will always be accompanied by an asymmetric current. The pin holes were dealt with by pulling the wire bond from the offending channel. Once this channel was fully disconnected its neighbours were no longer noisy.

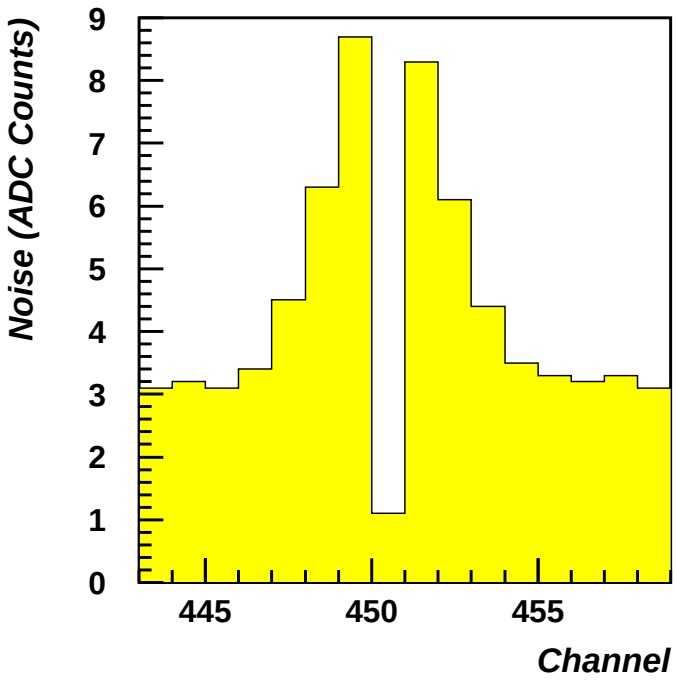

Figure 3.4: A pin hole at channel 450 of SB2W1L0

Initialisation and readout errors

Prior to the start of a run, the SVX3D chips on the ladder being tested were initialised and a short stream of settings were sent to the chips by the FIB and read back. The chips failed to initialise successfully if the data that was read back did not match that which was written. Initialisation also failed if there was a bad connection and power did not reach the chips.

The other failure mode related to the electronics was that of readout errors, which corrupt the data taken during a run. There are many different types of readout errors, any one of of which could indicate either a serious problem with a chip or damaged wire bonds on the control lines. One ladder had to be pulled from each of the three barrels as a result of readout

error problems that developed after installation. However, most readout and initialisation problems encountered during testing were not due to the ladders but due to the PC. The PCs used were mechanically very sensitive and ladders were frequently being connected and disconnected, resulting in the failure of a large number of PC channels.

3.2.3 Grassy Ladders

Some devices that were tested displayed a variation in noise level with channel number where the noise differed by a large amount from one channel to the next. The term 'grassy' was adopted to describe ladders with this feature that was observed in many Layer 2 ladders and a small number of Layer 4 ladders, all of which were manufactured by Micron Semiconductor. The problem did not affect Layers 0, 1 or 3, which were produced by a different manufacturer, Hamamatsu Photonics.

The large number of new noisy channels that constitute the grass had generally not been seen in any previous tests, and in most cases the effect only manifested itself in the short time between the pre-tests and the post-installation tests on the barrel. When compared with measurements taken before installation, a significant increase was observed in the value of the leakage currents of the affected ladders, with some devices producing currents as high as 100 μA.

Figure 3.5 shows that there are many new noisy channels in half-ladder SB5W5L2 after installation (c.f. Figure 3.3). After the ladders were installed in the barrels, the baseline noise level was about 1 ADC count lower than before due to better grounding on the barrel. While there are many individual

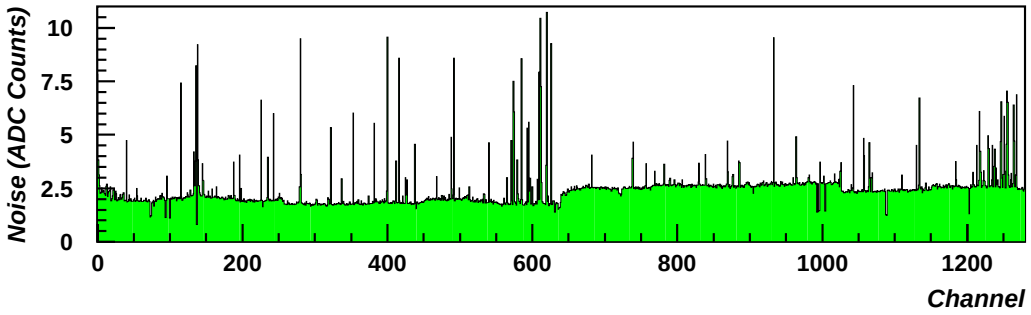

Figure 3.5: SB5W5L2 post-installation with many new noisy channels

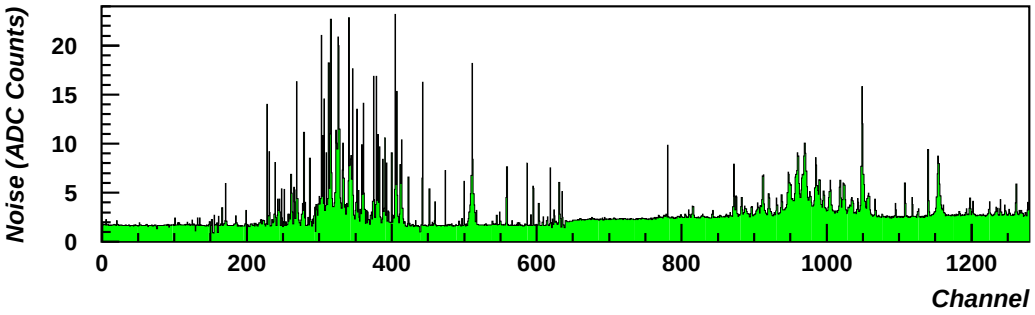

Figure 3.6: SB4W5L2 which developed a 'grassy knoll' after installation

noisy strips, the baseline noise is relatively flat across the ladder. However, this was not the case for a small number of grassy Layer 2 ladders where there is evidence of some structure. An example of this can be seen in Figure 3.6 for half-ladder SB4W5L2, the only device displaying such behaviour that was installed in SVXII. In this case there is a general elevation of all noise in some areas (channels 200-450 & 900-1100) in addition to the large strip-to-strip variations described above.

Over the course of a typical 2000 event run both the leakage current and the noise levels of grassy ladders fell gradually. In a special test an especially bad ladder was turned on for an extended 20,000 event run that

lasted approximately 40 minutes. This ladder was an extreme case and was not installed in the detector. As shown in Figure 3.7, the excessive noise is concentrated mainly on the ϕ-side (the first five chips or 640 channels), i.e. the p-side of the semiconductor. The first three chips on the z-side are also shown. The upper plot shows the noise after approximately 800 events and the lower plot shows how it had improved after 20,000 events (although there is some evidence of the noisy channels having migrated to the z-side). By the end of the run the leakage current had fallen from 376 μA to 78 μA.

No ladders with excessive numbers of noisy channels were found during the construction of Barrel 1, but there are seven half-ladders in Barrel 2 that became grassy only after they were installed in the barrel. There are four grassy half-ladders in Barrel 3. Two of these ladders were found to be grassy when pre-tested for possible installation in Barrel 2 and were held back, but due to problems with other Layer 2 devices they had to be used for Barrel 3. This is not a complete list of all grassy ladders in SVXII as new noisy channels did appear subsequently on some other devices. For example, further tests carried out after those discussed here showed that the problem had developed on some Layer 4 ladders in Barrel 1, which had no such ladders after initial assembly.

Data recorded during SVXII barrel construction was studied for each of the seven grassy ladders that were installed in the Barrel 2. The analysis focused on the the second chip of SB4W5L2, the noisiest chip of the worst affected ladder in the detector. Figure 3.8 illustrates the dramatic way in which the noise for this chip changed after installation. Figure 3.9 similarly compares the noise distributions.

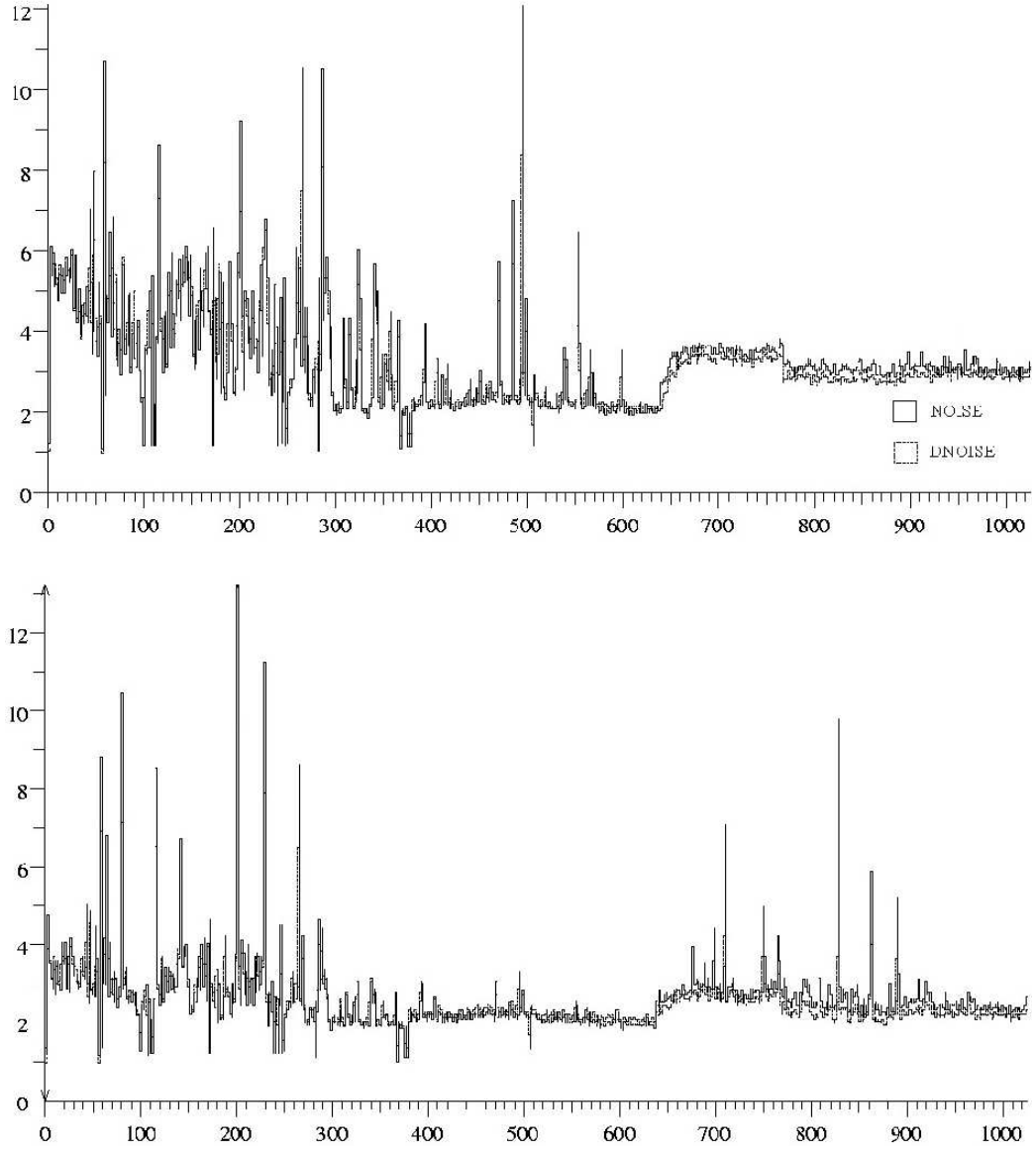

Figure 3.7: Noise levels after 5 minutes (top) and after 40 minutes (bottom)

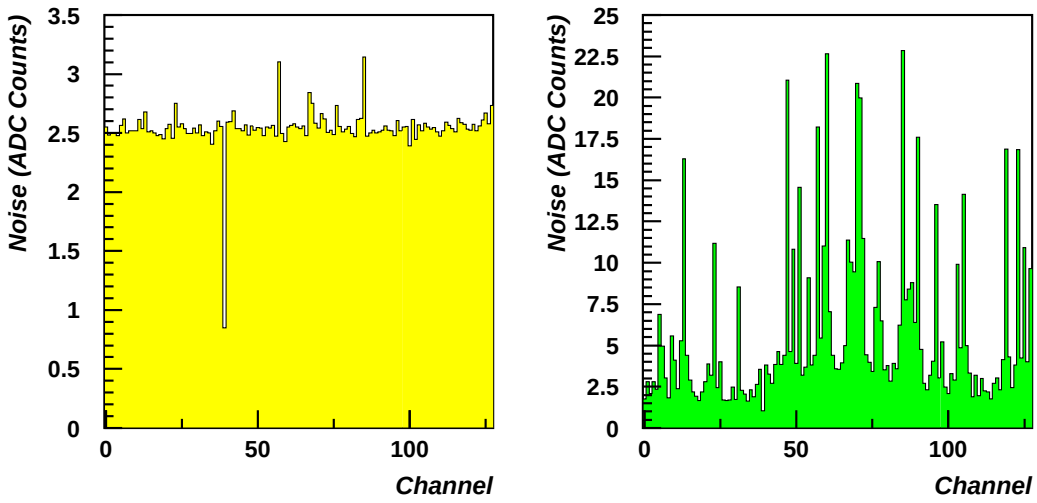

Figure 3.8: SB4W5L2 chip 2 noise before and after installation

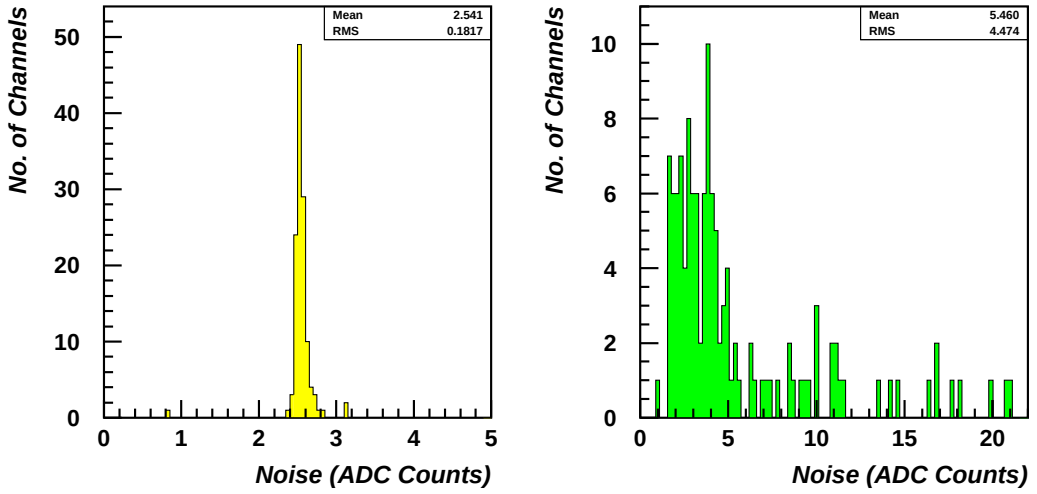

Figure 3.9: Noise distributions before and after installation in SVXII

The ADC count distributions were studied for every strip associated with this chip. The studies revealed large ADC fluctuations in noisy strips after installation. Figure 3.10 shows the distributions for three individual strips as they appeared when tested before and after installation. Channels 56 and 105 were originally good strips that later became noisy, but channel 85 can be identified in Figure 3.8 as one of two strips that were already slightly noisy. The entries contributing to the noise can be seen clustered around 70 ADC counts on a logarithmic scale in Figure 3.11, which includes channel 56 for comparison. After installation, Figure 3.10 shows that channel 56 remains of good quality (though not quite as good as before), but channel 105 is now very noisy with a large spread of ADC counts. Channel 85, which was already noisy and is now much worse, has an even wider distribution.

The pedestals for this chip were then studied to determine if the noisy strips displayed any noticeable variation with time. The pedestal was calculated separately for every 100 events of the 2000 events worth of data. Figure 3.12 shows that the pedestals for channels 85 and 105 were very stable prior to installation, as expected. However, after installation the pedestal is seen to wander considerably for both channels. This was observed to be the case for all of the grassy strips on the chip.

A similar investigation into the behaviour of noise versus time was carried out. Figure 3.13 compares this behaviour for the same strips before and after installation. Strip 105 initially had very stable noise but after installation there is a dramatic variation with time. The same effect is evident in strip 85, which is interesting because of the spike in the noise that occurred before installation at around 1300 events. Similar spikes were found for six other

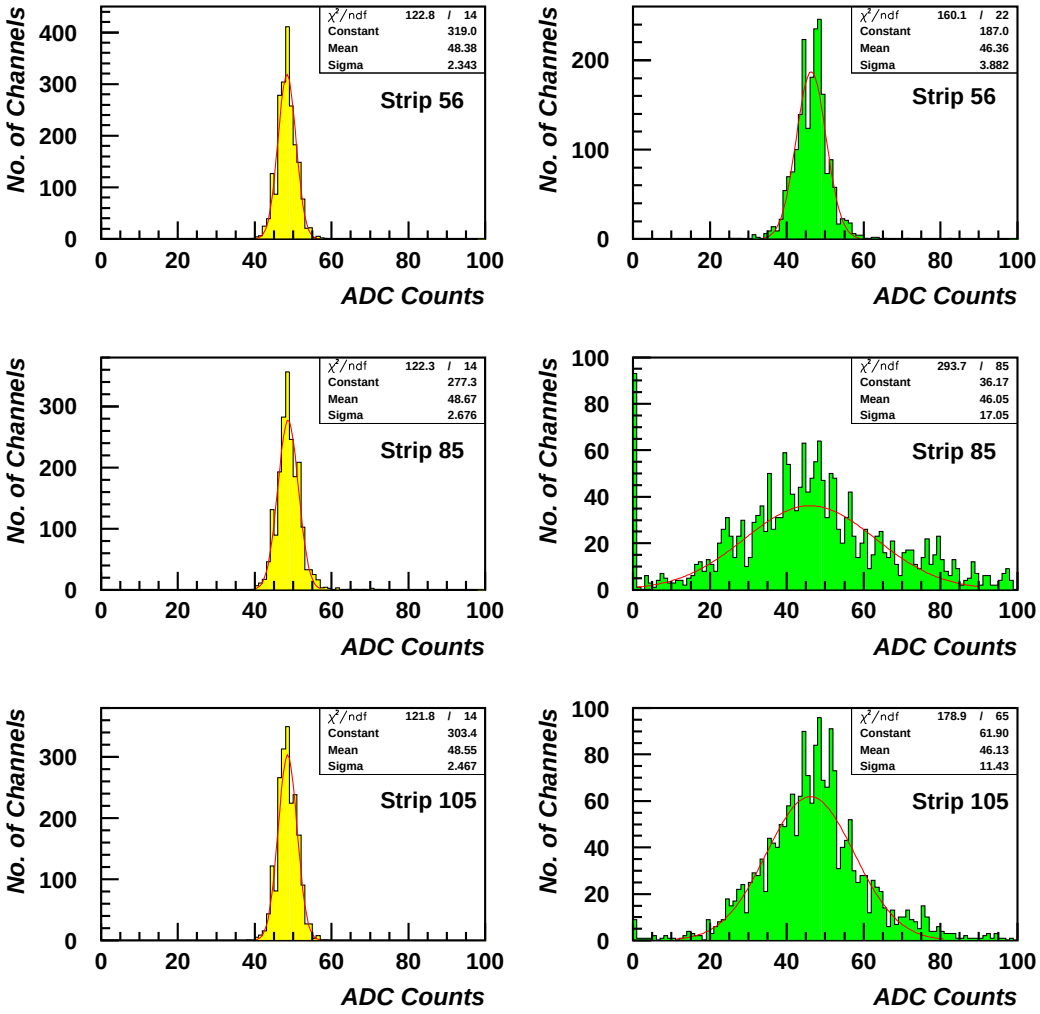

Figure 3.10: ADC distributions before (left) and after (right) installation

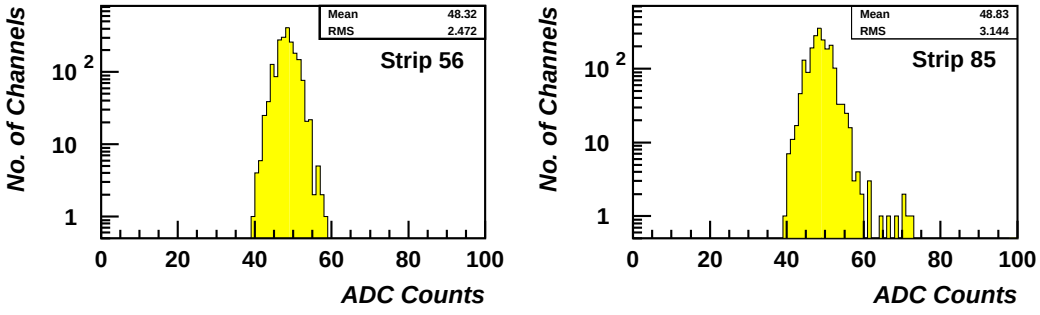

Figure 3.11: ADC distributions before installation on a logarithmic scale

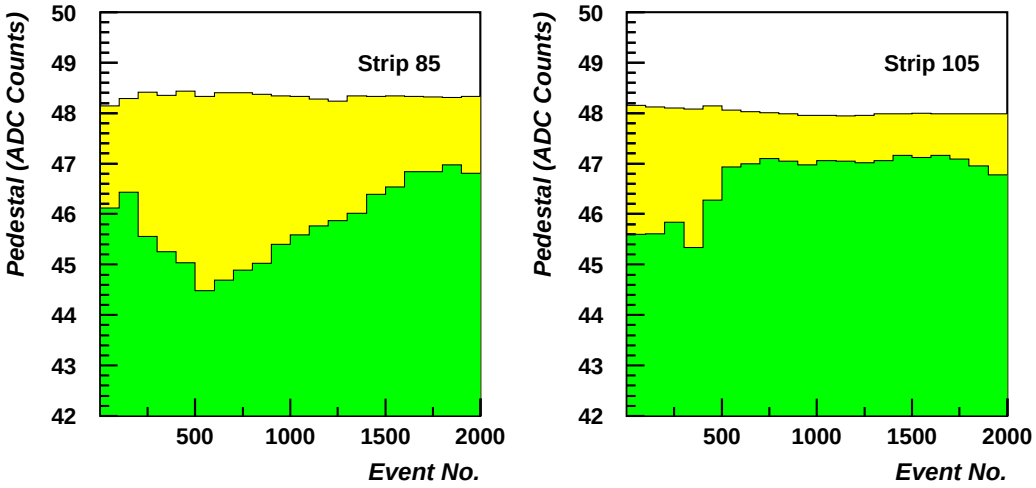

Figure 3.12: Pedestal vs time before (yellow) and after (green) installation

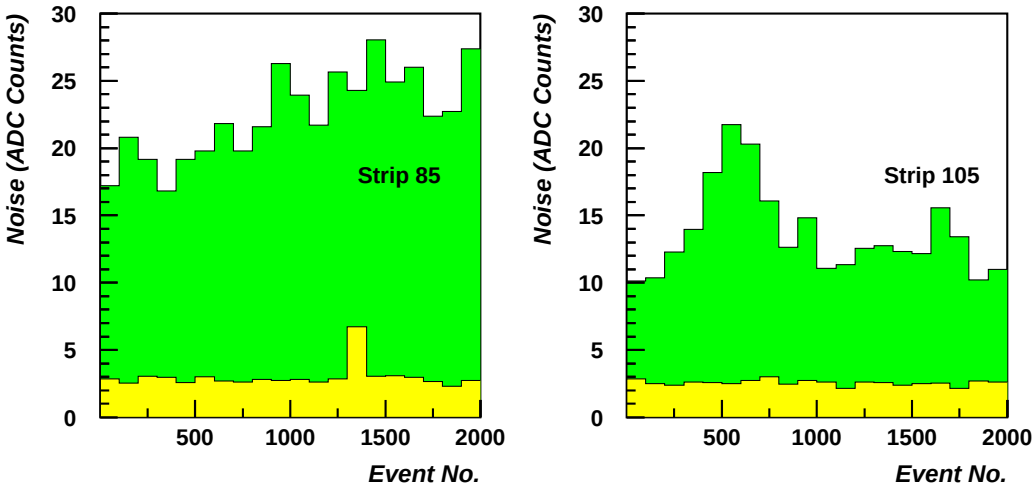

Figure 3.13: Noise vs time before (yellow) and after (green) installation

strips in this chip and in a total of 17 strips in the other four chips on the same side of the ladder. It was found that every strip that displayed this spike became very noisy after installation. In each case the ADC distribution during events 1300 to 1375 is much wider than during the rest of the 2000 event run and strongly resembles the distributions for noisy strips on grassy ladders. This was the only occasion where anything was observed in pre-installation test data that could be related to which strips would later become noisy. However, the majority of the strips that developed excessive noise did not already have this spike and a similar pattern did not emerge on any of the other grassy ladders. Originally it was thought that the noisy strips had high but stable noise levels. However, the noise variations in Figure 3.13 show fluctuations of up to 12 ADC counts, which make it more difficult for these noisy channels to be used effectively in tracking.

The silicon sensors are made of n-type bulk silicon implanted with longitudinal hole-collecting p^+ strips on one side and orthogonal electron-collecting n^+ strips on the other side. A possible explanation for the presence of these scattered channels with very high noise is micro-discharges [41] around the edge of the implanted strips, which can generate random pulse noise. They generally take place in a small area along the strip edge inside the silicon bulk. Typical symptoms are a steep increase in noise amplitude and leakage current, consistent with what was observed in all of the grassy ladders. Micro-discharge is considered to be a breakdown due to the high electric field that occurs along the strip edge inside the silicon bulk. One of the sources of such high fields along the strips is trapped charge either at an interface between the silicon dioxide in the capacitors on each strip implant and the

silicon bulk, or at defects inside the silicon dioxide. In an investigation of micro-discharges [42] it was also observed that the noise amplitude increased with decreasing temperature, so it is unlikely that the warmer operating temperatures at SiDet were a contributing cause.

The noisy ladders were spread out over the whole collection of Layer 2 and 4 ladders and thus could not be associated with an individual batch received from the manufacturer. Although two different manufacturers were used to construct ladders for the SVXII project, the fact that the small-angle stereo devices produced by Micron Semiconductor were the only ones affected suggests that the source of the problem may lie with individual steps in the processing that were specific to Micron.

3.3 Connecting the Silicon Detector to CDF

The 2000 tonne central section of the CDF detector was constructed in the CDF assembly hall and it was here that the completed silicon tracker was installed inside the COT in January 2001 (see Figure 3.14). The racks containing all the power supplies are located inside the collision hall, so silicon cabling could not begin until CDF had been rolled in from the adjoining assembly hall. The process of plugging in the silicon began in February 2001 but the vast majority of the work was completed in May 2001 during a five week access period in which the silicon experts worked around the clock in order to have as much of the detector as possible fully operational during an extended period of data taking planned for the Summer. Most of the plugging work was carried out at the face of the COT in conditions of very limited working space and visibility.

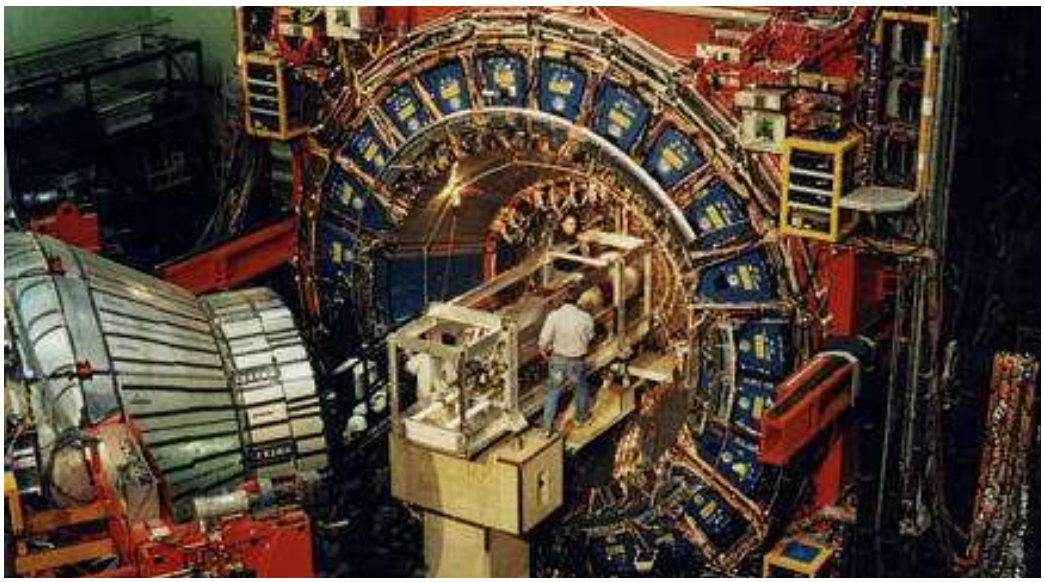

Figure 3.14: The end plug calorimeter was pulled out in order to install the silicon vertex tracker in CDF in January 2001

The inaccessible PCs for SVXII, ISL and L00 are all connected via heavy copper cables to inner Junction Cards (JC). The JCs are the accessible connection points for all the electronics and it is these devices that the shift crews spent five weeks plugging in. At each end of the tracker, just inside the COT face, 57 JCs (6 L00, 15 ISL, 36 SVX) are mounted on a JC ring, which is shown in Figure 3.15. The power supplies and FIBs are mounted in crates on racks fixed to the walls up to 30 feet above the floor of the collision hall, and the cables from these racks (power supply cables, FIB command cables, optical extension cables) were run to the COT face for connection to the JCs.

Figure 3.16 shows the connections that had to be made for a typical SVXII wedge. Three power supply cables and a FIB command cable were plugged into an outer JC, which was then placed in the appropriate slot in

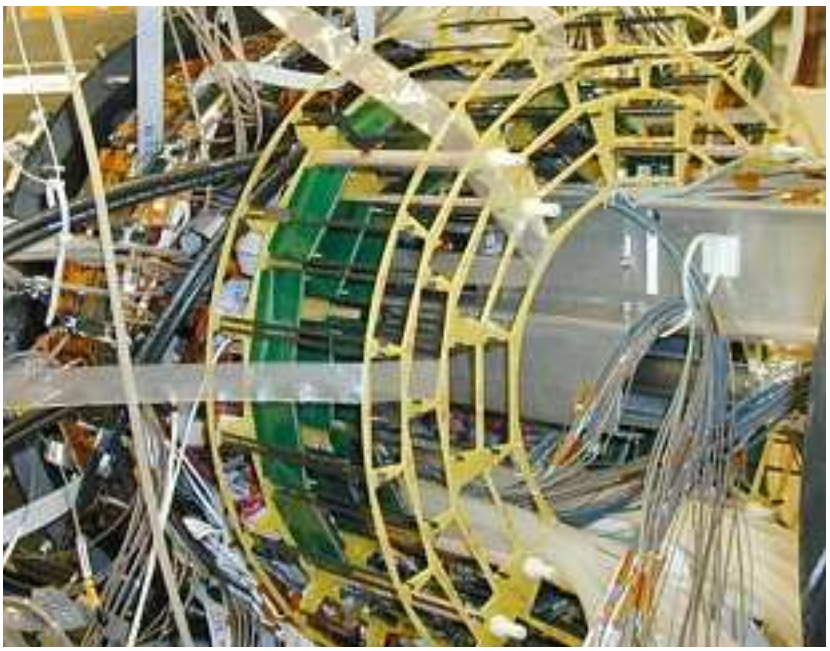

Figure 3.15: ISL port cards (orange), the junction card ring (yellow) and the inner junction cards (green) during construction at SiDet

the JC ring to connect with the corresponding inner JC. In addition, the five DOIM cables from the PCs had to be connected to the optical extension cables from the FIBs.

A safety-driven approach was adopted during plugging and a series of step-by-step procedures was followed to minimise the risk of damage to the detector. All of the subcomponents (silicon detector, DAQ hardware, power supplies) had been extensively pretested prior to installation but all had to be retested to ensure that they were still fully operational. It was also important to verify that all of the cables were in working order. The process of plugging in a wedge consisted of five main steps:

- Test the FIB command cable

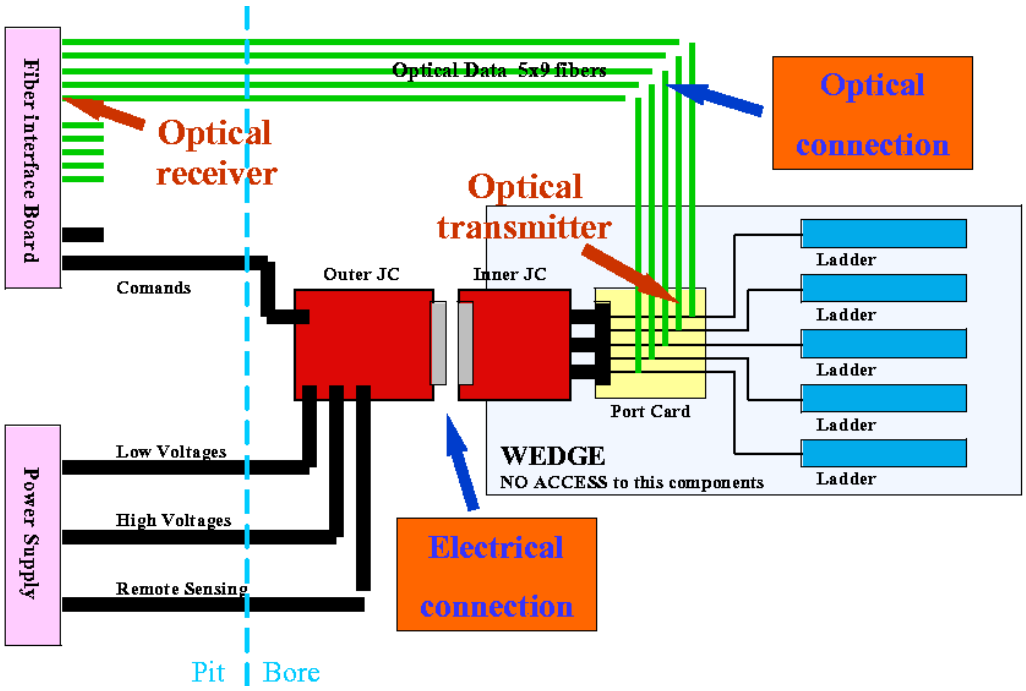

Figure 3.16: Diagram of the connections made while plugging in the silicon

- Test the power supply cables
- Test all FIB channels and optical cables
- Make the optical and electrical connections to the wedge
- Test the wedge for any internal problems

The FIB command cables for each wedge were tested using a custom-made 'blinky lights' board, which had one light to represent each signal from the FIB. The test was conducted by running a special procedure in the SXVII DAQ program. This was a simple test whereby all of the lights flashing indicated that the command signals were getting through and the cable was

good. Only one FIB command cable had to be replaced during the five week access.

The power supply and its cables were then tested using load boxes with appropriate load resistors. This procedure checked that voltages, current limits and other configuration parameters were correctly set, as well as establishing whether or not the cables were hooked up to the correct power supplies.

Next, a full DAQ test was carried out using a Wedge In a Box (WIB) [43]. A WIB is a full self-contained wedge of silicon that was used to verify that each DAQ channel was fully functional before connecting to the real detector. This test was designed to find any problems with the optical fibres connecting the PC to the FIB as well as problems at the FIB itself. If everything passed the WIB test then any problems found after plugging in the real wedge could usually be attributed to internal components to which there was no access. However, it was also possible for a problem to be associated with the interaction of external and internal components, e.g. light levels from internal components were not always the same as those from the WIB.

The next stage of the procedure involved connecting the optical fibres from the wedge to the extension cables and connecting the outer JC (to which the FIB command cable and power supply cables were now attached) to the inner JC. This was a delicate and time-consuming process that involved reaching into the JC ring with torches and dental mirrors to ensure that the 96-pin JC connectors were perfectly aligned. Finally, the DAQ channels of the real detector were tested and any problems found were isolated and attempts were made to fix them.

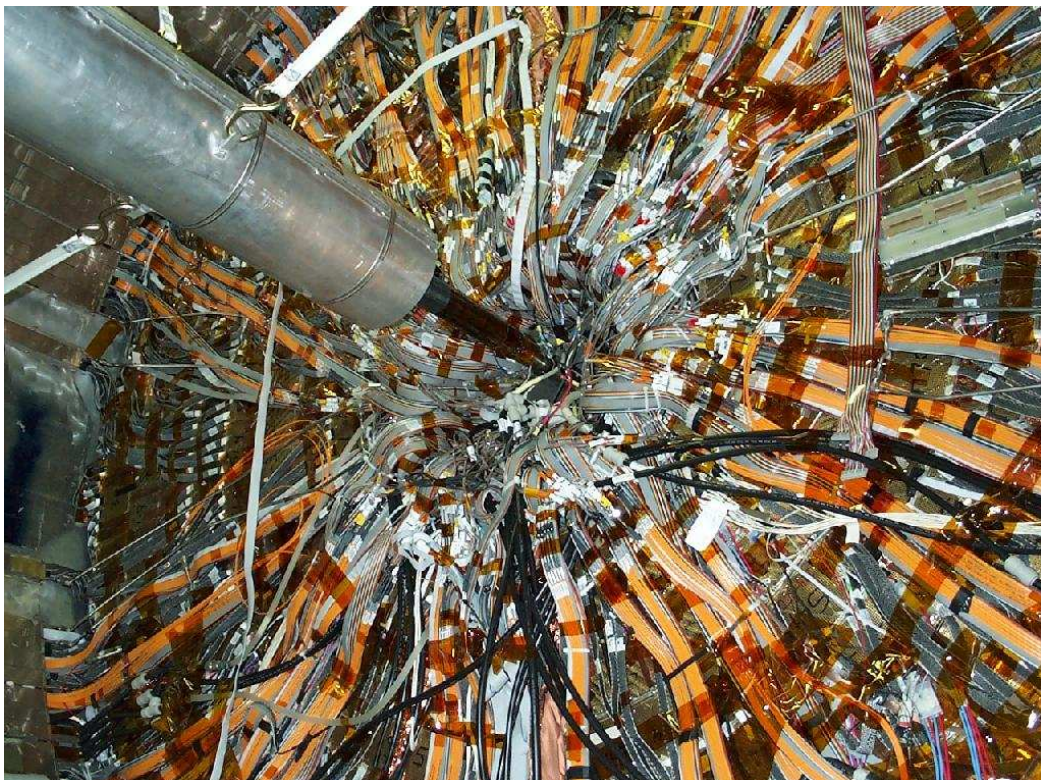

Figure 3.17: The East COT face after plugging was completed

Figure 3.17 shows the East COT face with the power supply and FIB command cables (grey) and the optical cables (orange) extending across the COT face and into the JC ring. The beam pipe is clearly visible passing through the centre of the detector. All of the cables had to be firmly secured to the COT face to minimise the strain on the JCs. When the entire silicon tracker was finally connected, all of the cables were dressed back to allow the end-plug calorimeters to be moved back in and closed without obstruction.

A number of external problems were found during the plugging and testing period but very few of these were related to the cables. Most of the problems were related to malfunctions in the power supplies and readout

boards. The failure rates for various components were as follows:

- FIB Command Cables: 1/114 (0.9%)
- Optical Extension Cables: 5/550 (0.9%)
- Power Supplies: 28/114 (24.6%)
- FIBs: 30/58 (51.7%)

The power supply problems included incorrect voltage settings, bad fuses and shorts as well as more serious failures such as supplies that refused to turn on or off, refused to trip, or had large voltage/current offsets. Half of these power supplies were repaired by experts at CDF, while the remainder were returned to the manufacturer (CAEN). None of the above failures were correlated with any damage to internal components of the system.

The largest source of problems was identified at the FIBs, where readout was often corrupted due to a mismatch between the light output of the transceiver DOIMs (TX) and the receivers (RX). If the light output of the TX is too high or too low then the optical signal cannot be translated correctly back into digital signals by the RX. This problem arose because each TX had not been previously matched up with its perfect RX partner due to time constraints during production. There were also additional complications due to the temperature, radiation exposure, and age dependence of the light output of the TXs.

High or low light levels could be adjusted by tuning the low voltage for the DOIMs. However, this adjustment can only be made for an entire wedge, so tuning the voltage to correct a problem with one ladder often caused a new problem in another. As an alternative in cases where there was high

light output, a thin layer of plastic could be inserted between the connectors to attenuate the light. This solution affects only one half-ladder, but since there is a large spread in light output even among the nine fibres in a single DOIM cable, this method was also not successful in every case.

Light output mismatches and bad FIB internal receivers resulted in problems with 30-50 fibres out of approximately 5000, i.e. a failure rate of less than 1%. One bad fibre corrupts the data for a whole ladder and so this translated into a problem with 30-50 ladders, i.e. a failure rate of just under 10%. However, with ten ladders connected to each FIB the final result was a problem at 30 FIBs out of 58. By the end of plugging, problems at twelve of the FIBs had been fixed and more work was done during subsequent accesses to address the remainder.

Finally, there were also internal failures of components that are no longer accessible [44]. These failures were due to internal damage to the readout chips or wire bonds. At the end of plugging, the internal failure rates for each of the sub-detectors were 0.96% for L00 (one chip), 4.9% for SVXII (three wedges and three ladders), and 3.4% for ISL (ten ladders).

Additional work was carried out during subsequent accesses to repair as many of these components as possible. The plugging period was the first opportunity to work with the complete silicon tracker in the real CDF environment. The number of problems encountered was large but most were fixed or clearly understood by the end of the access.

The assembly and commissioning of the CDF silicon tracker provided valuable experience in operating complex silicon systems, which is not only critical for CDF Run II, but is also of crucial importance to the success of

the large silicon detectors that are currently being constructed for the Large Hadron Collider at CERN.

3.4 SVXII Alignment

The intrinsic resolution of silicon microstrip detectors is determined by several factors including the strip pitch, precision of detector fabrication, signal-to-noise ratio and charge deposition fluctuations. The measurement resolution obtained in practice is limited by how accurately the individual detector elements are aligned to each other and to rest of the CDF detector. It is important that the detector alignment [45] be precisely determined for analyses that rely heavily on silicon tracking information.

Effective use of the precise information obtainable from silicon strip detectors depends on knowing the relative location of each strip. Within a silicon sensor, the locations of any two strips are known by the number of channels they are apart and the strip pitch, which is guaranteed by the fabrication technique to sub micron precision. Knowing the location of a strip on one sensor to that on a different sensor requires a careful mechanical construction and an accurate survey of the whole detector. The position of the four sensors within a ladder was determined using an optical survey device that focused on certain visible features which it measured with a precision of 1 μm. Measurements of the ladders with respect to the bulkheads of the barrel were made after after being placed on the barrel. The global mechanical position of the SVXII barrels was measured just before installing SVXII in the ISL.

However, despite their precision, the optical survey techniques are not

able to accurately predict the final alignment of the internal detector elements. As well as the mechanical motion of the detector after assembly, small systematic effects arising from detector readout can produce observable effects at the 5-10 μm level that mimic misalignments. In addition, no optical technique can determine the position of the silicon detector relative to the COT. Therefore, an offline alignment procedure using particle tracks has to be used to determine the global alignment of the silicon detector with respect to the COT and the internal alignment of the silicon ladders with respect to each other. The parameterisation is divided into two sets of constants that describe displacements from nominal positions. There are six global parameters defined in the CDF coordinate system and and six internal parameters defined in the local coordinate system of the ladders. These parameters correspond to three translations along the coordinate axes and three rotations about them.

The global alignment method establishes the offset in the position of the silicon detector by comparing the position of the beam axis observed using silicon information only to that obtained using only the COT. Having determined the global alignment, the silicon detector internal alignment procedure is then used to find the relative positions of the ladders. The internal alignment method attempts to find the alignment parameters by performing a series of track fits which initially ignore the misalignments. From the distribution of residuals between the track intersection with the ladder and the cluster position, the alignment parameters are deduced. It is assumed that the misalignments cancel in the average and the fitted track then gives a better approximation to the truth. Different classes of tracks are some-

times identified in order to constrain different parts of the detector. High p_{T} tracks may be used to align silicon wedges internally, tracks in the overlap regions might join wedges together, and cosmic rays may be used to remove overall deformations. After the internal alignment is completed, the global alignment procedure is repeated and, followed by a second iteration of the internal alignment. Consistency between the two iterations demonstrates that convergence has been obtained between the global and internal alignments.

Chapter 4

Silicon Tracking Efficiency and Detector Coverage

This chapter concentrates on evaluating the performance of SVXII using the dimuon data sample. Measurements of the hit efficiencies of SVXII ladders and the tracking efficiencies of SVXII wedges are presented, and SVXII readout error rates are also discussed.

4.1 Data Sample and Tracking Algorithm

The data sample used in this study extends from run 146805 to run 152625, a range over which the silicon coverage was relatively stable with 90% of the system running and good data being recorded by about 80% of it. Intermediate runs for which there was no SVXII beam position information available were excluded, as were runs where the silicon detectors were not integrated (i.e. switched on and read out by the DAQ). Figure 4.1 shows how the silicon coverage changed over time.

The data was analysed with the CDF software version released for the Winter 2003 conferences. In the default COT track collection, some tracks

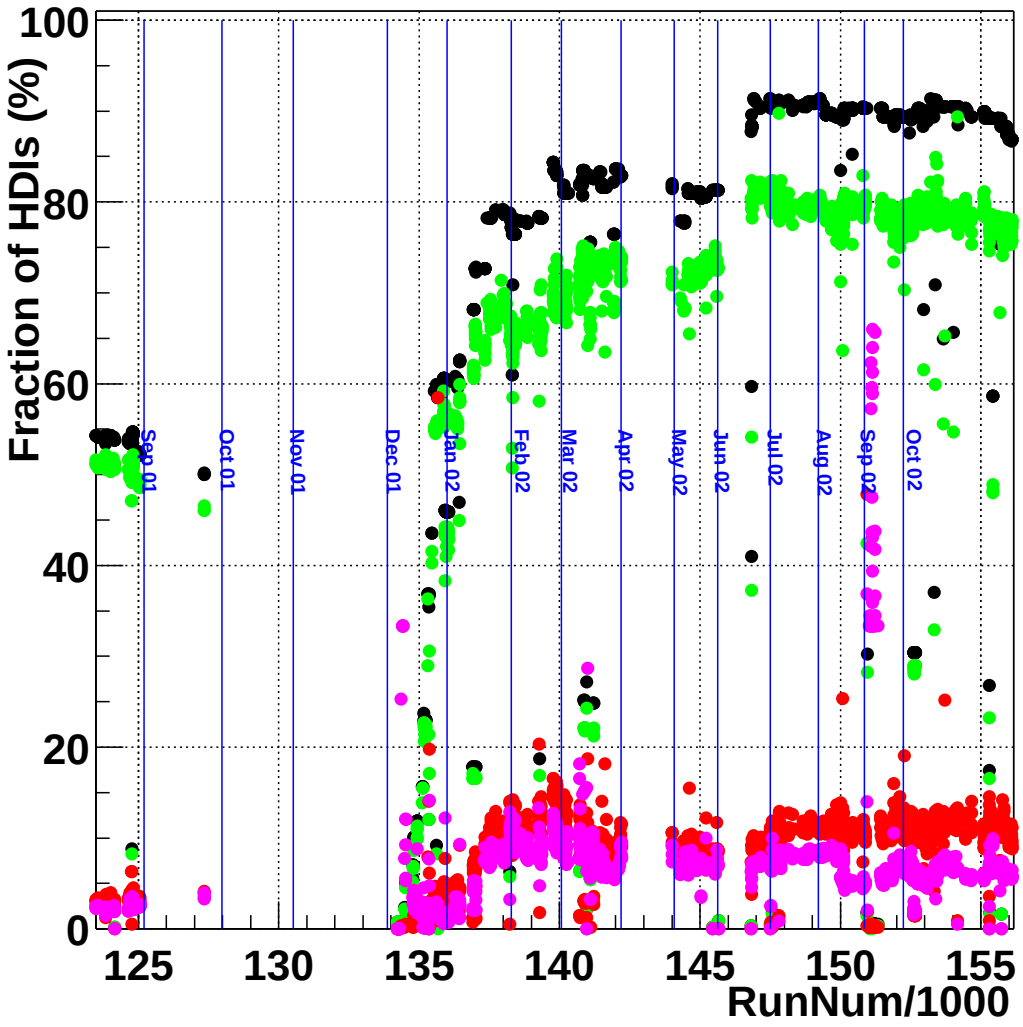

Figure 4.1: The performance of the silicon detector as a function of time, showing (from top to bottom) powered ladders in black, good ladders in green, bad ladders in red and the error rate in pink

have silicon hits associated with them and some do not. Tracks are reconstructed by first fitting axial and stereo COT hits. Then the default Outside-In 3D (OIZ) silicon tracking algorithm [46] employs a two-stage progressive fit. It starts with a COT track pointing into the silicon detector and progressively adds silicon hits found in close proximity to the extrapolated

path, beginning with the outermost layer of ISL. The first stage involves the Outside-In (OI) algorithm adding silicon r-ϕ hits to the COT track. At least 3 r-ϕ silicon hits must be found in L00/SVXII/ISL for an OI track to be made and written to an OI track collection. Then the OIZ algorithm takes over and adds r-ϕ and r-z hits simultaneously. The acceptance of such an OI tracking algorithm is limited by the pseudorapidity coverage of the COT. However, it is advantageous to use this rather than stand-alone silicon tracking as precise momentum measurements from the COT and precise impact parameter measurements from the silicon are combined to provide more accurate tracking information overall.

4.2 SVXII Hit Efficiency per Half-ladder

All COT tracks in the default COT track collection that have a corresponding track in the OIZ collection are projected into the silicon to give an intersection location. A comparison is then made with the OIZ silicon tracks, which are the default output of CDF track reconstruction. The hit efficiency per half-ladder in SVXII is determined by calculating how often there is a silicon hit (r-ϕ, r-z or both) on an OIZ track with $p_{\mathrm{T}} \geq 1.5$ GeV/c^2 when it is expected, based on where an extrapolated COT track intersects an integrated ladder. For each individual half-ladder, the hit efficiency is defined as follows:

$$\text{Efficiency} = \frac{\text{No. of silicon hits recorded when expected}}{\text{No. of silicon hits expected from COT track information}}$$

The COT track impact parameters are corrected for the movement of the beam spot that occurs due to changes in the orbit of the beam in the Tevatron. This correction is done by rotating the beam through an angle

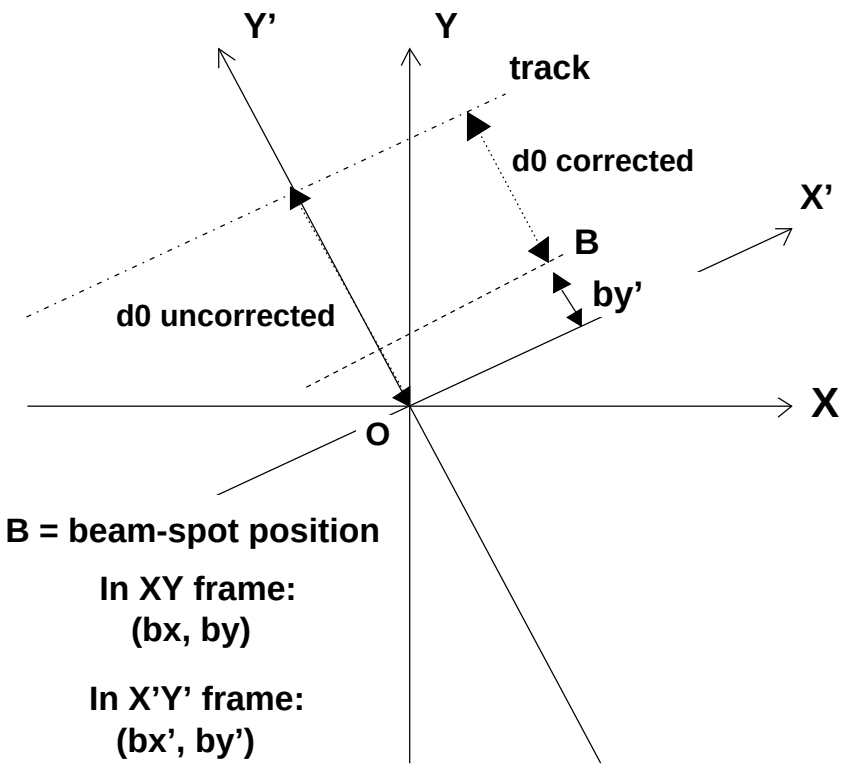

Figure 4.2: Illustration of beam position offset correction to d_0

ϕ_0 to coordinates where the track starts off parallel to the x-axis as shown in Figure 4.2. The corrected impact parameter is the difference between the uncorrected value and the rotated y-component of the beam position:

$$d_0' = d_0 - b_y' = d_0 + b_x \sin\phi_0 - b_y \cos\phi_0$$

where b_x and b_y are the run averaged beam position offsets relative to the detector axis. The beam spot position changes from run to run and also during runs, each of which may last up to eight hours. Figure 4.3 shows the beam spot position distributions for runs 146805 - 152625.

A pseudorapidity requirement of $|\eta| \leq 0.5$ is applied to the sample in order to remove tracks with large angles of incidence. In cases such as this

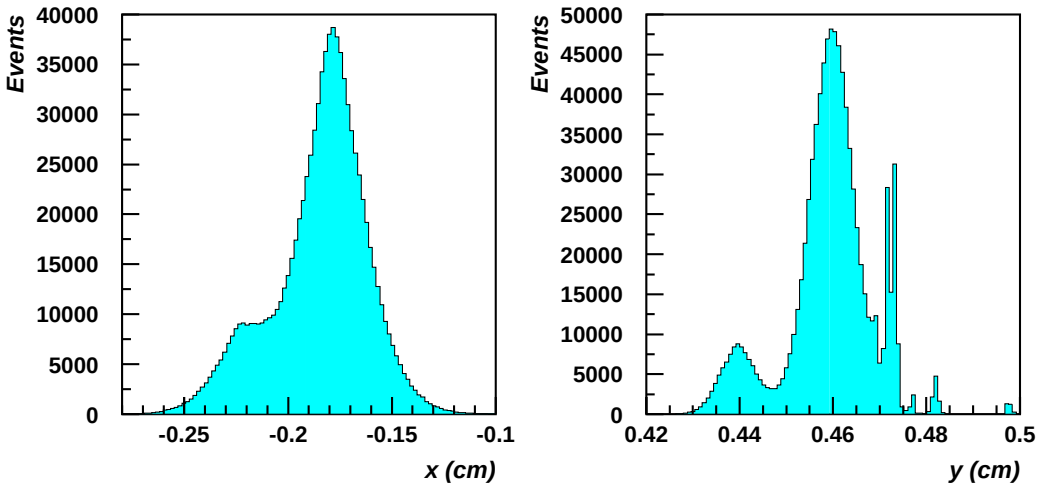

Figure 4.3: SVXII beam spot position distributions

the clustering efficiency is not as good and so the hit efficiency is lower. The following cuts are applied to obtain the best quality COT tracks:

- $p_{\mathrm{T}}(\mu) \geq 1.5$ GeV/c^2
- $\geq 36/24$ axial/stereo COT hits
- $|d_0'/d_0^{\mathrm{error}}| \leq 5$
- $|\eta| \leq 0.5$
- COT track must intersect at least 4 integrated L00/SVXII/ISL ladders

The COT track parameters are not measured to high precision so it can happen sometimes that silicon hits are not in the wedge predicted by the COT intersection location, especially in cases where the COT tracks go through the overlap regions. This effect will result in a small reduction in the apparent efficiency as the algorithm may not see any hits where it expects to.

	Integrated Ladders	Efficiency (all ladders)	Efficiency (integrated)	Efficiency (> 50%)
SVXII	341	79.0 %	83.4 %	85.9 %
Layer 0	69	76.3 %	79.6 %	81.2 %
Layer 1	69	81.0 %	84.5 %	85.4 %
Layer 2	64	75.8 %	85.0 %	86.6 %
Layer 3	70	85.8 %	88.3 %	89.5 %
Layer 4	69	76.2 %	79.5 %	86.4 %

Table 4.1: Average SVXII half-ladder hit efficiencies for all ladders, for integrated ladders only, and for all ladders with efficiencies above 50%

Figure 4.4 shows the number of silicon hits expected in each half-ladder in SVXII Bulkhead 0 overlaid with the number of hits actually observed. No silicon hits are expected in ladders which were not integrated into the DAQ readout. The total number of expected hits varies from ladder to ladder according to how often each device was included in a run, so direct comparisons of the absolute numbers of hits are not useful. Figures 4.5-4.10 show the efficiencies obtained for all half-ladders in Bulkheads 0 through 5.

Hit efficiency distributions for all 360 SVXII half-ladders are presented in Figure 4.11. It should be noted that these plots include 19 half-ladders that were not integrated during the runs contained in the data sample. The results in Figures 4.5-4.10 show that 14 integrated SVXII ladders have an efficiency of less than 50%. All of these low efficiency detectors have known problems associated with them as described in the Silicon Detector Working Group's ladder status summary database [47]. Table 4.1 lists the average efficiencies for each layer when only integrated ladders and ladders with at least 50% efficiency are considered.

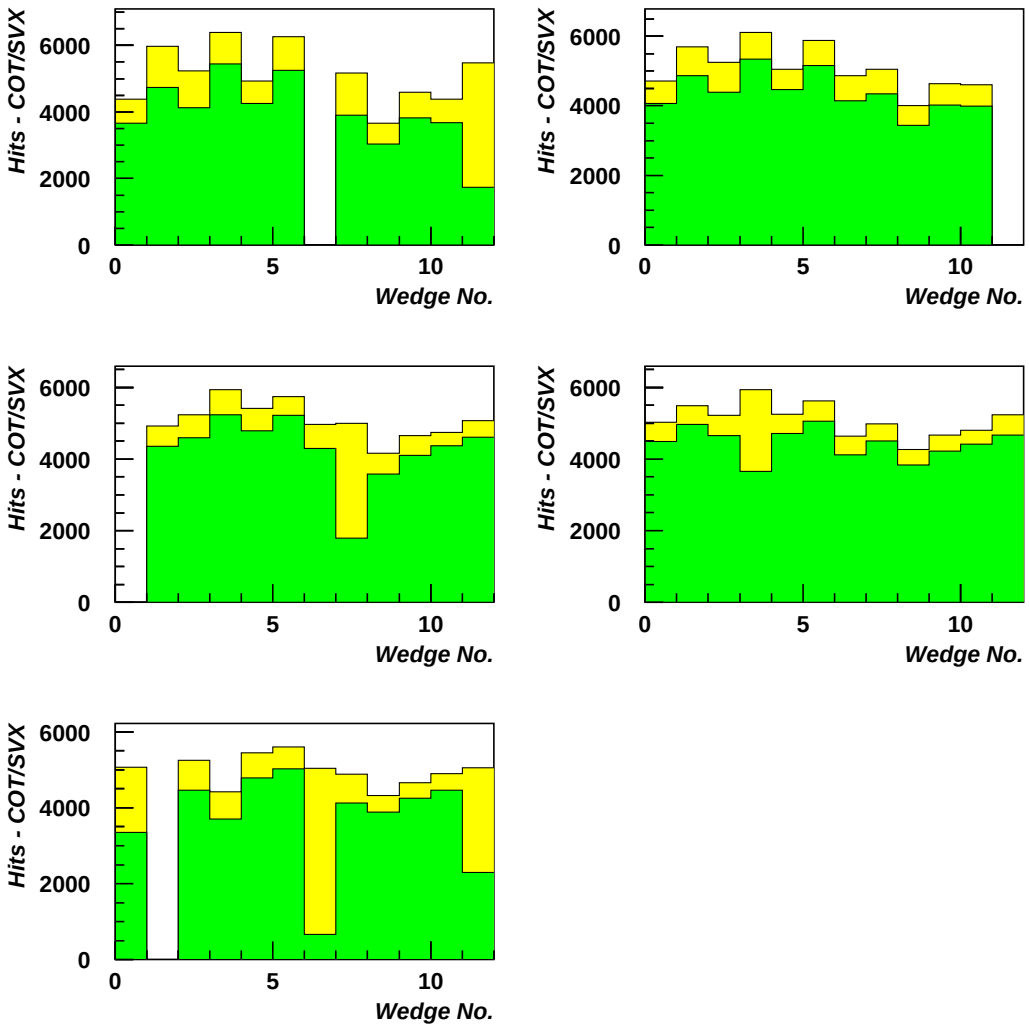

Figure 4.4: SVXII Bulkhead 0: Number of silicon hits expected (yellow) and actual number recorded (green) for Layers 0-4

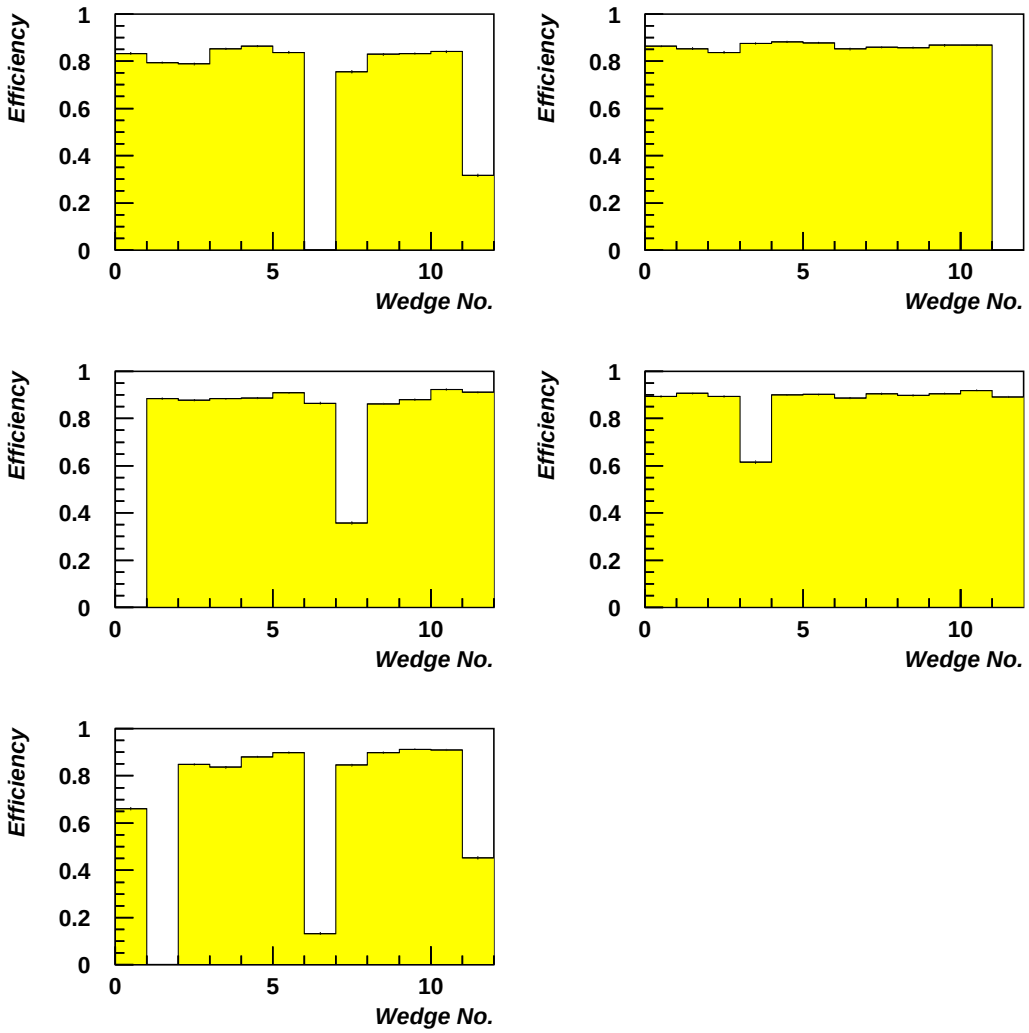

Figure 4.5: SVXII Bulkhead 0: Hit efficiencies for Layers 0-4

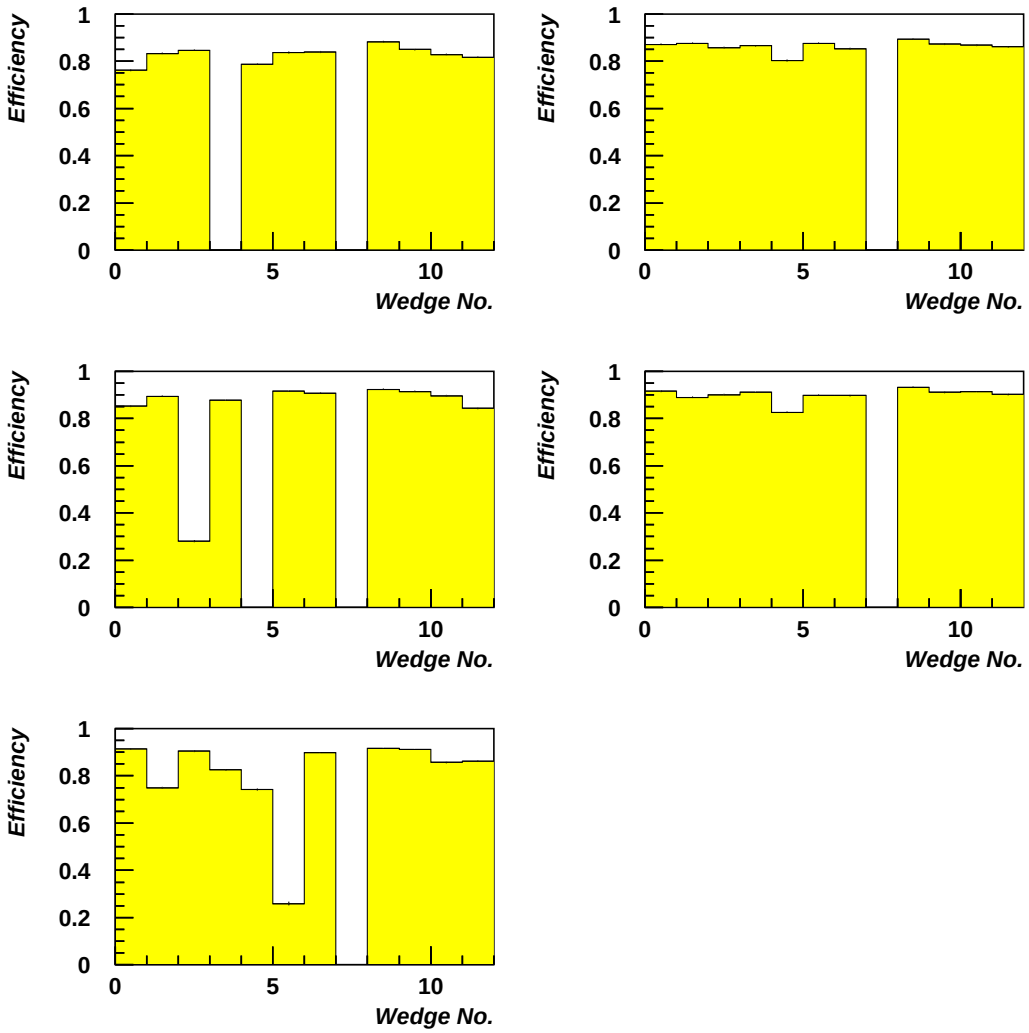

Figure 4.6: SVXII Bulkhead 1: Hit efficiencies for Layers 0-4

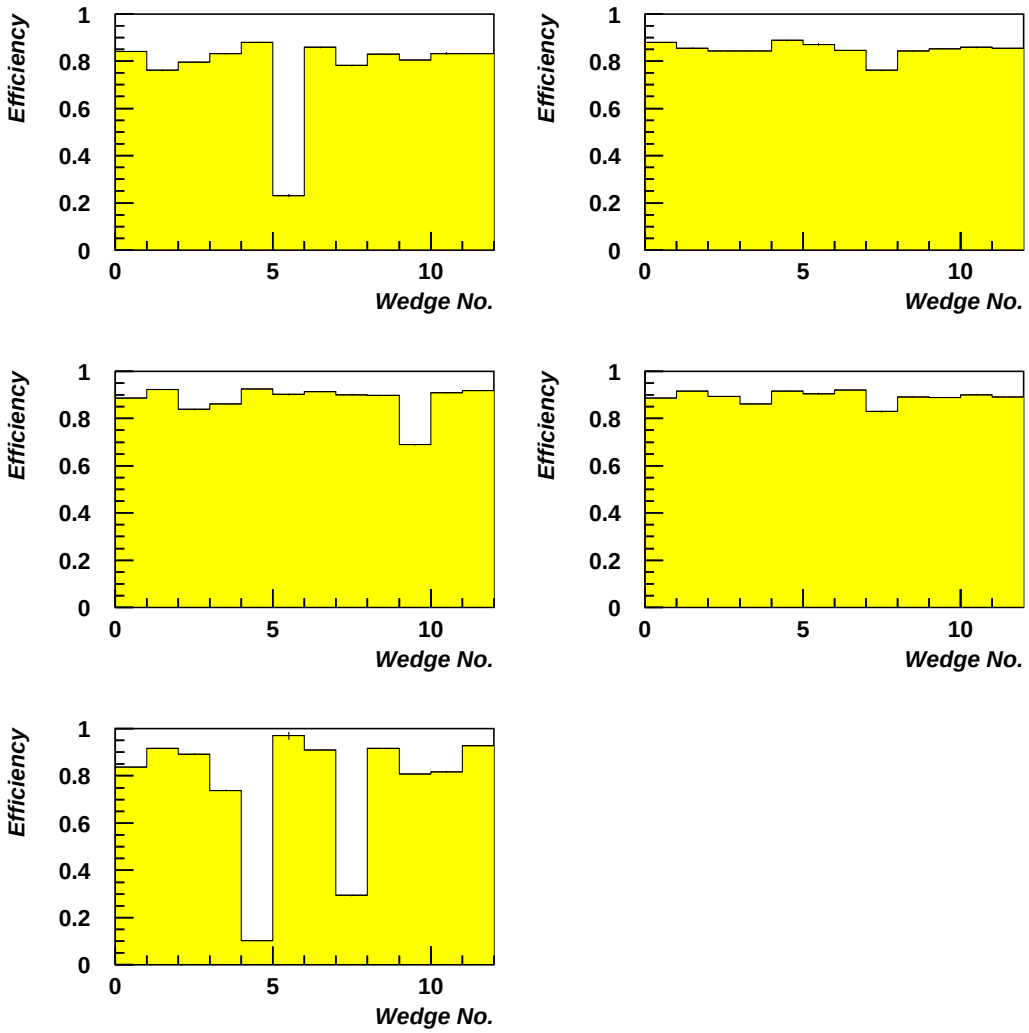

Figure 4.7: SVXII Bulkhead 2: Hit efficiencies for Layers 0-4

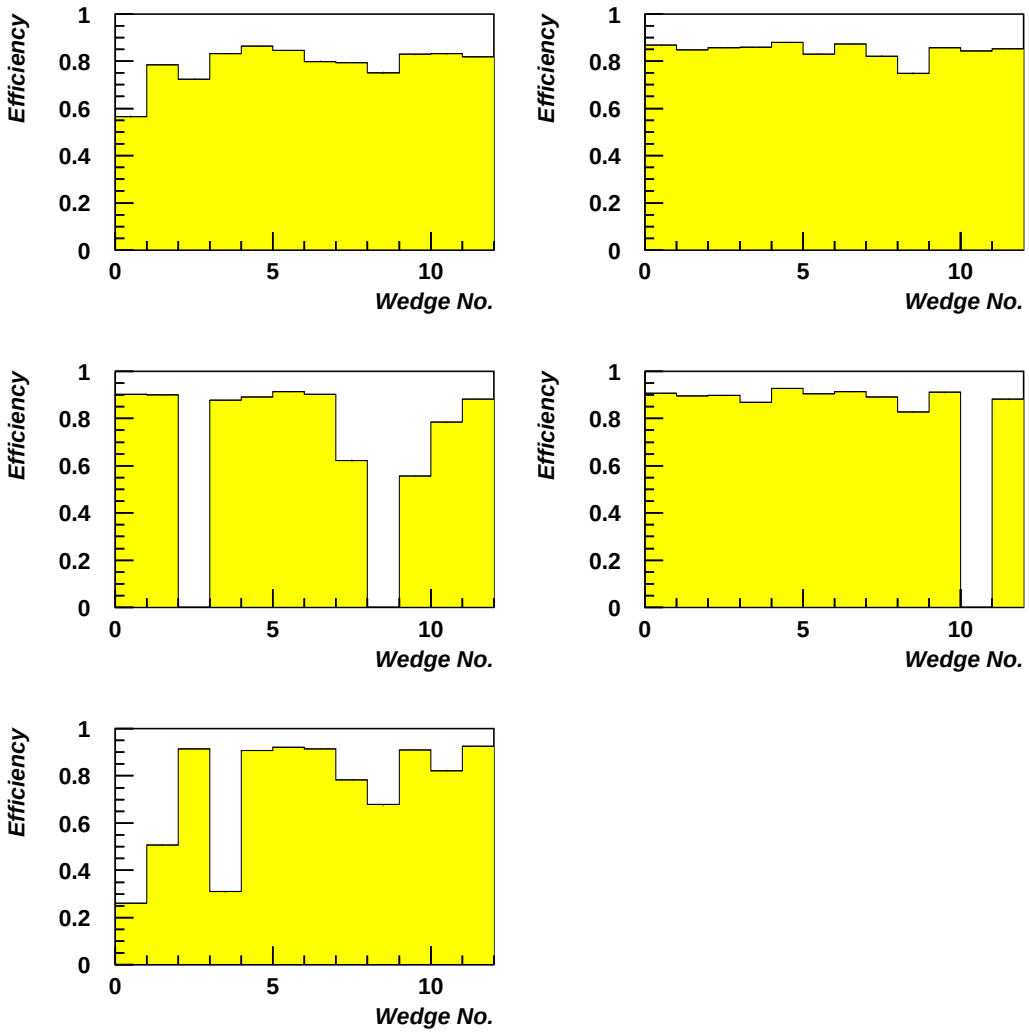

Figure 4.8: SVXII Bulkhead 3: Hit efficiencies for Layers 0-4

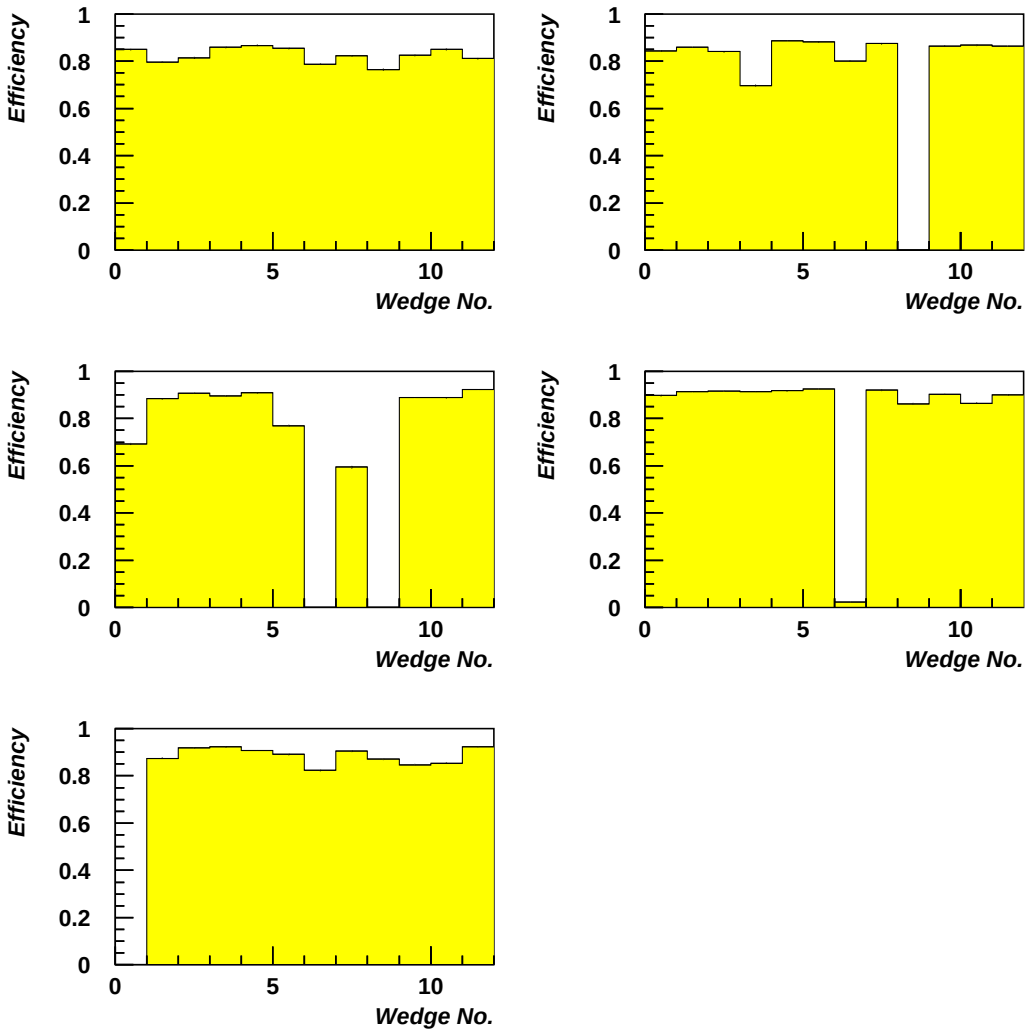

Figure 4.9: SVXII Bulkhead 4: Hit efficiencies for Layers 0-4

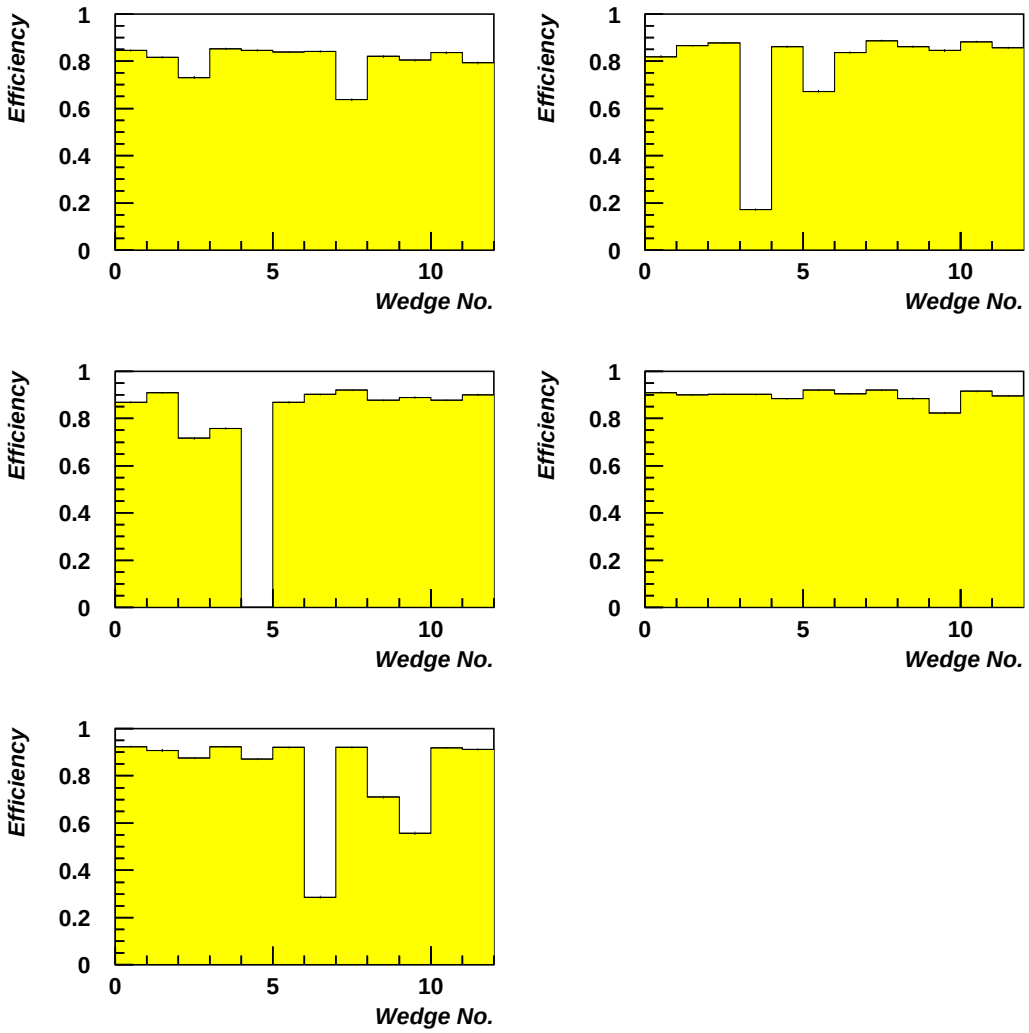

Figure 4.10: SVXII Bulkhead 5: Hit efficiencies for Layers 0-4

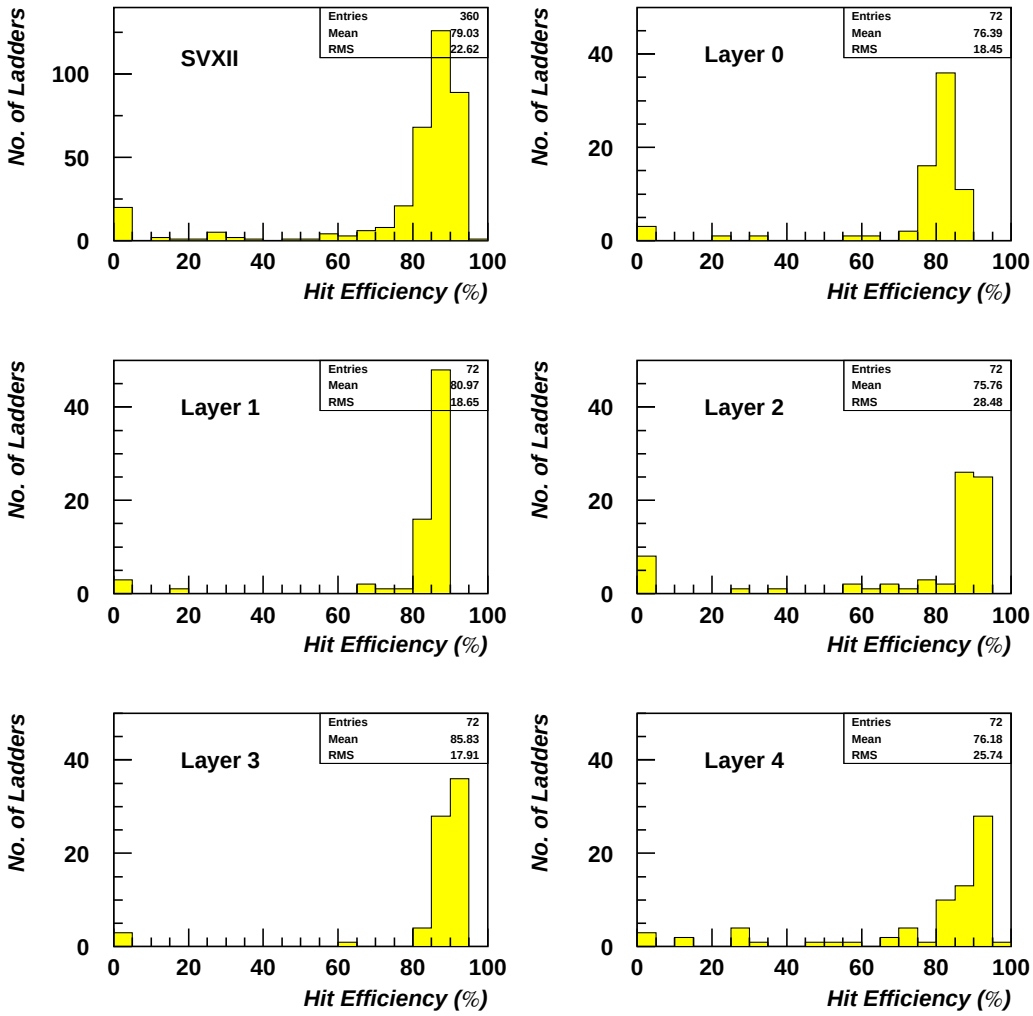

Figure 4.11: SVXII hit efficiency distributions for all 360 half-ladders

4.3 SVXII Tracking Efficiency per Wedge

To be used in tracking, each wedge must have three or more working ladders integrated with the rest of CDF since the tracking algorithm in the silicon vertex trigger requires at least 3 r-ϕ SVXII hits per track. This study evaluates the efficiency of such tracking wedges. The complete list of cuts applied to obtain high quality COT tracks is as follows:

- $p_{\mathrm{T}}(\mu) \geq 1.5$ GeV/c^2
- $\geq 36/24$ axial/stereo COT hits
- $|d_0'/d_0^{\mathrm{error}}| \leq 5$
- Each COT track must pass through all the layers of an SVXII wedge that has at least n integrated ladders ($n = 3, 4, 5$)

No η cut is applied since a projected COT track is constrained to pass through all of the layers in a wedge by requiring it to intersect Layers 0 and 4.

The n-hit tracking efficiency for a particular wedge is defined as follows:

$$\text{Efficiency} = \frac{\text{No. of COT tracks with} \geq n \text{ silicon hits}}{\text{No. of COT tracks passing through all 5 layers of the wedge}}$$

If there are three or more integrated ladders in a wedge then at least 3 r-ϕ silicon hits are expected on tracks that pass through all five layers. Figures 4.12, 4.14 and 4.16 show the wedge tracking efficiencies for observing 3, 4 and 5 r-ϕ hits. For the requirement of at least 3 r-ϕ hits, SB0W11 is the only integrated wedge to have an efficiency of less than 75%. (SB1W7 is not integrated.)

This study was repeated for r-z tracking. Figures 4.13, 4.15 and 4.17 show the r-z tracking efficiencies as a function of wedge for cases where 3, 4

Hit Requirement	Mean Efficiency (all wedges)	Qualifying Wedges	Mean Efficiency (qualifying wedges)
≥ 3 r-ϕ	93.1 %	71	94.4 %
≥ 4 r-ϕ	77.2 %	70	79.4 %
≥ 5 r-ϕ	44.8 %	58	55.6 %
≥ 3 r-z	76.5 %	71	77.6 %
≥ 4 r-z	56.3 %	70	57.9 %
≥ 5 r-z	23.1 %	58	28.7 %
≥ 2 90°	78.8 %	71	79.9 %
≥ 2 SAS	44.2 %	60	53.0 %

Table 4.2: Average wedge tracking efficiencies: (i) for all 72 wedges, (ii) for those wedges with enough integrated ladders to satisfy the hit requirements

and 5 r-z hits are observed. The r-z detector alignment is not as good as the r-ϕ alignment and consequently the average r-z tracking efficiencies turn out to be lower than the corresponding r-ϕ values. SB0W11, with the notably low r-ϕ efficiency, also has low r-z efficiency.

The efficiency distributions for the cases where at least 3, 4 and 5 r-ϕ or r-z hits were required are presented in Figure 4.18. As shown in Table 4.2, the average efficiencies are higher when only those wedges with enough integrated ladders to fulfill these requirements are considered in the calculation.

The r-z analysis was then broken down to allow the performance of the 90° (Layers 0, 1, 3) and small angle stereo (SAS) (Layers 2 & 4) ladders to be evaluated separately. Figure 4.19 shows the tracking efficiencies for the case where at least two 90° r-z hits are required. The corresponding results for SAS, where two SAS r-z hits are required are presented in Figure 4.20. Efficiencies for SAS are significantly lower but when comparing the results in Figures 4.19 and 4.20 it is important to remember that for SAS two out of two ladders are required to have hits, whereas for 90° r-z the requirement

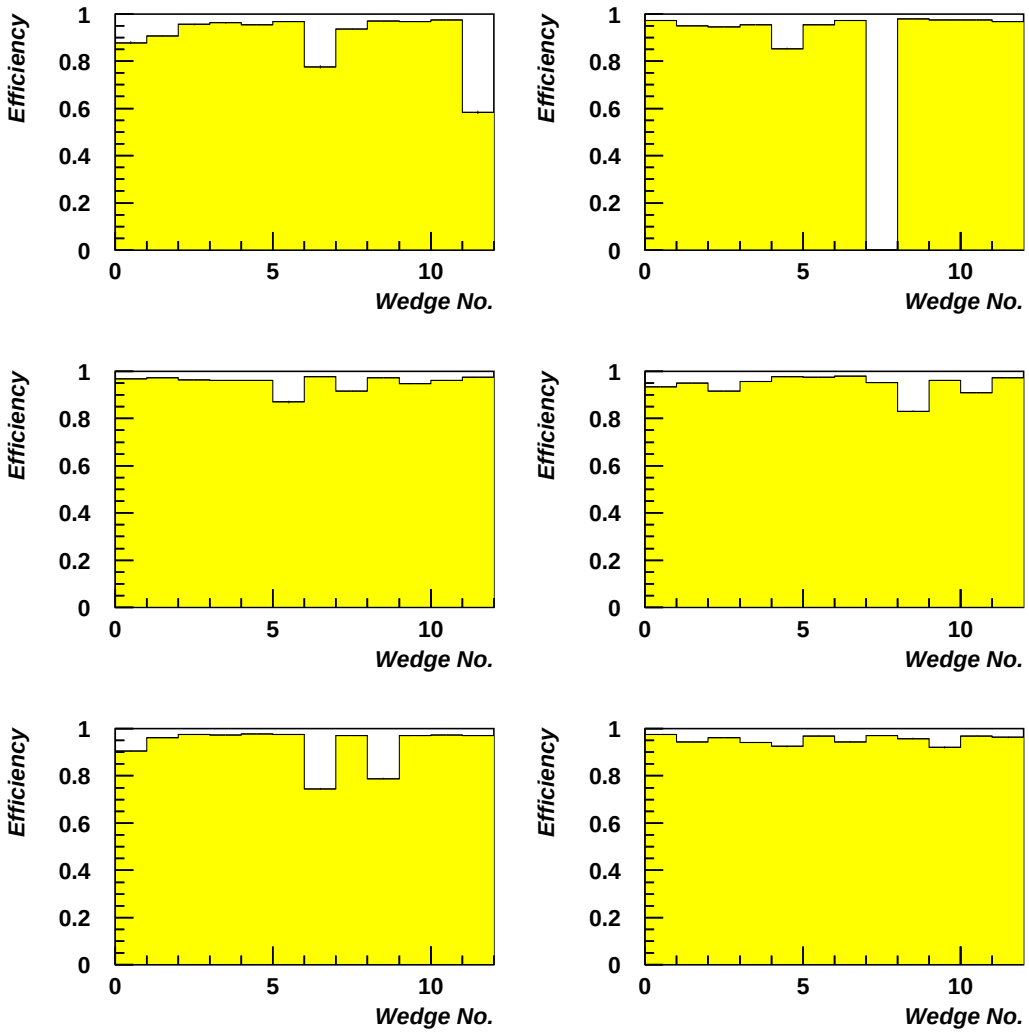

Figure 4.12: SVXII tracking efficiency for Bulkheads 0-5 for ≥ 3 r-ϕ hits

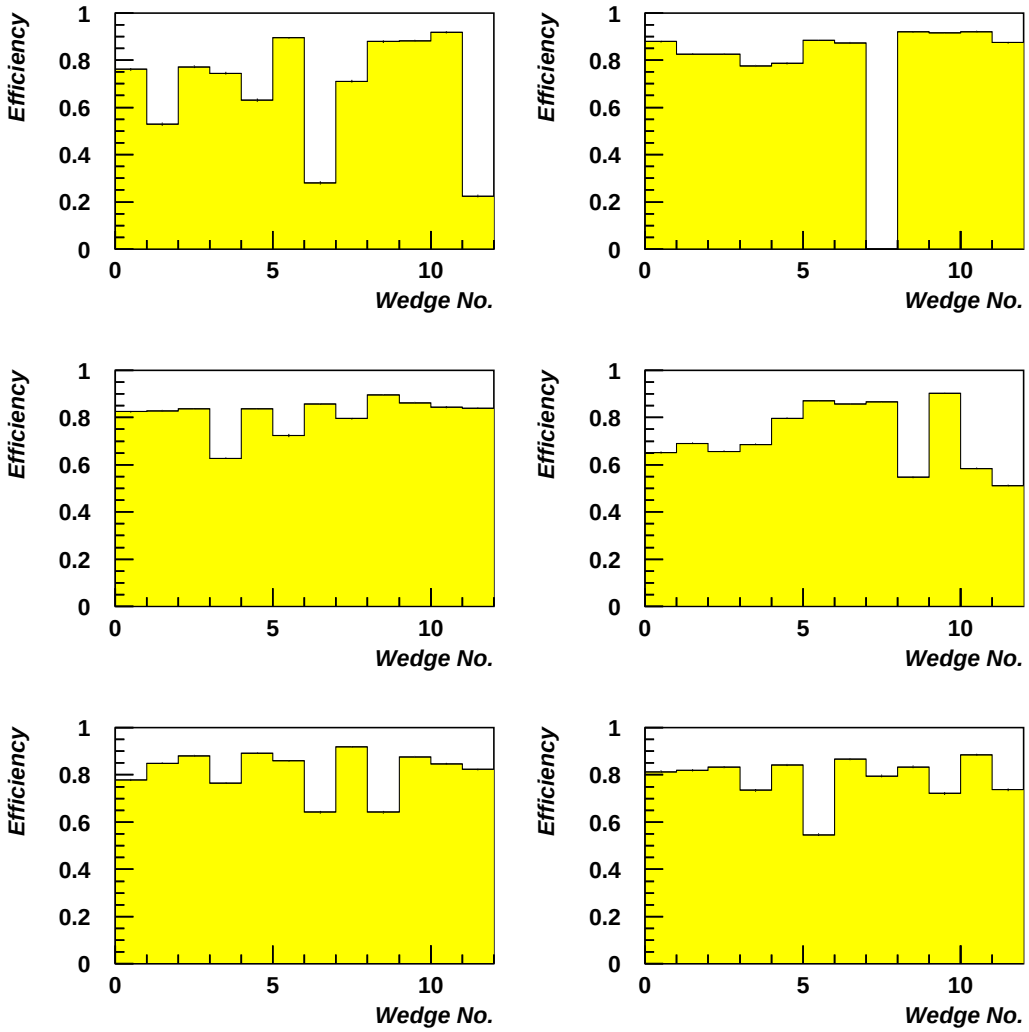

Figure 4.13: SVXII tracking efficiency for Bulkheads 0-5 for ≥ 3 r-z hits

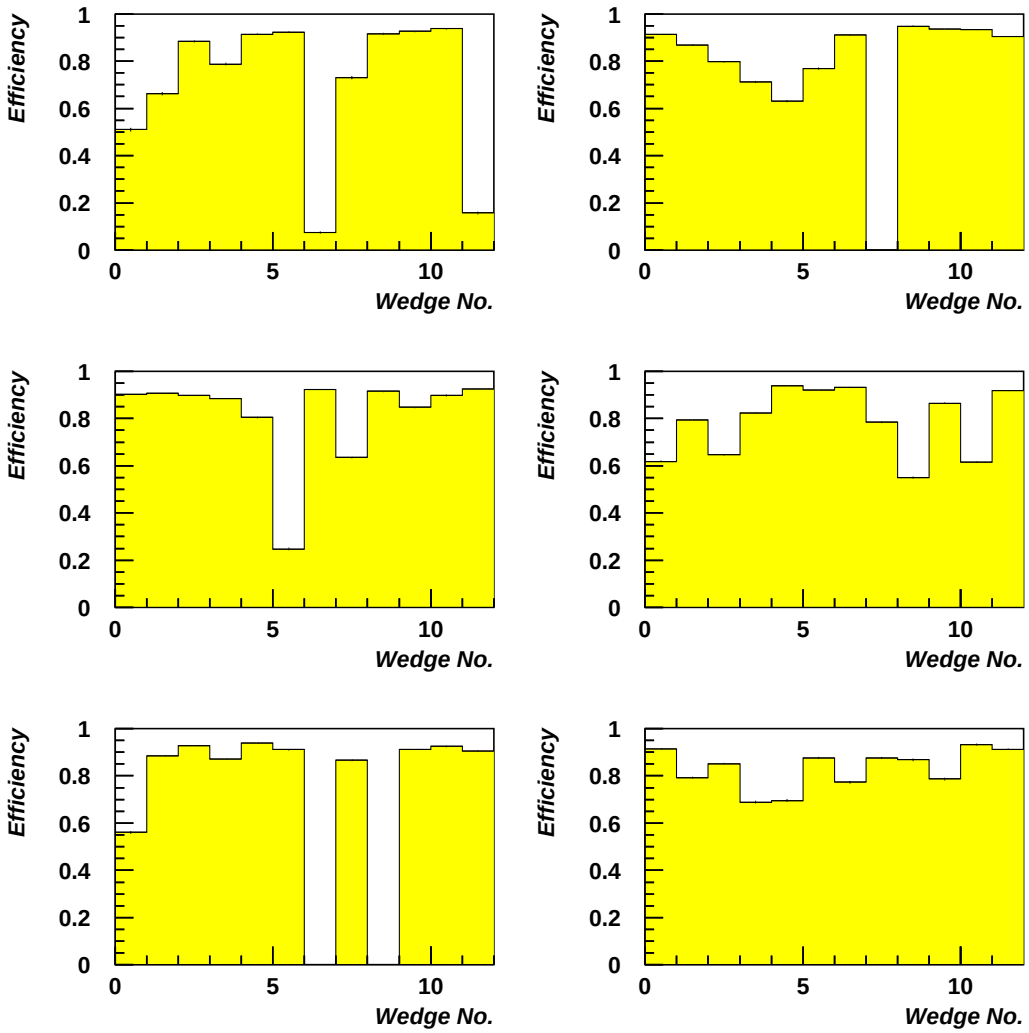

Figure 4.14: SVXII tracking efficiency for Bulkheads 0-5 for ≥ 4 r-ϕ hits

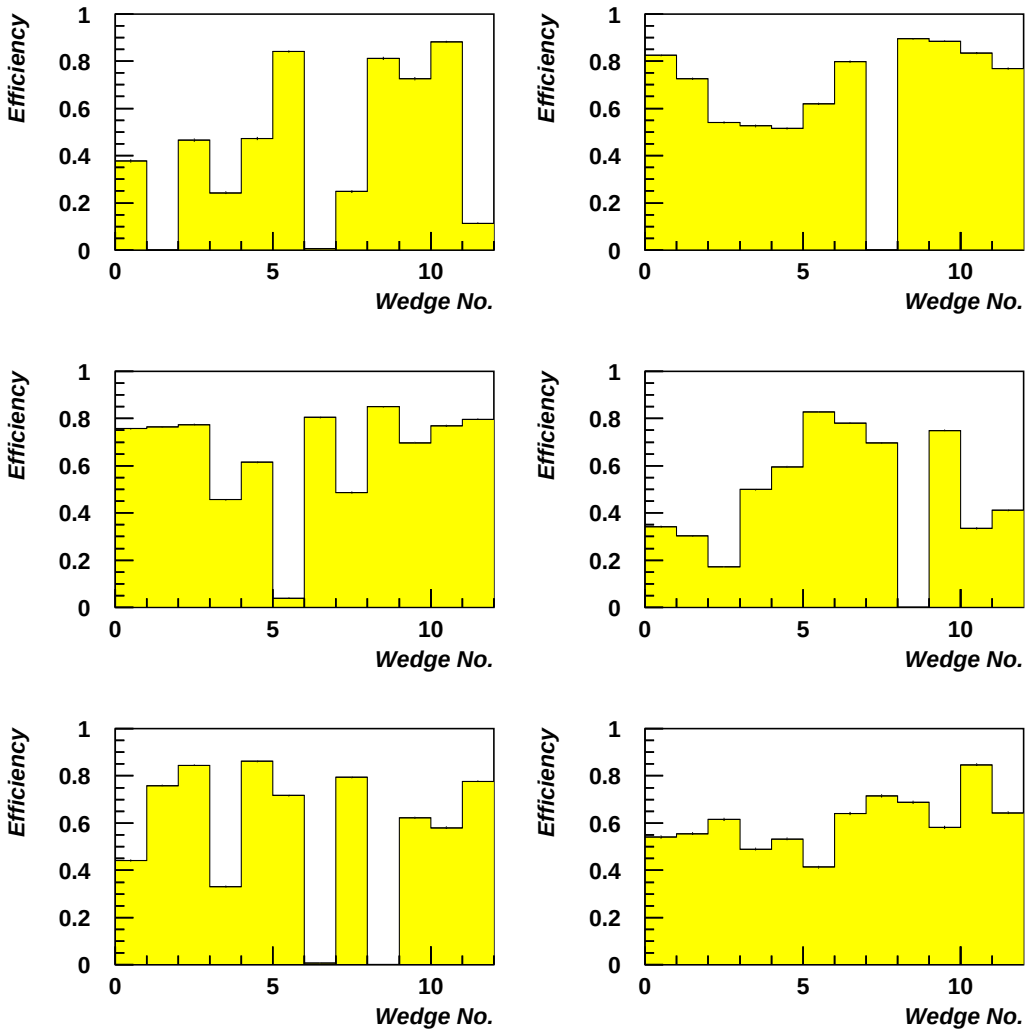

Figure 4.15: SVXII tracking efficiency for Bulkheads 0-5 for ≥ 4 r-z hits

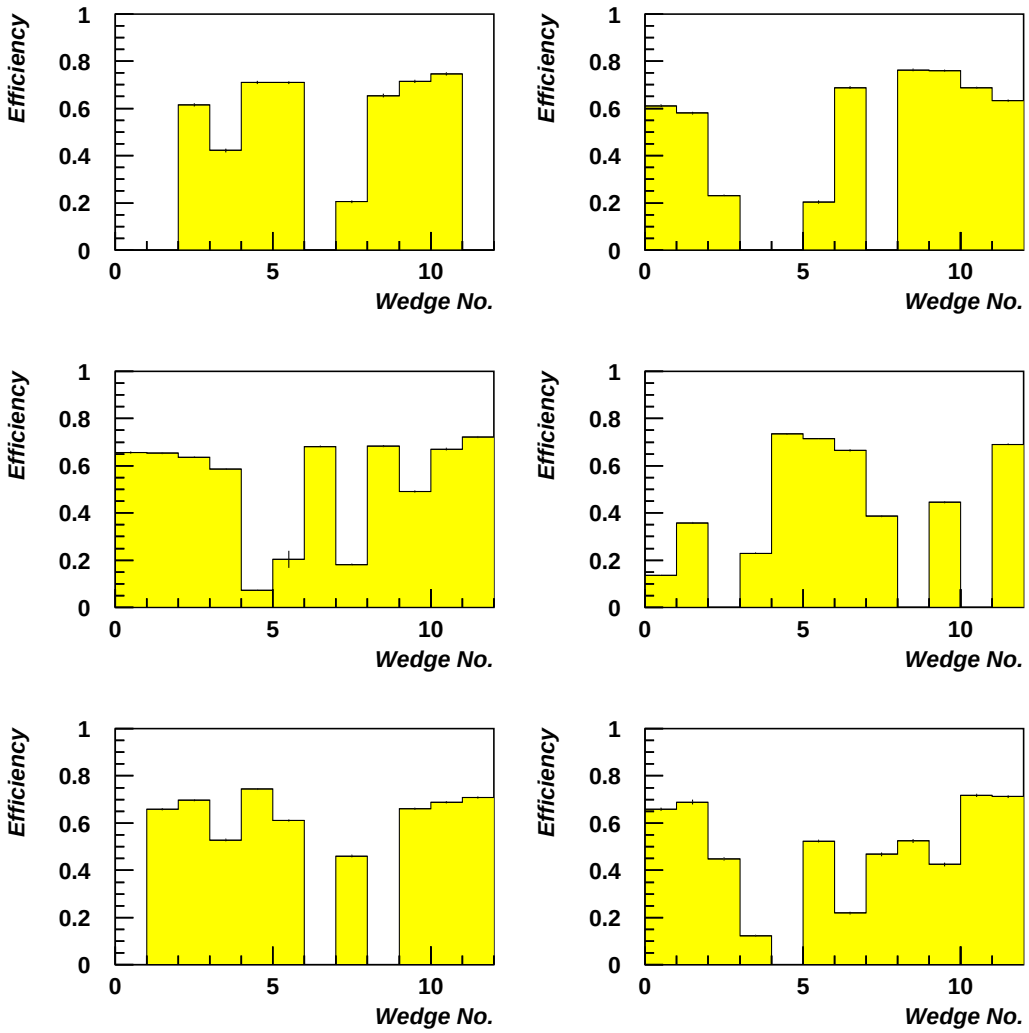

Figure 4.16: SVXII tracking efficiency for Bulkheads 0-5 for 5 r-ϕ hits

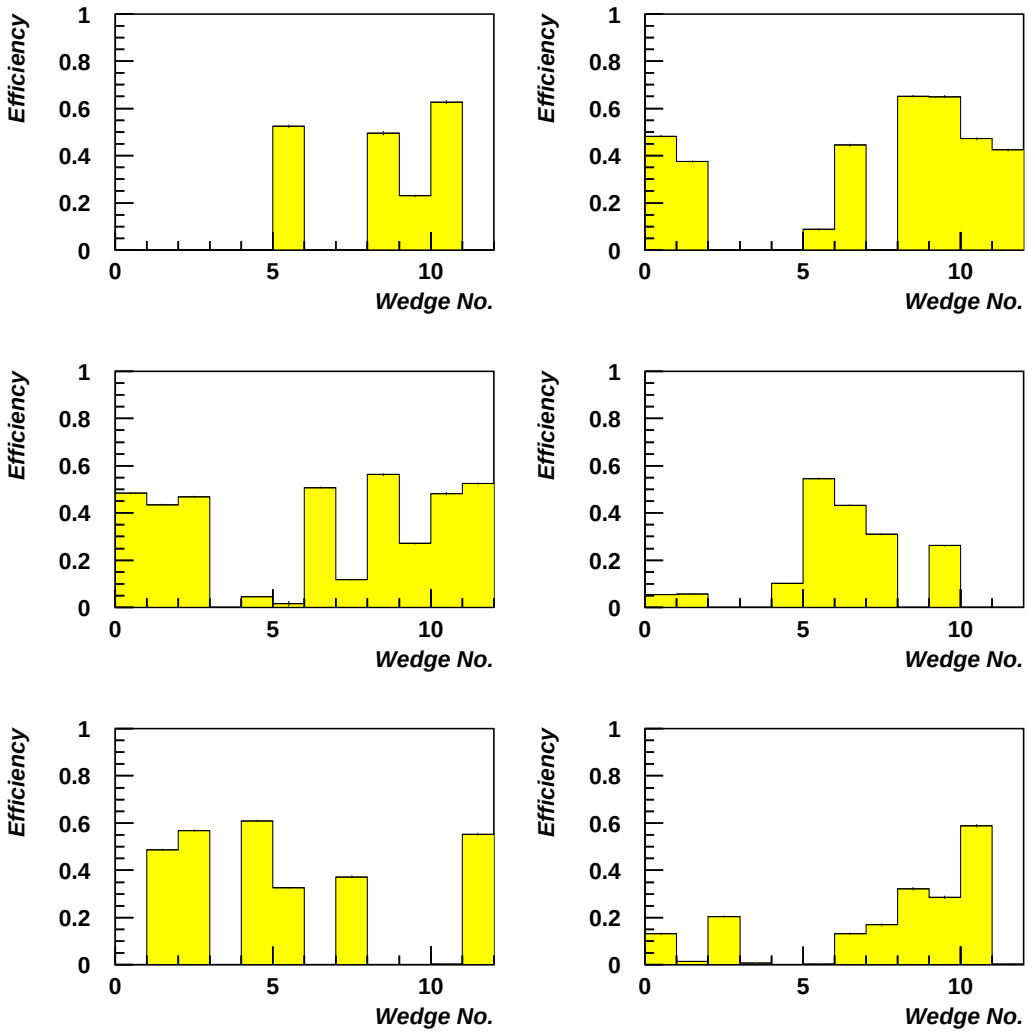

Figure 4.17: SVXII tracking efficiency for Bulkheads 0-5 for 5 r-z hits

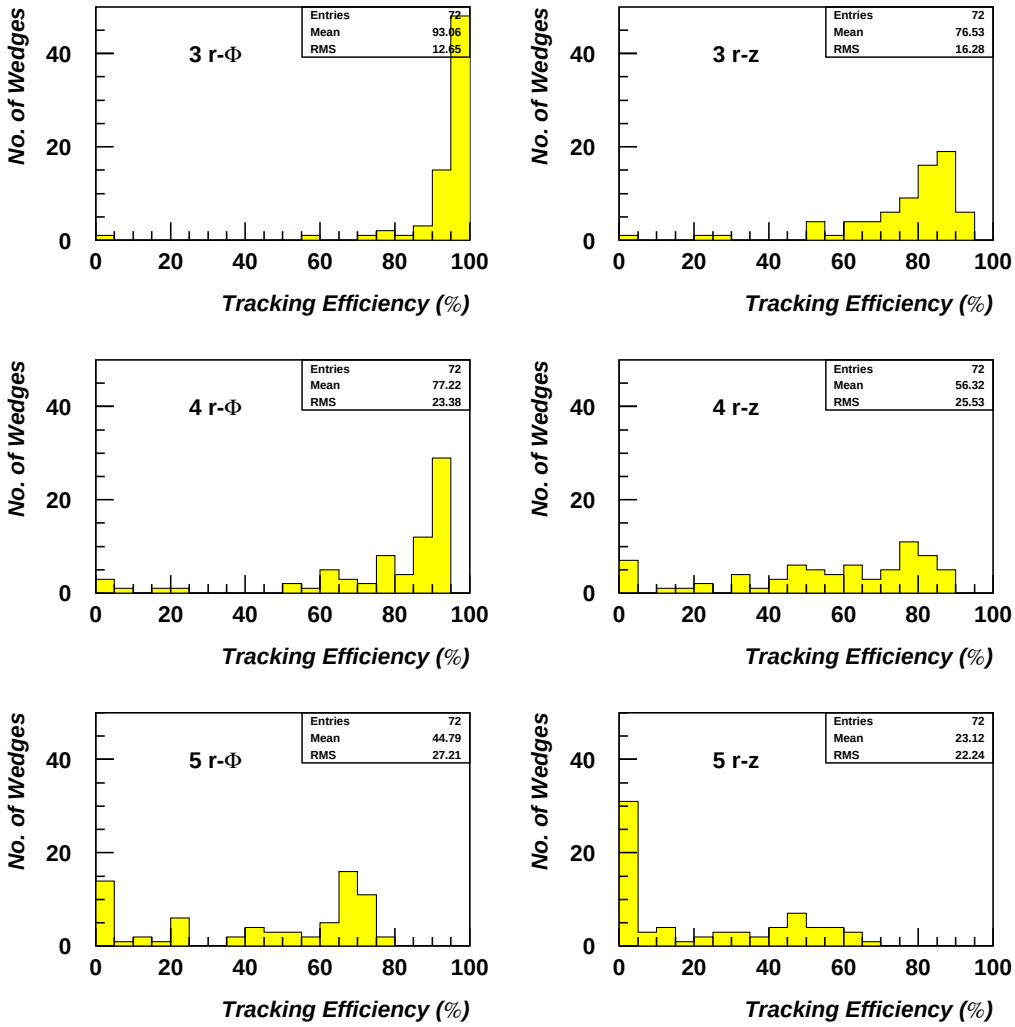

Figure 4.18: SVXII tracking efficiency distribution for all wedges with a requirement of at least 3, 4 and 5 r-ϕ and r-z hits

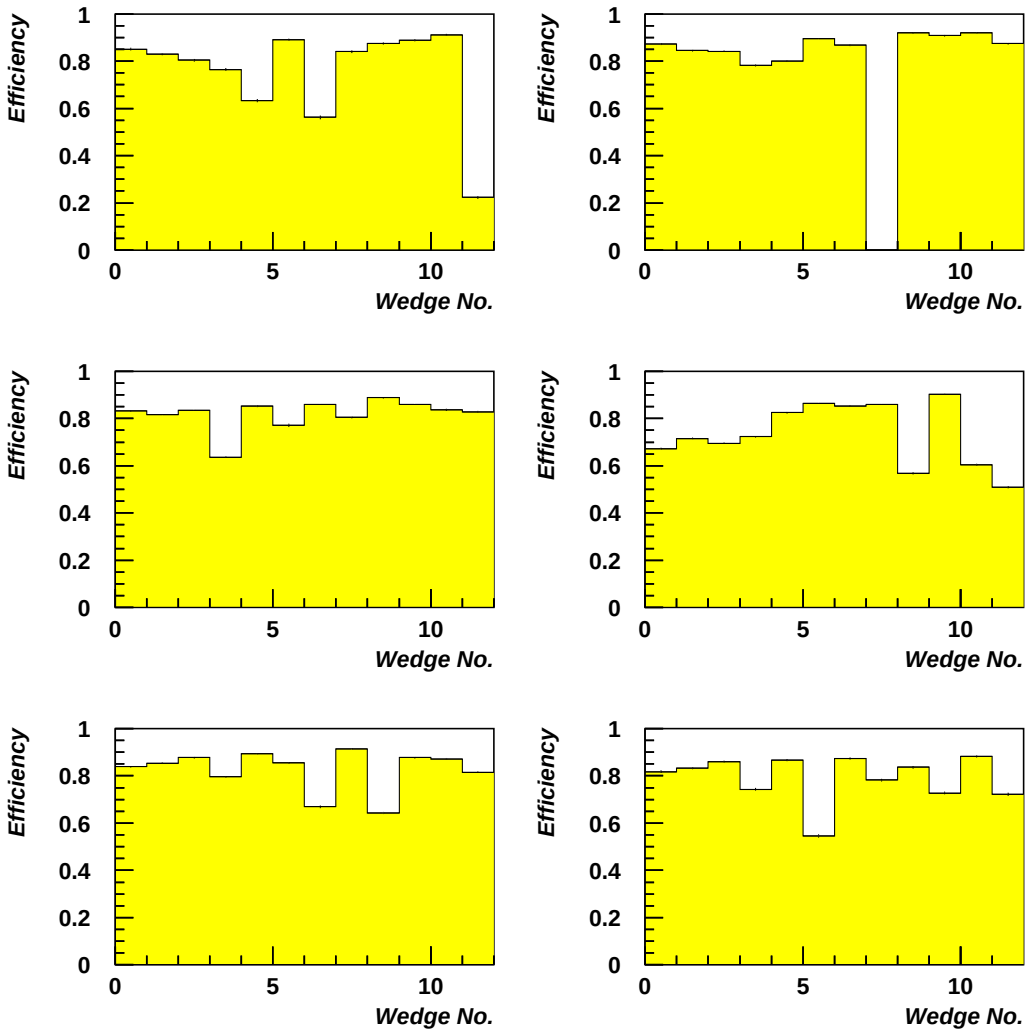

Figure 4.19: Tracking efficiency for Bulkheads 0-5 requiring ≥ 2 90° r-z hits

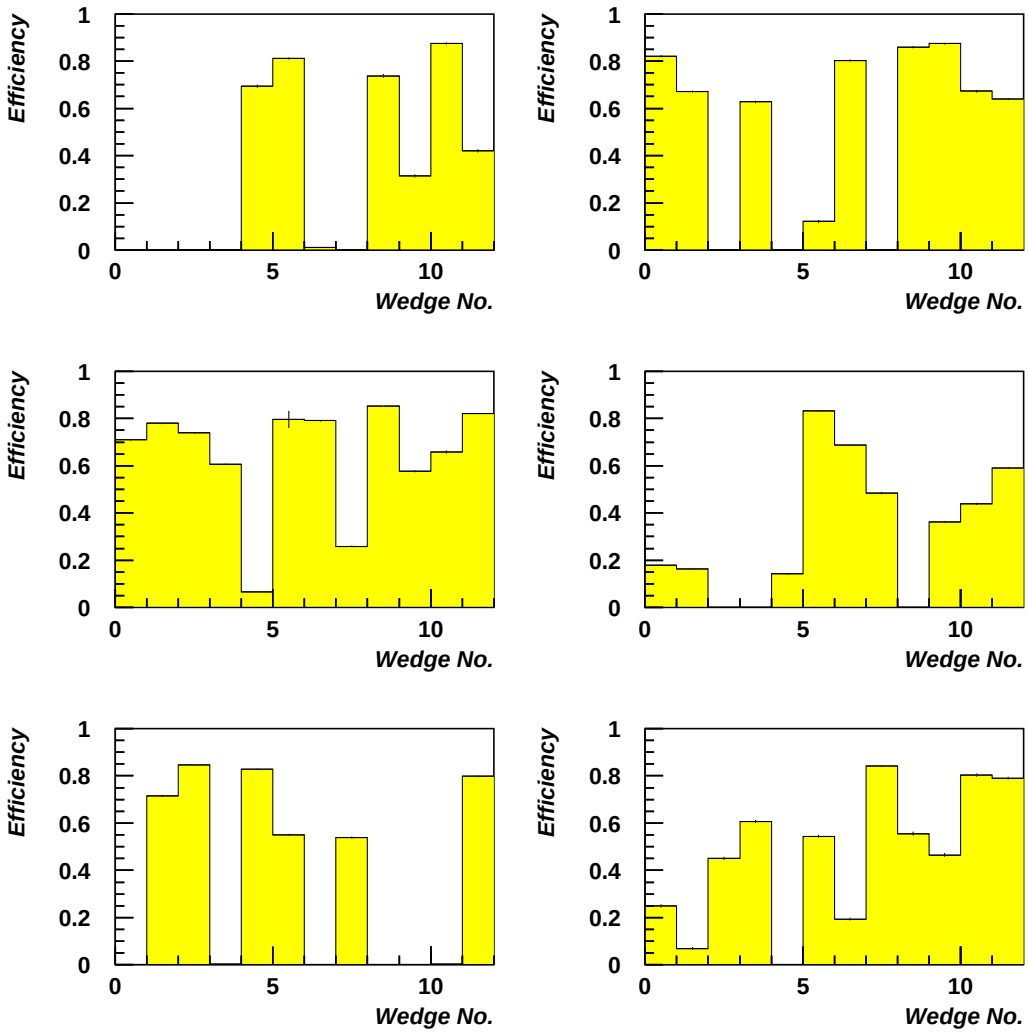

Figure 4.20: Tracking efficiency for Bulkheads 0-5 requiring 2 SAS r-z hits

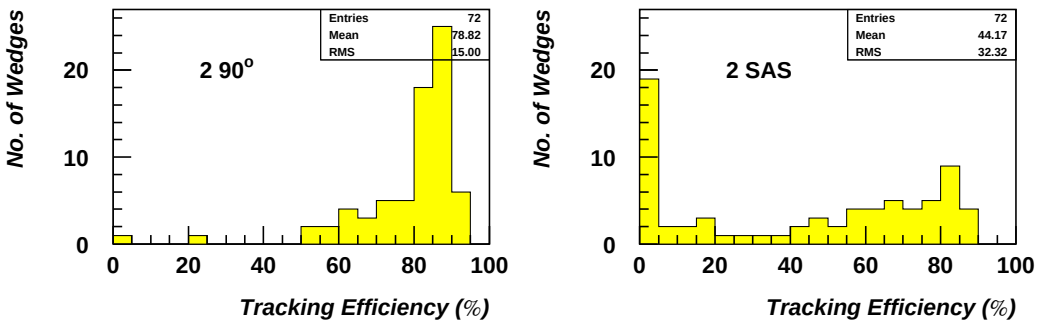

Figure 4.21: Tracking efficiency distribution for all wedges with a requirement of at least two 90° r-z hits (left) and two SAS r-z hits (right)

is two out of three.

Figure 4.21 shows the wedge tracking efficiency distributions for 90° r-z and SAS. The average efficiencies calculated when taking into account only wedges with the required number of integrated ladders are listed in Table 4.2.

4.4 SVXII Readout Error Rate per Ladder

The SiExpected package [48] provides information on ladder readout errors. This information was used in order to determine the SVXII readout error rate on tracks in the dimuon sample. The fraction of events in which an integrated ladder in the COT track path reports a readout error in one or more of its chips is calculated. The readout error rates per half-ladder for each SVXII layer are summarised in the distributions shown in Figure 4.22.

Note that no distinction is made between readout errors on the r-ϕ and r-z sides of a ladder and hit location information is only available at the half-ladder level. Therefore, if the the last chip in the readout has the readout error, this goes into the numerator even though the rest of the ladder returned

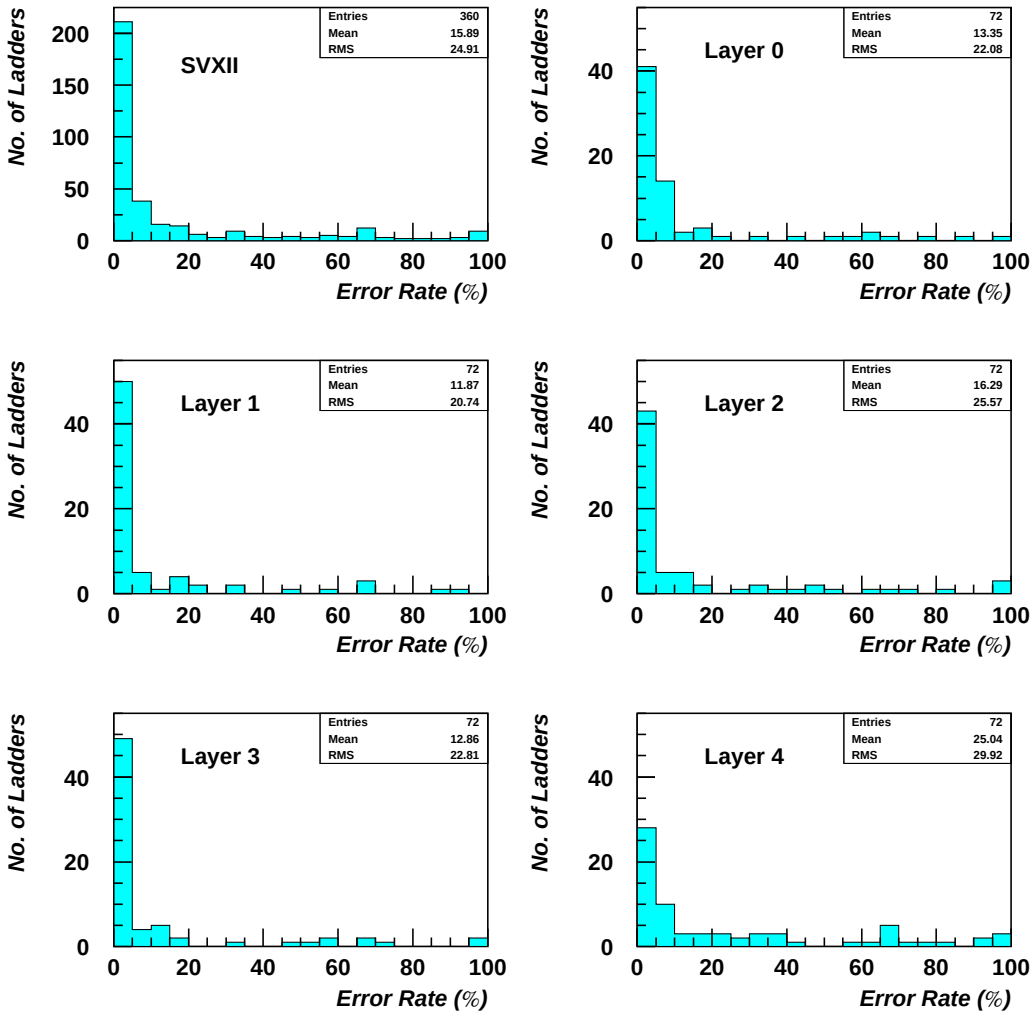

Figure 4.22: SVXII readout error rate distributions for all 360 half-ladders

good data. So the frequency of readout errors per ladder is not directly proportional to the amount of data lost. Studies have been carried out to investigate the error rate per chip [49]. The report shows that approximately 95% of all chips return good data more than 95% of the time. Therefore readout errors are not considered in the estimation of the number of expected hits per track, i.e. '$\geq n$ integrated ladders' are required rather than '$\geq n$ integrated ladders with no readout errors', because in many half-ladders the error rates are high and do not correspond directly to a hit inefficiency.

4.5 Comparing Ladder & Wedge Efficiencies

The aim of this study is to apply the cuts used in the wedge tracking efficiency study to the ladders and then repeat the half-ladder hit efficiency measurements. These results are then used to estimate what the corresponding wedge tracking efficiencies are expected to be. The predictions are compared with the tracking efficiencies that were measured directly to check for consistency. This study is done for the case where there is a requirement of 5 r-ϕ silicon hits in a wedge. The complete list of cuts applied to the muon tracks used to calculate the half-ladder hit efficiencies is as follows:

- $p_{\mathrm{T}}(\mu) \geq 1.5$ GeV/c^2
- $\geq 36/24$ axial/stereo COT hits
- $|d_0'/d_0^{\mathrm{error}}| \leq 5$
- Each COT track must pass through all the layers in an SVXII wedge that has at least 5 integrated ladders

The hit efficiency for a half-ladder is the probability that it will register a hit when expected based on the intersection location of an extrapolated COT track. Let ε_0, ε_1, ε_2, ε_3, ε_4 be the measured hit efficiencies for the half-ladders in Layers 0 through 4 of an individual SVXII wedge. Therefore, assuming uncorrelated efficiencies, the expected tracking efficiency for the wedge is

$$\varepsilon = \varepsilon_0\,\varepsilon_1\,\varepsilon_2\,\varepsilon_3\,\varepsilon_4.$$

The tracking efficiency for the wedge is limited by the efficiency of the least efficient ladder, i.e.

$$\varepsilon_{\max} = \min(\varepsilon_0, \varepsilon_1, \varepsilon_2, \varepsilon_3, \varepsilon_4).$$

A lower limit for the tracking efficiency is

$$\varepsilon_{\min} = \begin{cases} 1 - \sum_{i=0}^{4}(1-\varepsilon_i) & \text{for } \sum(1-\varepsilon_i) < 1 \\ 0 & \text{for } \sum(1-\varepsilon_i) \geq 1 \end{cases}$$

Since the tracking efficiency is being calculated for 5 r-ϕ hits, $\varepsilon_{\max} = \varepsilon_{\min} = 0$ in cases where a wedge contains one or more ladders that are not integrated. $\varepsilon \to \varepsilon_{\min}$ when the individual ladders fail to register expected hits in different events from each other. This results in a reduction in the number of events where all five ladders see the required hits. For example, if $\varepsilon_i = 0.8$ $(i = 0, 4)$ and each ladder misses an expected hit in a different 20% of the total number of events, then $\varepsilon = 0$ for this wedge. $\varepsilon \to \varepsilon_{\max}$ when the ladders in a wedge consistenly fail to register an expected hit in the same events as each other, i.e. if one ladder fails to see a hit there will be one or more other ladders that also recorded no hit.

The half-ladder hit efficiencies obtained using the wedge tracking efficiency cuts were then used to calculate ε, $\varepsilon_{\min}$ and $\varepsilon_{\max}$ for each SVXII wedge.

The results are illustrated in Figure 4.23. The values obtained when the tracking efficiency was calculated directly (see Figure 4.16) are also marked. While all of the measured efficiencies are consistent in that they lie between $\varepsilon_{\min}$ and $\varepsilon_{\max}$ without taking the value of either, they are all greater than or equal to the predicted values of ε. This indicates that there is a correlation between ladders when expected hits are not seen, i.e. $\varepsilon \to \varepsilon_{\max}$.

The half-ladder hit efficiencies are used to calculate the probability of two or more ladders failing to record an expected hit in the same event. This result is then compared with a direct measurement to prove that $\varepsilon \to \varepsilon_{\max}$. Consider the probability, ε', of fewer than two ladders failing to register an expected hit in the same event. This is equal to the probability of observing 4/5 or 5/5 expected hits, i.e.

$$\begin{aligned}
\varepsilon' &= \varepsilon_0\,\varepsilon_1\,\varepsilon_2\,\varepsilon_3\,\varepsilon_4 + (1-\varepsilon_0)\,\varepsilon_1\,\varepsilon_2\,\varepsilon_3\,\varepsilon_4 + \varepsilon_0\,(1-\varepsilon_1)\,\varepsilon_2\,\varepsilon_3\,\varepsilon_4 \\
&\quad + \varepsilon_0\,\varepsilon_1\,(1-\varepsilon_2)\,\varepsilon_3\,\varepsilon_4 + \varepsilon_0\,\varepsilon_1\,\varepsilon_2\,(1-\varepsilon_3)\,\varepsilon_4 + \varepsilon_0\,\varepsilon_1\,\varepsilon_2\,\varepsilon_3\,(1-\varepsilon_4) \\
&= \varepsilon_1\,\varepsilon_2\,\varepsilon_3\,\varepsilon_4 + \varepsilon_0\,\varepsilon_2\,\varepsilon_3\,\varepsilon_4 + \varepsilon_0\,\varepsilon_1\,\varepsilon_3\,\varepsilon_4 \\
&\quad + \varepsilon_0\,\varepsilon_1\,\varepsilon_2\,\varepsilon_4 + \varepsilon_0\,\varepsilon_1\,\varepsilon_2\,\varepsilon_3 - 4\,\varepsilon_0\,\varepsilon_1\,\varepsilon_2\,\varepsilon_3\,\varepsilon_4
\end{aligned}$$

It follows that the probability of two or more ladders failing to register an expected hit in the same event is

$$\varepsilon'' = 1 - \varepsilon'.$$

The half-ladder hit efficiencies were used to calculate the expected value of ε'' for each wedge in SVXII Bulkhead 2. The data used to determine the half-ladder hit efficiencies was then studied to check whether there was any evidence of a correlation between layers. This was done by calculating the fraction of all tracks passing through each wedge that failed to register two or

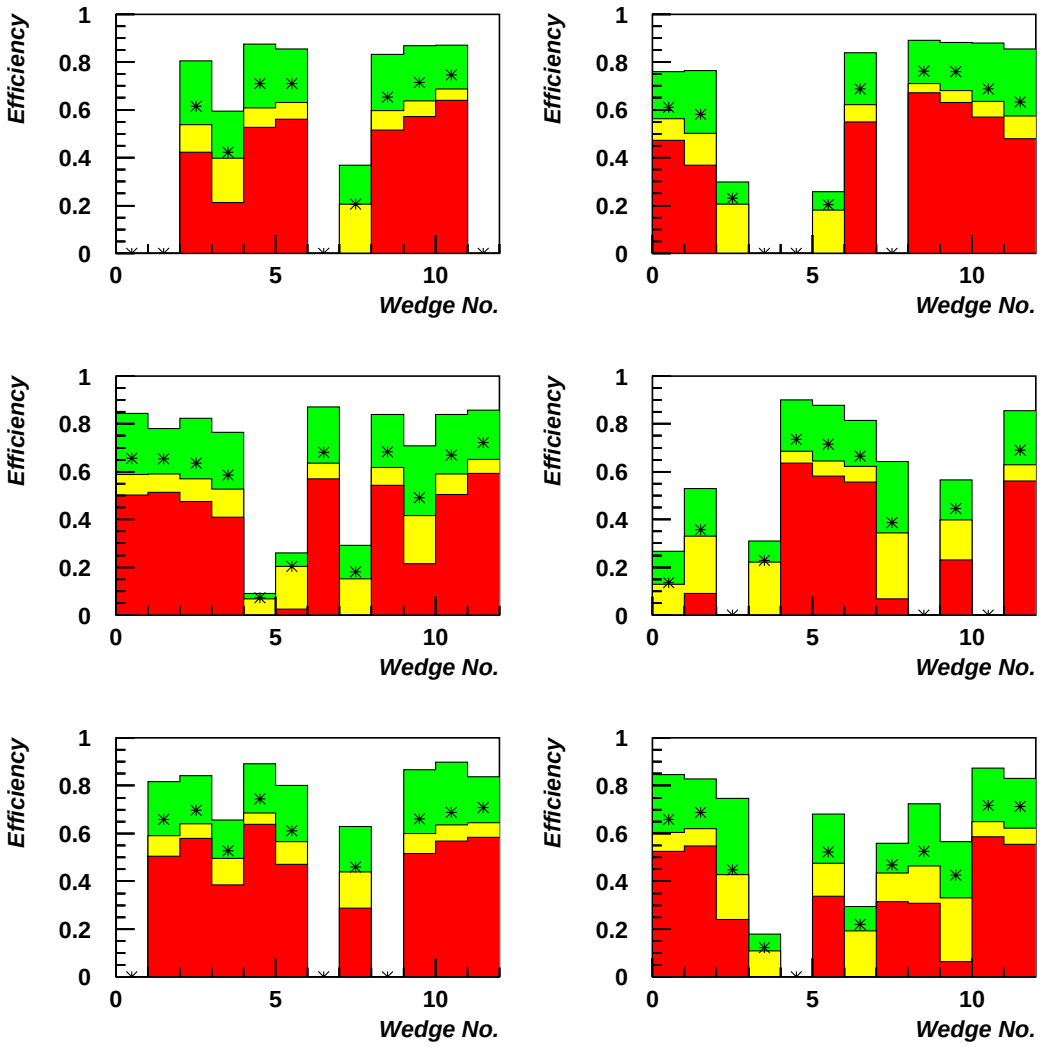

Figure 4.23: SVXII tracking efficiency for Bulkheads 0-5 calculated from half-ladder hit efficiencies with a requirement of 5 r-ϕ hits. The plots show $\varepsilon_{\min}$ in red, $\varepsilon_{\max}$ in green, and the expected efficiency ε in yellow. The stars indicate the values obtained when the tracking efficiency was calculated directly.

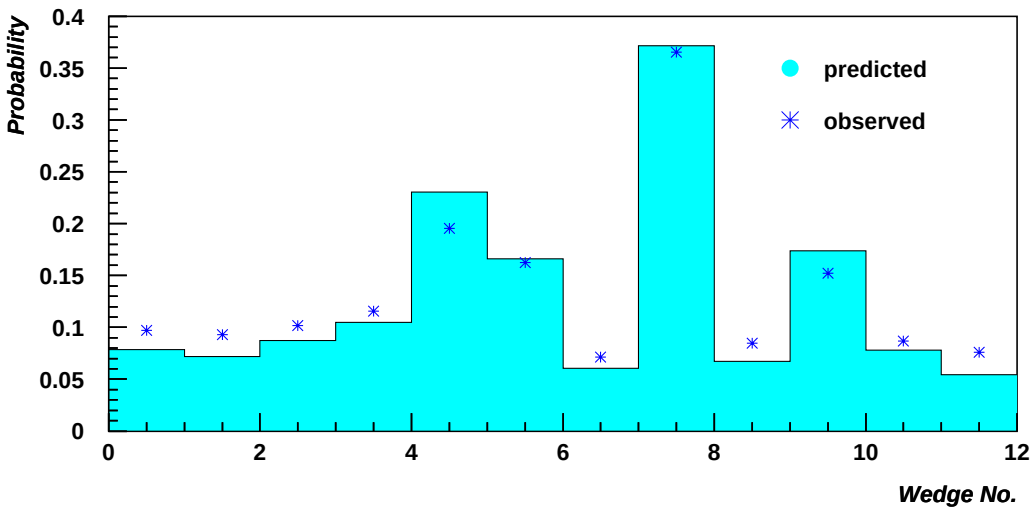

Figure 4.24: Observed and predicted values of ε'', the probability of more than one ladder failing to see an expected hit in a given event, for each of the wedges in SVXII Bulkhead 2

more expected hits. These are the observed values of ε''. Figure 4.24 shows both the predicted and observed values of ε'' for the wedges in Bulkhead 2.

The results in Figure 4.24 show that, except for wedges 4, 5, 7 & 9, each of which contain a low efficiency ladder (see Figure 4.7), when a ladder fails to see a hit in a particular event, at least one other ladder also fails to register a hit more often than expected. Therefore, the calculation supports the conjecture that there is a correlation between ladders when expected hits are not seen, i.e. $\varepsilon \rightarrow \varepsilon_{\max}$. This correlation explains why the directly measured tracking efficiency is greater than that deduced from the half-ladder hit efficiencies. The correlation may be due to the COT tracks occasionally being projected into the wrong SVXII wedge. In addition, the relative alignment of ladders in some wedges may better than in others. Finally, it is also possible that the half-ladder hit efficiencies are underestimated.

Chapter 5

Optimisation of Silicon Track Selection

The J/ψ inclusive cross-section has been measured using J/$\psi \rightarrow \mu\mu$ events reconstructed in the COT and CMU from 36 pb^{-1} of data in the run range 138425-152625 [50]. The J/ψ data sample is obtained from the Level 1 dimuon and track triggers. At Level 3 the muons are reconstructed from a COT track and stubs in the CMU detector.

In Chapter 6, the fraction of J/ψ's from b hadron decays is measured using an unbinned likelihood fit to the proper decay length of the J/ψ to separate the prompt and non-prompt components. The B-fraction result and the measurement of the SVXII/COT relative acceptance are then combined with the J/ψ inclusive cross-section measurement to obtain the B $\rightarrow$ J/ψ X inclusive cross-section at $\sqrt{s} = 1.96$ TeV.

This analysis benefits from the large number of J/$\psi \rightarrow \mu^+\mu^-$ decays that are available, but less than 20% of the J/ψ mesons produced in p$\bar{\text{p}}$ collisions at CDF come from the decay of b hadrons [51]. The remainder are either directly produced or come from the decay of directly produced higher mass charmonium states.

The large statistics in the inclusive J/ψ sample allows one to be highly selective when choosing which tracks to accept. This chapter describes the work performed to optimise the SVXII resolution and track quality selection in order to reduce the uncertainty on the B-fraction measurement. It begins with a review of the status of SVXII tracking and a description of the cuts used to select tracks for this analysis. This is followed by a statement of goals for the optimisation of cuts and an outline of the procedure used to achieve these goals. The chapter then concludes with the results of the optimisation study.

5.1 Overview of SVXII Tracking Status

To make a good lifetime measurement, it is crucial to have the best possible coverage in the innermost silicon layers. A detailed review of silicon tracking efficiency and detector coverage, using the dimuon data in the run range associated with the B-fraction analysis, was presented in Chapter 4. In this analysis the data can be divided into several run ranges to account for changes in detector performance. Figure 5.1 shows the SVXII half-ladder hit efficiency for Layer 0 ladders for runs 144013-145669 before the detector was shut down for maintenance in Summer 2002. Nine of the Layer 0 ladders had zero or lower than average efficiency. Figure 5.2 shows how the coverage in Layer 0 improved after the shutdown in runs 146805-152625. Three ladders in Bulkheads 2, 3 and 5 that were turned off in the earlier run range were reintegrated and all three low efficiency ladders were restored to average efficiency. However, one ladder (SB0W11L0) that was operating with a high hit efficiency in runs 144013-145669 experienced a 50% drop in efficiency after

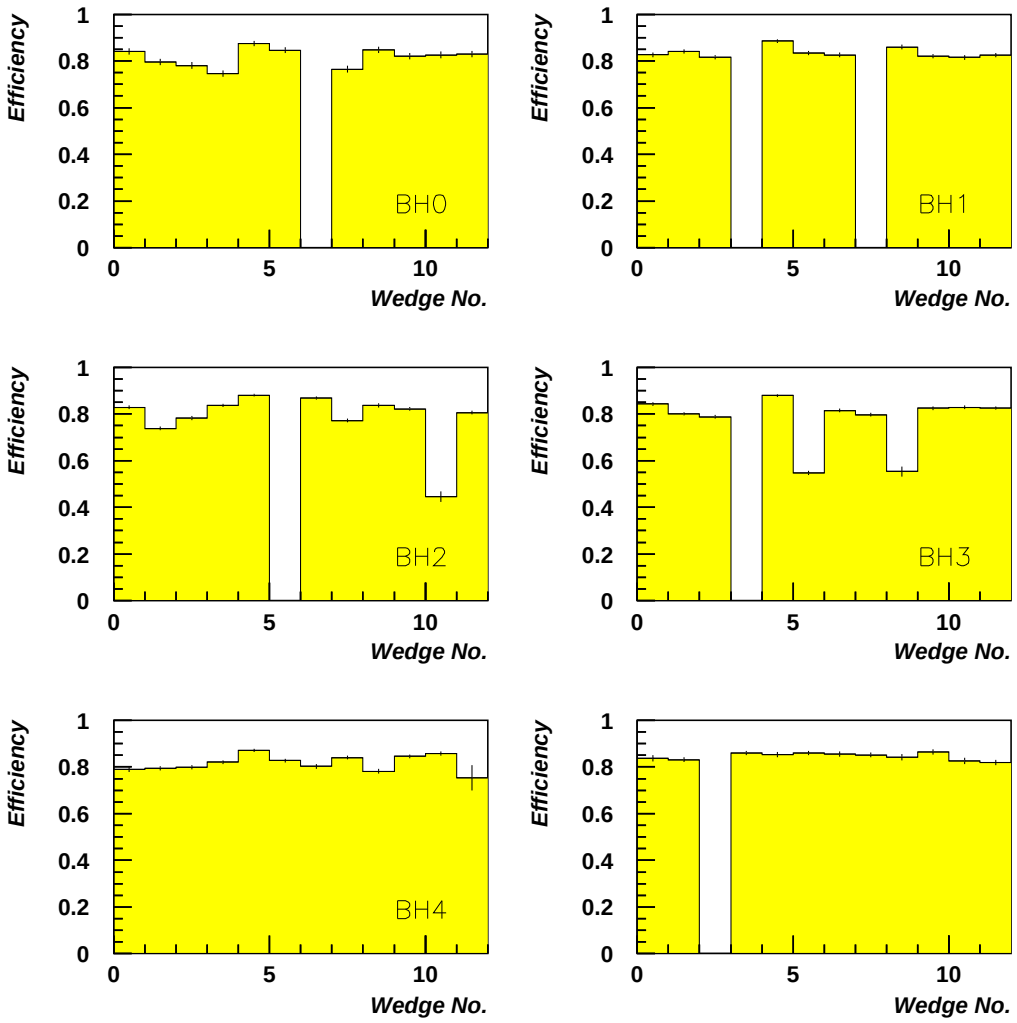

Figure 5.1: Layer 0 hit efficiency for Bulkheads 0-5 in runs 144013-145669

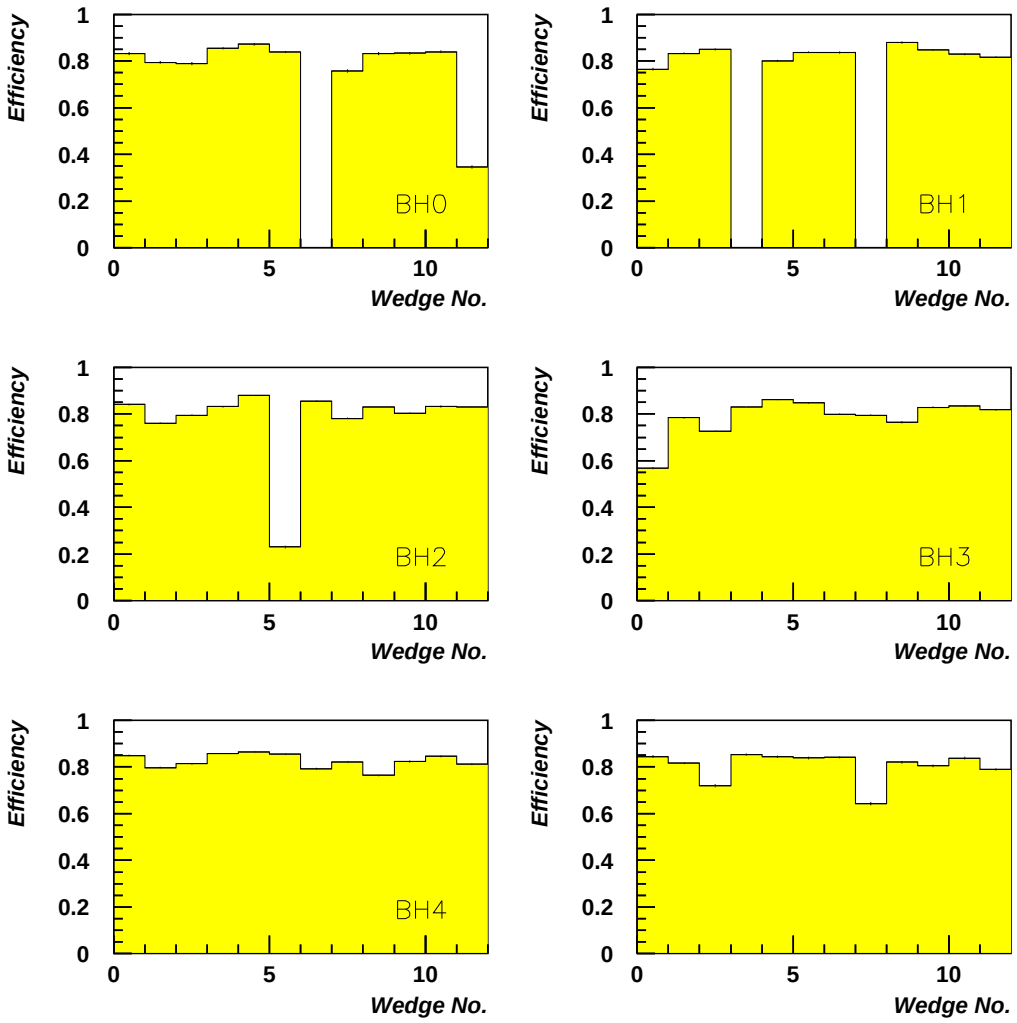

Figure 5.2: Layer 0 hit efficiency for Bulkheads 0-5 in runs 146805-152625

the shutdown. The substantial increase in the number of good and powered ladders after the shutdown can be seen clearly in Figure 4.1.

5.2 L_{xy}

A schematic of a J/ψ decay in the r-ϕ plane is presented in Figure 5.3. L_{xy} is defined as the signed projection of the secondary vertex momentum along the axis of the distance R_{xy} from the J/ψ decay vertex to the beam spot.

$$L_{xy} = \frac{\mathbf{L} \cdot \mathbf{p}_{\mathrm{T}}(\mathrm{J}/\psi)}{p_{\mathrm{T}}(\mathrm{J}/\psi)} = R_{xy} \cos\theta$$

where θ is the angle between the J/ψ and b hadron direction. Since L_{xy} is a signed quantity distributed symmetrically around $L_{xy} = 0$ for zero lifetime

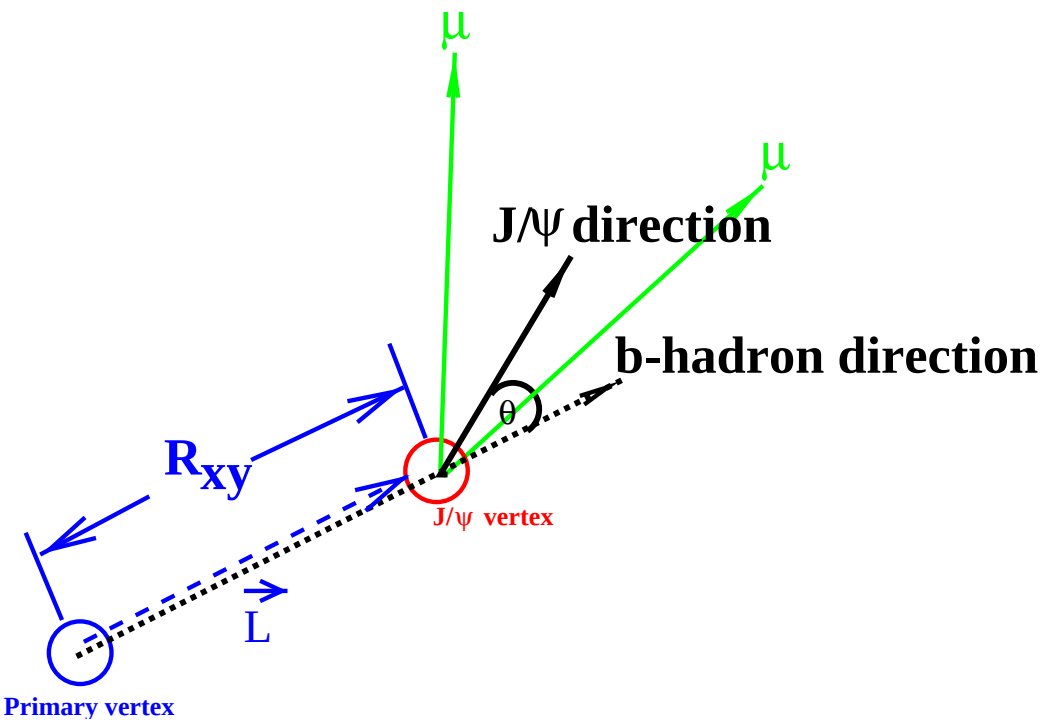

Figure 5.3: The variables used to define L_{xy} shown in the r-ϕ plane

events, the two-track flight distance resolution can be measured by examining the L_{xy} distributions of prompt J/ψ's in data.

A mixture of prompt J/ψ and B $\rightarrow$ J/ψ events were generated in a simple Monte Carlo. The fraction of B $\rightarrow$ J/ψ events in the overlap region of the prompt J/ψ distribution in L_{xy} is less than or equal to the fraction in the R_{xy} distribution for $p_{\rm T}({\rm J}/\psi) > 1.25$ GeV/c. As well as improving the separation between prompt and long-lived J/ψ, the main advantage of using L_{xy} is that prompt J/ψ events with negative values of L_{xy} are due to mismeasurements or resolution effects. This means that the negative tails of the distribution can be used to model the mismeasurements in the positive L_{xy} signal region, and the negative values of L_{xy} from the dominant prompt J/ψ decays can be used to extract the resolution function from the same data.

For $p_{\rm T}({\rm J}/\psi) < 1.75$ GeV/c, real B decays will produce negative values of L_{xy} due to large opening angles between the b hadron flight direction and the low momentum J/ψ. However, for events with $1.0 < p_{\rm T}({\rm J}/\psi) < 1.75$ GeV/c the fraction of these B events with negative tails is small compared to the resolution effects from prompt J/ψ events.

5.3 J/ψ Selection Cut Summary

The following selection criteria are applied by the Level 3 trigger:

- *Level 3 Selection Criteria*
  - CMU muons
  - $p_{\rm T}(\mu)_{\rm COT} > 1.5$ GeV/c
  - opposite sign muons

- $|z_0(\mu_1) - z_0(\mu_2)| < 5$ cm
- $2.7 < M_{\mu\mu} < 4.0$ GeV/c^2
- $\Delta\phi(\mu\mu) < 130^\circ$ when $p_{\rm T}({\rm J}/\psi) > 2.0$ GeV/c
- muon stub track match $\Delta(r\phi)_{\rm CMU} < 30$ cm

The J/ψ selection cuts that are subsequently applied are arranged into four groups. (1) *Muon Quality Cuts* are used to select good COT tracks and CMU muons independently of SVXII. (2) *Basic SVXII Cuts* are the default reconstruction cuts on a COT-SVXII track. (3) *SVXII Vertex Quality Cuts* are the minimal cuts used to ensure that the J/ψ vertex reconstructed in SVXII is good. (4) *SVXII Track Quality Cuts* are the track selections that will be explored in detail for the optimisation studies.

- *1: Muon Quality Cuts*
  - require CMU-CMU or CMU-CMP muon pairs only
  - $\geq$ 20/16 axial/stereo COT hits
  - CMU track-matching $\chi^2(\Delta r\phi) < 9$
  - $|y_{{\rm J}/\psi}| < 0.6$
- *2: Basic SVXII Cuts*
  - require CMU-CMU or CMU-CMP muon pairs only
  - ≥ 3 r-ϕ L00/SVXII/ISL hits
- *3: SVXII Vertex Quality Cuts*
  - Error on L_{xy}, $\sigma_{L_{xy}} \leq 0.025$ cm

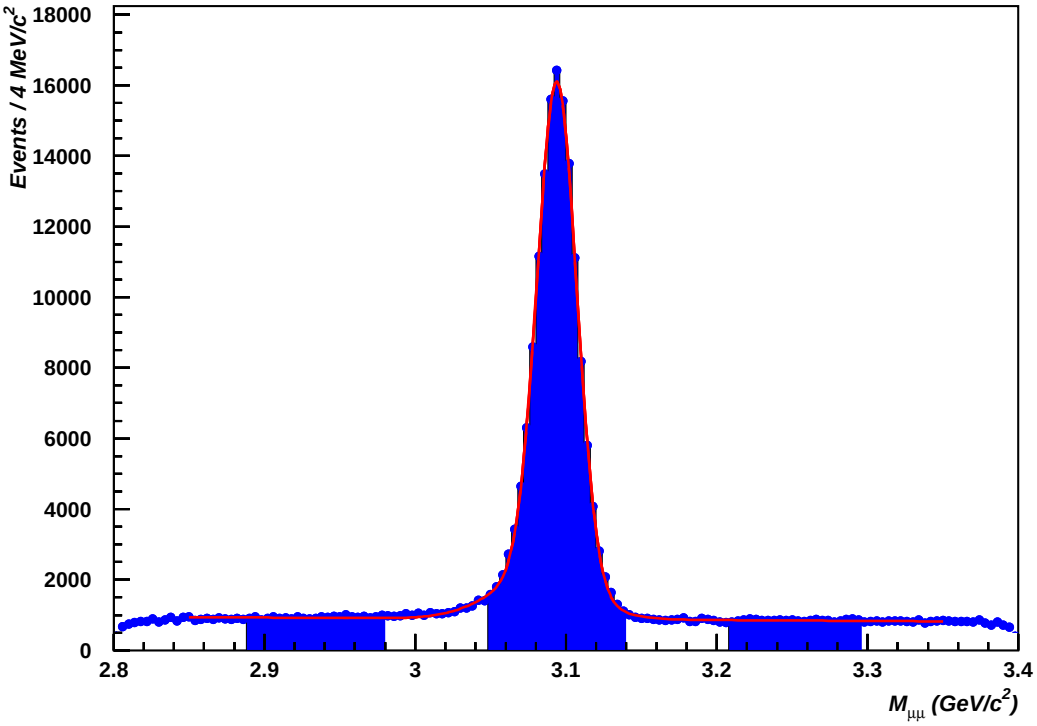

Figure 5.4: The dimuon invariant mass distribution fitted to a double Gaussian plus flat background after the full set of silicon cuts are applied

  - Fit probability ≥ 0.001

- *4: SVXII Track Quality Cuts*

  - Require a hit in Layer 0
  - Require a hit in Layer 1 when integrated
  - If a track intersects n integrated SVXII ladders, require at least $n - 1$ hits
  - Reject tracks that cross between barrels

All 3D hits found in SVXII and ISL during pattern recognition are used. Energy loss corrections using a muon particle hypothesis are applied to the

muon tracks during the refit to account for energy lost due to the material in the detector [52, 53]. A 3D constrained vertex fit is applied to the two muon tracks to reconstruct the J/ψ decay vertex position. The events are also required to have the run-averaged beam spot position calculated from silicon tracks in inclusive jet data.

Figure 5.4 shows the dimuon invariant mass distribution of accepted events fitted to a double Gaussian with flat background. The signal region is taken to be 3σ around the mean, where the mean and the width are the weighted averages of the two Gaussians used in the invariant mass fits. Throughout this optimisation study, the sideband subtractions are performed using a dimuon invariant mass signal region of $\pm 3\sigma$ and sideband regions of $\pm 8\sigma \rightarrow \pm 14\sigma$. Figure 5.5 shows the sideband subtracted distributions of some of the quantities that are cut on, with the background distributions superimposed.

5.4 Optimisation Goals

Without biasing the B-fraction measurement, the best two-track vertex quality is obtained by optimizing for minimum tails in the $L_{xy}/\sigma_{L_{xy}}$ distributions and the best L_{xy} resolution measured from prompt J/ψ's. Figure 5.6 shows the sideband and sideband subtracted L_{xy} and $L_{xy}/\sigma_{L_{xy}}$ distributions in the case where basic SVXII cuts (Set 2) are applied. Events with $L_{xy} > 200$ μm are excluded from the $L_{xy}/\sigma_{L_{xy}}$ distributions to minimise the bias from B decays. The $L_{xy}/\sigma_{L_{xy}}$ distributions are fitted with a single Gaussian, which fails to describe the data at large negative values.

Runs with the best silicon coverage (146805-152625) are used to study

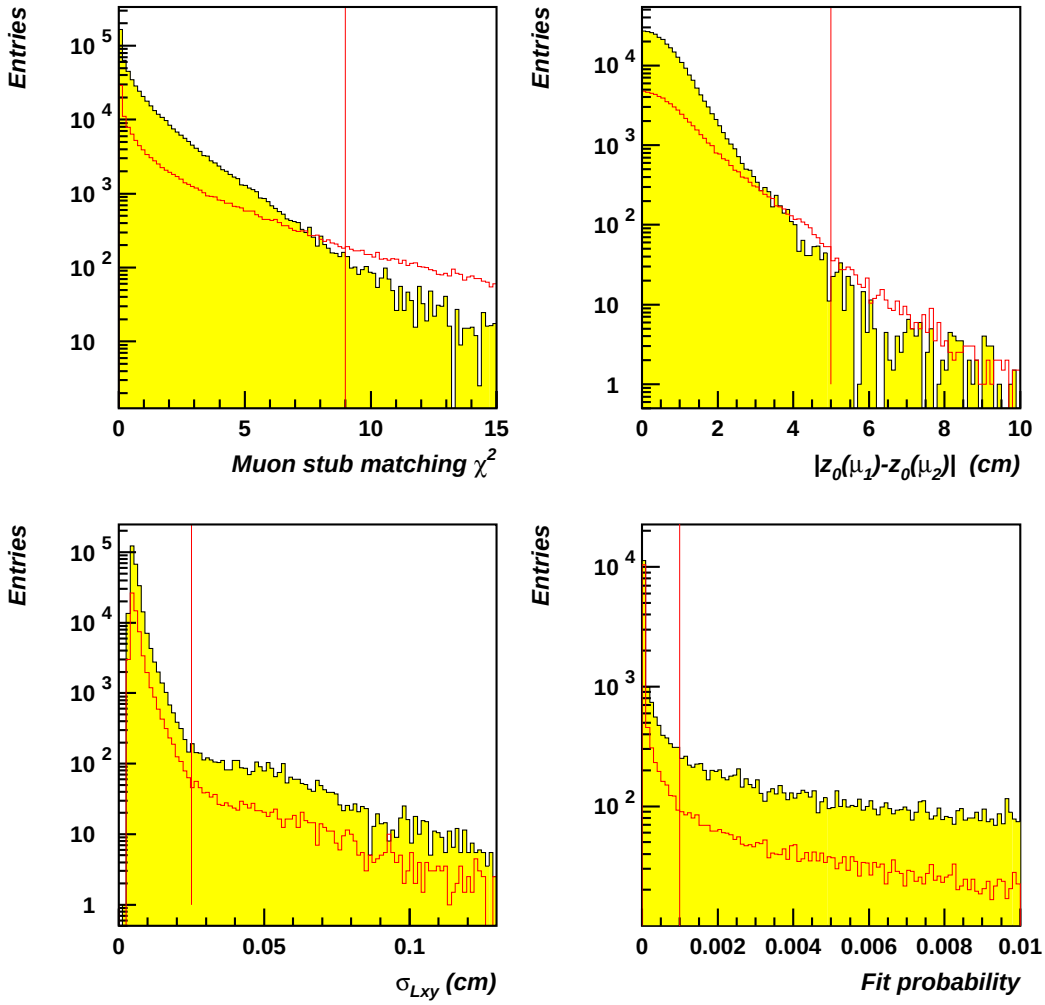

Figure 5.5: Sideband-subtracted distributions (yellow) with the sideband distributions superimposed for some of the quantities that are cut on (cuts denoted by the vertical line) where basic SVXII cuts are already applied

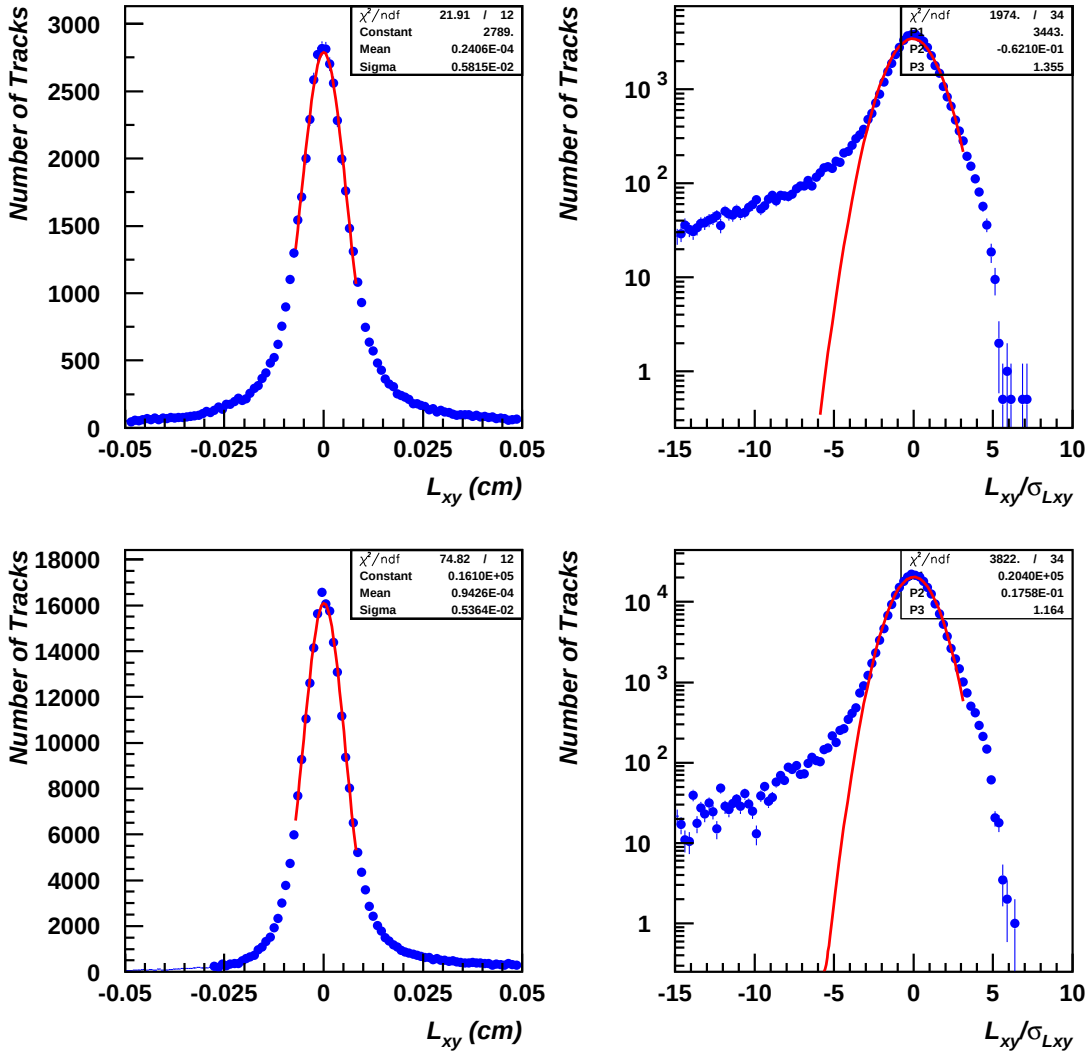

Figure 5.6: Sideband (top) and signal (bottom) L_{xy} and $L_{xy}/\sigma_{L_{xy}}$ distributions for CMU-CMU events with ≥ 3 r-ϕ silicon hits fitted with single Gaussians

	Slope	Acceptance	χ^2/ndf
$\Delta\phi$	-0.000439 $\pm$ 0.000037	0.6781 $\pm$ 0.0037	173/87
$p_{\rm T}(\rm J/\psi)$	0.004309 $\pm$ 0.000405	0.6868 $\pm$ 0.0036	291/94
$\eta_{\rm J/\psi}$	0.001662 $\pm$ 0.002390	0.6713 $\pm$ 0.0009	276/98

Table 5.1: Results of fits to the SVXII acceptance relative to the COT for tracks with ≥ 3 r-ϕ silicon hits as a function of $\Delta\phi$, $p_{\rm T}(\rm J/\psi)$ and $\eta_{\rm J/\psi}$

the initial SVXII acceptance relative to the COT for tracks with at least 3 r-ϕ silicon hits. The acceptance is measured as a function of $\Delta\phi$, $p_{\rm T}(\rm J/\psi)$ and $\eta_{\rm J/\psi}$, which is approximately the average pseudorapidity of the two muon tracks.

$$\text{Acceptance} = \frac{\text{No. of J/}\psi\text{'s with} \geq 3\ r\text{-}\phi\ \text{silicon hits on both tracks}}{\text{Total no. of quality CMU-CMU J/}\psi\text{'s}}$$

The numerator contains quality cuts Sets 1, 2 & 3, while the denominator contains only Set 1. Table 5.1 lists the slopes and errors for the linear fits to the acceptance plots that are presented in Figure 5.7. Here the $\Delta\phi$ acceptance distribution is fitted only for $\Delta\phi > 12^\circ$ as there is evidence of some non-linear behaviour at small angles. This region of $\Delta\phi$ will be treated in more detail in Section 5.3.

Since the slopes and the errors are very small, the uncertainty in the slopes can be used in conjunction with the absolute values of the acceptance to evaluate the resultant systematic error in the B-fraction measurement. The acceptance should remain flat as further silicon quality cuts are applied. If the acceptance does not depend strongly on $\Delta\phi$, $p_{\rm T}(\rm J/\psi)$ and $\eta_{\rm J/\psi}$, it is easier for the B-fraction result to be combined with the J/ψ inclusive cross-section to get the B $\rightarrow$ J/ψ X cross-section.

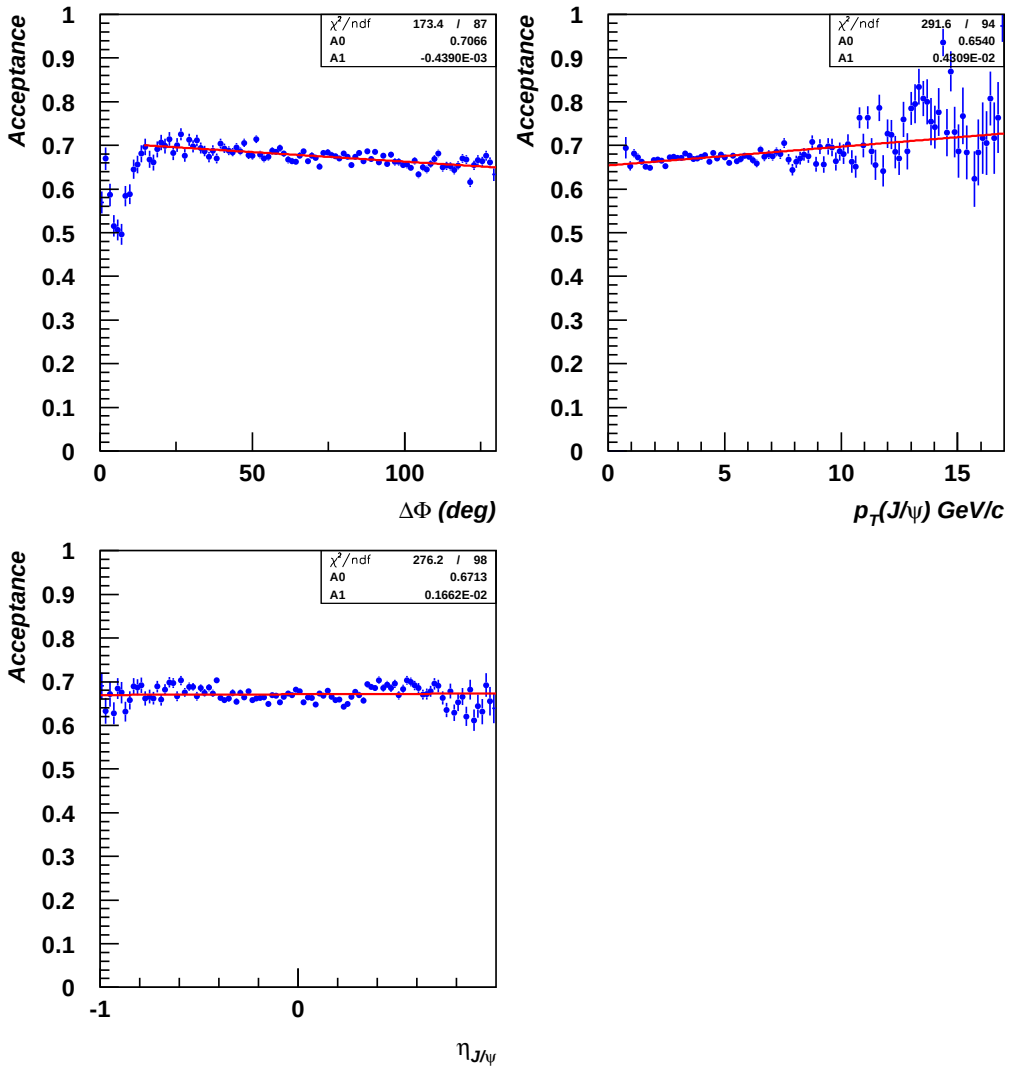

Figure 5.7: SVXII J/ψ acceptance relative to the COT for tracks with ≥ 3 r-ϕ silicon hits as a function of $\Delta\phi$, $p_{\mathrm{T}}(\mathrm{J}/\psi)$ and $\eta_{\mathrm{J}/\psi}$ (146805-152625)

5.5 SVXII Track Quality Optimisation Cuts

This section discusses the motivation for each of the SVXII track quality cuts and present results that show the benefits of applying them to the J/ψ sample in runs 138425-152625.

5.5.1 SVXII Layers 0 & 1

It is essential to have good coverage in the innermost layers of SVXII. Figure 5.8 shows how the resolution and tails of the sideband-subtracted impact parameter distributions for the high p_{T} muon of the J/ψ are affected when the track is missing hits in the inner layers. The distributions are normalised and a cut of $L_{xy} < 150$ μm was applied to favour more prompt J/ψ's, allowing the effect on the tails to be seen more clearly. The distributions for the low p_{T} muon are shown in Figure 5.9 and the results are summarised in Table 5.2.

For events passing the basic SVXII cuts (Set 2) in which the tracks are missing a hit in Layer 0, the impact parameter resolution for the high p_{T} muons is 54.3 μm. The resolution improves by 20% when a Layer 0 hit is

Hit Requirements	High p_{T} muon d_0 resolution (μm)	Low p_{T} muon d_0 resolution (μm)
no Layer 0	54.3	59.5
no Layer 1	49.5	51.5
Layer 0	43.3	46.9
Layer 1	44.0	47.7
Layer 0 + Layer 1	43.1	46.8

Table 5.2: d_0 resolutions for the high and low p_{T} muons from events passing the basic SVXII cuts with various hit requirements placed on the inner layers

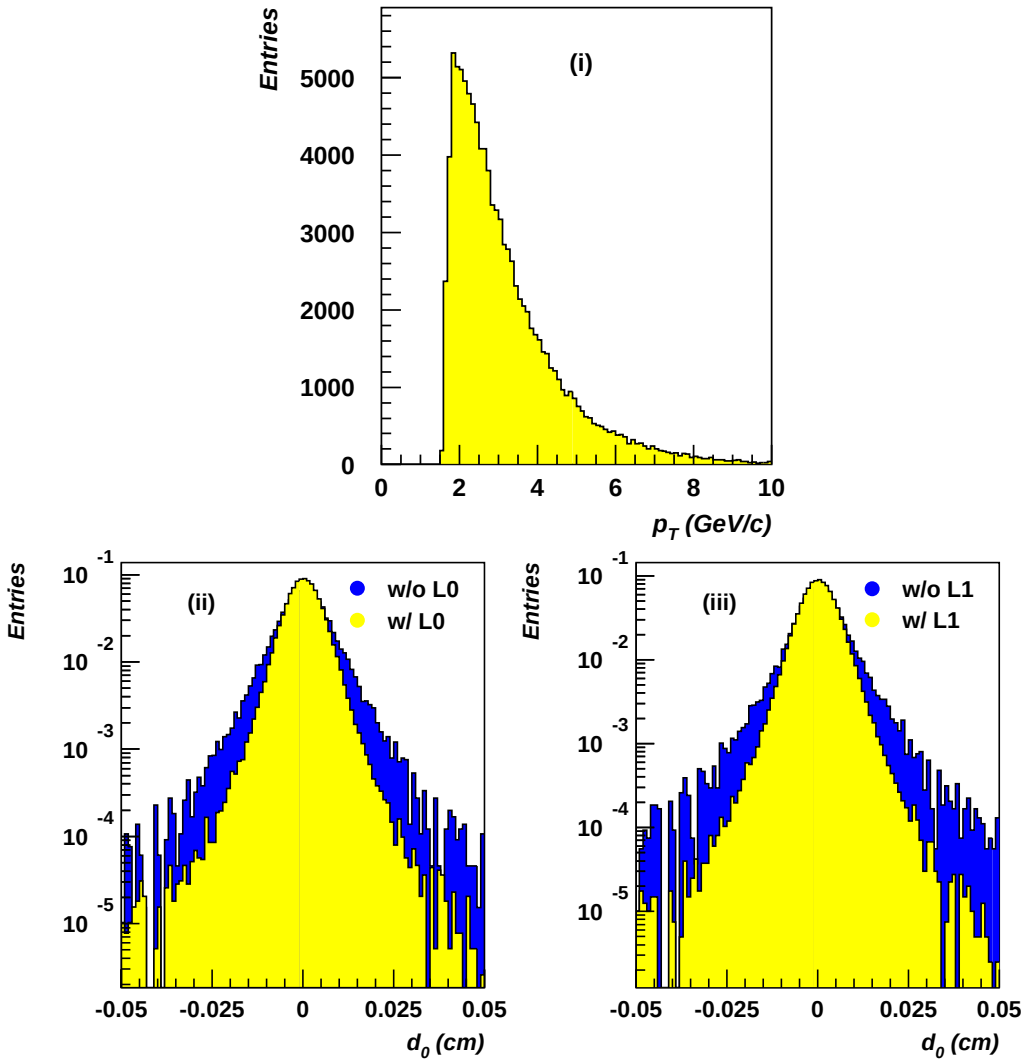

Figure 5.8: Normalised sideband-subtracted impact parameter distributions for the *high* pT muon: (i) pT distribution of the muons, (ii) d_0 distributions for events with an without a Layer 0 hit, (iii) d_0 distributions for events with an without a Layer 1 hit

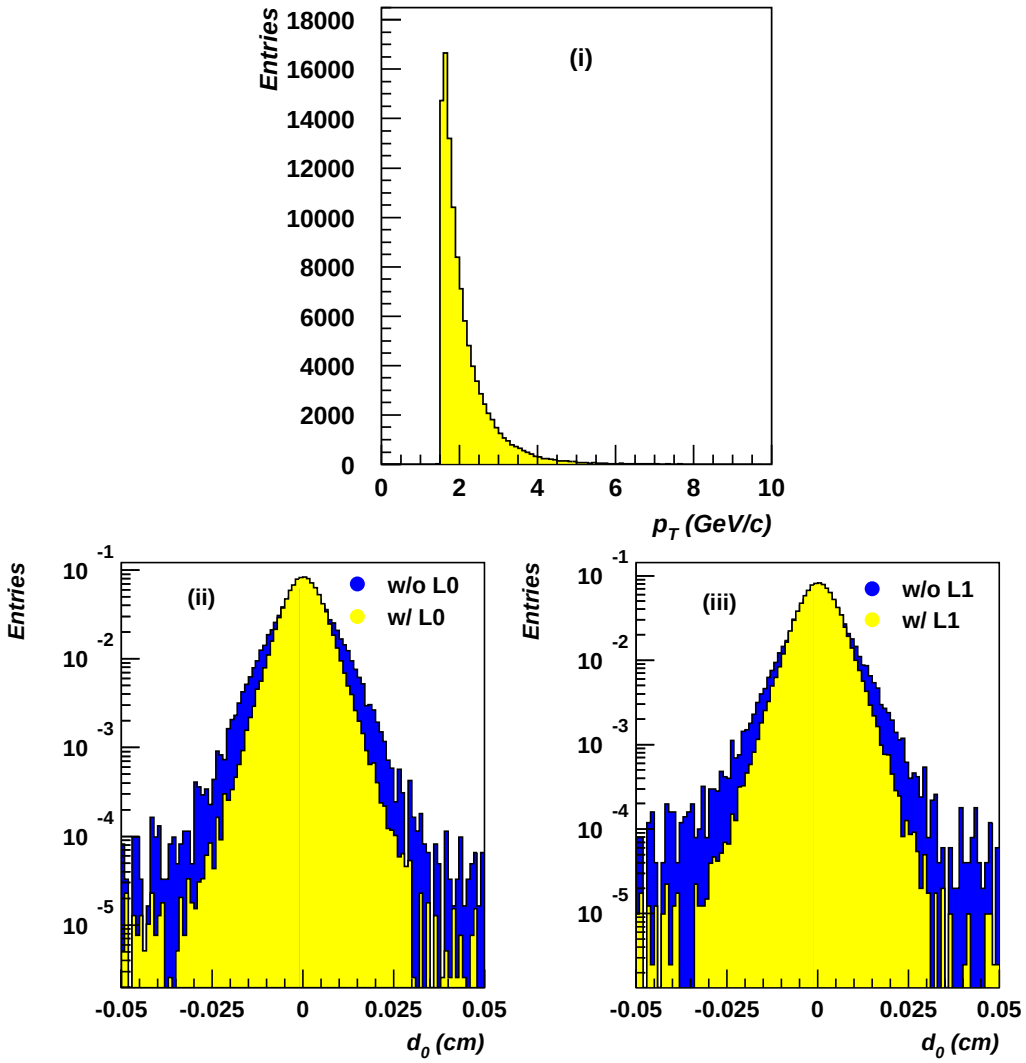

Figure 5.9: Normalised sideband-subtracted impact parameter distributions for the *low* pT muon: (i) pT distribution of the muons, (ii) d_0 distributions for events with an without a Layer 0 hit, (iii) d_0 distributions for events with an without a Layer 1 hit

required, but requiring a hit in Layer 1 at the same time results in no further significant improvement. The resolution in events without hits in Layer 1 is about 5 μm better than in events where the missing hit is in Layer 0, so it is not as important to have a hit in Layer 1 as it is to have a hit in Layer 0. Requiring a Layer 1 hit improves the resolution by 11% when compared with events where the Layer 1 hit is missing.

The corresponding percentage improvements in resolution for the low p_{T} muons in events with and without Layer 0 and Layer 1 hits are 21% and 7% respectively. Since it does not offer as big an improvement in resolution and it is not located at as small a radius as Layer 0, hits are only required in Layer 1 when that ladder is integrated. So, for example, quality tracks with hits in Layers 0, 2, 3 and 4 in wedges where Layer 1 is turned off are not rejected.

The impact parameter resolution for the low p_{T} muon as a function of $p_{\mathrm{T}}(\mu)$ is presented in Figure 5.10. It shows the variation in resolution for tracks with and without a hit in SVXII Layer 0. When Layer 0 hits are required, the dependence $p_{\mathrm{T}}(\mu)$ is not as strong. Therefore, in addition to improving the position resolution, requiring a hit on the inner layer of SVXII also reduces the effect of multiple scattering on the resolution, which can be an important effect at low p_{T}.

5.5.2 $n-1$ hits

There are many ladders throughout the SVXII detector that are not integrated, so placing a fixed cut requiring at least three or four hits in SVXII does not make optimal use of SVXII hit information. Instead the requirement

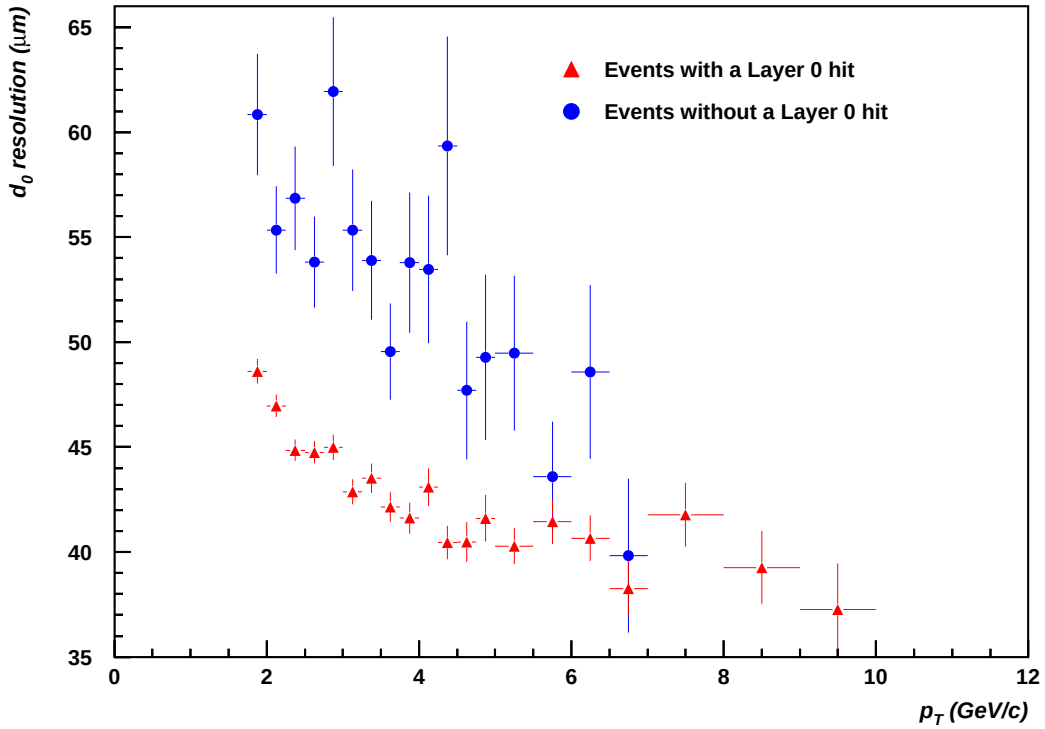

Figure 5.10: Impact parameter resolution of the low p_{T} muon as a function of $p_{\mathrm{T}}(\mu)$ for tracks with and without a Layer 0 hit

is that if the original COT track projection intersects at least n integrated SVXII ladders then there must be at least $n-1$ SVXII hits (r-ϕ, r-z or both). This choice was validated in a study carried out by the CDF Tracking Group [54] which concluded that "the number of missed hits may be a better indicator of track quality than the number of hits, since some ladders are not integrated and readout errors are common." As discussed in Chapter 4, readout errors are not considered in the estimation of the number of expected hits per track, i.e. 'at least n integrated ladders' are required rather than 'at least n integrated ladders with no readout errors'.

5.5.3 Barrel-crossing cut

SVXII must be able to determine with high resolution the position of tracks as close to the interaction point as possible. Therefore, it is important that the amount of material in the detector does not degrade the track quality due to excessive multiple scattering.

The final silicon cut is used to help reduce the effect of SVXII material on resolutions and mismeasurements. This is demonstrated in Figure 5.11 where, after basic SVXII cuts, the z vertex distributions indicate that many J/ψ's in the negative tails of the $L_{xy}/\sigma_{L_{xy}}$ distribution come from regions between the barrels. These events are excluded by rejecting tracks which cross barrels. Most of these events are already excluded by the previously discussed SVXII track quality cuts, so this cut usually rejects less then 1% of the surviving events. However, when applied on its own without any other

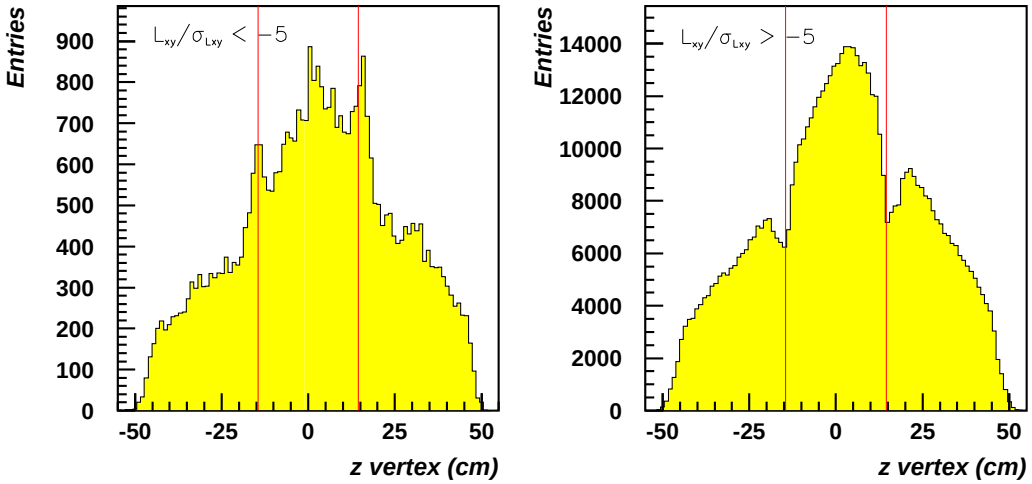

Figure 5.11: There is an excess of events with $L_{xy}/\sigma_{L_{xy}} < -5$ in the two regions where barrels meet as indicated by the red lines

SVXII track quality cuts, the barrel-crossing cut was found to reject up to 70% of events normally excluded by the Layer 0 & 1 requirements. There is a similar effect due to the hybrids but they cover too large a region to exclude.

5.6 Optimisation Results

This section describes the effect of the selection cuts on the impact parameter resolution, L_{xy} resolution and the size of the tails in the $L_{xy}/\sigma_{L_{xy}}$ distributions.

5.6.1 Impact Parameter Resolution

Table 5.3 shows the improvement in impact parameter resolution for high and low p_{T} CMU-CMU muons with $L_{xy} < 150$ μm and at least 3 r-ϕ silicon hits after each successive set of quality cuts is applied. The results for the case where the barrel-crossing cut is the only SVXII track quality cut to be applied are included to illustrate the power of this cut in the absence of the

Hit Requirements	High p_{T} muon d_0 resolution (μm)	Low p_{T} muon d_0 resolution (μm)
Set 2	44.52	48.08
+ Sets 1 & 3	44.46	47.99
+ $\geq n-1$ SVXII hits	43.40	46.91
+ Layer 0	42.64	46.10
+ Layer 1 (int)	42.46	46.13
+ no BCs	42.43	46.04
Sets 1, 2 & 3 + no BCs	43.01	46.44

Table 5.3: d_0 resolutions for both the high and low p_{T} muons of the J/ψ after each set of quality cuts is applied consecutively

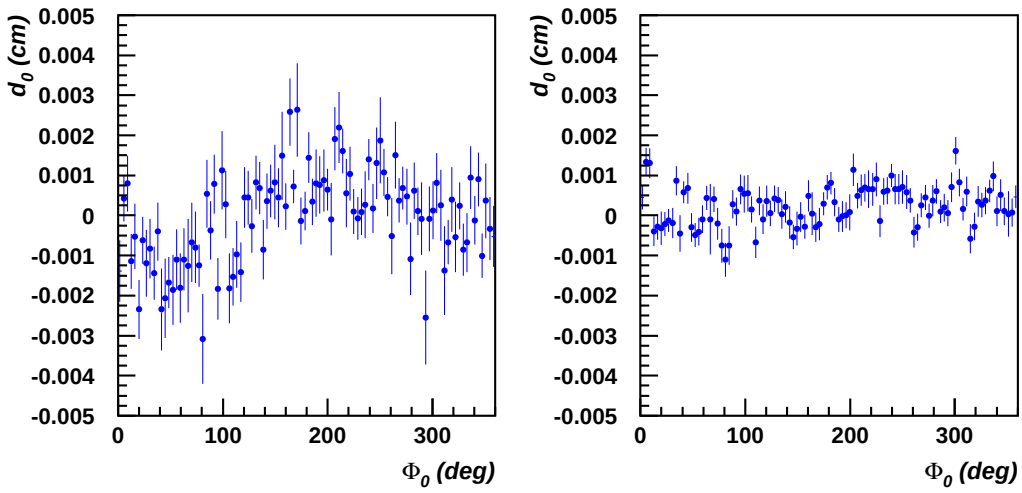

Figure 5.12: d_0 vs ϕ_0 for CMU-CMU events with ≥ 3 $r-\phi$ silicon hits (left) and after all silicon cuts are applied (right). The marked points are the mean values of the d_0 distribution in each bin and the error bars represent the standard deviation.

other three. Figure 5.12 shows how the complete set of cuts described above also helps to remove a small variation in d_0 vs ϕ_0 that is present when only Set 1 of the cuts is applied.

5.6.2 L_{xy} Resolution and Tails

The full set of cuts can also be applied to the $L_{xy}/\sigma_{L_{xy}}$ distributions to measure their effect on the negative tails, which are defined to be events with $L_{xy}/\sigma_{L_{xy}} < -5$. The J/$\psi$ mass distributions after basic cuts, which are presented in Figure 5.13, demonstrate that events in the negative tails are dominated by background. Figure 5.14 shows the sideband subtracted L_{xy} and $L_{xy}/\sigma_{L_{xy}}$ distributions after all SVXII track quality cuts are applied. Comparing these distributions to the ones in Figure 5.6, where only basic cuts were required, a significant reduction in the size of the background-

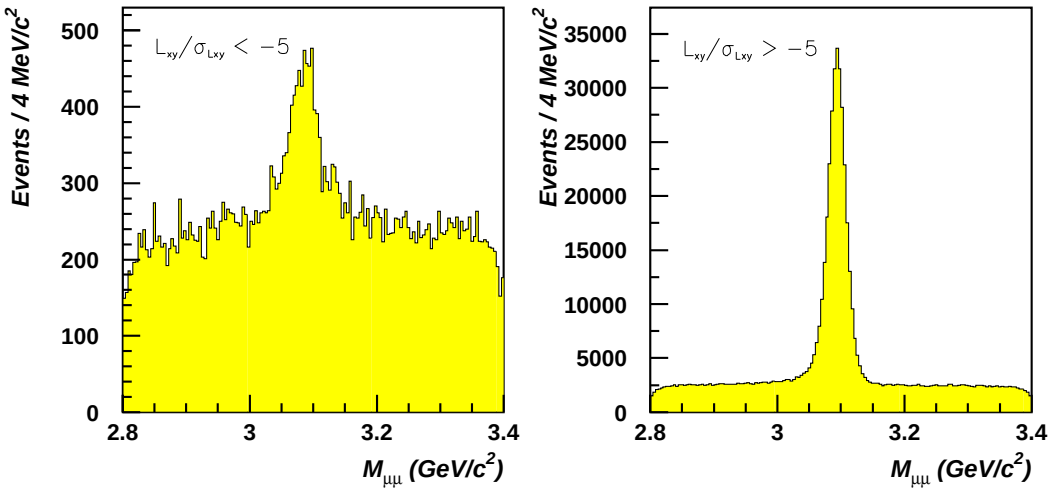

Figure 5.13: The dimuon invariant mass distributions for events with (i) $L_{xy}/\sigma_{L_{xy}} < -5$ and (ii) $L_{xy}/\sigma_{L_{xy}} > -5$, demonstrating that the events in the negative tails of $L_{xy}/\sigma_{L_{xy}}$ are mostly background

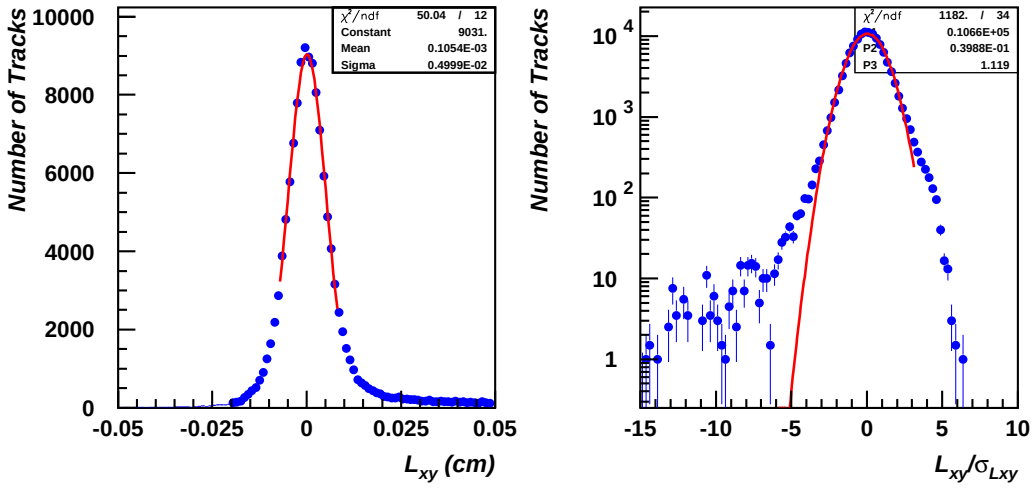

Figure 5.14: L_{xy} and $L_{xy}/\sigma_{L_{xy}}$ after all silicon cuts are applied

Hit Requirements	% events	% −ve tails	L_{xy} res (μm)
Set 2	-	1.242	53.64
+ Sets 1 & 3	92.6	0.879	53.41
+ $\geq n-1$ SVXII	71.7	0.359	51.55
+ Layer 0	57.1	0.316	50.06
+ Layer 1 (int)	50.1	0.262	50.11
+ no BCs	49.6	0.254	49.98
+ ≥ 4 SVXII	57.4	0.250	50.75
+ Layer 0	49.0	0.252	49.58
+ Layer 1 (int)	43.8	0.224	49.66
+ no BCs	43.5	0.214	49.53

Table 5.4: Percentage of ≥ 3 r-ϕ CMU-CMU J/ψ events retained after each set of cuts is applied, the fraction of events in the *negative* $L_{xy}/\sigma_{L_{xy}}$ tails and the L_{xy} resolution

dominated negative tails is observed

Table 5.4 shows the percentage of CMU-CMU events with at least 3 r-ϕ hits that are retained after each successive cut is applied as well as the fraction of events with $L_{xy}/\sigma_{L_{xy}} < -5$. The full set of cuts helps reduce the size of the negative tails by 80%. The table also gives figures to allow for comparison with the case where the standard $n-1$ cut is replaced by a requirement of ≥ 4 SVXII hits.

The L_{xy} resolution as a function of $p_{\mathrm{T}}(\mathrm{J}/\psi)$ for the best SVXII track selection obtained from a single Gaussian fit to the core of the distributions is shown in Figure 5.15. Unlike the impact parameter resolution, which improves with p_{T}, the L_{xy} resolution increases from 47 to 100 μm between 1.75 and 17 GeV/c.

Figure 5.16 shows that the width of the L_{xy} core with all SVXII cuts applied improves as the opening angle between the two muons increases.

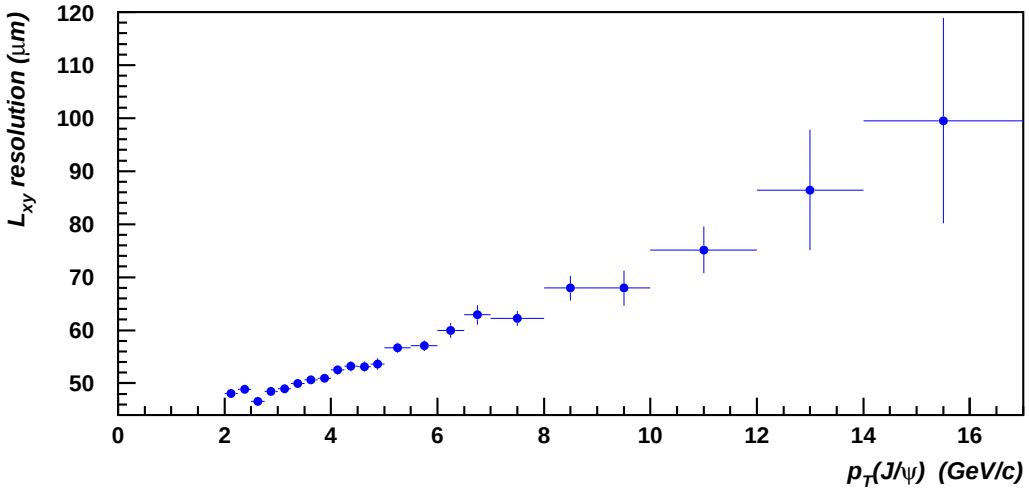

Figure 5.15: L_{xy} resolution as a function of $p_{\mathrm{T}}(\mathrm{J}/\psi)$

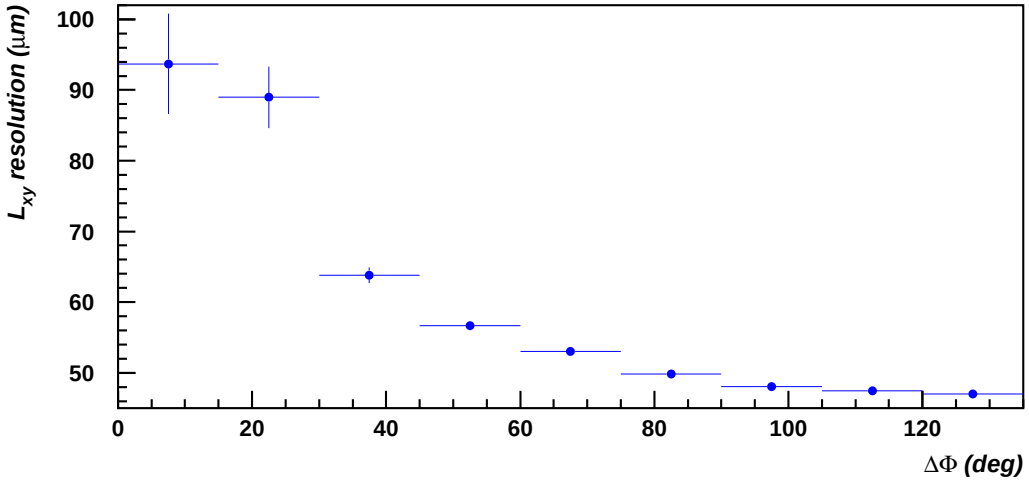

Figure 5.16: L_{xy} resolution as a function of opening angle

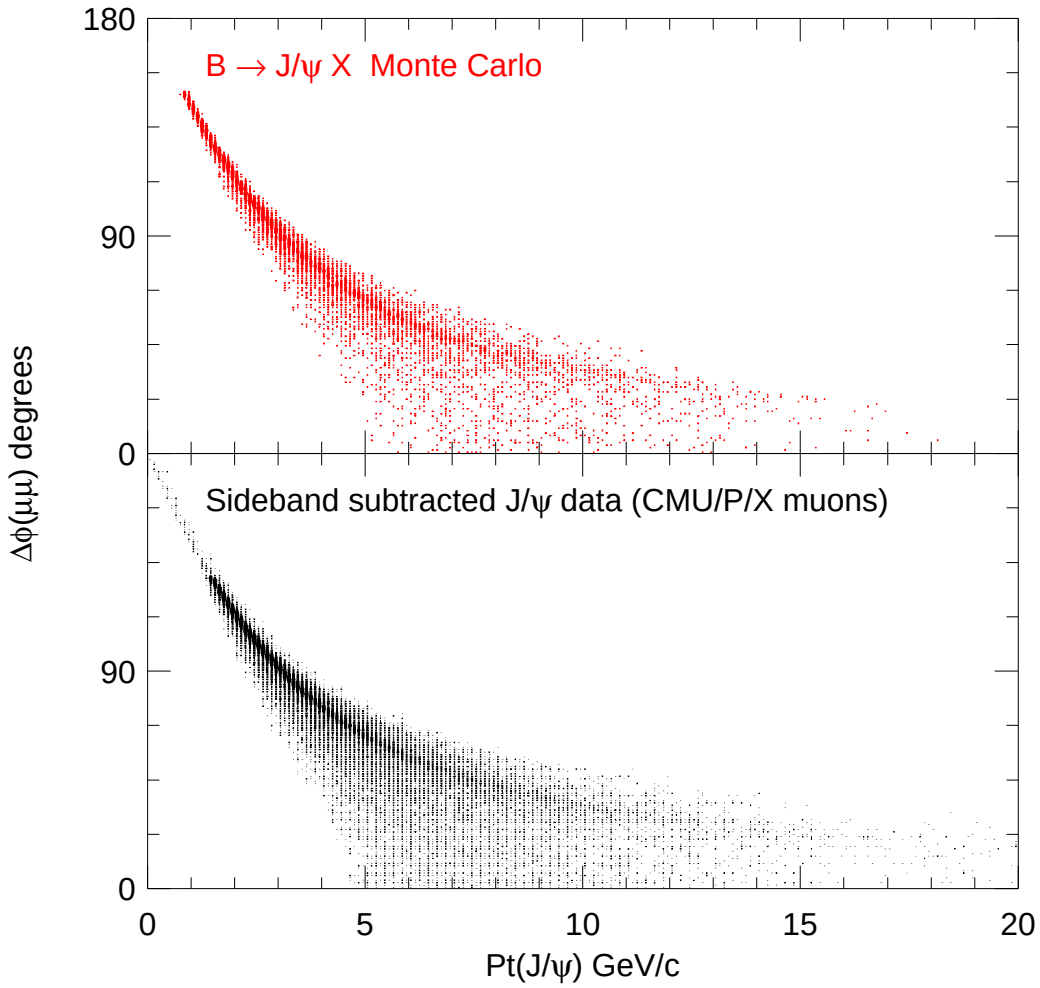

Figure 5.17: $\Delta\phi$ vs $p_{\mathrm{T}}(\mathrm{J}/\psi)$ from Monte Carlo and data

The opening angle in r-ϕ between the muons of the J/ψ candidates is related to the transverse momentum of the J/ψ. This correlation is illustrated in Figure 5.17 which shows $\Delta\phi$ vs p_{T} in both Monte Carlo and data.

At large opening angles there are more low p_{T} muons and at low p_{T} there is more multiple scattering. However, it was previously demonstrated in Figure 5.10 that requiring a hit in Layer 0 of SVXII reduces the effect of

multiple scattering and so the impact parameter resolution no longer depends so strongly on p_{T}. Therefore, the behaviour of the L_{xy} resolution as a function of transverse momentum is mainly because of the the opening angle.

5.6.3 L_{xy} Resolution Function Shape

Fits to the $L_{xy}/\sigma_{L_{xy}}$ distribution for J/ψ events with $L_{xy} < 200$ μm for all p_{T} are shown in Figure 5.18. The distribution is fitted separately with a single Gaussian, a double Gaussian, and a double Gaussian with an exponential tail. The double Gaussian does not fully describe the non-Gaussian component in the tail of the distribution. The amount of non-Gaussian tails is at the sub-percent level and varies with the momenta of muon tracks.

The $L_{xy}/\sigma_{L_{xy}}$ distributions are then fitted in each of the J/ψ transverse momentum bins where a measurement of the B-fraction is to be made. The distributions are fitted with single and double Gaussians in the range $-4 < L_{xy}/\sigma_{L_{xy}} < 2.5$. Table 5.5 contains a summary of the widths and χ^2/ndf in each J/ψ transverse momentum bin. The widths of the double Gaussian fits are the weighted averages of the widths of the individual Gaussians. A double Gaussian is found to be a better fit in most cases, except for very high p_{T} where the single Gaussian fit results are equally good.

5.6.4 Υ(1S) Studies

The J/ψ study is repeated using the sample of prompt decays of Υ(1S) into two muons in order to study the effect of mismeasurement on the positive L_{xy} tail. Any non-Gaussian component not taken into account in the fit to the J/ψ resolution function could bias the lifetime measurement. The

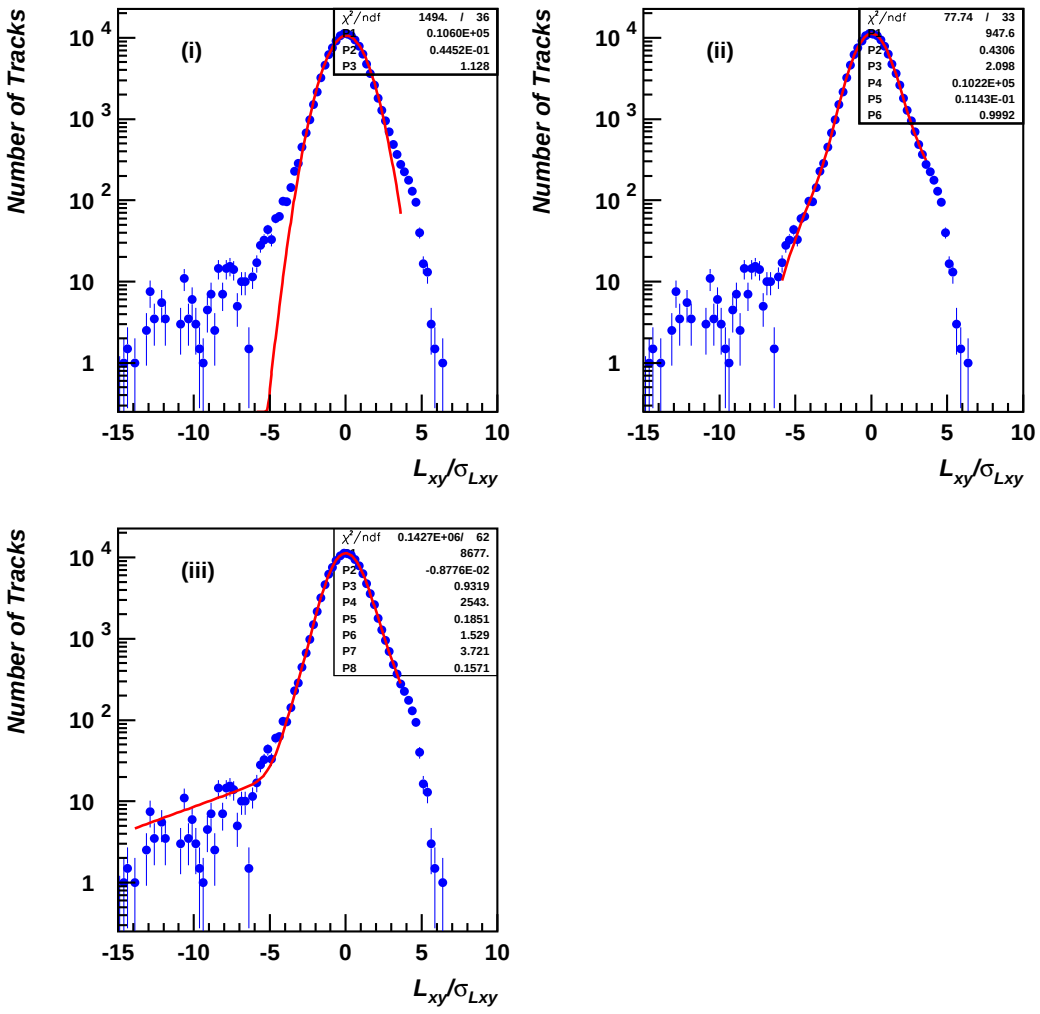

Figure 5.18: Fits to $L_{xy}/\sigma_{L_{xy}}$ with $L_{xy} < 200$ μm using (i) single Gaussian, (ii) double Gaussian, (iii) double Gaussian plus exponential tail with all silicon cuts applied

$p_{\mathrm{T}}(\mathrm{J}/\psi)$ (GeV/c)	Single σ	Single χ^2/ndf	Double σ	Double χ^2/ndf
$2.0-2.25$	1.091	51/24	1.109	35/21
$2.25-2.5$	1.085	59/24	1.095	47/21
$2.5-2.75$	1.044	84/24	1.009	46/21
$2.75-3.0$	1.076	56/24	1.043	34/21
$3.0-3.25$	1.078	64/24	1.046	29/21
$3.25-3.5$	1.091	70/24	1.022	42/21
$3.5-3.75$	1.084	50/24	1.100	37/21
$3.75-4.0$	1.079	66/24	1.052	40/21
$4.0-4.25$	1.117	49/24	1.080	35/21
$4.25-4.5$	1.106	48/24	1.068	21/21
$4.5-4.75$	1.119	44/24	1.052	26/21
$4.75-5.0$	1.097	55/24	1.053	44/21
$5.0-5.5$	1.128	79/24	1.091	47/21
$5.5-6.0$	1.129	34/24	1.087	20/21
$6.0-6.5$	1.121	34/24	1.075	23/21
$6.5-7.0$	1.163	44/24	1.102	29/21
$7.0-8.0$	1.121	62/24	1.104	47/21
$8.0-9.0$	1.150	21/24	1.130	16/21
$9.0-10.0$	1.074	51/24	1.062	48/21
$10.0-12.0$	1.119	20/24	1.122	19/21
$12.0-14.0$	1.120	44/23	1.120	41/20
$14.0-17.0$	1.155	256/22	1.076	230/19

Table 5.5: The widths and χ^2/ndf of single and double Gaussian fits ($-4 < L_{xy}/\sigma_{L_{xy}} < 2.5$) to the $L_{xy}/\sigma_{L_{xy}}$ distributions in each p_{T} bin

mass distribution for the Υ(1S) resonance after the full set of silicon track quality cuts are applied is shown in Figure 5.19 for runs 138425-152625. The statistics are small compared with the J/ψ sample. There are only 1433 events in the $\pm 3\sigma$ region of the mass distribution and this number falls to 678 after all remaining cuts are applied. The statistics are too low to be used in a quantitative systematic error estimate for the J/ψ tails.

This zero-lifetime sample consists only of prompt decays of Υ(1S) into two muons. Therefore it can be used to make an independent measurement

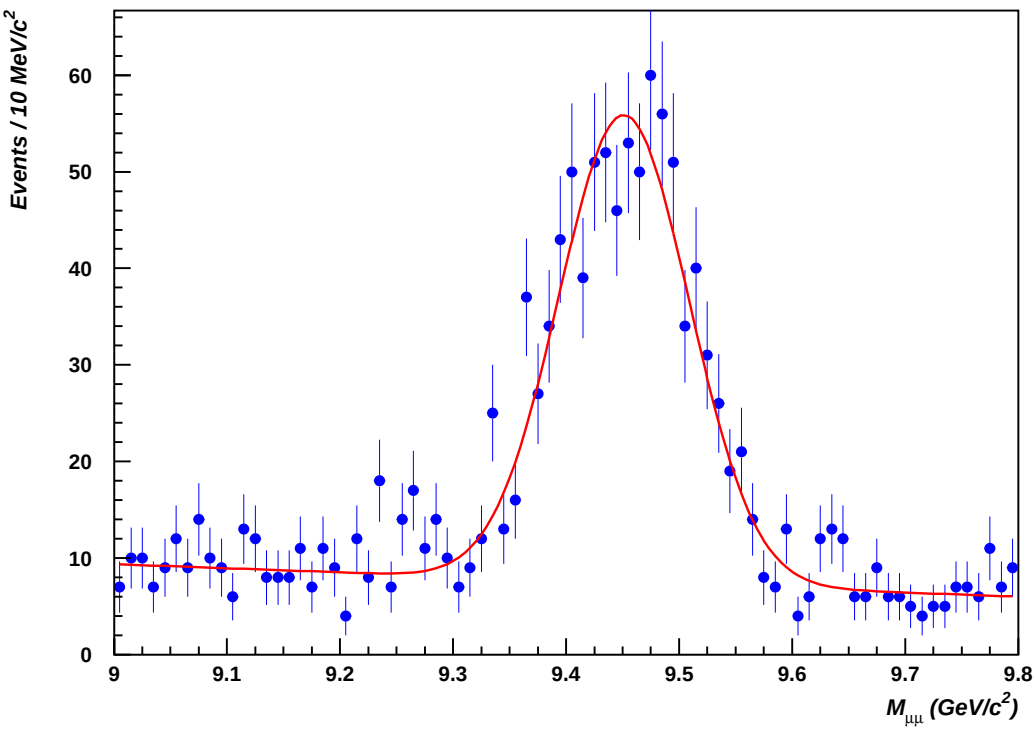

Figure 5.19: The dimuon invariant mass distribution in the $\Upsilon(1S)$ range fitted to a single Gaussian plus flat background after the full set of silicon track quality cuts are applied

of the shape of the L_{xy} resolution function. The proper decay length distribution of a zero lifetime sample should be a Gaussian peaked at $L_{xy} = 0$ and when the distribution is normalised by its error, $\sigma_{L_{xy}}$, the resultant Gaussian distribution is expected to have a sigma of 1. The sideband-subtracted L_{xy} and $L_{xy}/\sigma_{L_{xy}}$ distributions for events passing all silicon track quality cuts are shown in Figure 5.20, which also contains the $L_{xy}/\sigma_{L_{xy}}$ distribution for events passing only the basic SVXII cuts (Set 2). Due to the close proximity of the $\Upsilon(1S)$ and $\Upsilon(2S)$ resonances, the sideband regions are forced to be next to the signal region at $\pm 3\sigma \rightarrow \pm 6\sigma$. The $L_{xy}/\sigma_{L_{xy}}$ distribution after all

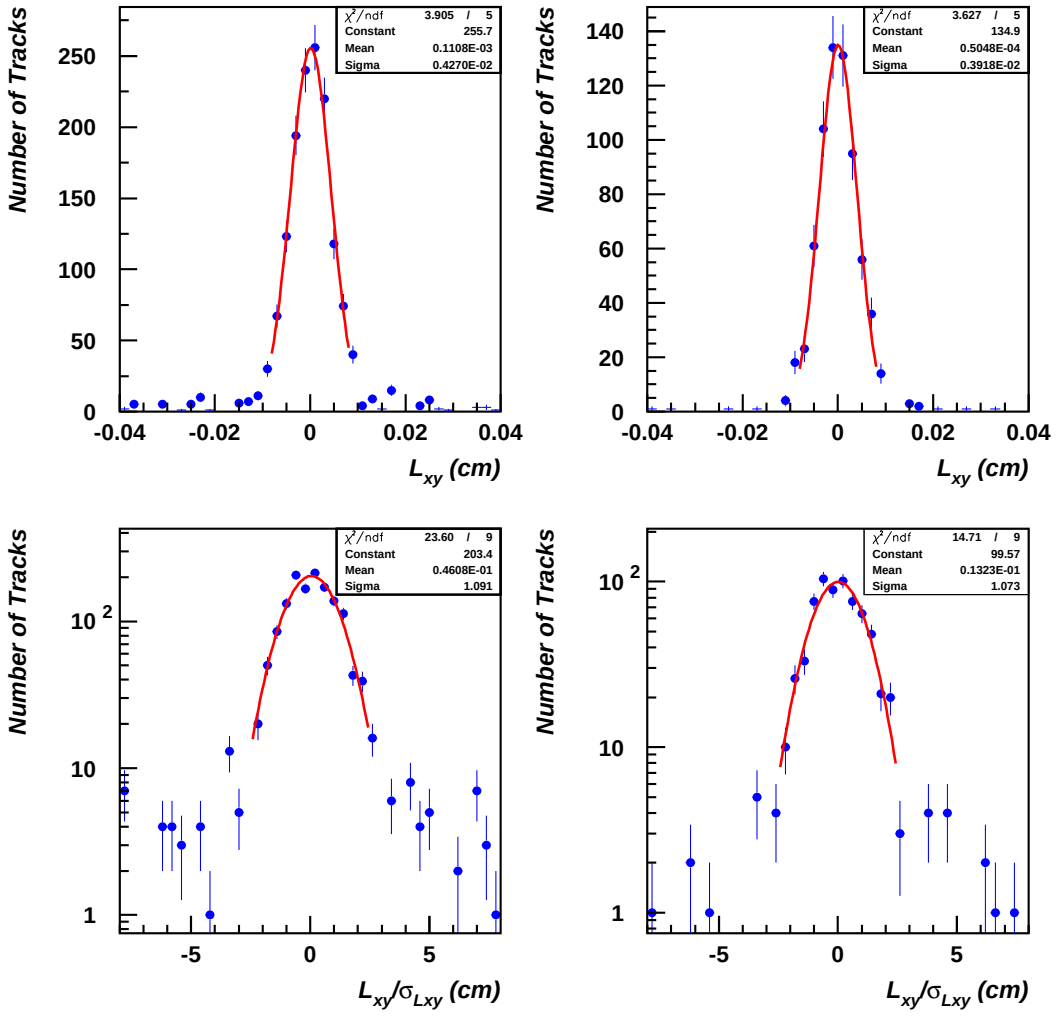

Figure 5.20: $\Upsilon(1S) \rightarrow \mu^+\mu^-$: Single Gaussian fits to the L_{xy} distribution (top) and the $L_{xy}/\sigma_{L_{xy}}$ distribution (bottom) after basic SVXII cuts (left) and after all silicon cuts are applied (right)

cuts fits well to a single Gaussian with a sigma of 1.073.

5.7 SVXII J/ψ Acceptance

Figure 4.1 illustrated the variation in silicon coverage versus run number. To investigate the effect that the changing silicon coverage has on the kinematic acceptance of the J/ψ, the data is divided into five separate run ranges according to where the silicon coverage changed. Table 5.6 lists each run range and the corresponding integrated luminosity.

The study of the SVXII acceptance relative to the COT in Section 5.1.3 is repeated with all silicon quality cuts applied. The numerator now contains all four sets of cuts, while the denominator contains only Set 1. Figure 5.21 presents the final SVXII J/ψ acceptance as a function of $\Delta\phi$, p_{T}(J/ψ) and $\eta_{\mathrm{J}/\psi}$ after all silicon cuts were applied for the run range containing the best silicon coverage: 146805-152625. The acceptance remains flat after the complete set of cuts are applied. The spread of values at small $\Delta\phi$ is less than in Figure 5.7. Tables 5.7-5.9 list the slopes and errors for the fits to the acceptance plots. The slopes and errors remain small after all silicon quality cuts are applied.

Run Range	$\mathcal{L}$ (pb^{-1})
138425-139383	0.684
139774-140315	0.638
140721-142227	3.708
144013-145669	4.287
146805-152625	26.509

Table 5.6: Five run ranges and the integrated luminosities of all good runs

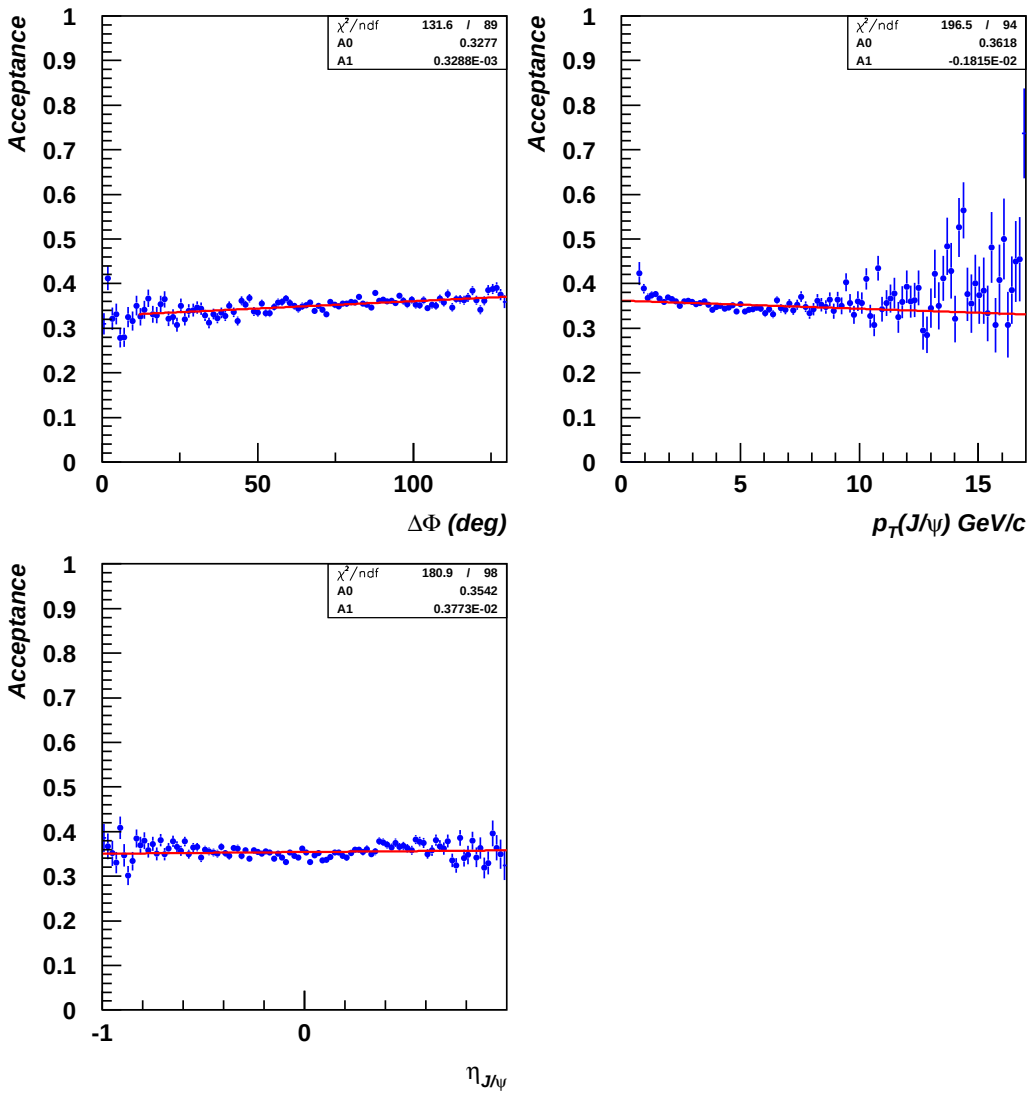

Figure 5.21: CMU-CMU SVXII J/ψ acceptance for all silicon cuts as a function of $\Delta\phi$, $p_{\rm T}$(J/ψ) and $\eta_{\rm J/\psi}$(146805-152625)

Run Range	Slope (deg^{-1})	Acceptance	χ^2/ndf
138425-139383	0.000115 ± 0.000125	0.3251 ± 0.0131	206/98
139774-140315	0.000201 ± 0.000142	0.3329 ± 0.0148	127/98
140721-142227	0.000264 ± 0.000091	0.3883 ± 0.0095	155/98
144013-145669	0.000132 ± 0.000068	0.2412 ± 0.0071	125/98
146805-152625	0.000340 ± 0.000034	0.3488 ± 0.0035	154/98

Table 5.7: Slopes and errors for fits to J/ψ silicon acceptance versus $\Delta\phi$

Run Range	Slope ($\mathrm{GeV}^{-1}c$)	Acceptance	χ^2/ndf
138425-139383	-0.000272 ± 0.001605	0.3272 ± 0.0144	179/86
139774-140315	-0.000473 ± 0.001801	0.3341 ± 0.0162	159/64
140721-142227	-0.001229 ± 0.001154	0.3870 ± 0.0104	168/92
144013-145669	-0.000023 ± 0.000872	0.2429 ± 0.0078	113/88
146805-152625	-0.001815 ± 0.000427	0.3480 ± 0.0038	196/94

Table 5.8: Slopes and errors for fits to J/ψ silicon acceptance versus p_{T}(J/ψ)

Run Range	Slope	Acceptance	χ^2/ndf
138425-139383	0.005703 ± 0.009443	0.3273 ± 0.0036	215/98
139774-140315	0.003540 ± 0.010430	0.3360 ± 0.0040	122/98
140721-142227	-0.010716 ± 0.006808	0.3913 ± 0.0026	170/98
144013-145669	0.018997 ± 0.004992	0.2430 ± 0.0019	121/98
146805-152625	0.003773 ± 0.002451	0.3542 ± 0.0009	181/98

Table 5.9: Slopes and errors for fits to J/ψ silicon acceptance versus $\eta_{\mathrm{J}/\psi}$

The acceptance study for $\Delta\phi$ was repeated, focusing on events with $\Delta\phi < 12^\circ$ where there remains some evidence of the structure discussed in Section 5.1.3. Figure 5.22 shows that the straight line is a reasonable fit to the data and so the effect at low $\Delta\phi$ is not considered to be inconsistent with a flat acceptance.

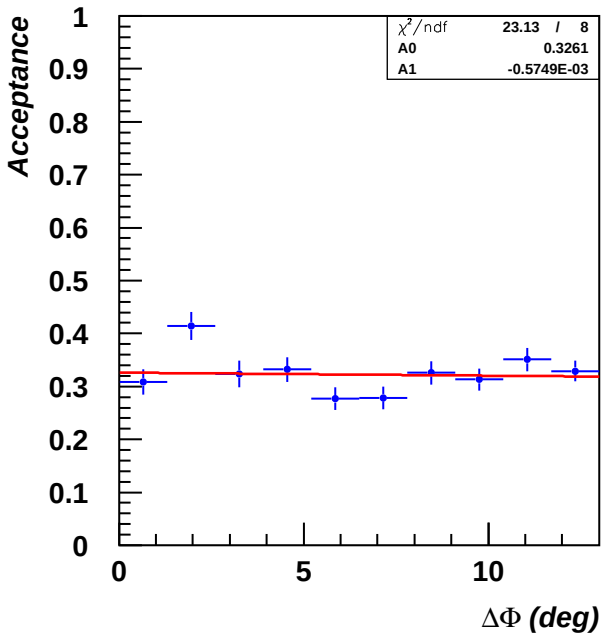

Figure 5.22: CMU-CMU SVXII J/ψ acceptance for $\Delta\phi < 12°$

To calculate the overall acceptances, the results from the five run ranges are combined for each of the three distributions. The overall acceptances for runs 138425-152625 are the luminosity weighed average acceptances from each of the run ranges, i.e.

$$\mathcal{A} = \frac{\sum \mathcal{L}_i \mathcal{A}_i}{\sum \mathcal{A}_i}$$

with the statistical errors also appropriately weighed.

$$\mathcal{A}_{\Delta\phi} = 0.3393 \pm 0.0049$$

$$\mathcal{A}_{p_{\mathrm{T}}} = 0.3388 \pm 0.0054$$

$$\mathcal{A}_{\eta} = 0.3438 \pm 0.0013$$

Since the B-fraction is measured in bins of p_{T}, $\mathcal{A}_{p_{\mathrm{T}}}$ is the most important of these three results.

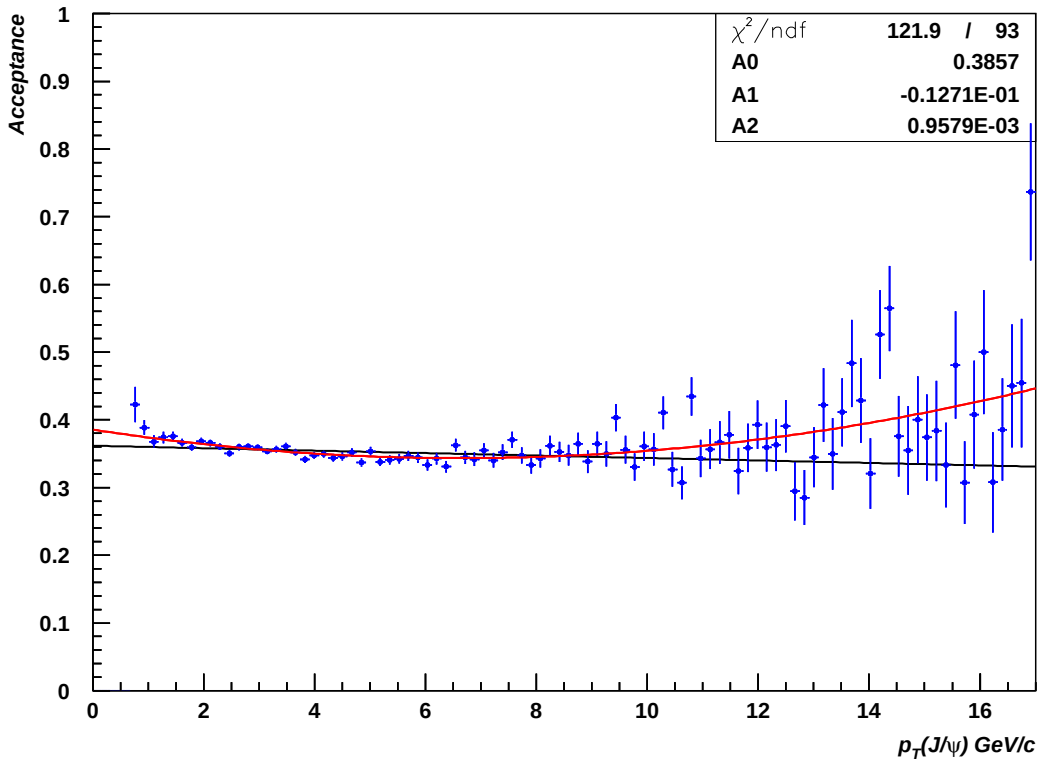

Figure 5.23: CMU-CMU SVXII J/ψ acceptance for all silicon cuts as a function of $p_{\mathrm{T}}(\mathrm{J}/\psi)$ fitted with a quadratic, which gives a better χ^2/ndf than the linear fit used in Figure 5.21

To improve the quality of the fit, the $p_{\mathrm{T}}(\mathrm{J}/\psi)$ acceptance is refitted with a quadratic rather than a straight line. Figure 5.23 allows the quadratic and linear fits to be compared for runs 146805-152625. The quadratic χ^2/ndf of 122/93 is significantly better than the straight line fit result in Table 5.8. The acceptance is calculated for the central values of each p_{T} bin in which the B-fraction is measured using both the straight line and quadratic fits in order to determine the systematic error on the overall acceptance. Table 5.10 lists the average of the acceptances obtained from the linear and quadratic fits, i.e. $(\mathcal{A}_{\mathrm{lin}} + \mathcal{A}_{\mathrm{quad}})/2$. The error quoted for each acceptance measurement is

$p_{\mathrm{T}}(\mathrm{J}/\psi)$	Acceptance
2.0 - 2.25	0.3605 ± 0.0025
2.25 - 2.5	0.3592 ± 0.0017
2.5 - 2.75	0.3580 ± 0.0009
2.75 - 3.0	0.3568 ± 0.0002
3.0 - 3.25	0.3557 ± 0.0004
3.25 - 3.5	0.3547 ± 0.0010
3.5 - 3.75	0.3537 ± 0.0015
3.75 - 4.0	0.3528 ± 0.0020
4.0 - 4.25	0.3519 ± 0.0024
4.25 - 4.5	0.3511 ± 0.0027
4.5 - 4.75	0.3504 ± 0.0030
4.75 - 5.0	0.3497 ± 0.0033
5.0 - 5.5	0.3488 ± 0.0035
5.5 - 6.0	0.3478 ± 0.0036
6.0 - 6.5	0.3471 ± 0.0034
6.5 - 7.0	0.3465 ± 0.0030
7.0 - 8.0	0.3462 ± 0.0020
8.0 - 9.0	0.3466 ± 0.0002
9.0 - 10.0	0.3480 ± 0.0034
10.0 - 12.0	0.3518 ± 0.0099
12.0 - 14.0	0.3603 ± 0.0220
14.0 - 17.0	0.3762 ± 0.0425

Table 5.10: The average acceptances with errors for the central value of each p_{T} bin obtained from linear and quadratic fits to the $p_{\mathrm{T}}(\mathrm{J}/\psi)$ acceptance

$(\mathcal{A}_{\mathrm{lin}} - \mathcal{A}_{\mathrm{quad}})/2$. The acceptance is expected to increase at higher momentum due to the smaller opening angle between the two muons. When the opening angle is less than the 30° angular width of a single SVXII wedge, the SVXII track reconstruction efficiency for both tracks is the same as for a single track.

The momentum spectrum of prompt J/ψ's is softer than for J/ψ's produced by b hadron decays. Therefore, a bias in acceptance as a function of p_{T} could introduce a systematic bias in the fraction of b hadrons counted in a particular bin. In Table 5.10 there is a $\pm 4\%$ variation in the relative

SVXII/COT acceptance over the entire transverse momentum range of 15 GeV/c. The B-fraction analysis is performed in bins of width $\Delta p_{\rm T} << 15$ GeV/c where the largest bin size is 3 GeV/c. Therefore, since the systematic bias within a bin is $< 1\%$, this will have a negligible effect on the B-fraction.

5.8 L_{xy} Asymmetry

The systematic dependencies of the B-fraction on z, ϕ_0 and $\eta_{\rm J/\psi}$ is explored by studying the asymmetry in the decay length of the J/ψ:

$$A_{L_{xy}} = \frac{(\#\text{ events } L_{xy} > 0) - (\#\text{ events } L_{xy} < 0)}{(\#\text{ events } L_{xy} > 0) + (\#\text{ events } L_{xy} < 0)}$$

This asymmetry, which is related to the fraction of J/ψ's from B's that lie in the positive tails of the $L_{xy}/\sigma_{L_{xy}}$ distributions, was calculated for runs 138425-152625 with all cuts applied. The asymmetry is not an exact measure of the B-fraction as it is possible for real B's to have negative L_{xy}, particularly for low $p_{\rm T}$(B) due to large opening angles between the B flight direction and the J/ψ. Figure 5.24 illustrates the relationship between the asymmetry and the B-fraction using a Monte Carlo tuned to match the data:

$$f_{\rm B} = \frac{\text{Area 1 + Area 2}}{\text{Total Area}}\,, \qquad A_{L_{xy}} = \frac{\text{Area 1}}{\text{Total Area}}.$$

This relationship implies that the systematic error on the asymmetry must be added in quadrature with the rest of the errors on the B-fraction.

Figure 5.25 shows the measured asymmetry as a function of z vertex position, ϕ_0 and $\eta_{\rm J/\psi}$. The asymmetry is expected to be independent of each of these variables. If x represents the number of events with $L_{xy} > 0$ and y

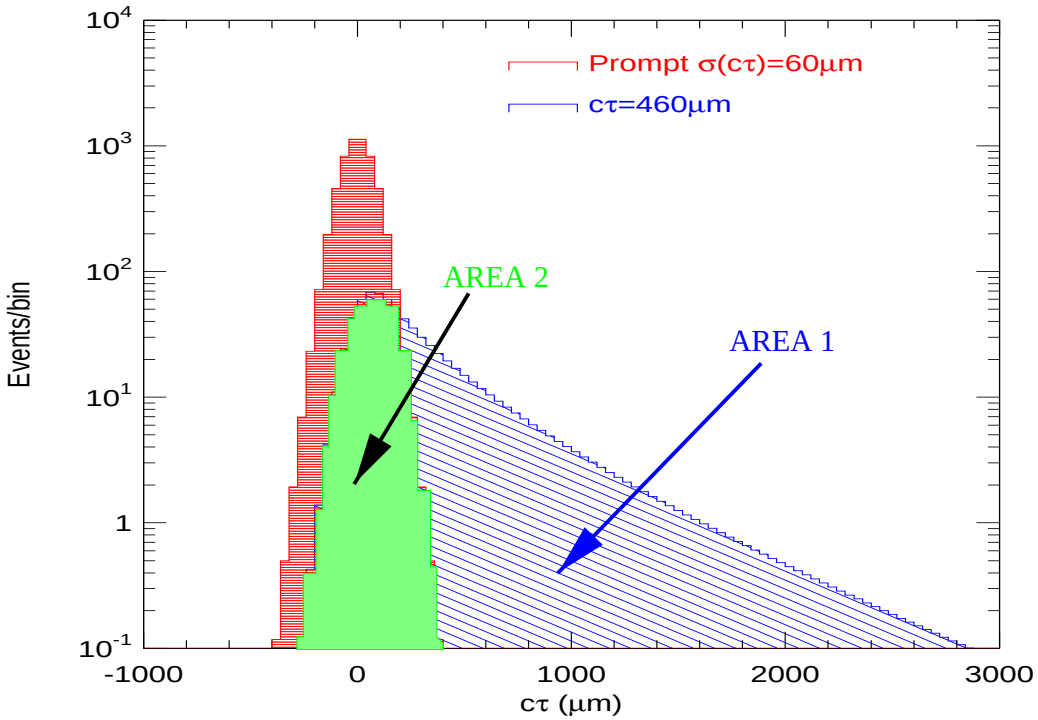

Figure 5.24: The relationship between L_{xy} asymmetry and the B-fraction. 77% of the B-fraction is contained in Area 1.

is the number of events with $L_{xy} < 0$, then

$$A_{L_{xy}} = \frac{x - y}{x + y}$$

and the error on the asymmetry in each bin is

$$\varepsilon_A = \sqrt{\left(\frac{\partial A}{\partial x}dx\right)^2 + \left(\frac{\partial A}{\partial y}dy\right)^2} = \frac{2}{(x+y)^2}\sqrt{xy^2 + x^2y}.$$

Table 5.11 lists the slopes and errors for the fits to the asymmetry distributions in Figure 5.25. The overall asymmetry is the average of the asymmetries for each kinematic variable, combined with the average statistical error:

$$A_{L_{xy}} = 0.1168 \pm 0.0037.$$

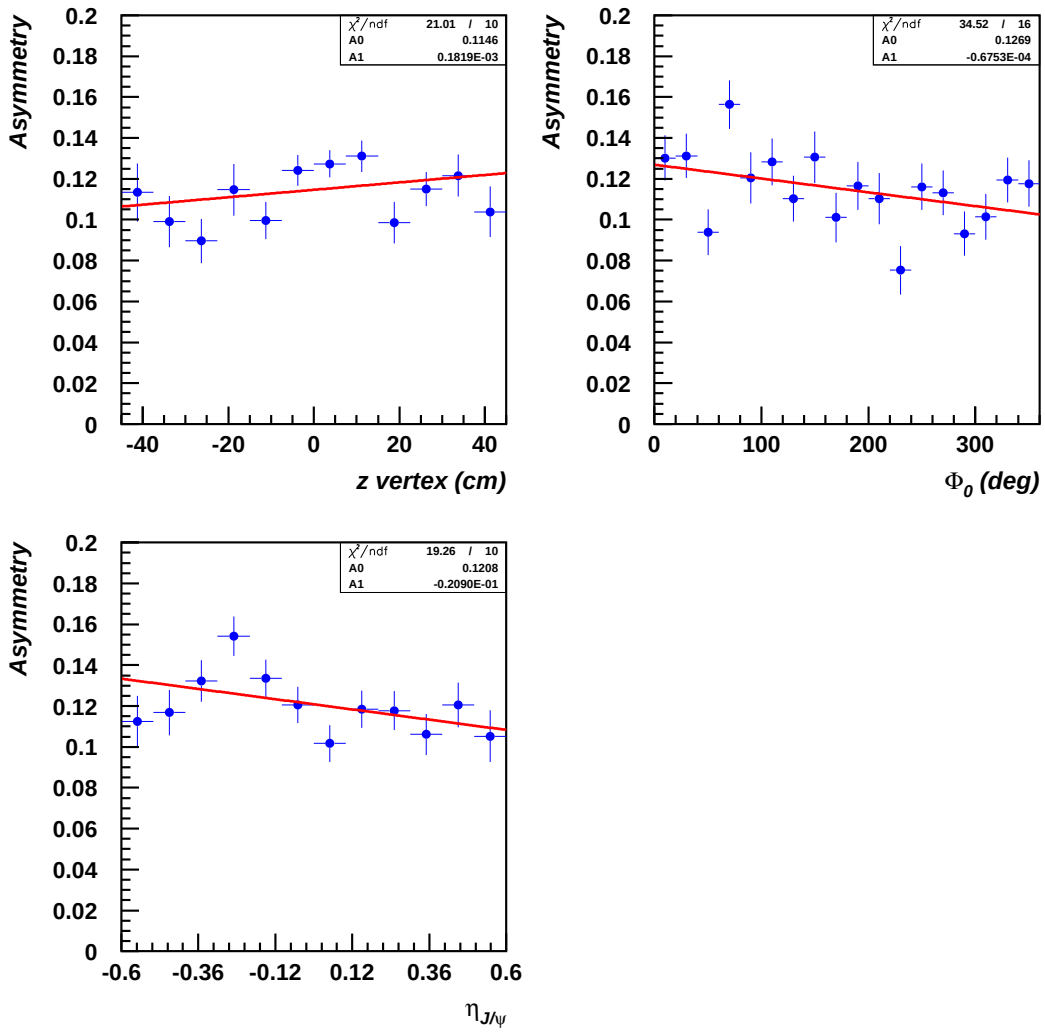

Figure 5.25: The L_{xy} asymmetry as a function of z, ϕ_0 and $\eta_{J/\psi}$

	Slope	Asymmetry	χ^2/ndf
z-vertex	0.000182 ± 0.000127 cm^{-1}	0.1146 ± 0.0028	21/10
ϕ_0	-0.000068 ± 0.000025 deg^{-1}	0.1148 ± 0.0054	35/16
$\eta_{J/\psi}$	-0.02090 ± 0.0093	0.1209 ± 0.0029	19/10

Table 5.11: Slopes and errors for the fits to the L_{xy} asymmetry

5.8.1 Systematic Uncertainty from L_{xy} Asymmetry

L_{xy} asymmetry is directly proportional to the B-fraction:

$$A_{L_{xy}} = c(\sigma_{L_{xy}}, \beta\gamma) \cdot f_{\mathrm{B}}$$

where c is a correction factor that depends on the value of the L_{xy} resolution and the boost. $\sigma_{L_{xy}}$ varies with the SVXII detector geometry. For example, the single track position resolution is worse for tracks passing through the bulkhead and hybrid regions of the detector than for tracks passing through the centre of the SVXII sensors. SVXII wedges also have different resolutions depending on their alignment and which ladders are functioning.

The number of B's with $L_{xy} < 0$ is dominated by the effect of smearing from detector resolution. The resolution function used in this analysis is averaged over the detector geometry. Therefore, regions in the detector which have better or worse resolution than the average will have different numbers of B's with $L_{xy} < 0$ and hence different asymmetries. A reasonable systematic uncertainty must then be assigned to account for the fact that the resolution function in ϕ_0, $\eta_{J/\psi}$ and z is not modeled as well as in $p_{\mathrm{T}}(\mathrm{J}/\psi)$. By studying the variation in L_{xy} asymmetry as a function of detector geometry, the fluctuation in number of B's can be used to assign a systematic uncertainty to the B-fraction.

$A_{L_{xy}}$ vs ϕ_0: The asymmetry distribution was divided into eighteen 20° bins. The variation in ϕ_0 fits well to a constant value of 0.114 ± 0.003 (χ^2/ndf = 1.1) when the regions from 60-80° and 220-240° are excluded. The asymmetries in those regions are 0.156 ± 0.012 and 0.075 ± 0.012 respectively. The deviation from the constant value of 0.114 in each region is divided by its relative area, i.e. if there is a deviation in one ϕ bin of 0.03 then the assigned uncertainty is 0.03/18. Therefore, in this case a systematic uncertainty of ± 0.002 is assigned, i.e. $\pm 2\%$ of the B-fraction integrated over ϕ_0.

$A_{L_{xy}}$ vs z: The variation with z vertex position fits well to a constant value of 0.108 ± 0.004 (χ^2/ndf = 1) in the two outer barrels and 0.123 ± 0.004 (χ^2/ndf = 2.7) in the inner barrel. The asymmetry averaged over the whole z region is 0.115 ± 0.003. Two thirds of the observed J/ψ's have a z vertex located within the central barrel region. The systematic uncertainty is therefore $+5\%$, -2%.

$A_{L_{xy}}$ vs $\eta_{J/\psi}$: The variation with rapidity was studied since there is a variation in resolution with track pseudo-rapidity. The asymmetry distribution was divided into twelve bins from -0.6 to 0.6. The region between -0.3 and -0.2 has an asymmetry of 0.154 ± 0.010 and the rest of the distribution from -0.6 to 0.6 fits well to a constant value of 0.117 ± 0.003 (χ^2/ndf = 1.1). Therefore, the systematic uncertainty on the total B-fraction integrated over rapidity is $+3\%$.

The SVXII geometry is correlated. A region with poor resolution in z could be due to a bad ϕ wedge and bad resolution in the outer barrels could be because tracks passing through that region tend to have larger rapidities.

Therefore, the uncertainties above are combined so that the total systematic uncertainty on the B-fraction due to SVXII geometry is $+6\%$, -3%.

5.9 Summary

Applying the full set of silicon cuts used in this study to all ≥ 3 r-ϕ CMU-CMU events results in an 80% reduction in the negative tails of the $L_{xy}/\sigma_{L_{xy}}$ distribution with a corresponding reduction in statistics of 50%.

The selection cuts applied here to optimise SVXII track quality are used to fit the J/ψ lifetime and to determine the B-fraction as will be described in detail in Chapter 6.

The systematic bias in SVXII/COT acceptance as a function of p_{T} has a negligible effect on the B-fraction. However, any bias in the measurement of L_{xy} can bias the measurement of the B-fraction. Observed fluctuations in L_{xy} asymmetry are larger than expected from statistical uncertainties and a systematic uncertainty of $+6\%$, -3% is assigned.

Chapter 6

The $B \to J/\psi\ X$ Cross-section

The lifetime of charmed particles is an order of magnitude smaller than that of b hadrons and so they travel a much shorter distance before decaying. However, J/ψ's from B decays have secondary decay vertices well separated from the primary vertex. In this chapter, the contribution to the inclusive J/ψ cross section from $B \to J/\psi\ X$ decays is separated using an unbinned likelihood fit to the proper decay length distribution of the inclusive J/ψ's.

Theoretical predictions and previous measurements of b hadron production cross-sections at CDF Run I were discussed in Chapter 1. The Run I results included b hadrons with $p_T > 5$ GeV/c, allowing only about 10% of the total cross-section to be observed. Therefore, it could not be determined from the data whether the excess in the measured cross-section was due to an overall increase in the $b\bar{b}$ production rate or a shift in the spectrum towards higher p_T. The inclusive J/ψ cross-section at CDF Run II has been measured for all events with $p_T(J/\psi) < 17$ GeV/c [50]. Therefore, if the fraction of inclusive J/ψ's from B's can be calculated for J/ψ's with low transverse momenta, then the $B \to J/\psi\ X$ inclusive cross-section measurement can be extended far below the p_T limit of the Run I result in Figure 1.7.

6.1 Event Selection

The data sample used in this study consists of J/ψ events in runs 138425-152625 selected by the dimuon trigger paths described in Chapter 2. The following selection criteria were applied to the COT and CMU muon track parameters. Note that for the dimuon triggers, Level 2 performs an auto-accept of Level 1 and so there are no additional Level 2 selection criteria.

Level 1 Selection Criteria:

- $p_{\mathrm{T}}(\mu)_{\mathrm{XFT}} > 1.5$ GeV/c
- Muons stubs matched to trigger stubs
- Dimuon candidate stubs separated by two CMU 2.4° towers
- Muon tracks matched to XFT tracks and XTRP projections
- Exclude tracks which pass within 1.5 cm of the centre of the COT wire planes in any of the 4 axial layers
- Exclude events where both muons fall in the range 240-270° [55]

Level 2 Selection Criteria: None

Level 3 Selection Criteria:

- CMU muons
- $p_{\mathrm{T}}(\mu)_{\mathrm{COT}} > 1.5$ GeV/c
- opposite sign muons
- $|z_0(\mu_1) - z_0(\mu_2)| < 5$ cm
- $2.7 < M_{\mu\mu} < 4.0$ GeV/c^2

- $\Delta\phi(\mu\mu) < 130^\circ$ when $p_{\rm T}({\rm J}/\psi) > 2.0$ GeV/c
- muon stub track match $\Delta(r\phi)_{\rm CMU} < 30$ cm

Additional COT/CMU Offline Selection:

- require CMU-CMU or CMU-CMP muons only
- $\chi^2(\Delta r\phi)_{\rm CMU} < 9$
- $|y_{{\rm J}/\psi}| < 0.6$
- $\geq 20/16$ axial/stereo COT hits

Both muon tracks are required to have hits in the COT and SVXII. Additional silicon track selections made to ensure a good lifetime measurement were discussed in detail in Chapter 5. Both muon tracks are required to have a hit in the innermost layer of SVXII and a hit in the next layer out if it is functioning. The total number of hits expected in SVXII is calculated and tracks with more than one missing hit are rejected. Tracks crossing the boundaries between SVXII barrels are also rejected.

Although all 3D hits found in SVXII are used, during a subsequent refit of the COT muon tracks, ISL and L00 hits are dropped as these detectors were not properly aligned during the run range under consideration. Energy loss corrections are also applied to the tracks during the refit [52, 53]. A 3D constrained vertex fit is then applied to the two muon tracks to reconstruct the J/ψ decay vertex position. The probability of the χ^2 of the 3D vertex fit to the dimuon vertex is required to be greater than 0.001. The dimuon invariant mass distribution of accepted events is shown in Figure 6.1.

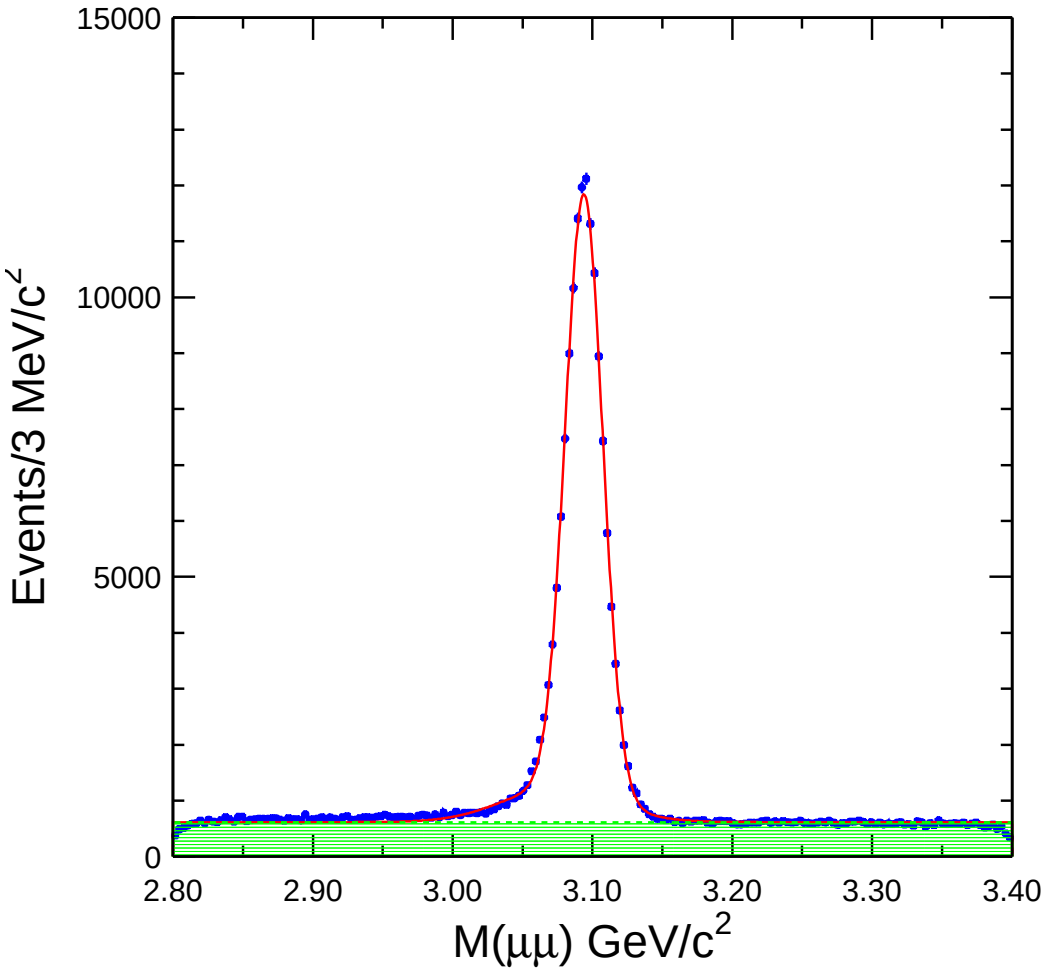

Figure 6.1: Dimuon invariant mass distribution in the J/ψ mass range

6.2 Monte Carlo Simulations

To extract the fraction of inclusive J/ψ events from b hadron decays and then measure the B $\rightarrow$ J/ψ X inclusive cross-section, the number of J/ψ events with displaced secondary vertices must be counted. Monte Carlo simulations are required to model the kinematic distributions of the momentum spectrum and the flight distances of J/ψ's from b hadron decays, which can then be used to distinguish prompt J/ψ events from B $\rightarrow$ J/ψ X events in data.

6.2.1 Modelling the b Hadron Production Spectrum

A parametric simulation [50] of the energy loss in SVXII material, CMU fiducial volume, kinematic acceptance and Level 1 muon trigger efficiency is used. The acceptance of the Level 1 trigger is simulated using the measured Level 1 muon trigger efficiency as a function of $p_{\mathrm{T}}(\mu)$ [55]. The muons are required to have $p_{\mathrm{T}} \geq 1.5$ GeV/c and $|\eta| < 0.6$ (CMU) and for J/ψ's the requirement is $|y| < 0.6$ to ensure consistency with the inclusive cross-section measurement.

The Bgenerator package [56] is used to generate b hadrons using a b quark $d\sigma/dp_{\mathrm{T}}dy$ spectrum as input for the Monte Carlo generation. The input spectrum is shown in Figure 6.2. The input b quark spectra are histograms with 200 GeV/c granularity in p_{T}(b). MRST 2000 proton structure functions [57] and a b quark mass of 4.75 GeV/c^2 is used by the Monte Carlo to generate a mix of b hadron states [3] in the ratio

$$\mathrm{B_d} : \mathrm{B_u} : \mathrm{B_s} : \Lambda_\mathrm{b} = 0.389 : 0.389 : 0.106 : 0.116.$$

The input b hadron masses and lifetimes are listed in Table 6.1. The b hadrons are decayed to final states containing J/$\psi \to \mu\mu$. The variation in the output b hadron production spectrum as a function of the shape of the Peterson fragmentation function is shown in Figure 6.3.

b hadron	Mass (GeV/c^2)	Lifetime (ps)	Fragmentation fraction
$B^{\pm}$	5.28	1.64	0.389
B^0	5.28	1.62	0.389
B_s	5.38	1.55	0.106
Λ_b	5.641	1.69	0.116

Table 6.1: b hadron properties used by the Monte Carlo decay package

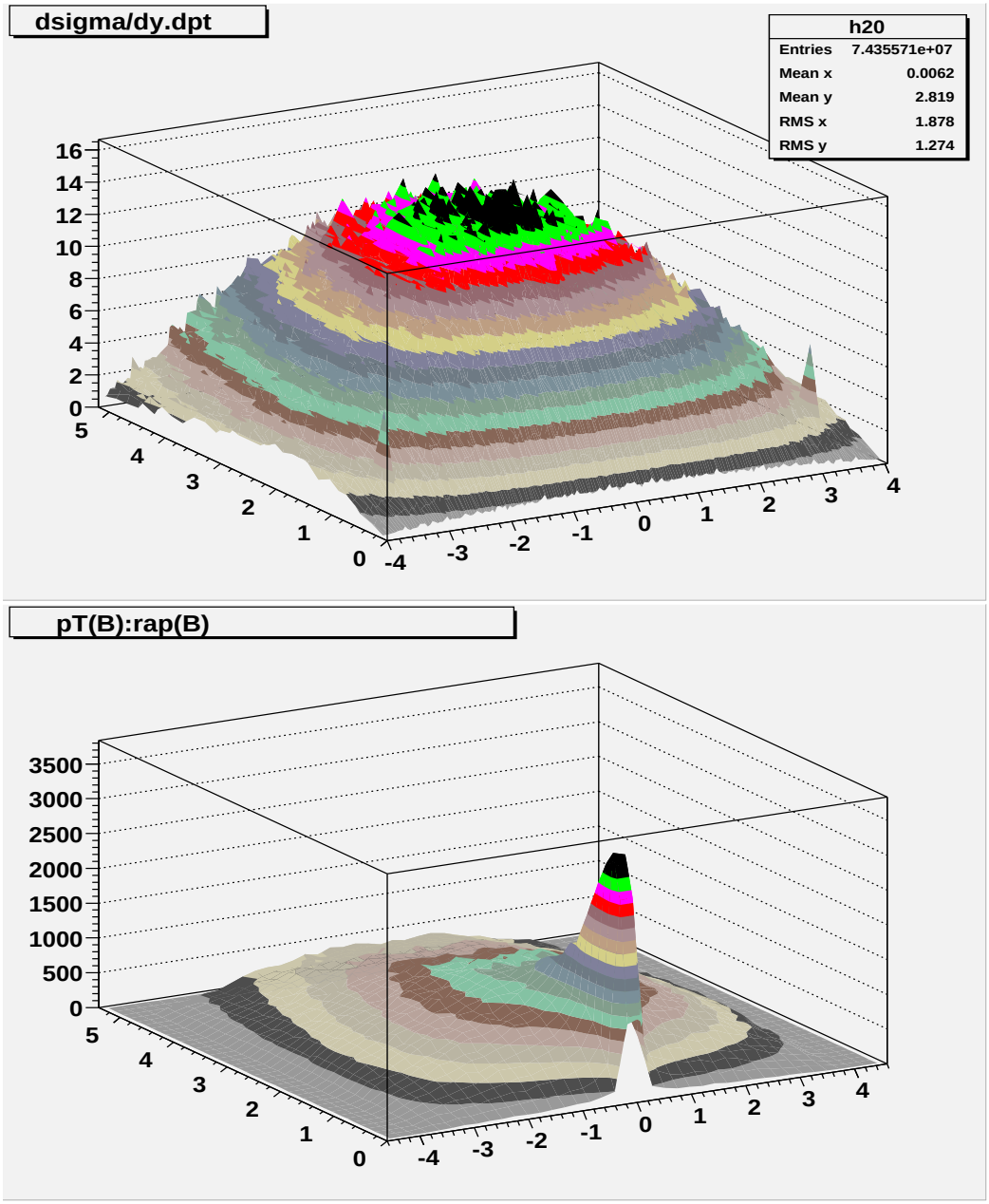

Figure 6.2: The b quark $d\sigma/dp_{\mathrm{T}}dy$ input spectrum and the resultant b hadron spectrum after fragmentation using a Peterson function with $\epsilon = 0.006$

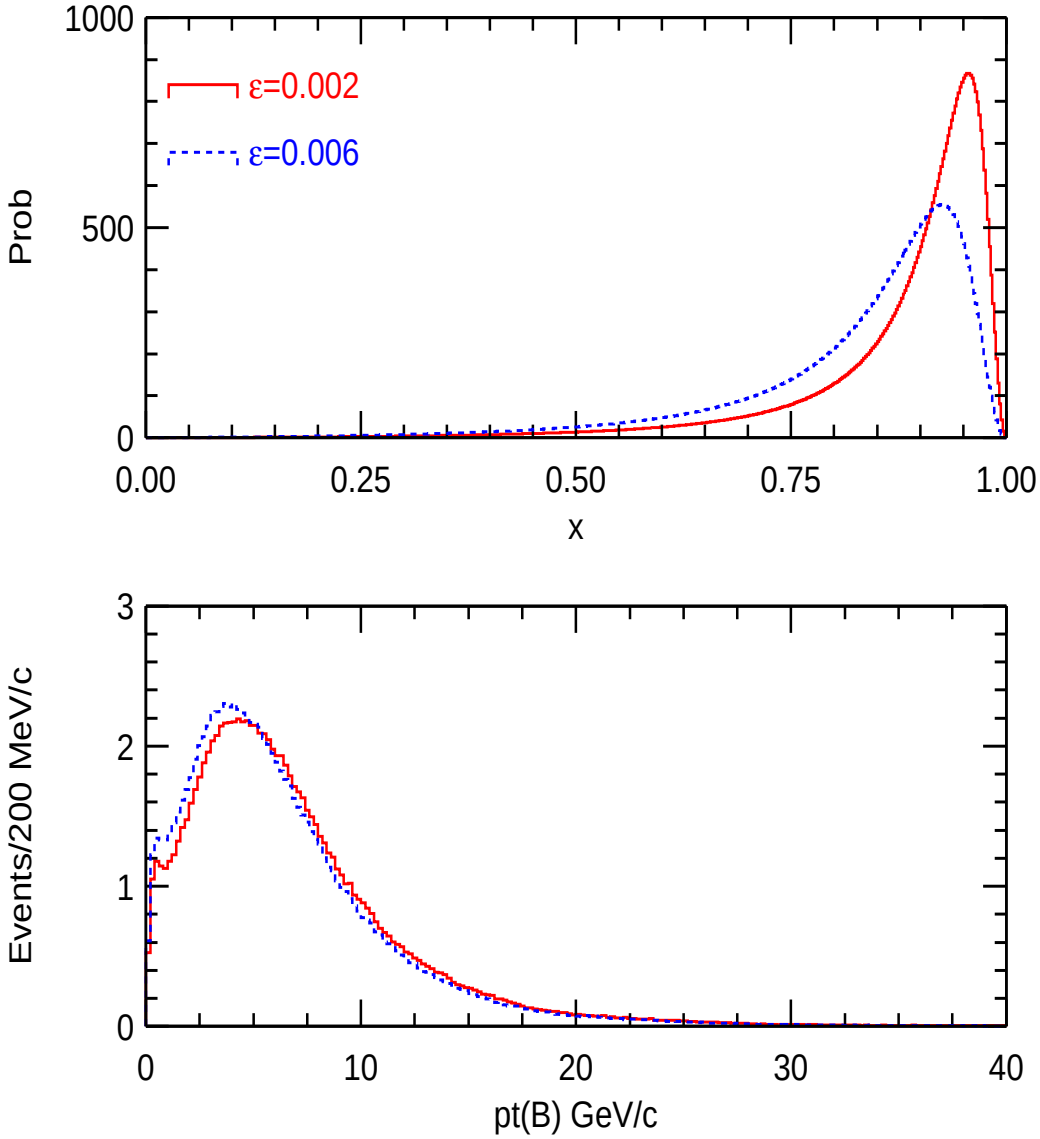

Figure 6.3: Peterson Fragmentation function (top) and b hadron p_{T} distributions from Monte Carlo (bottom). The dashed lines are the distributions obtained using the default Peterson parameter $\epsilon = 0.006$ and the solid lines use a Peterson parameter $\epsilon = 0.002$

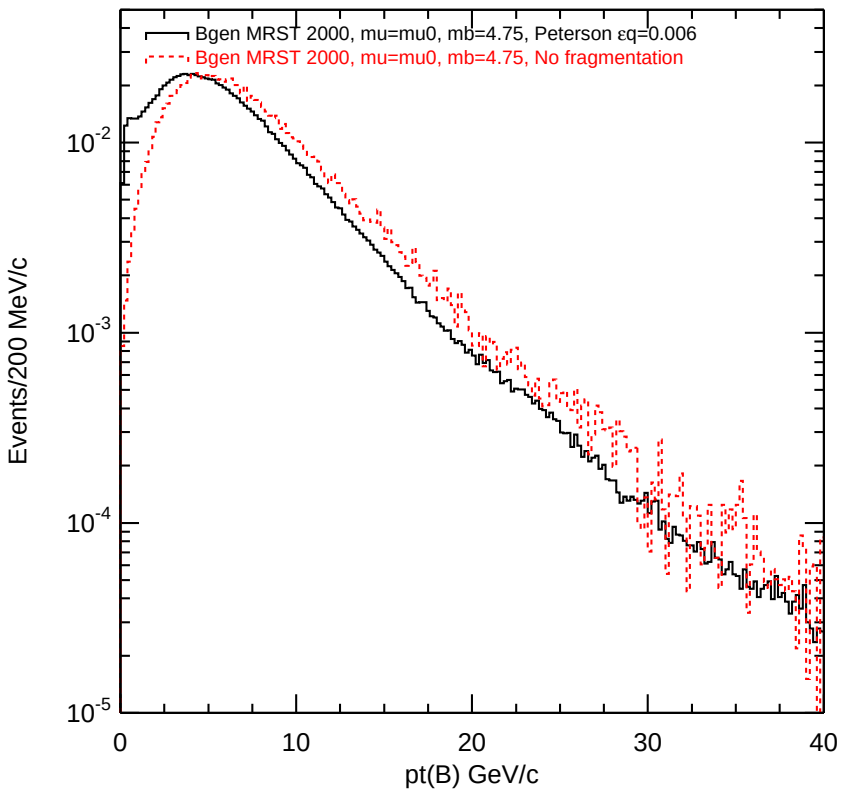

Figure 6.4: The solid line is the transverse momentum spectrum of b hadron parents with the fragmentation turned on and the dashed line is the spectrum used in the analysis with the fragmentation switched off

An excess of events at low $p_{\mathrm{T}}(\mathrm{B})$ is observed in the output b hadron spectrum shown in Figure 6.2. The source of this excess is not understood. However, since the momentum fraction carried away by b quarks is close to 1, it is possible to proceed using the b-quark spectrum as a b-hadron spectrum. Therefore, in order to model the shape of the low momentum b hadron spectrum used in the Monte Carlo, the fragmentation option in Bgenerator is switched off and the b hadron spectrum used in the analysis is shown in Figure 6.4.

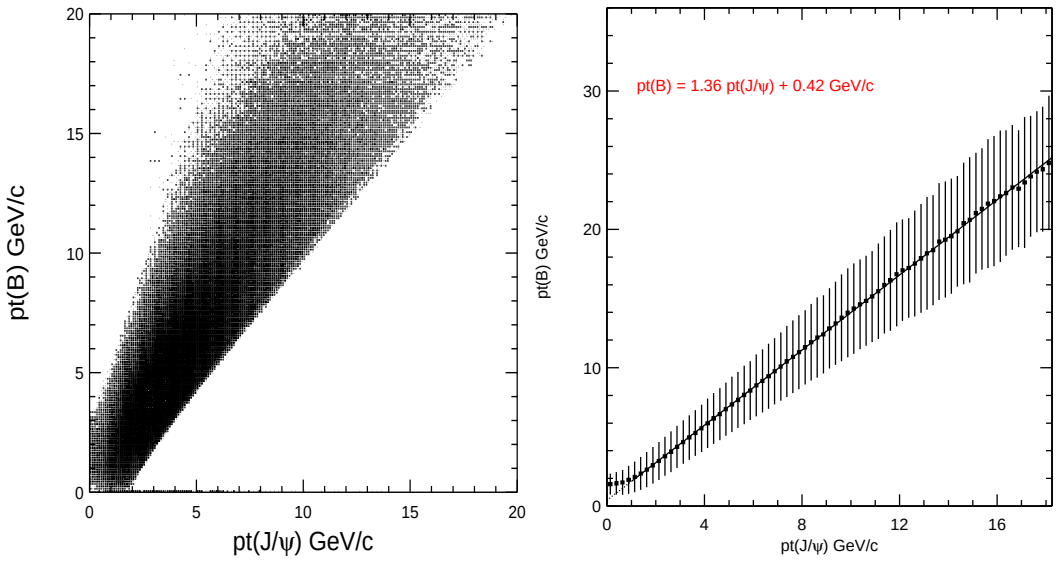

Figure 6.5: Transverse momentum of the parent b hadron versus $p_{\mathrm{T}}(\mathrm{J}/\psi)$ (left). The mean and RMS of the b hadron transverse momentum versus $p_{\mathrm{T}}(\mathrm{J}/\psi)$ with a straight line fit (right).

The transverse momentum of the parent b hadrons is plotted against the transverse momentum of the reconstructed J/ψ in Figure 6.5. At $p_{\mathrm{T}}(\mathrm{J}/\psi) =$ 2.0-2.25 GeV/c, b hadrons are probed down to $p_{\mathrm{T}}(\mathrm{B}) = 500$ MeV/c but these account for only 0.2% of all B's in this J/ψ transverse momentum bin. This corresponds to $\gamma\beta c\tau \approx 45$ μm, which is similar to the 50 μm resolution of the flight distance of J/ψ events measured in the previous chapter. Figure 6.5 also illustrates the linear correlation between the average B transverse momentum and the average J/ψ transverse momentum for $p_{\mathrm{T}}(\mathrm{J}/\psi) > 1.0$ GeV/c. A straight line fit to the mean of the $p_{\mathrm{T}}(\mathrm{B})$ distribution yields the result

$$\bar{p}_{\mathrm{T}}(\mathrm{B}) = 1.36\ \bar{p}_{\mathrm{T}}(\mathrm{J}/\psi) + 0.42\ \mathrm{GeV}/c.$$

Below $p_{\mathrm{T}}(\mathrm{J}/\psi) = 1.0$ GeV/c, the B momentum spectrum is approximately constant and the linear correlation no longer applies. Therefore, B $\rightarrow$ J/ψ X

events with $p_{\mathrm{T}}(\mathrm{J}/\psi) < 1.0$ GeV/c cannot be used to determine the shape of the b hadron cross-section.

6.2.2 Using Scale Factors to Determine the B Lifetime

The flight distance of the reconstructed J/ψ from the primary vertex to the secondary decay vertex is used to separate prompt J/ψ's from those produced in the decay of b hadrons:

$$L_{xy} = \frac{\mathbf{L} \cdot \mathbf{p}_{\mathrm{T}}(\mathrm{J}/\psi)}{p_{\mathrm{T}}(\mathrm{J}/\psi)}$$

The L_{xy} distribution of prompt J/ψ's is symmetric around zero and is used to extract the shape of the resolution function from the data.

The J/ψ pseudo-lifetime is defined as

$$x = L_{xy}(\mathrm{J}/\psi)\frac{M(\mathrm{J}/\psi)}{p_{\mathrm{T}}(\mathrm{J}/\psi)}.$$

At $p_{\mathrm{T}}(\mathrm{J}/\psi) > 5.0$ GeV/c, the pseudo-lifetime of J/ψ events from B decays is a pure exponential distribution with an invariant (p_{T} independent) slope of 378 μm as shown in Figure 6.6. The J/ψ pseudo-lifetime is the kinematic variable used for all J/ψ transverse momentum ranges to minimise variations in the signal shape between the different bins and to reduce the dependency on the Monte Carlo simulation of the b hadron spectrum.

A Monte Carlo simulation [58] is required to model the x distribution in B $\rightarrow$ J/ψ X events. The Lorentz invariant proper decay length of a b hadron that decays to J/ψ X is

$$c\tau = \frac{L}{\beta\gamma} = L_{xy}(B)\,\frac{M(\mathrm{B})}{p_{\mathrm{T}}(\mathrm{B})} = L_{xy}(\mathrm{J}/\psi)\,\frac{M(\mathrm{J}/\psi)}{p_{\mathrm{T}}(\mathrm{J}/\psi)}\,\frac{1}{F} = \frac{x}{F}$$

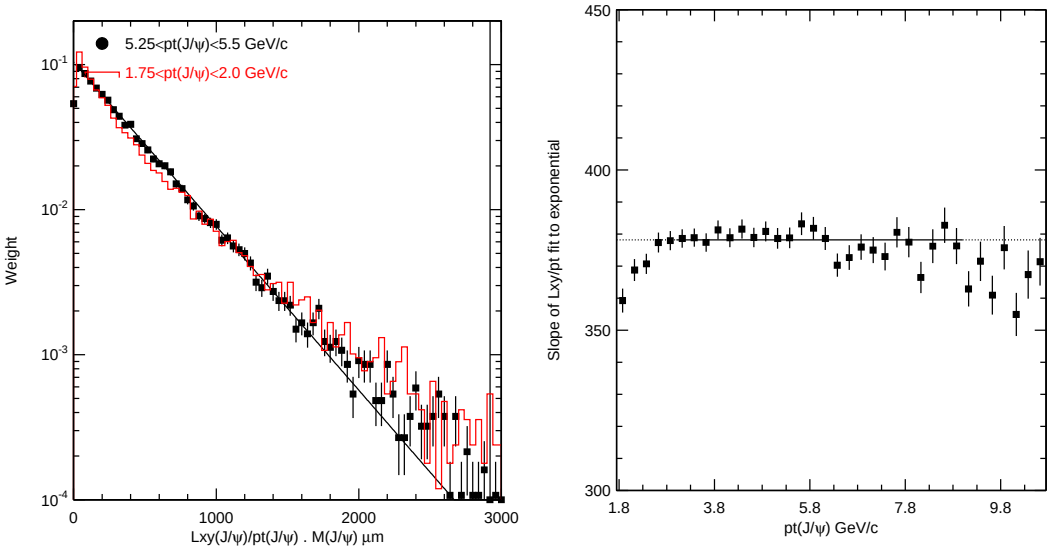

Figure 6.6: For $p_{\mathrm{T}}(\mathrm{J}/\psi) > 5.0$ GeV/c the pseudo-$c\tau$ distribution is well described by a single exponential with a characteristic slope of 378 μm

where L is the length of the path the b hadron traveled before decaying, and F is a scale factor defined as

$$F = \frac{p_{\mathrm{T}}(\mathrm{B})\, M(\mathrm{J}/\psi)\, \cos\theta}{p_{\mathrm{T}}(\mathrm{J}/\psi)\, M(\mathrm{B})}$$

where θ is the angle between the B and J/ψ momenta. The scale factor F is calculated from B $\rightarrow$ J/ψ X Monte Carlo. The F distributions in different J/ψ transverse momentum regions are shown in Figure 6.7. The mean of the scale factor distribution plotted in Figure 6.8 is constant for all values of $p_{\mathrm{T}}(\mathrm{J}/\psi) > 1.0$ GeV/c and is found to be 0.83. The RMS of the distribution is determined largely by the B $\rightarrow$ J/ψ X decay kinematics and increases with decreasing p_{T}.

The F-factors from Monte Carlo are used to correct x measured in data in order to calculate the b hadron proper decay length. The value of $c\tau$ obtained is convoluted with the x resolution function measured in the data

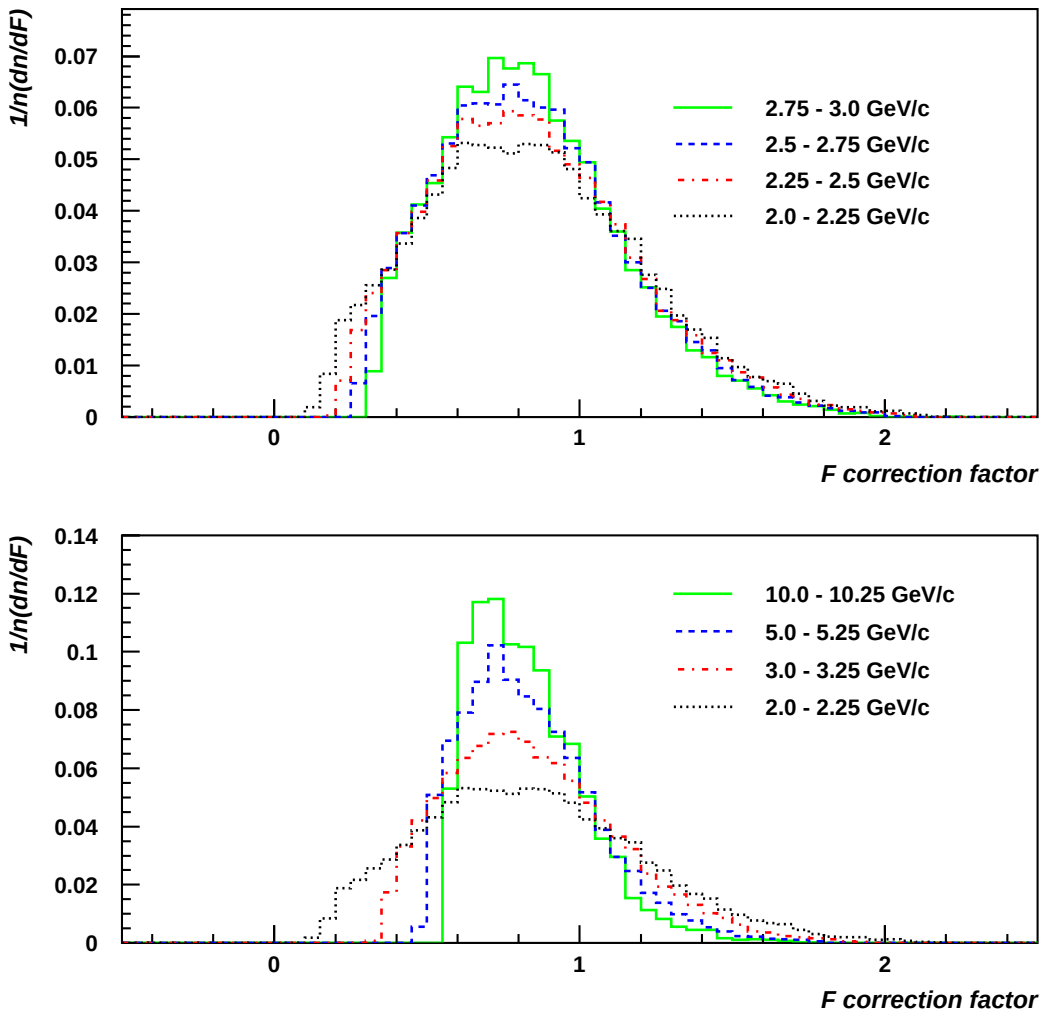

Figure 6.7: Momentum correction factor, F, distributions from generator level B $\rightarrow$ J/ψ X decays in representative J/ψ p_{T} bins.

and an exponential function. The b hadron inclusive lifetime (slope of the exponential) is then extracted simultaneously from the same fit as the B-fraction. However, this method only works in J/ψ transverse momentum ranges where there are no b hadron parents produced at rest and where the J/ψ and B flight directions are strongly correlated. Below p_{T}(J/ψ) = 2.0 GeV/c, b hadrons produced at rest begin to be probed and so this provides a

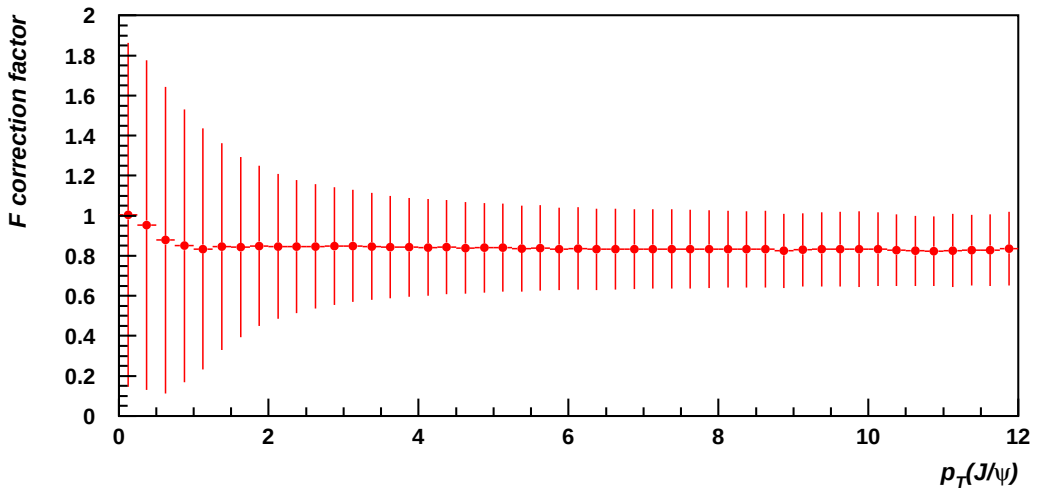

Figure 6.8: Momentum correction factor, F, mean and RMS distributions from generator level B $\rightarrow$ J/ψ X decays in all J/ψ p_{T} bins

lower limit to the J/ψ transverse momentum range considered in this analysis. The upper limit of $p_{\mathrm{T}}(\mathrm{J}/\psi) = 17.0$ GeV/c is dictated by statistics.

6.2.3 Full Detector Simulation

A full CDF detector simulation of the generated B $\rightarrow$ J/ψ X events including realistic SVXII coverage and beamlines from 20 different runs was performed. Using an unbinned likelihood fit to the reconstructed J/ψ pseudo-lifetime distributions from the Monte Carlo convoluted with the F-factor distributions and detector resolutions, the inclusive B-lifetime was extracted in different $p_{\mathrm{T}}(\mathrm{J}/\psi)$ ranges. The Monte Carlo and fit distributions in three representative bins shown in Figure 6.9 are in good agreement. Fitting the inclusive B-lifetime to a straight line yields

$$c\tau_{\mathrm{MC}} = (479 \pm 3) + (-0.3 \pm 0.4) \cdot p_{\mathrm{T}}(\mathrm{J}/\psi).$$

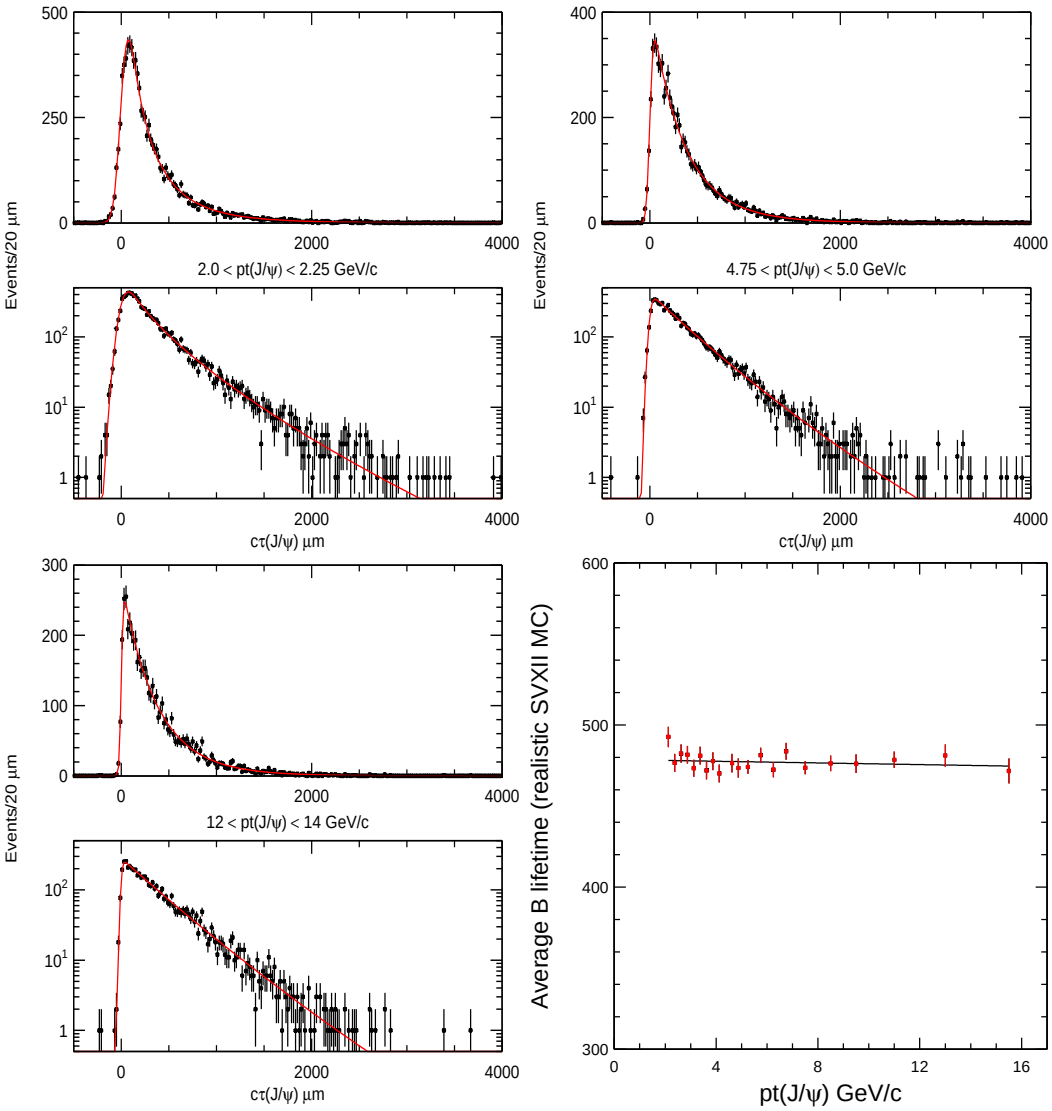

Figure 6.9: Fit to the realistic Monte Carlo B $\rightarrow$ J/ψ X pseudo-$c\tau$ shape using F factors in different $p_{\rm T}$(J/ψ) bins. The bottom right plot shows the value of the b hadron inclusive lifetime obtained from the fit in all bins from 2-17 GeV/c. The fit to a straight line is $c\tau_{\rm MC} = (479\pm3)+(-0.3\pm0.4)*p_{\rm T}({\rm J}/\psi)$.

From the mix of b hadrons generated, the average value is $c\tau = 475\ \mu$m. This cross-check demonstrates that the shape of the smeared J/ψ $c\tau$ distribution and b hadron inclusive lifetime can be correctly modeled using a convolution with the F distributions for all J/ψ's in the $p_{\rm T}$ range under consideration.

6.3 Fitting Method

An unbinned maximum likelihood fit is used to extract the B-fraction from the data. The J/ψ pseudo-lifetime, x, its error, σ, and the invariant mass of the dimuon, $m_{\mu\mu}$, are the input variables. The mass and lifetime of all J/ψ events in the region $2.85 < m_{\mu\mu} < 3.35$ GeV/c^2 are simultaneously fit using the log-likelihood function

$$\ln \mathcal{L} = \sum_{i=1}^{N} \ln \mathcal{F}(x_i, m_{\mu\mu}),$$

where N is the total number of events in the dimuon invariant mass window. The invariant mass and pseudo-lifetime distributions are described by the following function:

$$\mathcal{F}(x, m_{\mu\mu}) = f_{\rm sig} \cdot \mathcal{F}_{\rm sig}(x) \times \mathcal{M}_{\rm sig}(m_{\mu\mu}) + (1 - f_{\rm sig}) \cdot \mathcal{F}_{\rm bkg}(x) \times \mathcal{M}_{\rm bkg}(m_{\mu\mu})$$

where $\mathcal{F}_{\rm sig,bkg}$ and $\mathcal{M}_{\rm sig,bkg}$ are functional forms describing the pseudo-lifetime and invariant mass distributions in the signal and background regions respectively. The fit parameter $f_{\rm sig}$ is the fraction of J/$\psi \to \mu\mu$ events in the invariant mass signal region.

6.3.1 Functional Forms

The function for modelling the J/ψ signal events consists of two parts, the B $\rightarrow$ J/ψ X decay and prompt decay functions:

$$\mathcal{F}_{\rm sig}(x) = f_{\rm B} \cdot \mathcal{F}_{\rm B}(x) + (1 - f_{\rm B}) \cdot \mathcal{F}_{\rm p}(x)$$

where $f_{\rm B}$ is the B-fraction. The function for the B $\rightarrow$ J/ψ X inclusive lifetime, $\mathcal{F}_{\rm B}(x)$, is assumed to be a pure exponential lifetime distribution, convoluted with a resolution function $R(x' - x, s\sigma)$, where s is an error scale factor representing the possible amount that the uncertainty on x in the data is under or overestimated. To model the shape of the b hadron lifetime distribution, the F factor distributions in each transverse momentum bin, $\mathcal{H}(F, p_{\rm T}({\rm J}/\psi))$, are convoluted with the resolution function and the B-lifetime exponential such that

$$\mathcal{F}_{\rm B}(x) = \frac{1}{F\ c\tau} \exp\left(-\frac{x}{F\ c\tau}\right) \otimes R(x' - x, s\sigma) \otimes \mathcal{H}(F, p_{\rm T}({\rm J}/\psi))$$

where $c\tau$ is the average inclusive b hadron lifetime from the fit. The function for prompt J/ψ's is assumed to have zero lifetime and is therefore the resolution function:

$$\mathcal{F}_{\rm p} = R(x, s\sigma).$$

The invariant mass shape, $\mathcal{M}_{\rm sig}$, is a double Gaussian:

$$\mathcal{M}_{\rm sig}(m_{\mu\mu}) = G_1(m_{\mu\mu} - M, \sigma_M) + f_2 \cdot G_2(m_{\mu\mu} - (M + D), r_2\sigma_M).$$

The invariant mass fit parameters are M, the mean of the mass distribution; σ_M, the width of the first Gaussian; f_2, the fraction of the second Gaussian; D, the shift in the mean of the second Gaussian; and r_2, the ratio of the widths of the two Gaussians.

The pseudo-lifetime background function consists of four parts representing the zero lifetime component, an exponential function with a positive slope, an exponential function with a negative slope, and a symmetric exponential function with both positive and negative slopes. Some of the background described by the exponential background function may be from other long lived B events, so the background exponential tails are also convoluted with the resolution function. The background shape is then described by

$$\begin{aligned}
\mathcal{F}_{\rm bkg}(x) &= (1 - f_+ - f_- - f_{\rm sym})\, R(x, s\sigma) \\
&\quad + \frac{f_+}{\lambda_+} \exp\left(-x'/\lambda_+\right) \otimes R(x' - x, s\sigma) \\
&\quad + \frac{f_-}{\lambda_-} \exp\left(x'/\lambda_-\right) \otimes R(x' - x, s\sigma) \\
&\quad + \frac{f_{\rm sym}}{2\lambda_{\rm sym}} \exp\left(-x'/\lambda_{\rm sym}\right) \otimes R(x' - x, s\sigma) \\
&\quad + \frac{f_{\rm sym}}{2\lambda_{\rm sym}} \exp\left(x'/\lambda_{\rm sym}\right) \otimes R(x' - x, s\sigma)
\end{aligned}$$

where $f_{+,-,\rm sym}$ are the fractions of the background distribution in the negative, positive, and symmetric exponential tails respectively, and $\lambda_{+,-,\rm sym}$ are the corresponding exponential slopes.

The invariant mass background is modeled using a first order polynomial:

$$\mathcal{M}_{\rm bkg}(m_{\mu\mu}) = \frac{1}{m_{\mu\mu}^{\rm max} - m_{\mu\mu}^{\rm min}} + M_{\rm slope}\left(m_{\mu\mu} - \frac{m_{\mu\mu}^{\rm max} + m_{\mu\mu}^{\rm min}}{2}\right)$$

where $m_{\mu\mu}^{\rm min}$ to $m_{\mu\mu}^{\rm max}$ is the dimuon invariant mass range over which the fit is performed and $M_{\rm slope}$ is the slope of the linear background distribution.

The 19 fit parameters are summarised in Table 6.2.

	B signal lifetime fit parameters
$c\tau$	inclusive b hadron lifetime
f_{B}	$\mathrm{B} \to \mathrm{J}/\psi$ X fraction
s_{sig}	scale factor on x measurement uncertainty for signal events
f_{sig}	fraction of J/ψ signal events in $\mu^+\mu^-$ combinations
f_2	fraction of resolution function in wider Gaussian
μ	relative width of second Gaussian in resolution function
	Dimuon invariant mass fit parameters
M	mean of the J/ψ signal mass distribution
σ_M	width of the first Gaussian
f_2	fraction of the second Gaussian
D	shift in the mean of the second Gaussian
r_2	ratio of the widths of the two Gaussians
M_{slope}	slope of the linear mass background
	J/ψ pseudo-lifetime background fit parameters
f_-	fraction of background distribution in negative exponential tails
λ_-	slope of negative exponential background
f_+	fraction of background distribution in positive exponential tails
λ_+	slope of positive exponential background
f_{sym}	fraction of background distribution in symmetric exponential tails
λ_{sym}	slope of symmetric exponential background
s_{bg}	scale factor on x measurement uncertainty for background events

Table 6.2: Fit parameters used in the simultaneous mass and pseudo-lifetime fit used to extract the fraction of $\mathrm{B} \to \mathrm{J}/\psi$ X events from inclusive J/ψ data

6.3.2 The Pseudo-lifetime Resolution

The most important element of extracting the B-fraction from inclusive J/ψ events is understanding and modelling the shape of the resolution function. The behavior of the measured L_{xy} resolution as a function of the J/ψ transverse momentum from a single Gaussian fit to the core of the distribution after all silicon quality cuts are applied was illustrated in Figure 5.15. The pseudo-lifetime resolution used in the fit is shown in Figure 6.10. It fits well to a parametric function:

$$\begin{aligned}\sigma(X, p_{\mathrm{T}}(\mathrm{J}/\psi)) &= \sigma(L_{xy}, p_{\mathrm{T}}(\mathrm{J}/\psi))\frac{M(\mathrm{J}/\psi)}{p_{\mathrm{T}}(\mathrm{J}/\psi)} \\ &= (25 \pm 4) \times \left(1 + \exp\left[-\frac{p_{\mathrm{T}} - (3.4 \pm 0.7)}{(2.1 \pm 0.7)}\right]\right).\end{aligned}$$

For lower momenta, the resolution in x rapidly deteriorates at the same time that the distribution of x from B events is getting shorter and the capability

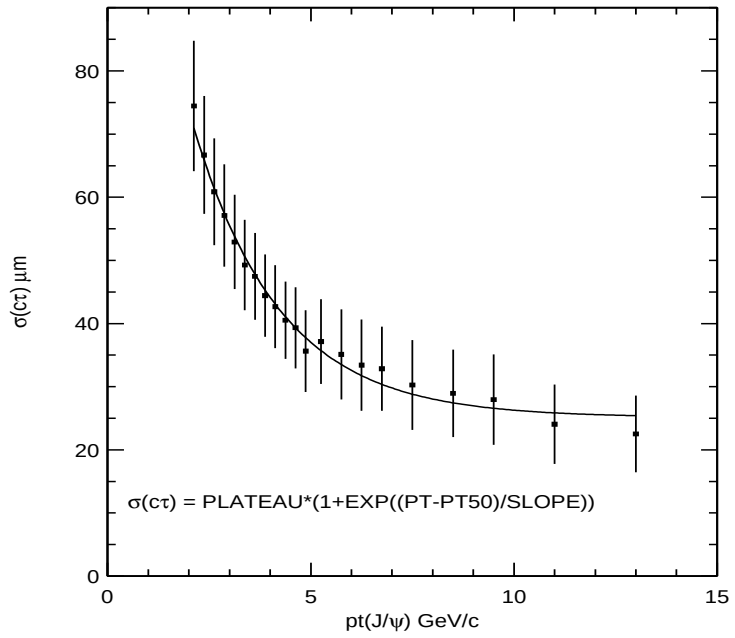

Figure 6.10: J/ψ pseudo-$c\tau$ resolution as a function of $p_{\mathrm{T}}(\mathrm{J}/\psi)$

of resolving long lived J/ψ's from prompts becomes worse. The generator level Monte Carlo showed that more than 40% of B events are under the prompt peak for events with $p_{\mathrm{T}}(\mathrm{J}/\psi) < 2.75$ GeV/c (assuming a B-fraction of 10%).

6.3.3 Modelling the L_{xy} Resolution Function Shape

Figure 5.18 showed that the L_{xy} resolution function in data has non-Gaussian tails that are not fully described by the double Gaussian fit. Several exponential distributions are used to model non-Gaussian tails in the J/ψ background region. To determine whether these distributions are part of the resolution function, the distribution of J/ψ pseudo-lifetime in the mass sideband and sideband subtracted signal regions are examined in Figure 6.11. The two distributions are normalised so that the number of events in the $c\tau = 0$ bin are identical. A preliminary fit using a double Gaussian resolution function is overlaid. The non-Gaussian tails in the background from fake J/ψs are clearly much larger than in the the negative tails of the signal region. Therefore the exponential tails in the J/ψ mass background are treated separately in the fit. In the background there is a symmetric long lived component, which is longer than the signal because the probability of mismeasurements is higher in the background. Therefore there is a larger distribution of events distributed over negative and positive L_{xy} that is not Gaussian, but by virtue of the fact that they are symmetrically distributed they do not constitute a real physics signal. The positive tails in the background are larger because of cascade semileptonic decays of long-lived b hadrons where $\mathrm{b} \to \mathrm{c}l^{-}\nu$ and $\mathrm{c} \to \mathrm{s}l^{+}\nu$, producing opposite sign muons that come from highly displaced

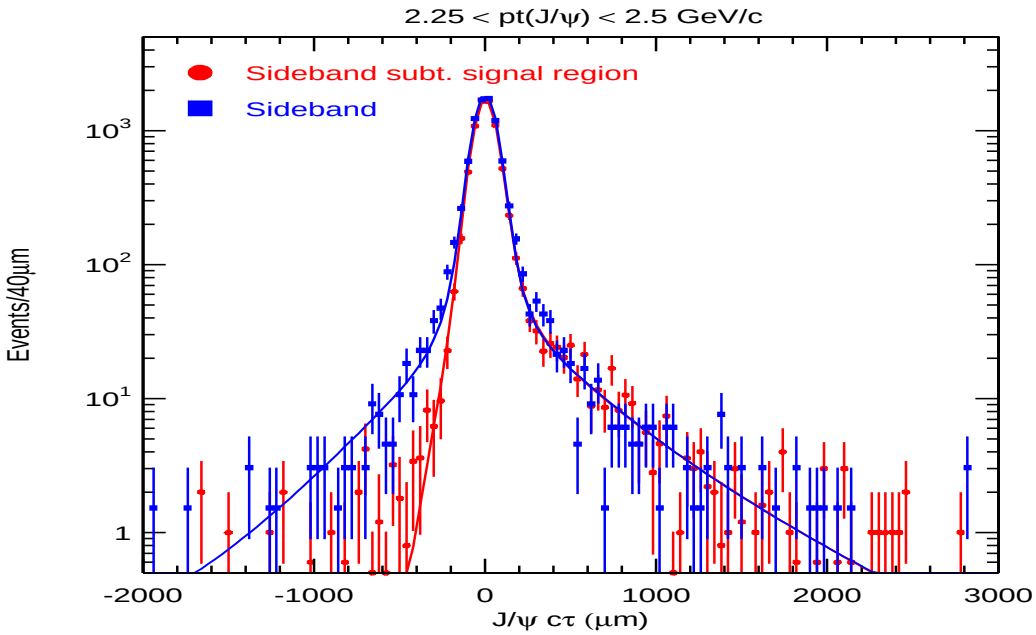

Figure 6.11: Background shape overlaid with the sideband subtracted signal shape and a preliminary fit. Symmetric tails in the background from fake J/ψs are not evident in the sideband subtracted mass signal region

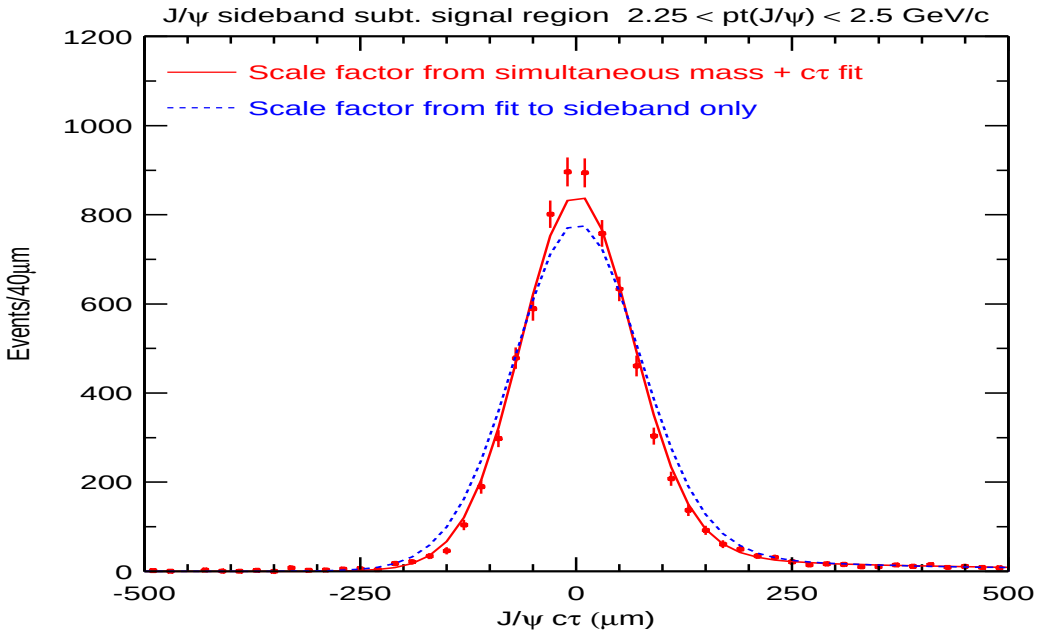

Figure 6.12: Using the same pseudo-$c\tau$ scale factor to fit the prompt component in signal and background and using different scale factors

vertices.

A scale factor is used to correct for inaccuracies in the $\sigma_{L_{xy}}$ value returned by the vertex fitter. The scale factor determines the width of the zero lifetime distributions and resolution function used in both the background and signal regions. Fits to the x distributions using the same scale factor for signal and background indicate that the zero lifetime component in the signal region is poorly described as shown in Figure 6.12. Therefore, in the final fit model, the signal and background shapes are decoupled in the fit and two different scale factors, $s_{\rm sig}$ and $s_{\rm bkg}$ are used.

The resolution function used for the central fit result is a double Gaussian with relative area, f_2, and relative width, μ, fixed to the values obtained from the fit in Figure 5.18. $f_2 = 8.5\%$ and $\mu = 2.1 \times \sigma'(x)$, where $\sigma'(x) = s \cdot \sigma(x)$ and s is the scale factor. The non-Gaussian tails that are not modeled in the resolution function will be treated as a systematic uncertainty.

6.4 Fit Results

Lifetime distributions in the data with the fits overlaid are presented in Appendix A for all J/ψ momentum bins between 2.0 and 17.0 GeV. The value of the B-lifetime extracted from the fits is shown in Figure 6.13. From a fit to a straight line, the average b hadron lifetime is measured to be $c\tau_{\rm b} = 455.3 \pm 4.9$ μm, which corresponds to

$$\tau_{\rm b} = 1.519 \pm 0.016 \text{ ps}.$$

This result, with statistical uncertainties only, is consistent with the average b hadron lifetime measured at CDF in Run I using events containing a J/$\psi \rightarrow$

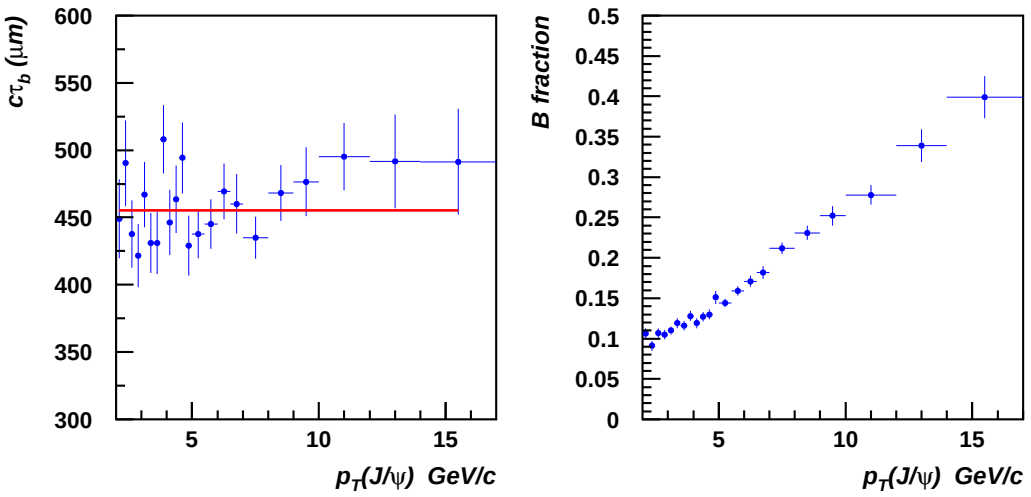

Figure 6.13: B-lifetime obtained using F factor convolutions in the fitting procedure with a straight line fit and the B-fraction versus $p_{\mathrm{T}}(\mathrm{J}/\psi)$

$\mu^+\mu^-$ decay in the final state: $\tau_{\mathrm{b}} = 1.533 \pm 0.015\ (\mathrm{stat})^{+0.035}_{-0.031}\ (\mathrm{syst})$ ps [59].

The values of the B-fraction returned from the fits are also shown in Figure 6.13 with statistical errors. The B-fractions increase linearly as a function of $p_{\mathrm{T}}(\mathrm{J}/\psi)$ from $\sim 10\%$ to $\sim 40\%$.

The fraction of background events in the fit, $1 - f_{\mathrm{sig}}$, and the signal and background scale factors in the different p_{T} bins are shown in Figure 6.14. The error scale factors measured in the signal and background regions differ by about 15% until $p_{\mathrm{T}}(\mathrm{J}/\psi) \approx 10$ GeV/c, with the scale factor extracted from the background region being the larger of the two. The scale factors increase as a function of p_{T} in the lower transverse momentum bins. For $p_{\mathrm{T}}(\mathrm{J}/\psi) > 10$ GeV/c both scale factors are the same within statistical uncertainties.

The lifetime background and invariant mass fit results in each p_{T} bin are shown in Figures 6.15 and 6.16. The fraction of the symmetric exponential in the background is approximately constant and is $\sim 7\%$ of the background.

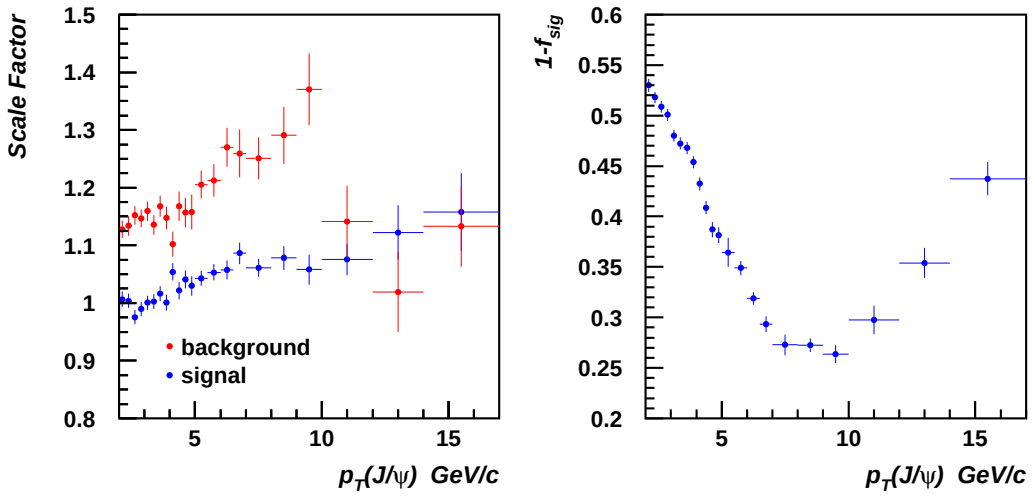

Figure 6.14: Lifetime uncertainty scale factors as a function of $p_{\mathrm{T}}(\mathrm{J}/\psi)$ (left). The fraction of background events in the fit (right).

The fraction of background events in the positive exponential tail increases with $p_{\mathrm{T}}(\mathrm{J}/\psi)$, varying from 4% to 25% in the range 4-14 GeV/c and is approximately constant at 2-3% from 2-4 GeV/c, indicating the presence of a long-lived physics signal in the background.

6.5 Systematic Uncertainties

This section describes and quantifies the various sources of systematic uncertainty in the analysis, the most important of which relate to the modelling of the resolution function used in the fits.

6.5.1 Quality of the Fits

The results of the fits for signal, background and invariant mass are histogramed into bins and compared to the data distributions. A Kolmogorov-

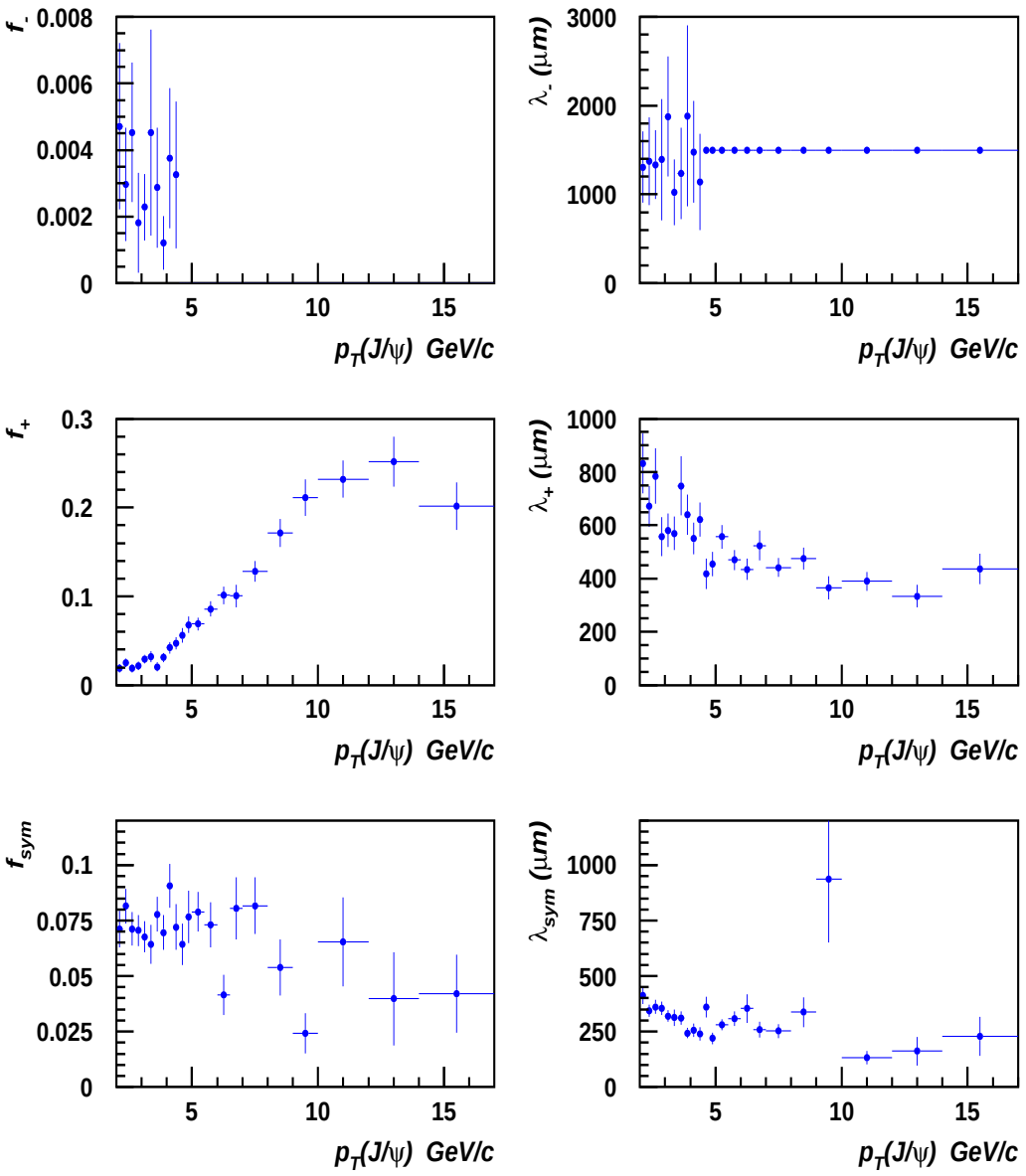

Figure 6.15: Lifetime background fit parameters as a function of $p_{\mathrm{T}}(\mathrm{J}/\psi)$ returned from the simultaneous J/ψ mass and lifetime fit

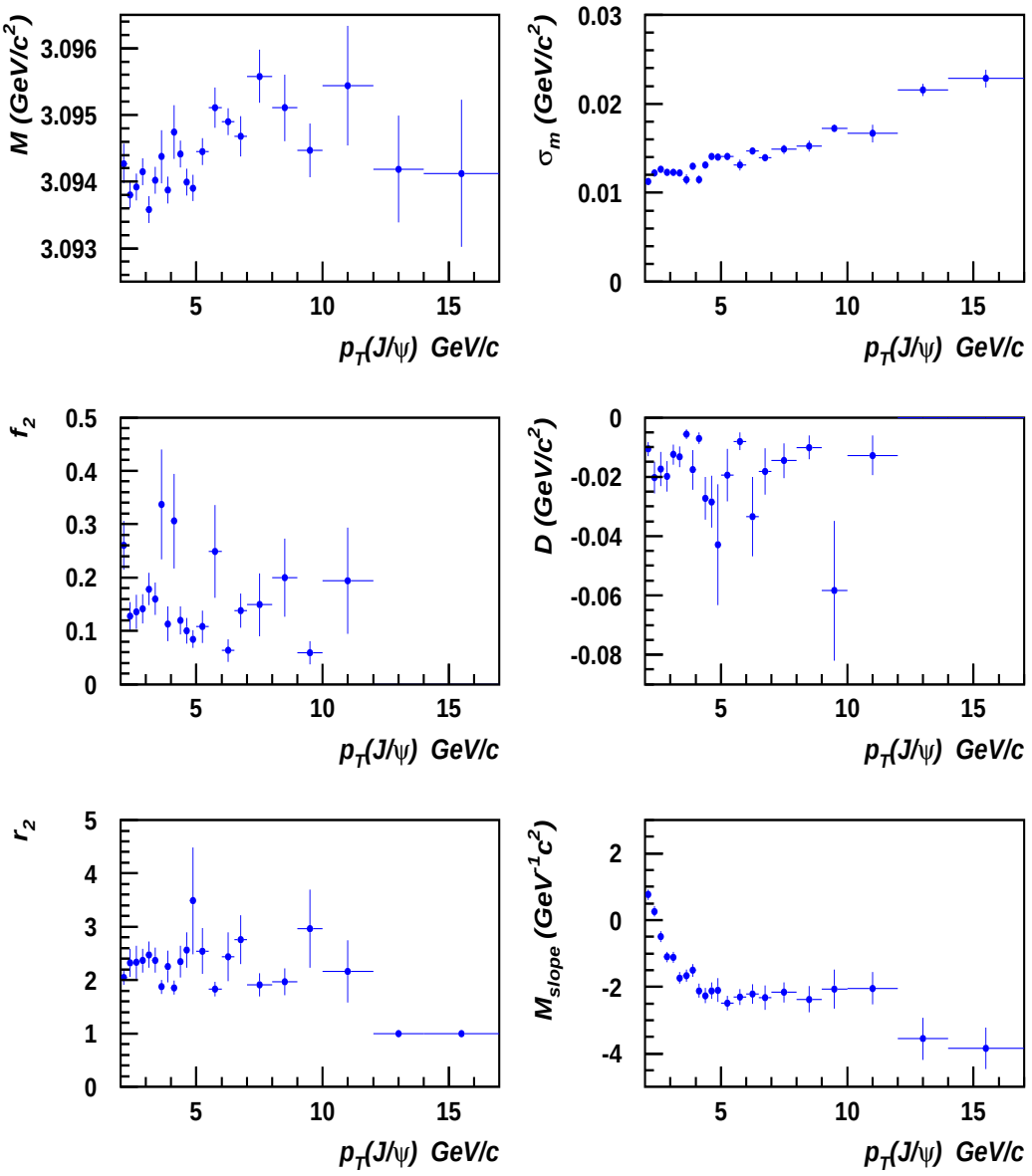

Figure 6.16: Invariant mass fit parameters as a function of $p_{\mathrm{T}}(\mathrm{J}/\psi)$ returned from the simultaneous J/ψ mass and lifetime fit

Distributions compared	K-S prob. mean Data	K-S prob. mean Monte Carlo
x dist. of all events in fit	0.66	0.71
x dist. in signal region	0.80	0.74
x dist. in sideband region	0.47	0.42
Invariant mass distribution	0.33	0.49

Table 6.3: Average K-S probability values returned from the comparison between data and fit in the bins from 2.0 to 5.0 GeV/c compared to the expected mean obtained from Monte Carlo studies.

Smirnov test [60] is used to compare the fit and data distributions in order to estimate the quality of the fit. The bin size chosen is 5 μm for the x distributions. The following comparisons are made:

- The total pseudo-lifetime distribution is compared to the data.
- The pseudo-lifetime distribution from the mass sideband subtracted signal region is compared to the J/ψ prompt signal and B $\rightarrow$ J/ψ X fit distributions.
- Sideband regions are compared to the background fit histogram.
- Invariant mass distributions for signal and background are compared.

The K-S probability values for each distribution listed above in the different transverse momentum bins are shown in Figure 6.17. To determine how well these values represent the quality of the fits, 80 statistically independent Monte Carlo samples were generated to match the x, $\sigma(x)$ and $M_{\mu\mu}$ distributions in data in the 2.0-2.25 GeV/c bin and fitted in the same way as the data. Table 6.3 summarises the mean of the K-S probability value in the 12 bins from 2.0 to 5.0 GeV/c and the mean value of the Monte Carlo K-S

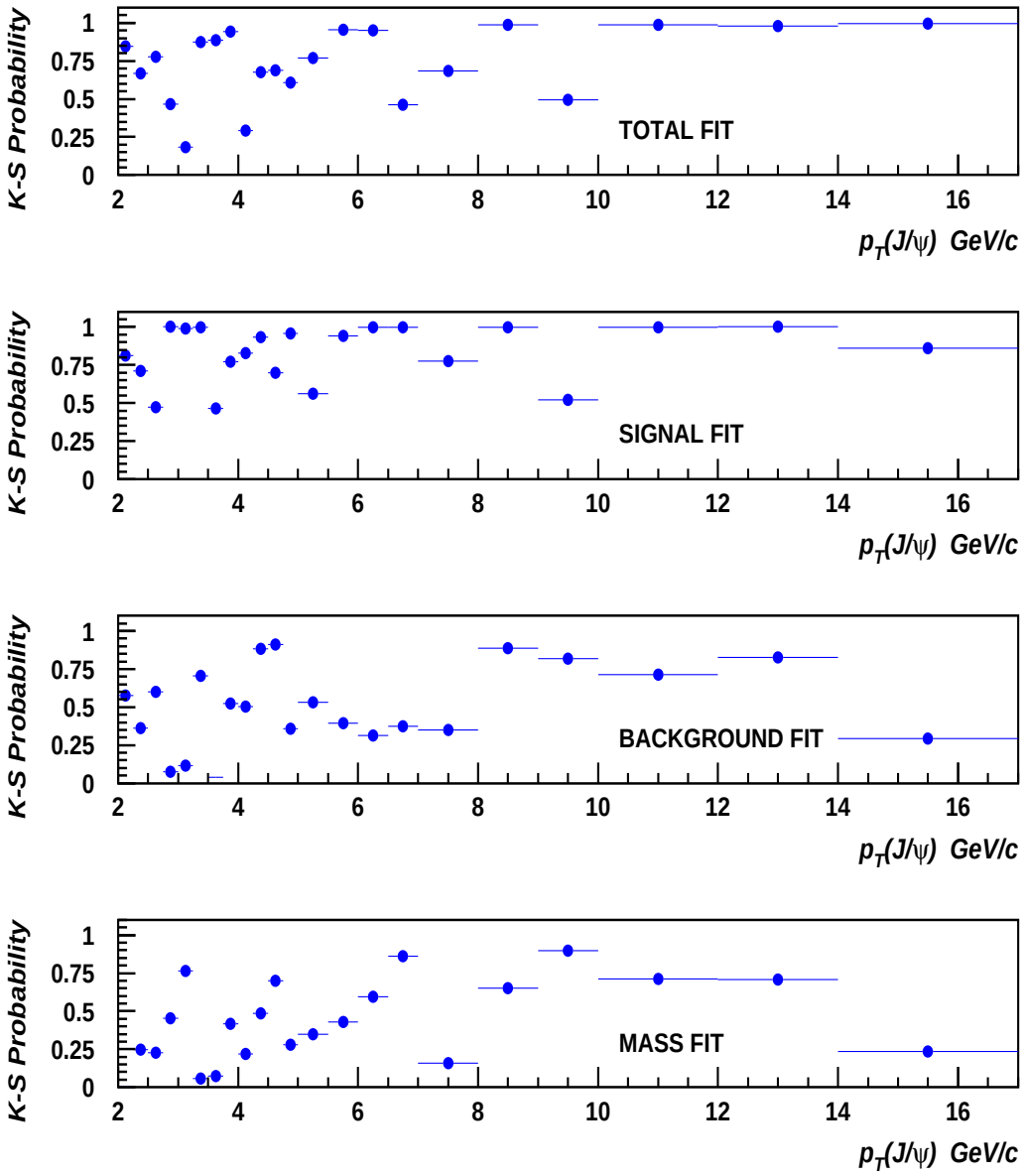

Figure 6.17: Probability values returned from a Kolmogorov-Smirnov comparison between the data distributions and the final fit distributions.

probability distribution. The means are in reasonable agreement (difference is less than 0.1) for all x distributions.

6.5.2 Biases Observed in Monte Carlo

Monte Carlo can also be used to determine the reliability of the B-fraction values obtained from the fit. The fit parameters in three representative transverse momentum ranges (2.0-2.25, 5.0-5.5, 10.0-12.0 GeV/c) are used to generate Monte Carlo events with the same invariant mass and pseudo-lifetime distributions as the data. The number of events generated is chosen to match the data with the same signal fraction $f_{\rm sig}$. The B-lifetime generated is smeared by the F-factor distribution for each bin to simulate the pseudo-lifetime distribution in the data. The uncertainty on the x measurement in the Monte Carlo events is taken from the data distributions of σ_x. In each test bin, 500 statistically independent Monte Carlo samples are generated. The (fit value $-$ generated value)/$\sigma_{\rm fit}$ distributions for the B-lifetime and B-fraction are shown in Figure 6.18 and the mean values and widths of the distributions are summarised in Table 6.4. A small bias in the B-fractions extracted is evident at low momentum and is included as a systematic un-

$p_{\rm T}({\rm J}/\psi)$ (GeV/c)	2.0-2.25	5.0-5.5	10.0-12.0
$c\tau$ mean	0.18 ± 0.05	-0.09 ± 0.05	-0.10 ± 0.05
$c\tau$ width	0.96 ± 0.03	1.00 ± 0.04	1.02 ± 0.03
$f_{\rm B}$ mean	0.24 ± 0.05	0.28 ± 0.04	0.05 ± 0.05
$f_{\rm B}$ width	1.04 ± 0.04	0.97 ± 0.04	0.94 ± 0.03

Table 6.4: Means and widths of the (fit value $-$ generated value)/$\sigma_{\rm fit}$ distributions for B-fractions and B-lifetimes in Figure 6.18

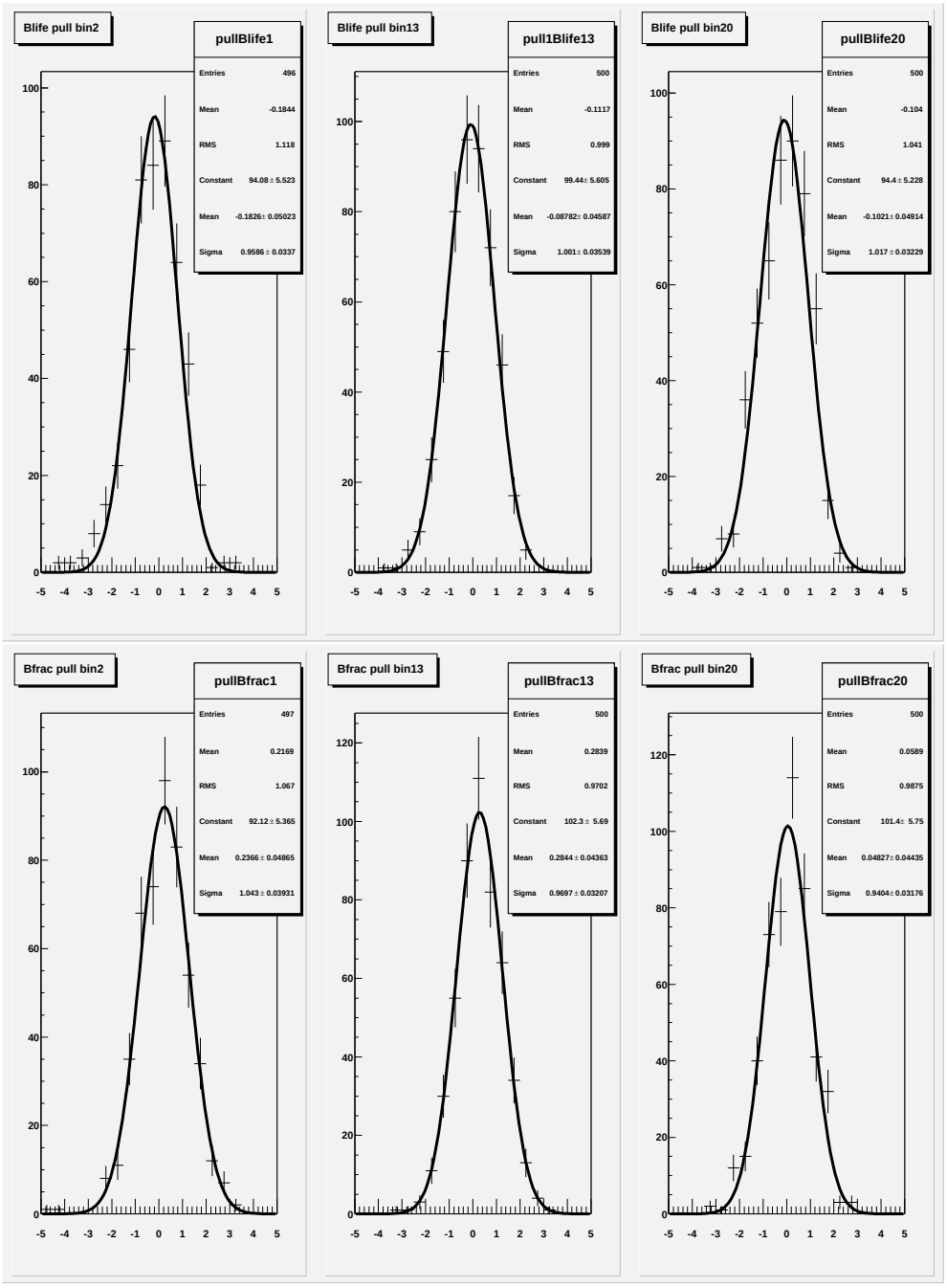

Figure 6.18: (fit value − generated value)/σ_{fit} distributions for B-lifetimes (top) and B-fractions (bottom) in a Monte Carlo sample generated to match the data distributions in three transverse momentum bins

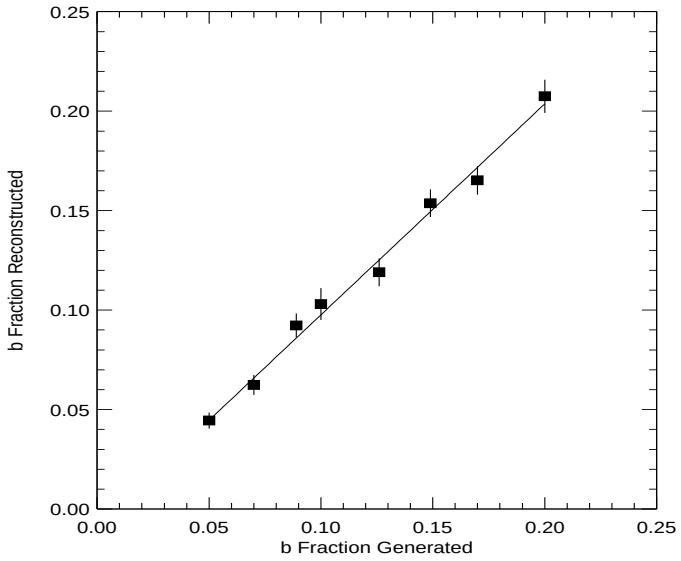

Figure 6.19: Reconstructed versus generated B-fractions in a Monte Carlo sample generated to match the data distributions in the 2.0-2.25 GeV/c bin

certainty. A smaller bias in the lifetime measurement at low momentum is also observed but it is consistent with zero for $p_{\rm T} > 5.0$ GeV/c.

Using the signal and background fit shape parameters extracted from the fit to the data in the 2.0-2.25 GeV/c bin, the B-fraction is varied and the fit performed. Figure 6.19 shows the generated versus reconstructed values of the B fractions. The reconstructed values are consistent with the generated values within statistical errors. A straight line fit to the reconstructed versus generated values has a slope of 1.060 ± 0.045 and $\chi^2/{\rm ndf} = 0.7$.

The systematic uncertainties assigned to the B-fraction measurement due to the biases observed in the Monte Carlo studies are $\sim 2\%$ for $p_{\rm T}({\rm J}/\psi) =$ 2.0-5.0 GeV/c, $\sim 1\%$ for $p_{\rm T}({\rm J}/\psi) =$ 5.0-12.0 GeV/c, and $\sim 0\%$ for $p_{\rm T}({\rm J}/\psi) =$ 12.0-17.0 GeV/c.

6.5.3 Varying the Resolution Function

A change is observed in the value of the B-fraction returned from the fit when the resolution function is modeled using: (i) a single Gaussian, (ii) a double Gaussian where all parameters are allowed to float, and (iii) the same scale factor to fit the zero lifetime component in signal and background. The variation in the shape of the resolution function in data using single and double Gaussians is illustrated in Figure 6.20.

To obtain a better estimate of the systematic uncertainty due to long-lived low statistics tails that are not included in the resolution function, the sign of x in the negative pseudo-lifetime tails, where $\sigma_x/x < -4$, is flipped so that these events would now appear under the positive long-lived $\mathrm{B} \to \mathrm{J}/\psi\ \mathrm{X}$ signal region as shown in Figure 6.21. No other variables are changed and the fit is performed using the same signal shapes. As expected, the values of the B-fractions increase. The systematic uncertainty due to the badly modeled long lived tails is therefore taken to be the negative of the fractional increase in the B-fractions observed when the reflection of the negative tails is performed.

The p_{T} dependent systematic uncertainties arising due to the modelling of the resolution function shape are illustrated in Figure 6.22. Since there are large correlations between the systematic uncertainties from the shape of the resolution function, the negative tails and the variation in the scale factor, the maximum positive and negative deviation from the central value of the B-fraction in Figure 6.22 is used as a conservative estimate of the systematic uncertainty on the resolution function parameterisation.

The fit was repeated with the background shape changed so that only

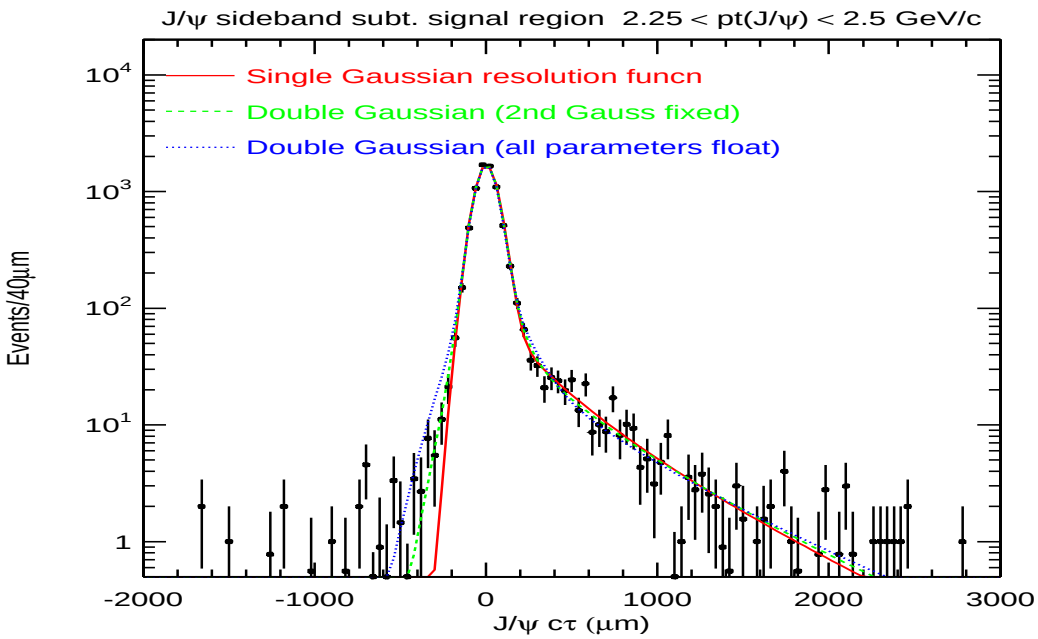

Figure 6.20: Varying resolution function shape in data using (i) single Gaussian, (ii) double Gaussian with the relative area and width of the 2nd Gaussian fixed (iii) double Gaussian with all parameters determined by the fit

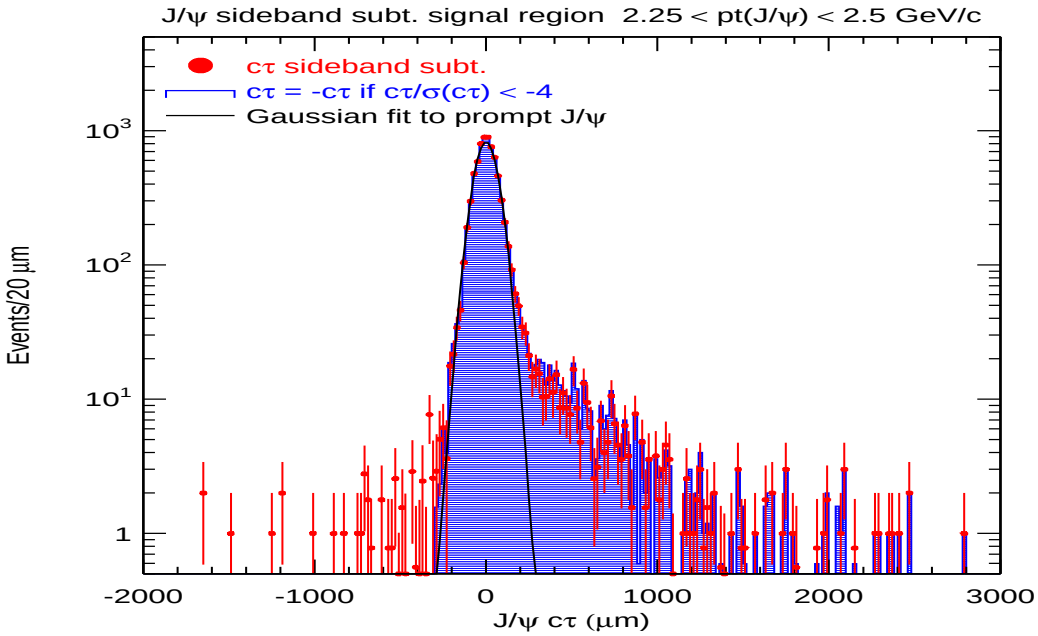

Figure 6.21: The sign of x in the negative tails, where $\sigma_x/x < -4$, is flipped so that these events now appear under the positive lifetime peak

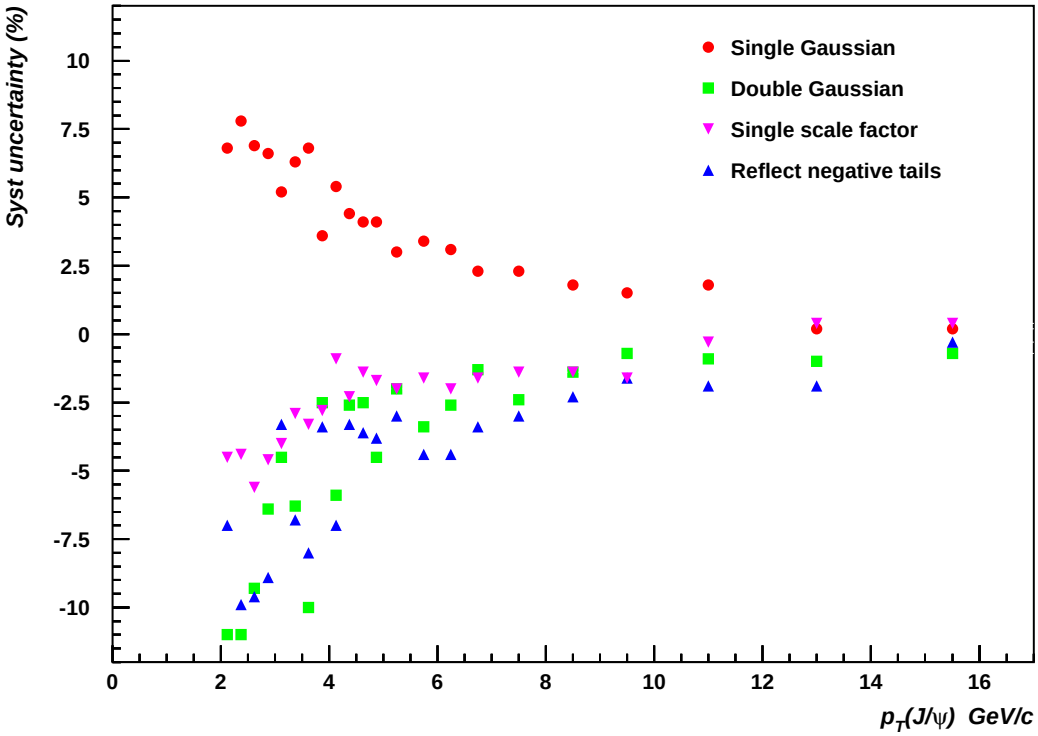

Figure 6.22: The p_{T} dependent J/ψ inclusive lifetime fit systematic uncertainties related to the modelling of the resolution function

a positive and negative exponential is used with no symmetric exponential. The differences in the B-fraction values extracted from the fit are small. The corresponding systematic uncertainties are illustrated in Figure 6.23.

6.5.4 Invariant Mass Line Shapes

Monte Carlo mass line shapes from a realistic SVXII Monte Carlo simulation of J/ψ events are used to fit the invariant mass distribution in the simultaneous mass and lifetime fit instead of a double Gaussian parameterisation. The data and Monte Carlo mass templates are shown in Figure 6.24. The Monte Carlo reproduces the data invariant mass distributions well in the lower mo-

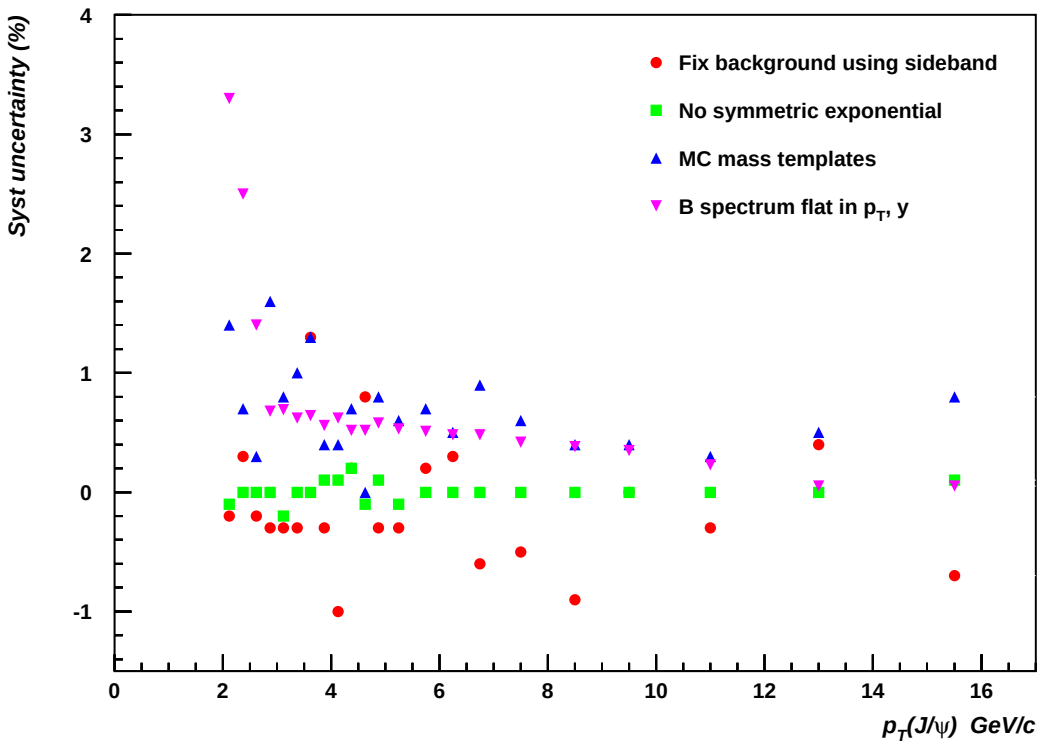

Figure 6.23: The p_{T} dependent J/ψ inclusive lifetime fit systematic uncertainties related to the modelling of the signal and background lifetime shapes, the invariant mass shape, and the modelling of the input b hadron spectrum used to determine the F-factor

mentum bins but underestimates the resolution in the higher momentum bins. Since the Monte Carlo models the contribution of the J/ψ radiative tail more accurately at small invariant masses than the double Gaussian shape used in the lifetime fit, this comparison is used to check whether any significant bias in the signal fraction has been introduced. The difference in the measured value of the B-fraction using the two different methods of modelling the invariant mass line shape is taken as a systematic uncertainty.

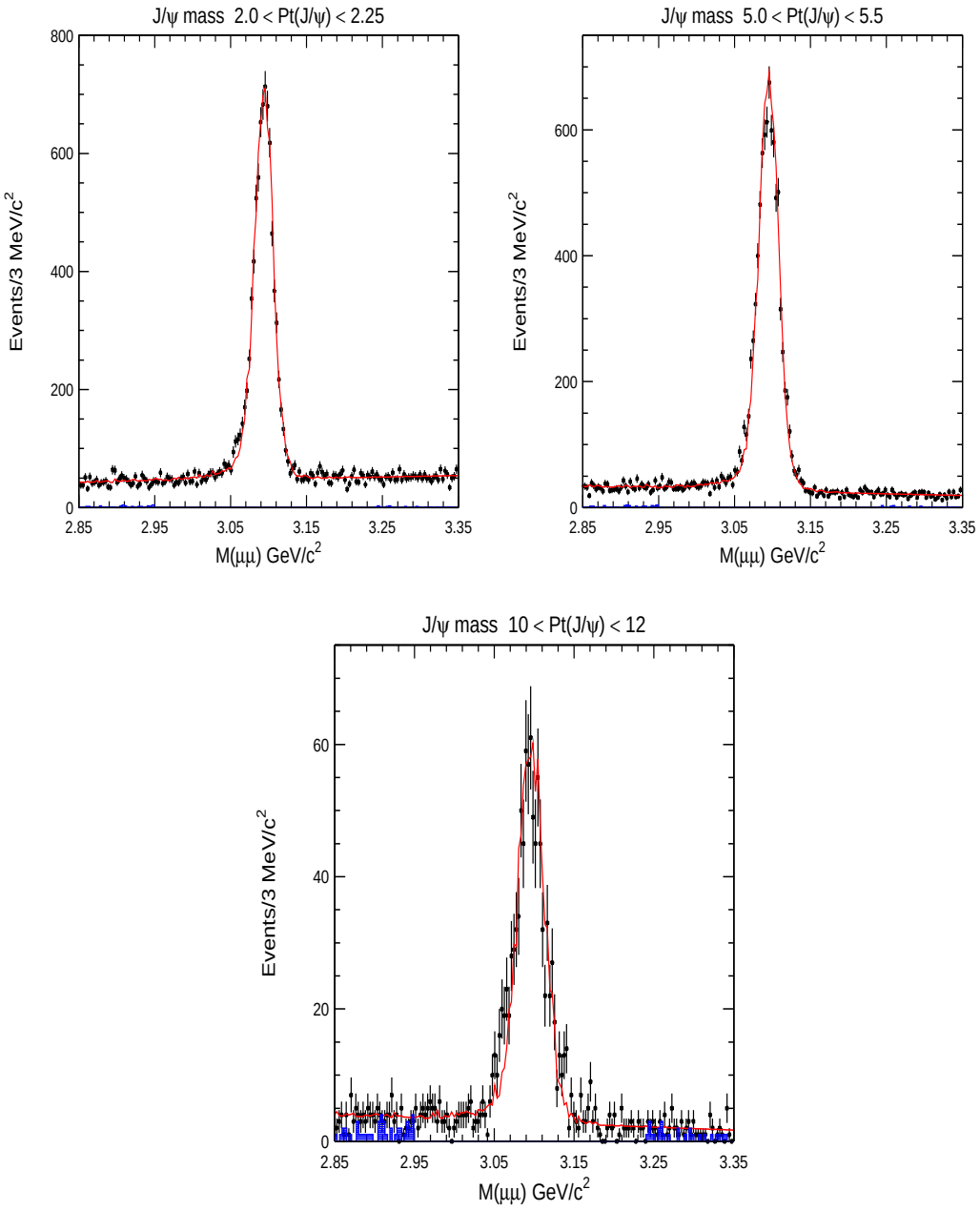

Figure 6.24: Monte Carlo invariant mass templates used to fit the data

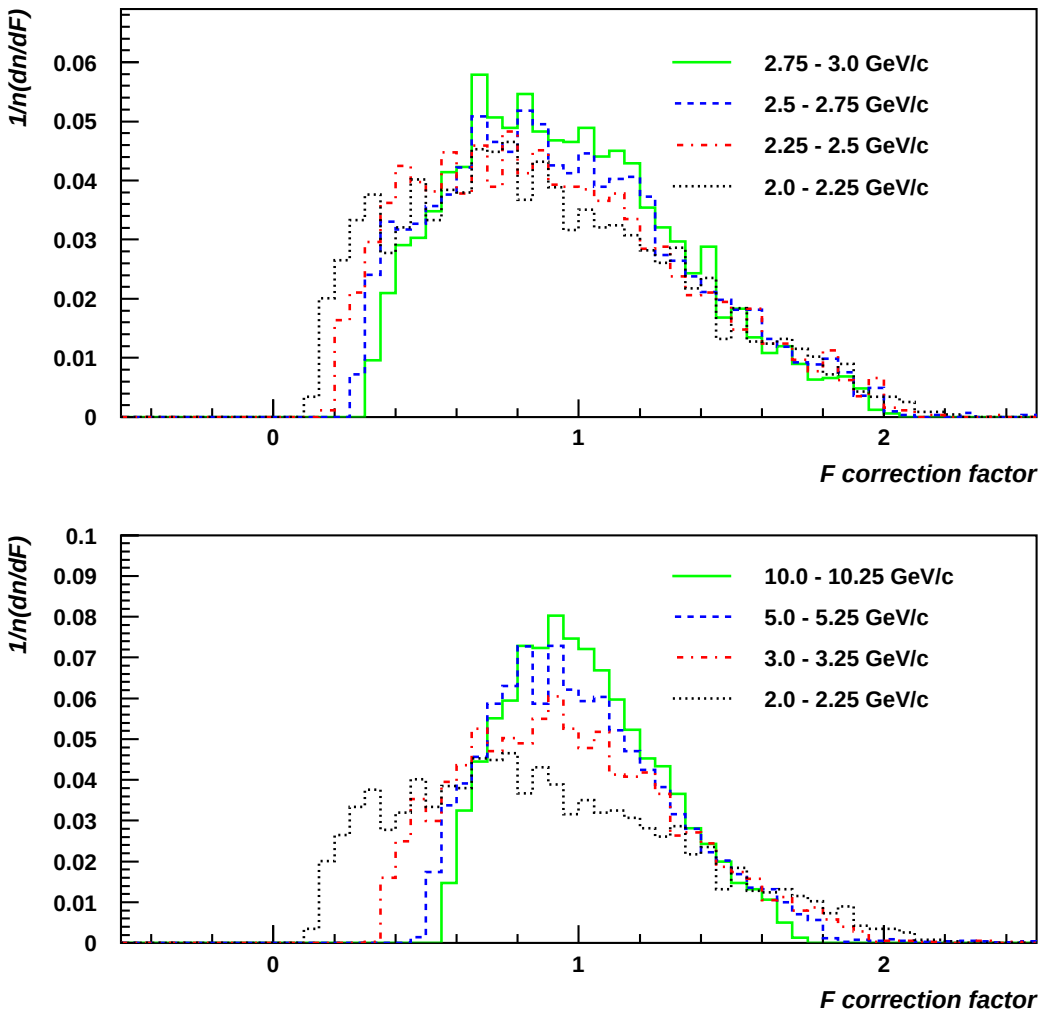

Figure 6.25: Momentum correction factor, F, distributions from $B \to J/\psi\ X$ decays generated using a b hadron spectrum flat in p_T and y

6.5.5 Monte Carlo Modelling of the B Spectrum

To investigate the dependency of the B-fractions extracted from the F-factor fit on the modelling of the b hadron spectrum used in the Monte Carlo, a flat distribution in p_T and rapidity of the b production spectrum used to generate the F-factors was produced and the fits were repeated. The F-factor distributions from the flat Monte Carlo are presented in Figure 6.25. The

change in the B-fraction extracted from the fit using the flat input spectrum is less than 0.7% for $p_{\mathrm{T}}(\mathrm{J}/\psi) > 2.75$ GeV/c. The flat input spectrum is unrealistic but is a useful tool for assessing the dependance of the final result on the Monte Carlo model. The p_{T}-dependant systematic effect is illustrated in Figure 6.23.

6.5.6 Comparing 2D and 3D SVXII Hit Information

L_{xy} can be measured using 3D (r-ϕ + r-z) or 2D (r-ϕ only) silicon hit information. More events are accepted when only 2D hit information is required but the signal-to-background ratio is worse. The mean and RMS of the difference between 2D and 3D L_{xy} measurements are plotted in Figure 6.26 as a function of $p_{\mathrm{T}}(\mathrm{J}/\psi)$. The mean of the distribution is not observed to deviate significantly from zero. The B-lifetime is expected to be sensitive to biases in SVXII, so the difference in the lifetime measured using 2D and 3D silicon hits is shown in each $p_{\mathrm{T}}(\mathrm{J}/\psi)$ bin in Figure 6.27. The observed fluctuations in the lifetime are consistent with statistical uncertainties, so there is no evidence of a bias being introduced by using 3D silicon hits.

6.5.7 Detector Bias and Selection Criteria

The systematic uncertainties on the B-fraction that could be introduced by detector biases due to the requirements on SVXII track quality were discussed in detail in Chapter 5. The L_{xy} asymmetry is equivalent to 77% of the B-fraction measured for $p_{\mathrm{T}} > 2$ GeV/c. Therefore, since any bias in the measurement of L_{xy} due to SVXII coverage can lead to a bias in the B-fraction measurement, the L_{xy} asymmetry was investigated as a function of

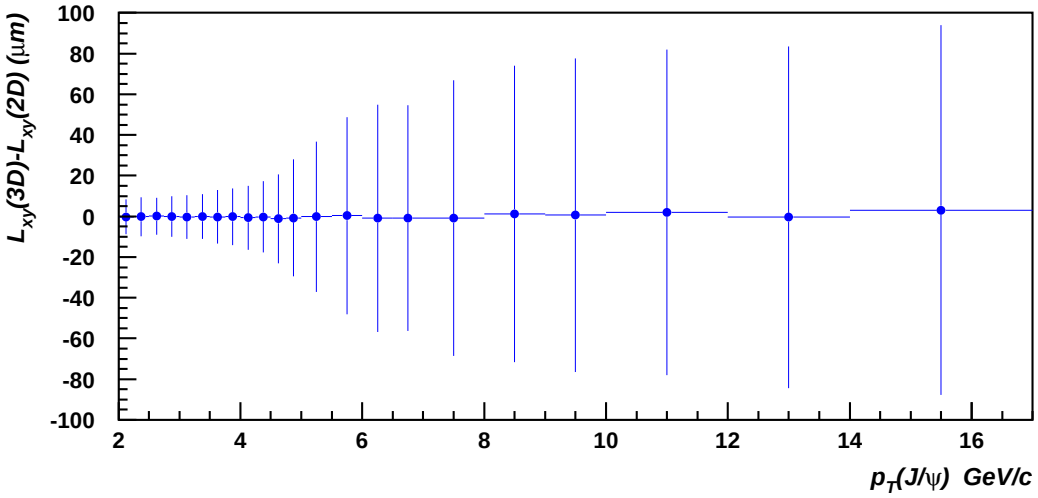

Figure 6.26: The difference in L_{xy} values calculated using 2D and 3D silicon hit information

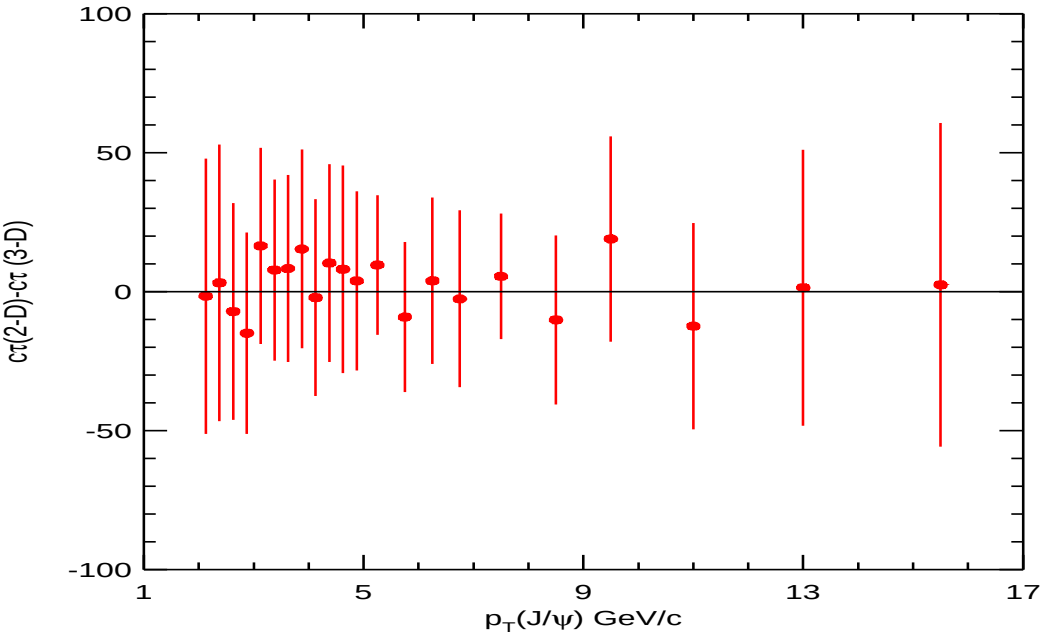

Figure 6.27: The difference in B-lifetime values calculated using 2D and 3D silicon hit information

z, ϕ_0 and $\eta_{J/\psi}$. Fluctuations in the L_{xy} asymmetry that are larger than expected from statistical uncertainties were observed and a corresponding systematic uncertainty of $+6\%$, -3% is assigned.

6.6 B-fraction Results

The value of the B-fraction from the final fit models with statistical and systematic uncertainties is listed in Table 6.5 and the distribution is shown

$p_T(J/\psi)$ GeV/c	Run II B-Fraction	Run I B-Fraction
$2.0 - 2.25$	$0.106 \pm 0.007(\text{stat})^{+0.007}_{-0.012}(\text{syst})$	
$2.25 - 2.5$	$0.091 \pm 0.006^{+0.007}_{-0.010}$	
$2.5 - 2.75$	$0.107 \pm 0.006^{+0.007}_{-0.010}$	
$2.75 - 3.0$	$0.105 \pm 0.006^{+0.007}_{-0.007}$	
$3.0 - 3.25$	$0.110 \pm 0.005^{+0.006}_{-0.005}$	
$3.25 - 3.5$	$0.119 \pm 0.006^{+0.006}_{-0.007}$	
$3.5 - 3.75$	$0.116 \pm 0.006^{+0.008}_{-0.012}$	
$3.75 - 4.0$	$0.128 \pm 0.006^{+0.005}_{-0.004}$	
$4.0 - 4.25$	$0.119 \pm 0.006^{+0.007}_{-0.007}$	
$4.25 - 4.5$	$0.127 \pm 0.006^{+0.006}_{-0.004}$	
$4.5 - 4.75$	$0.130 \pm 0.006^{+0.006}_{-0.004}$	
$4.75 - 5.0$	$0.151 \pm 0.008^{+0.006}_{-0.007}$	
$5.0 - 5.5$	$0.144 \pm 0.005^{+0.005}_{-0.004}$	$0.148 \pm 0.005(\text{stat})$
$5.5 - 6.0$	$0.159 \pm 0.006^{+0.006}_{-0.006}$	0.165 ± 0.005
$6.0 - 6.5$	$0.171 \pm 0.007^{+0.006}_{-0.005}$	0.178 ± 0.006
$6.5 - 7.0$	$0.182 \pm 0.008^{+0.005}_{-0.004}$	0.191 ± 0.006
$7.0 - 8.0$	$0.212 \pm 0.007^{+0.005}_{-0.006}$	0.207 ± 0.005
$8.0 - 9.0$	$0.231 \pm 0.009^{+0.005}_{-0.005}$	0.232 ± 0.007
$9.0 - 10.0$	$0.252 \pm 0.012^{+0.005}_{-0.003}$	0.236 ± 0.010
$10.0 - 12.0$	$0.278 \pm 0.012^{+0.004}_{-0.004}$	0.300 ± 0.010
$12.0 - 14.0$	$0.339 \pm 0.020^{+0.004}_{-0.005}$	0.317 ± 0.017
$14.0 - 17.0$	$0.399 \pm 0.026^{+0.003}_{-0.004}$	0.387 ± 0.024

Table 6.5: The fraction of inclusive J/ψ's from b hadron decays

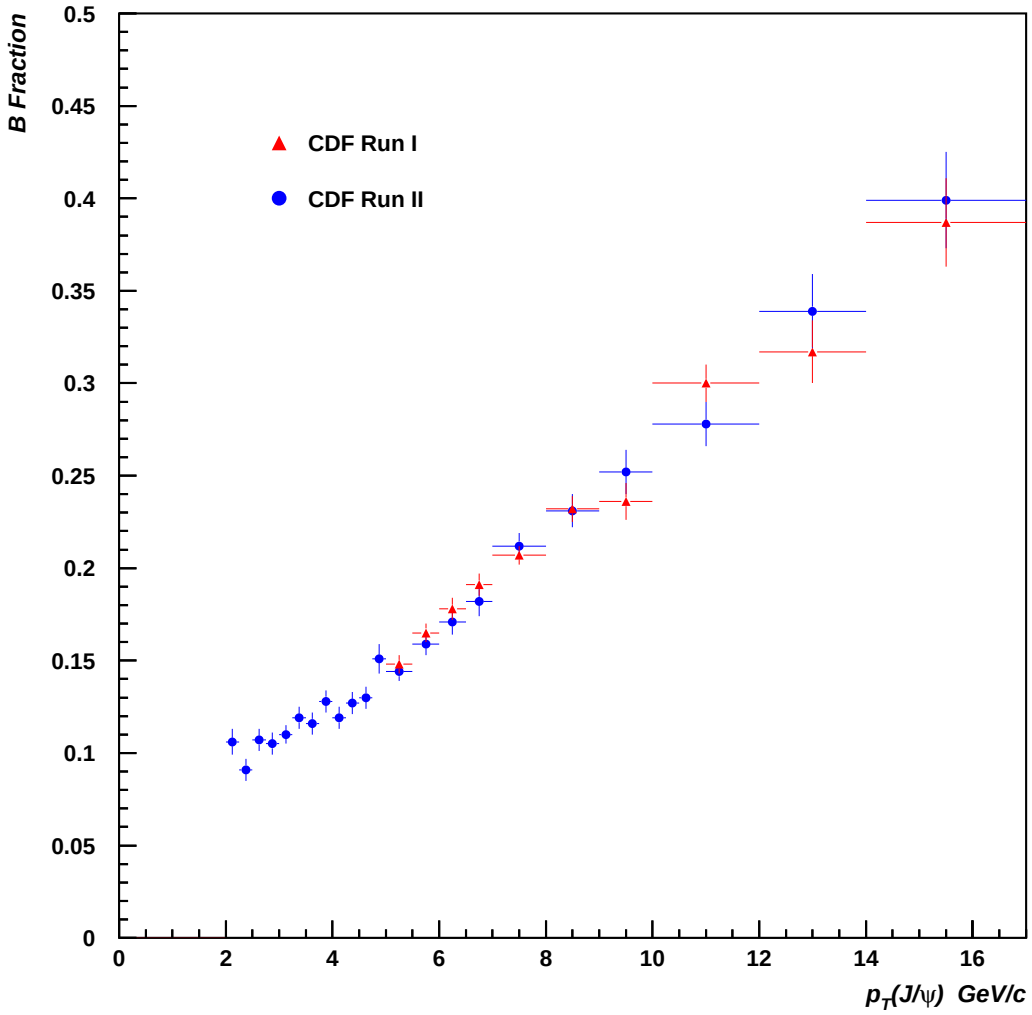

Figure 6.28: Fraction of J/ψ events from b hadrons at CDF Runs I & II

in Figure 6.28. Results from CDF Run I are also listed. The Run II measurement has been extended down to J/ψ transverse momenta of 2.0 GeV/c. Both Run II and Run I measurements of the B-fractions are in good agreement for $p_{\mathrm{T}} > 5$ GeV/c. The statistical accuracy of the Run II measurements in the high transverse momentum bins is similar to Run I.

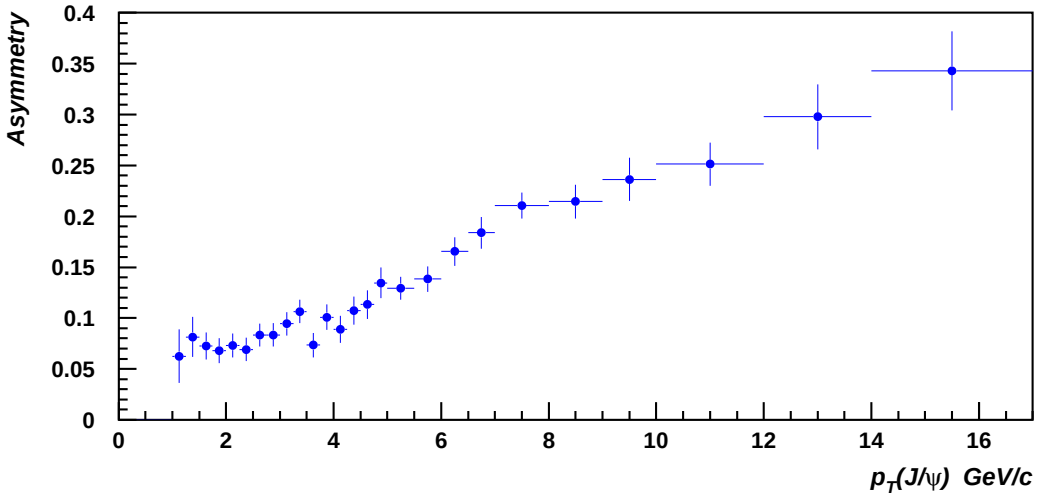

Figure 6.29: L_{xy} asymmetry as a function of $p_{\mathrm{T}}(\mathrm{J}/\psi)$

The B-fraction is proportional to the L_{xy} asymmetry:

$$f_{\mathrm{B}} = \frac{A_{L_{xy}}}{c(\sigma_{L_{xy}})}.$$

Therefore, as a simple cross-check, the measurement of the L_{xy} asymmetry vs $p_{\mathrm{T}}(\mathrm{J}/\psi)$ shown in Figure 6.29 can be used to calculate the B-fraction using a simple counting method:

$$\#\text{ b hadrons} = \frac{(\#\ \mathrm{J}/\psi\text{'s with } L_{xy} > 0) - (\#\ \mathrm{J}/\psi\text{'s with } L_{xy} < 0)}{\text{Efficiency from Monte Carlo}}.$$

The prompt contribution is symmetric about zero so it cancels out in the numerator regardless of what the resolution function shape is. The efficiency is extracted using L_{xy} from Monte Carlo B $\rightarrow$ J/ψ X. The generated L_{xy} of the J/ψ is smeared with a single Gaussian of width equal to the value of $\sigma_{L_{xy}}$ measured in the data as a function of $p_{\mathrm{T}}(\mathrm{J}/\psi)$. The correction factor $c(\sigma_{L_{xy}})$ is the L_{xy} asymmetry of J/ψ's from b hadrons. The values obtained from Monte Carlo vary from 0.63 to 0.94 over the range 1.0-17.0 GeV/c. In

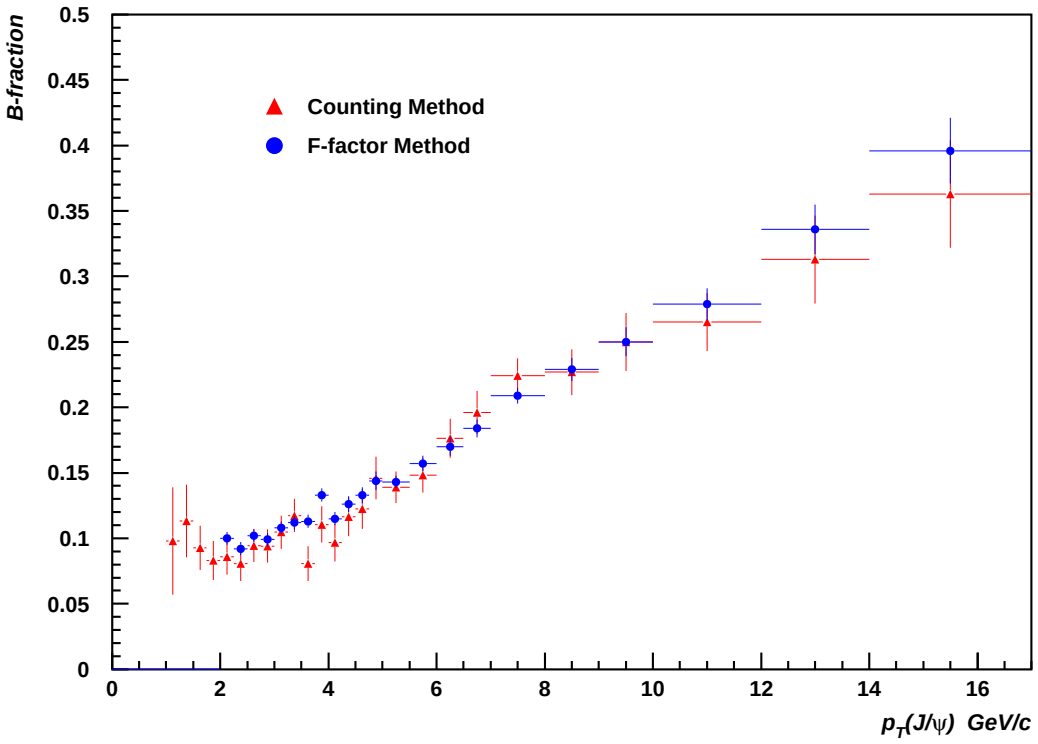

Figure 6.30: Comparing the fraction of J/ψ events from b hadrons measured using the standard F-factor method and a simple counting method

this particular method the dependency on the modelling of the resolution function shape is smaller than in the fitting method, but the statistical uncertainty is greater. Figure 6.30 compares the B-fraction values obtained using the F-factor and counting methods and both agree well within statistical fluctuations. Since there is no fitting procedure involved, the counting method allows B-fractions to be extracted below 2.0 GeV/c.

6.7 The Inclusive $B \to J/\psi\ X$ Cross-section

The B-fractions can be now multiplied by the results of the inclusive J/ψ cross-section analysis [50] to obtain the $B \to J/\psi\ X$ inclusive cross-section for $p_T(J/\psi) > 2.0$ GeV/c and $|y_{J/\psi}| < 0.6$:

$$\frac{d\sigma(J/\psi, B)}{dp_T(J/\psi)} = f_B \frac{d\sigma(J/\psi)}{dp_T(J/\psi)}.$$

Table 6.6 summarises the systematic uncertainties on the b-hadron inclusive cross-section. The 6.7% fully correlated systematic uncertainty from the J/ψ cross-section measurement accounts for uncertainties arising from luminosity measurements, track reconstruction efficiency in the software, data quality, and the Level 1 trigger efficiency. The J/ψ and $B \to J/\psi\ X$ inclusive cross-section results with statistical and p_T dependent systematic uncertainties are both listed in Table 6.7.

The differential cross-section with all statistical and systematic errors added is plotted in Figure 6.31. The comparison with theory [15] and Run I results are also shown. The theory curves only extend down as far as $p_T(J/\psi) = 5$ GeV/c as this is the limit below which the theoretical predictions become unreliable. The measured cross-section is consistent with both the

Source of Uncertainty	Value
B-fraction fit model	$< 2\%$ (p_T dependent)
Resolution function shape	1-12% (p_T dependent)
Mass fit model	$< 2\%$ (p_T dependent)
b hadron Monte Carlo spectrum	$< 3.5\%$ (p_T dependent)
SVXII selection	$+6\%$, -3% (p_T dependent)
Inclusive J/ψ cross-section	6-15% (p_T dependent)
Fully correlated (from inclusive)	$\pm 6.7\%$

Table 6.6: Summary of systematic uncertainties

$p_{\mathrm{T}}(\mathrm{J}/\psi)$ (GeV/c)	$\frac{d\sigma}{dp_{\mathrm{T}}} \cdot \mathcal{B}$ (nb/GeV/c)	$\frac{d\sigma}{dp_{\mathrm{T}}} \cdot \mathcal{B}$ (nb/GeV/c)
	J/ψ inclusive	$\mathrm{B} \to \mathrm{J}/\psi\ \mathrm{X}$
$2.0 - 2.25$	$69.4 \pm 0.8^{+8.6}_{-6.8}$	$7.36 \pm 0.49^{+1.03}_{-1.10}$
$2.25 - 2.5$	$66.0 \pm 1.0^{+7.8}_{-5.9}$	$6.01 \pm 0.41^{+0.85}_{-0.85}$
$2.5 - 2.75$	$57.2 \pm 0.9^{+6.4}_{-4.9}$	$6.12 \pm 0.36^{+0.79}_{-0.78}$
$2.75 - 3.0$	$51.9 \pm 0.8^{+5.5}_{-4.3}$	$5.45 \pm 0.32^{+0.68}_{-0.58}$
$3.0 - 3.25$	$43.3 \pm 0.7^{+4.4}_{-3.4}$	$4.76 \pm 0.23^{+0.55}_{-0.43}$
$3.25 - 3.5$	$37.5 \pm 0.8^{+3.7}_{-2.9}$	$4.46 \pm 0.24^{+0.49}_{-0.43}$
$3.5 - 3.75$	$30.8 \pm 0.5^{+2.9}_{-2.3}$	$3.57 \pm 0.19^{+0.42}_{-0.46}$
$3.75 - 4.0$	$26.5 \pm 0.4^{+2.4}_{-1.9}$	$3.39 \pm 0.17^{+0.33}_{-0.27}$
$4.0 - 4.25$	$22.9 \pm 0.4^{+2.1}_{-1.7}$	$2.73 \pm 0.15^{+0.30}_{-0.26}$
$4.25 - 4.5$	$18.5 \pm 0.3^{+1.7}_{-1.4}$	$2.35 \pm 0.12^{+0.24}_{-0.19}$
$4.5 - 4.75$	$16.8 \pm 0.3^{+1.5}_{-1.2}$	$2.18 \pm 0.11^{+0.22}_{-0.17}$
$4.75 - 5.0$	$13.3 \pm 0.3^{+1.1}_{-0.9}$	$2.01 \pm 0.12^{+0.18}_{-0.16}$
$5.0 - 5.5$	$10.4 \pm 0.15^{+0.9}_{-0.71}$	$1.50 \pm 0.06^{+0.14}_{-0.11}$
$5.5 - 6.0$	$7.32 \pm 0.12^{+0.58}_{-0.48}$	$1.16 \pm 0.05^{+0.10}_{-0.09}$
$6.0 - 6.5$	$5.21 \pm 0.09^{+0.39}_{-0.33}$	$0.891 \pm 0.040^{+0.074}_{-0.062}$
$6.5 - 7.0$	$3.62 \pm 0.07^{+0.26}_{-0.22}$	$0.659 \pm 0.032^{+0.051}_{-0.043}$
$7.0 - 8.0$	$2.36 \pm 0.04^{+0.16}_{-0.14}$	$0.500 \pm 0.019^{+0.036}_{-0.033}$
$8.0 - 9.0$	$1.24 \pm 0.03^{+0.08}_{-0.07}$	$0.286 \pm 0.013^{+0.019}_{-0.017}$
$9.0 - 10.0$	$0.672 \pm 0.018^{+0.077}_{-0.074}$	$0.169 \pm 0.009^{+0.020}_{-0.019}$
$10.0 - 12.0$	$0.320 \pm 0.009^{+0.051}_{-0.050}$	$0.089 \pm 0.005^{+0.014}_{-0.014}$
$12.0 - 14.0$	$0.146 \pm 0.006^{+0.023}_{-0.023}$	$0.049 \pm 0.004^{+0.008}_{-0.008}$
$14.0 - 17.0$	$0.072 \pm 0.004^{+0.014}_{-0.011}$	$0.029 \pm 0.002^{+0.006}_{-0.004}$

Table 6.7: Run II inclusive b hadron differential cross-section with statistical and p_{T} dependent systematic uncertainties. For each measurement, the first uncertainty is statistical and the second is the systematic

Run I results and the MRST theory prediction [57] throughout their common transverse momentum range, with the exception of the final 14.0-17.0 GeV/c bin where statistics are limited.

The integrated $\mathrm{B} \to \mathrm{J}/\psi\ \mathrm{X}$ cross-section is the integral of the results plotted in Figure 6.31. It is measured to be

$$\sigma(\mathrm{J}/\psi, \mathrm{B}) \cdot \mathcal{B}(\mathrm{J}/\psi \to \mu\mu) = 16.02 \pm 0.24\ (\mathrm{stat})^{+2.26}_{-2.20}\ (\mathrm{syst})\ \mathrm{nb}$$

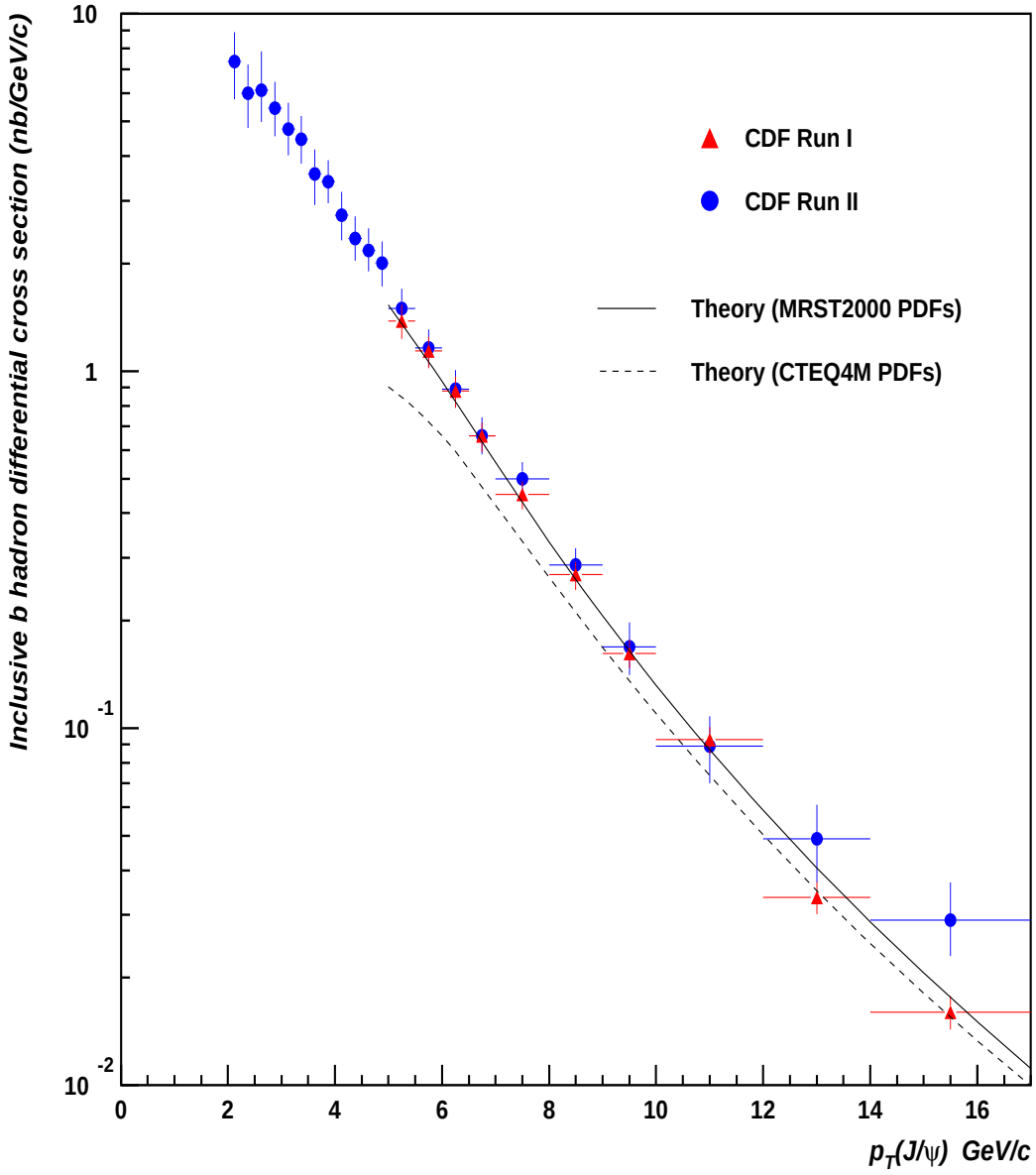

Figure 6.31: CDF Run II differential cross-section for B $\rightarrow$ J/ψ X as a function of p_{T}(J/ψ) compared with Run I results and theory predictions [15, 57]

where

$$\sigma(\mathrm{J}/\psi, \mathrm{B}) = \sigma(\mathrm{p\bar{p}} \to \mathrm{BX}, p_{\mathrm{T}}(\mathrm{J}/\psi) > 2\ \mathrm{GeV}/c, |y_{\mathrm{J}/\psi}| < 0.6) \cdot \mathcal{B}(\mathrm{B} \to \mathrm{J}/\psi\ \mathrm{X}).$$

The uncorrelated statistical errors are added in quadrature:

$$\varepsilon_{\mathrm{tot}}^{\mathrm{stat}} = \sqrt{\sum_{i=1}^{n} \left(\varepsilon_i^{\mathrm{stat}} \cdot \omega_i\right)^2}$$

where n is the total number of J/ψ transverse momentum bins, $\varepsilon_i^{\mathrm{stat}}$ is the statistical uncertainty on the measurement in the i^{th} p_{T} bin, and ω_i is the width of the i^{th} bin measured in GeV/c. The p_{T} dependent systematic errors are added in quadrature with the fully correlated uncertainty of 6.7%:

$$\varepsilon_{\mathrm{tot}}^{\mathrm{syst}} = \sqrt{\sum_{i=1}^{n} \left[\left(\varepsilon_i^{\mathrm{syst}}\right)^2 + (0.067 d\sigma_i)^2\right]}$$

where $d\sigma_i$ is the differential cross-section in the i^{th} bin, and $\varepsilon_i^{\mathrm{syst}}$ is the systematic uncertainty on the measurement in the i^{th} bin independent of the correlated systematic uncertainty of 6.7%.

In Run I the analysis was limited to $p_{\mathrm{T}}(\mathrm{J}/\psi) > 5.0$ GeV/c. Therefore, in order to accurately compare the new measurement to the Run I results, the integrated cross-section is recalculated above 5 GeV/c:

$$\sigma(\mathrm{J}/\psi, \mathrm{B}) \cdot \mathcal{B}(\mathrm{J}/\psi \to \mu\mu)_{\mathrm{RunI}} = 3.23 \pm 0.05\ (\mathrm{stat})^{+0.28}_{-0.30}\ (\mathrm{syst})\ \mathrm{nb}$$

$$\sigma(\mathrm{J}/\psi, \mathrm{B}) \cdot \mathcal{B}(\mathrm{J}/\psi \to \mu\mu)_{\mathrm{RunII}} = 3.42 \pm 0.05\ (\mathrm{stat})^{+0.25}_{-0.23}\ (\mathrm{syst})\ \mathrm{nb}$$

The Run II cross-sections are expected to be approximately 9% higher than the Run I measurements due to the centre-of-mass energy in Run II being 1.96 TeV compared with only 1.8 TeV for Run I. Taking this into account, the Run I cross-section would be approximately 3.52 nb if measured at the same energy as Run II. The new measurement at CDF Run II is consistent with the result obtained in Run I within the quoted uncertainties.

6.8 Conclusions

The inclusive B $\rightarrow$ J/ψ X cross-section in p$\bar{\text{p}}$ interactions at a centre-of-mass energy $\sqrt{s} = 1.96$ TeV/c^2 is measured using 36 pb^{-1} of the J/ψ data sample collected by CDF between February and October 2002. The differential cross section for inclusive B $\rightarrow$ J/ψ X events is obtained by combining the B-fraction result with a measurement of the J/ψ differential cross-section.

The integrated B $\rightarrow$ J/ψ X cross-section for $p_{\text{T}}(\text{J}/\psi) > 2.0$ GeV/c is

$$\sigma(\text{J}/\psi, \text{B}) \cdot \mathcal{B}(\text{J}/\psi \rightarrow \mu\mu) = 16.02 \pm 0.24 \text{ (stat)}^{+2.26}_{-2.20} \text{ (syst) nb.}$$

Above 5.0 GeV/c, the measured cross-section is found to agree very well with previous results obtained in the same $p_{\text{T}}(\text{J}/\psi)$ range at CDF Run I. By extending the analysis to below 5.0 GeV/c, much more of the cross-section has now been observed to provide a far more accurate measurement.

The b hadron decay imparts up to about 1.7 GeV/c of momentum to the J/ψ, so once a measurement can be made below this value, some sensitivity is gained to b hadrons near $p_{\text{T}}(B) = 0$. Techniques are currently being refined to push the $p_{\text{T}}(\text{J}/\psi)$ threshold even lower. Monte Carlo generated X distributions for all J/ψ transverse momentum ranges will be used to separate the B $\rightarrow$ J/ψ X events from the prompt J/ψ X distributions in the signal region for $p_{\text{T}}(\text{J}/\psi) > 1.0$ GeV/c. At the same time, improvements in the method of extracting the shape of the resolution function will bring about a reduction in one of the dominant systematic effects.

CDF Run II aims to record up to 4 fb$^-$1 of data by 2009. The greatly increased statistics will allow the b hadron cross-sections to be measured more precisely than ever before, particularly in the high J/ψ transverse momentum range where data is very limited.

Appendix A

Fit Distributions

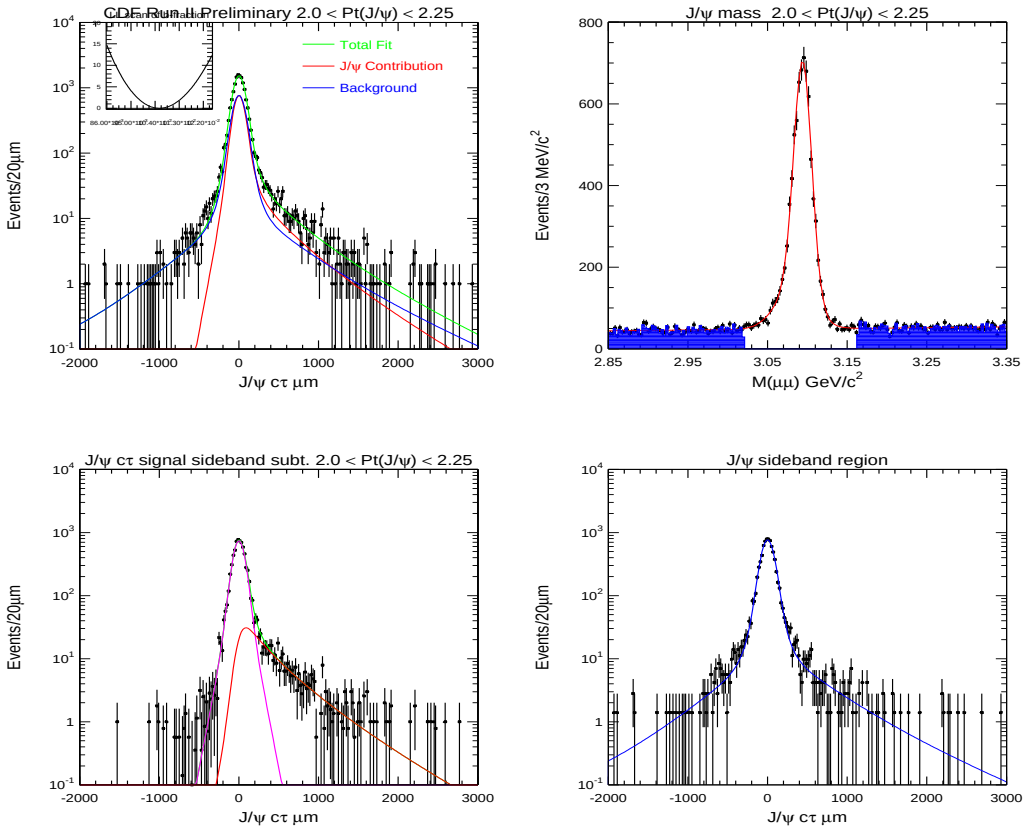

Figure A.1: B lifetime fit results projected onto J/ψ invariant mass and decay length distributions in p_{T} bin 2.0-2.25 GeV/c

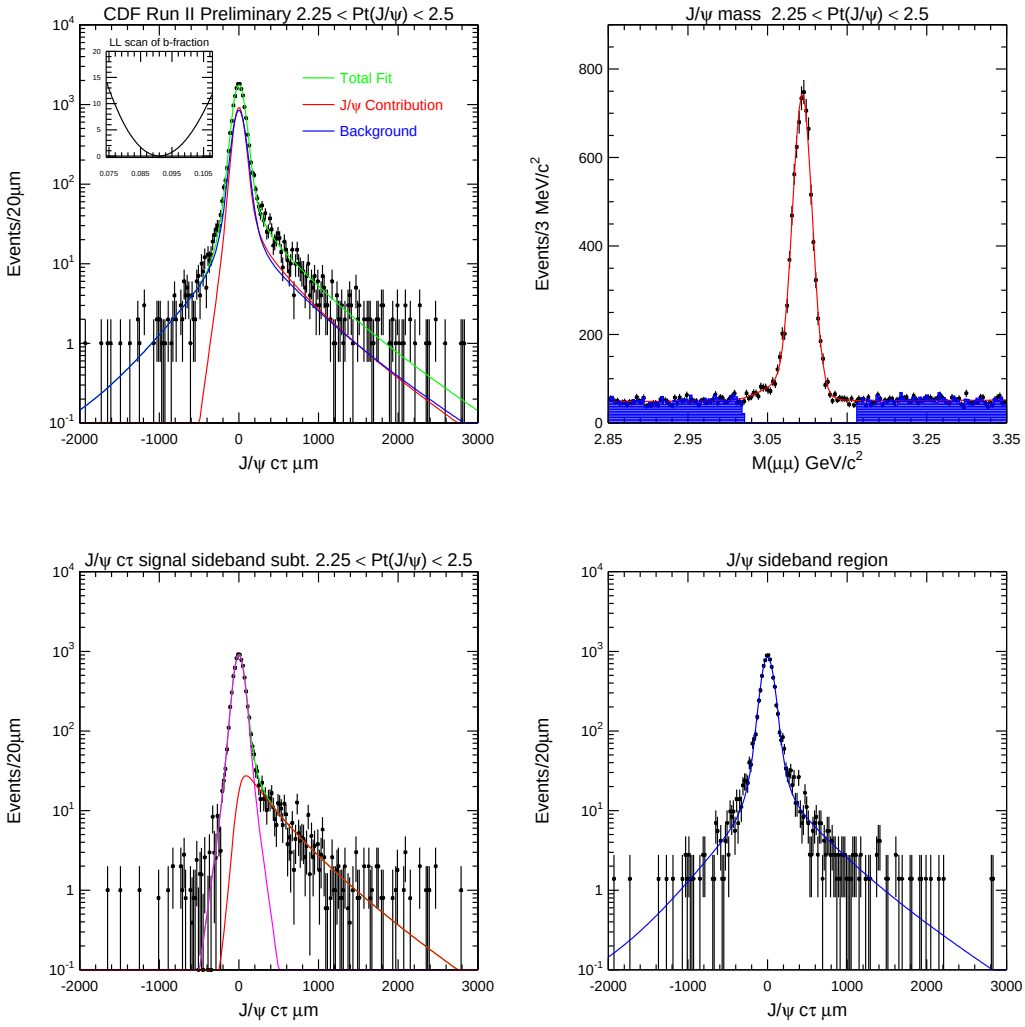

Figure A.2: B lifetime fit results projected onto J/ψ invariant mass and decay length distributions in p_{T} bin 2.25-2.5 GeV/c

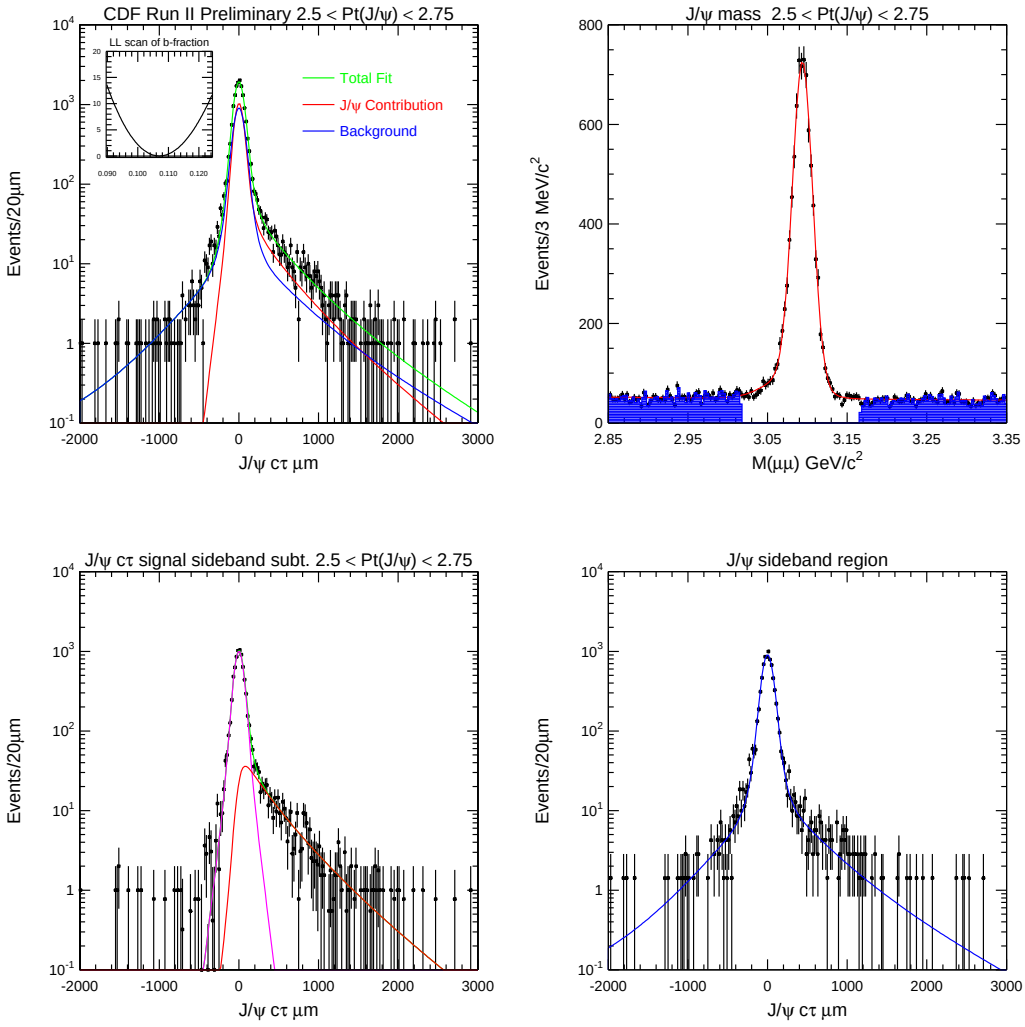

Figure A.3: B lifetime fit results projected onto J/ψ invariant mass and decay length distributions in p_{T} bin 2.5-2.75 GeV/c

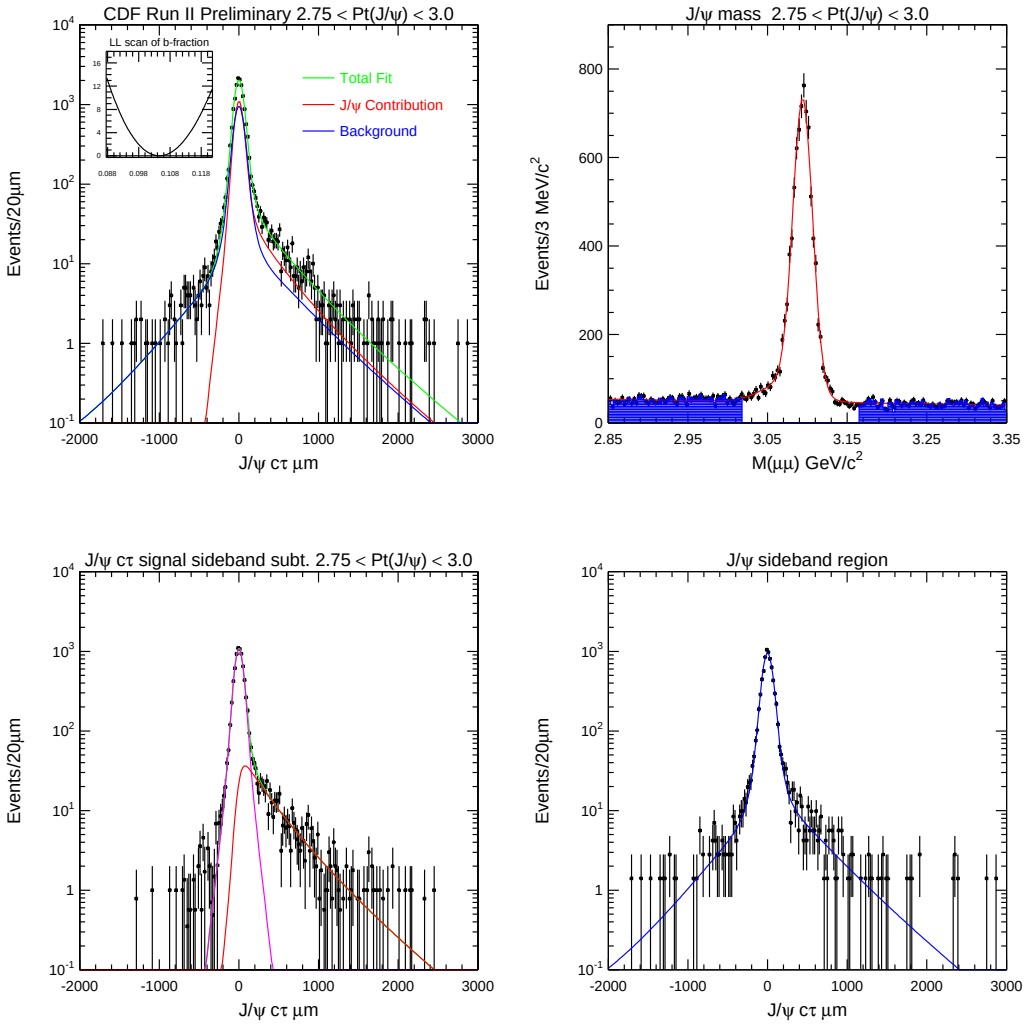

Figure A.4: B lifetime fit results projected onto J/ψ invariant mass and decay length distributions in p_{T} bin 2.75-3.0 GeV/c

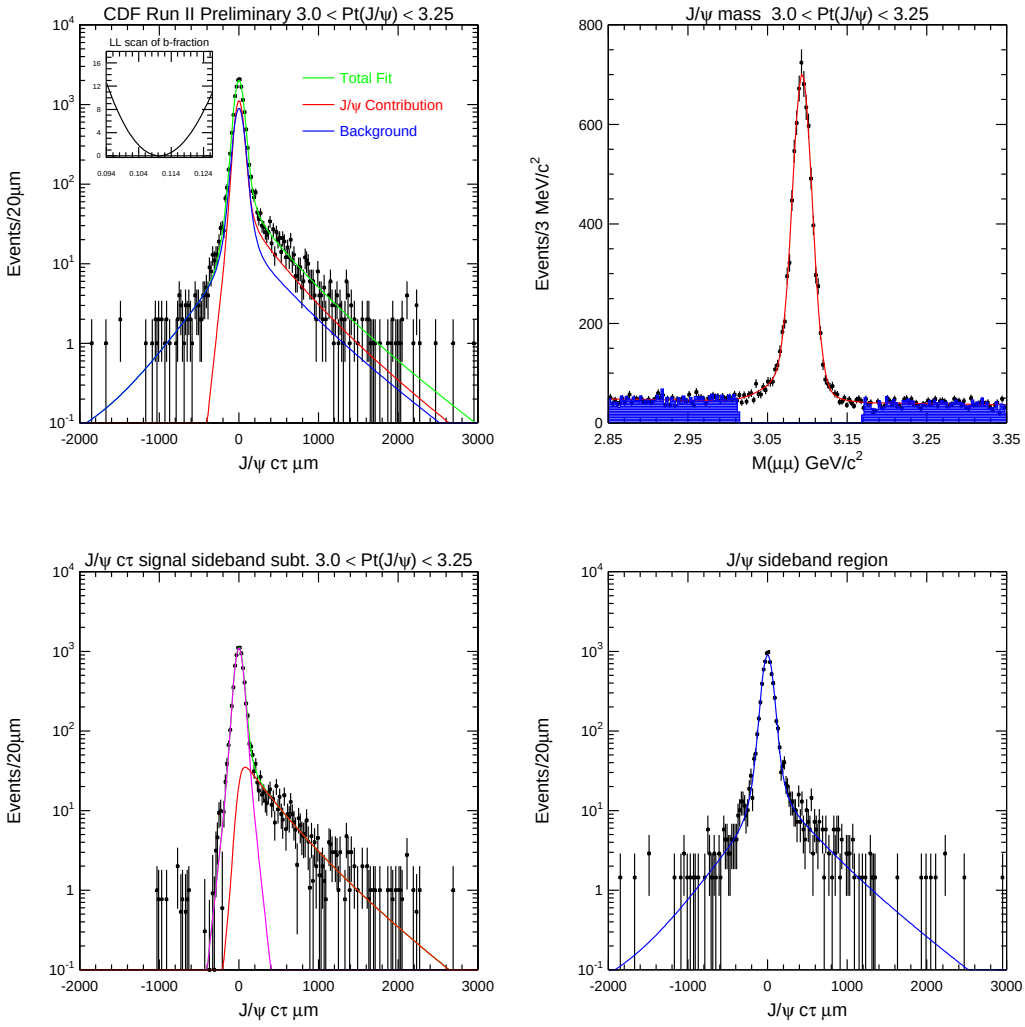

Figure A.5: B lifetime fit results projected onto J/ψ invariant mass and decay length distributions in p_{T} bin 3.0-3.25 GeV/c

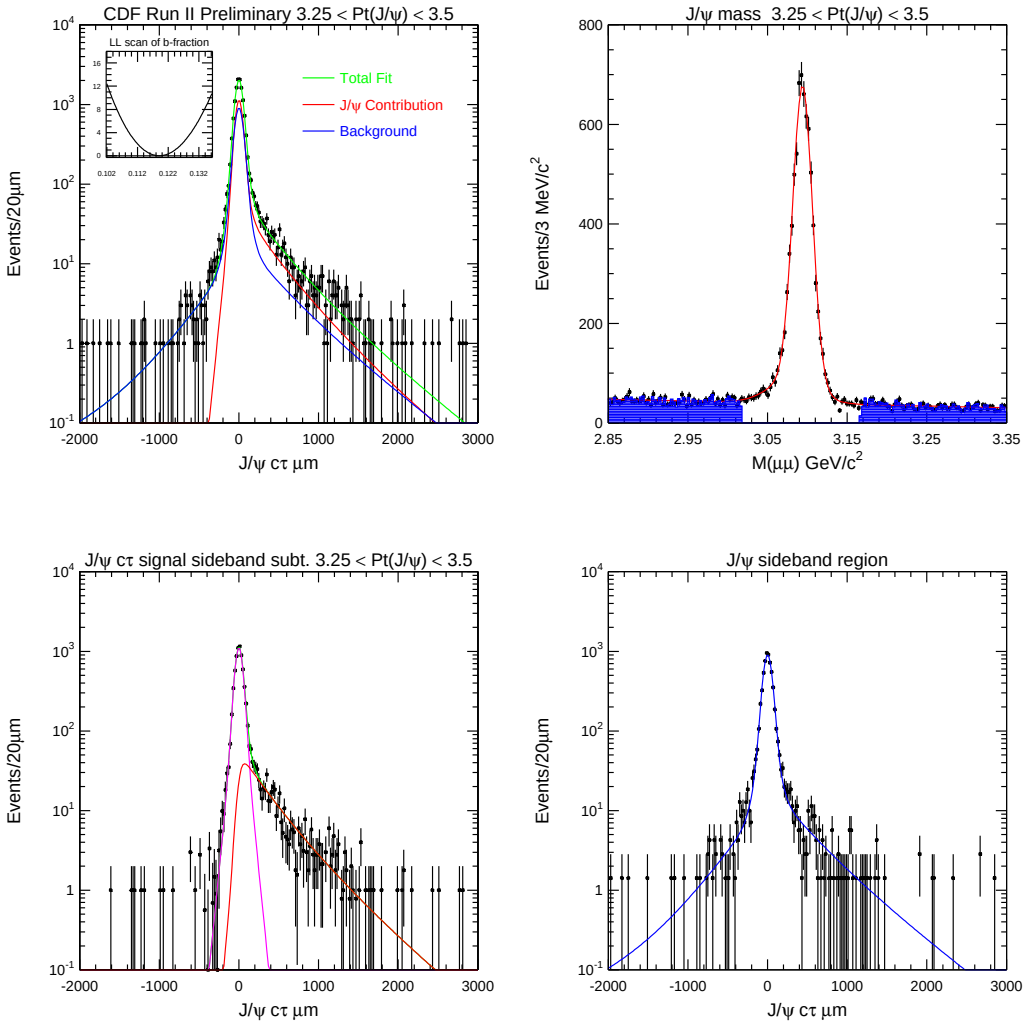

Figure A.6: B lifetime fit results projected onto J/ψ invariant mass and decay length distributions in p_{T} bin 3.25-3.5 GeV/c

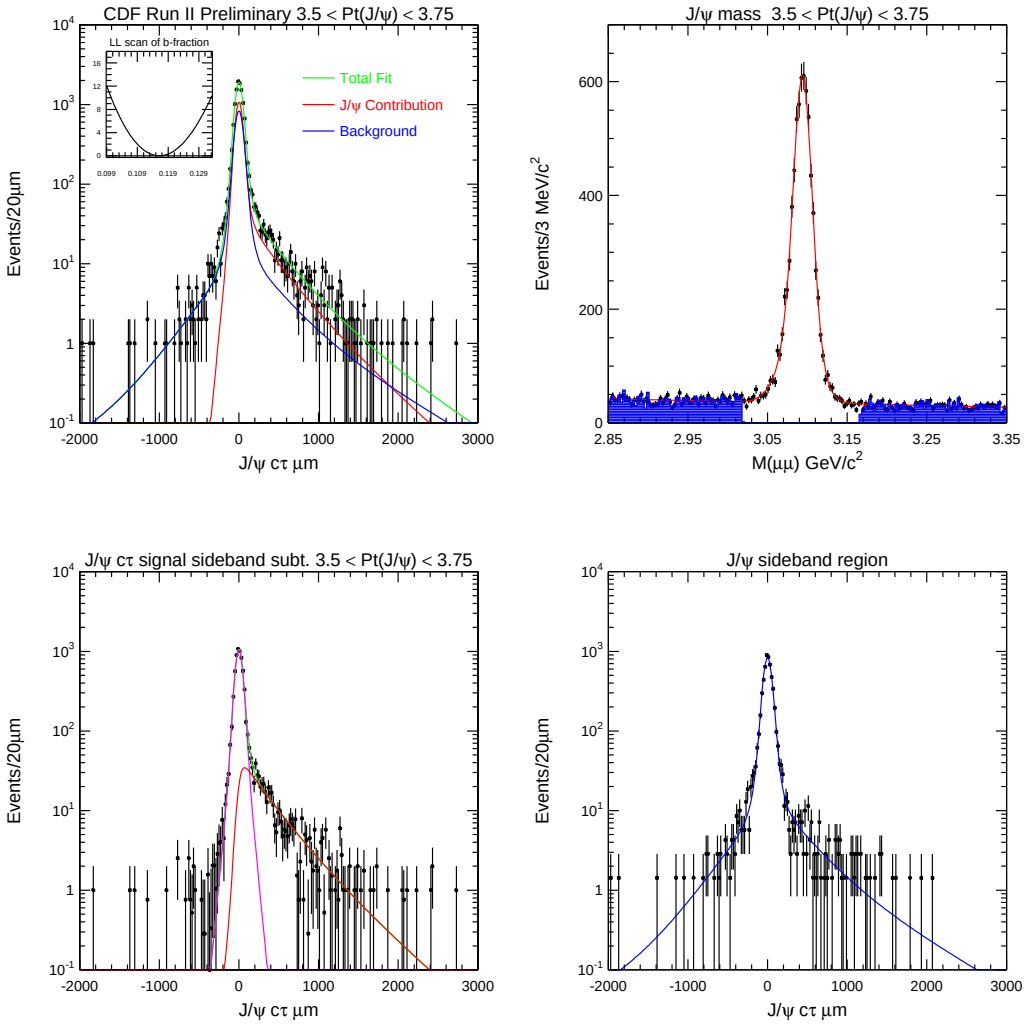

Figure A.7: B lifetime fit results projected onto J/ψ invariant mass and decay length distributions in p_{T} bin 3.5-3.75 GeV/c

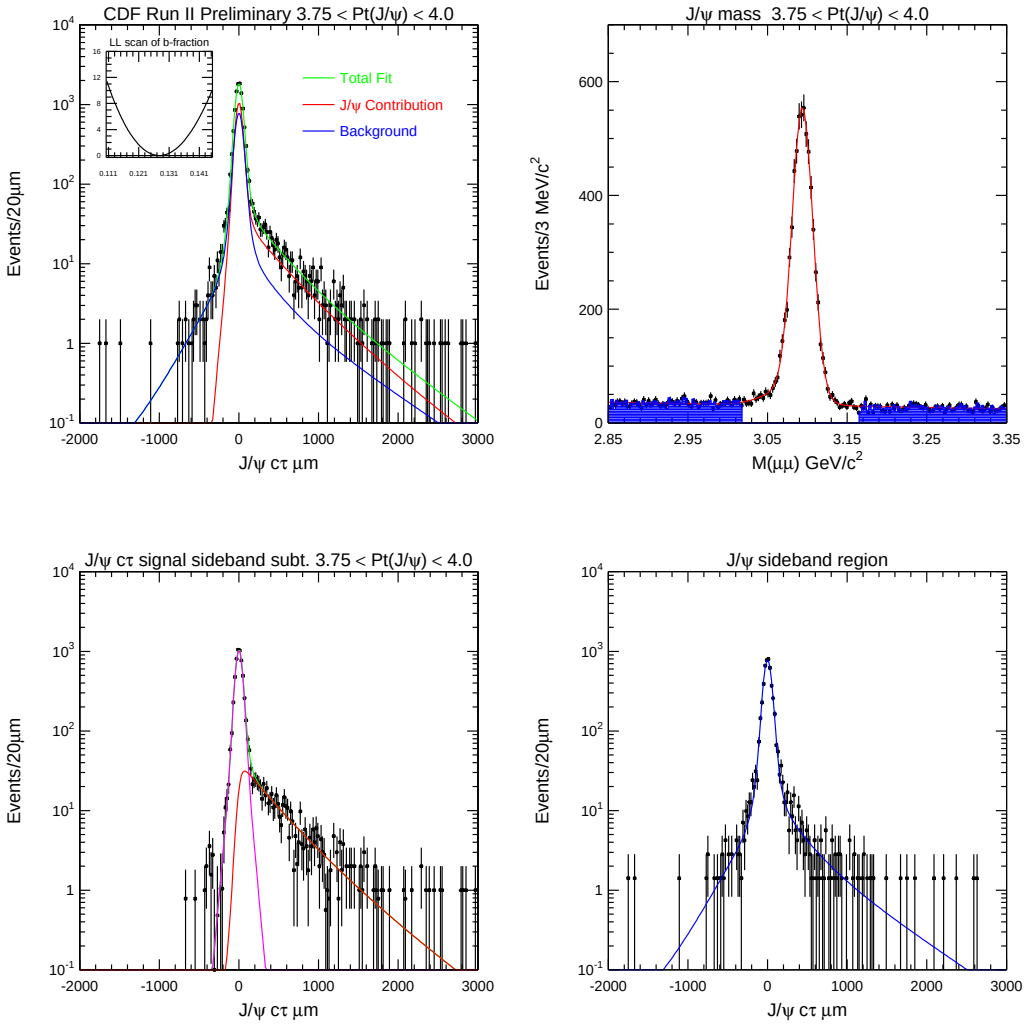

Figure A.8: B lifetime fit results projected onto J/ψ invariant mass and decay length distributions in p_{T} bin 3.75-4.0 GeV/c

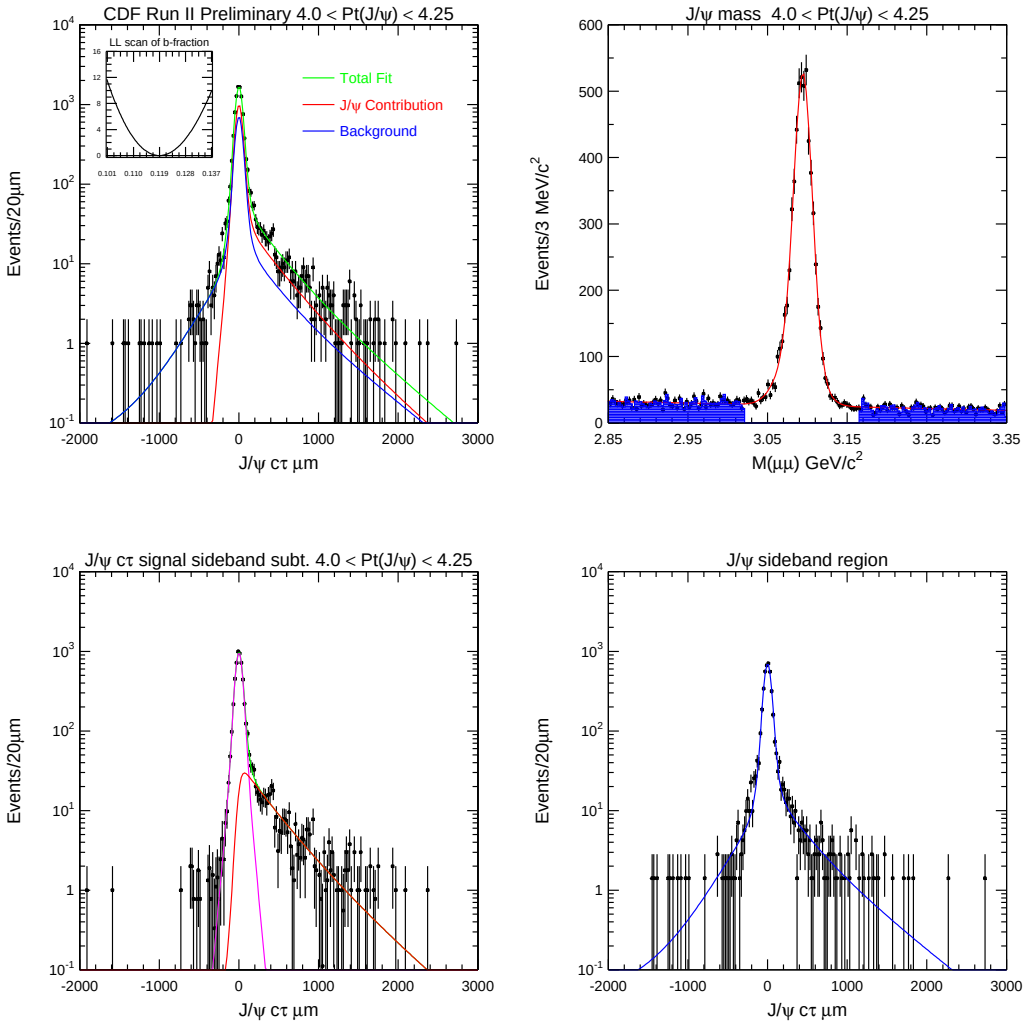

Figure A.9: B lifetime fit results projected onto J/ψ invariant mass and decay length distributions in p_{T} bin 4.0-4.25 GeV/c

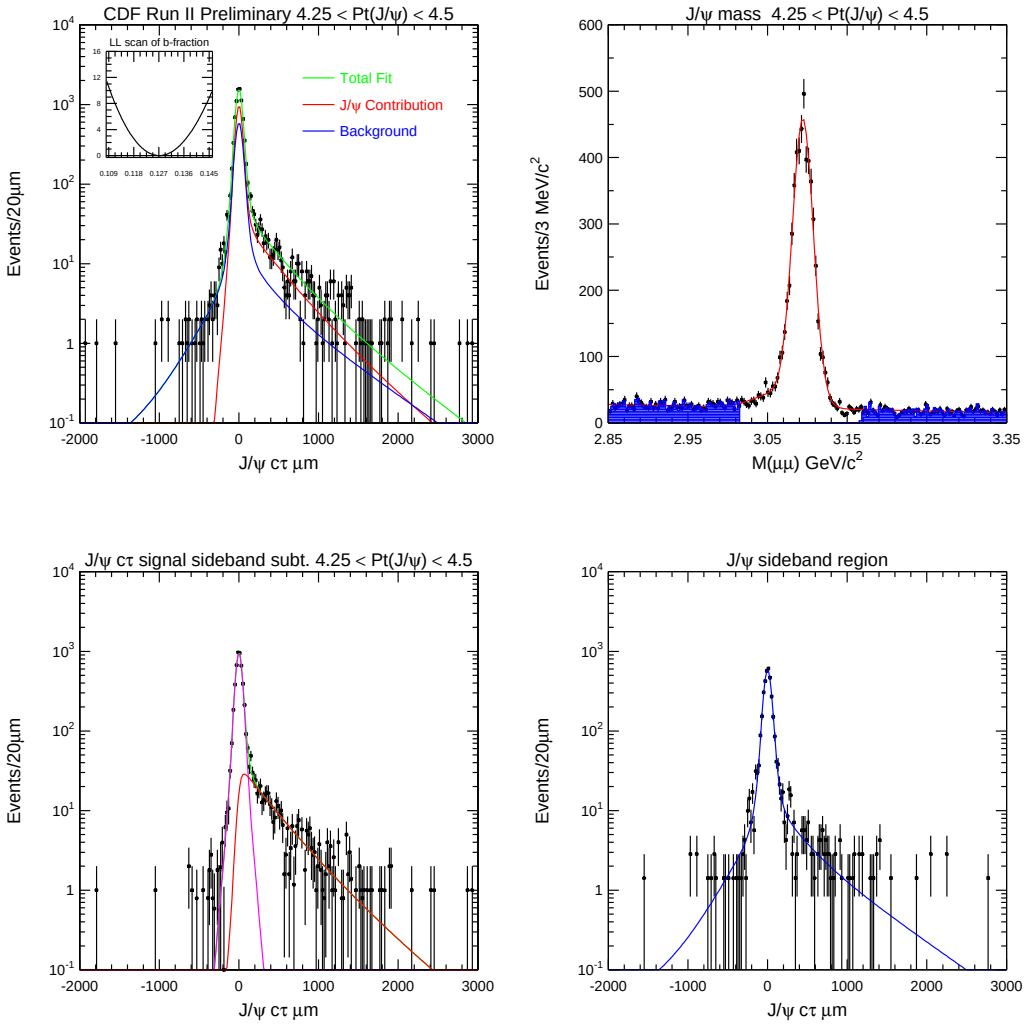

Figure A.10: B lifetime fit results projected onto J/ψ invariant mass and decay length distributions in p_{T} bin 4.25-4.5 GeV/c

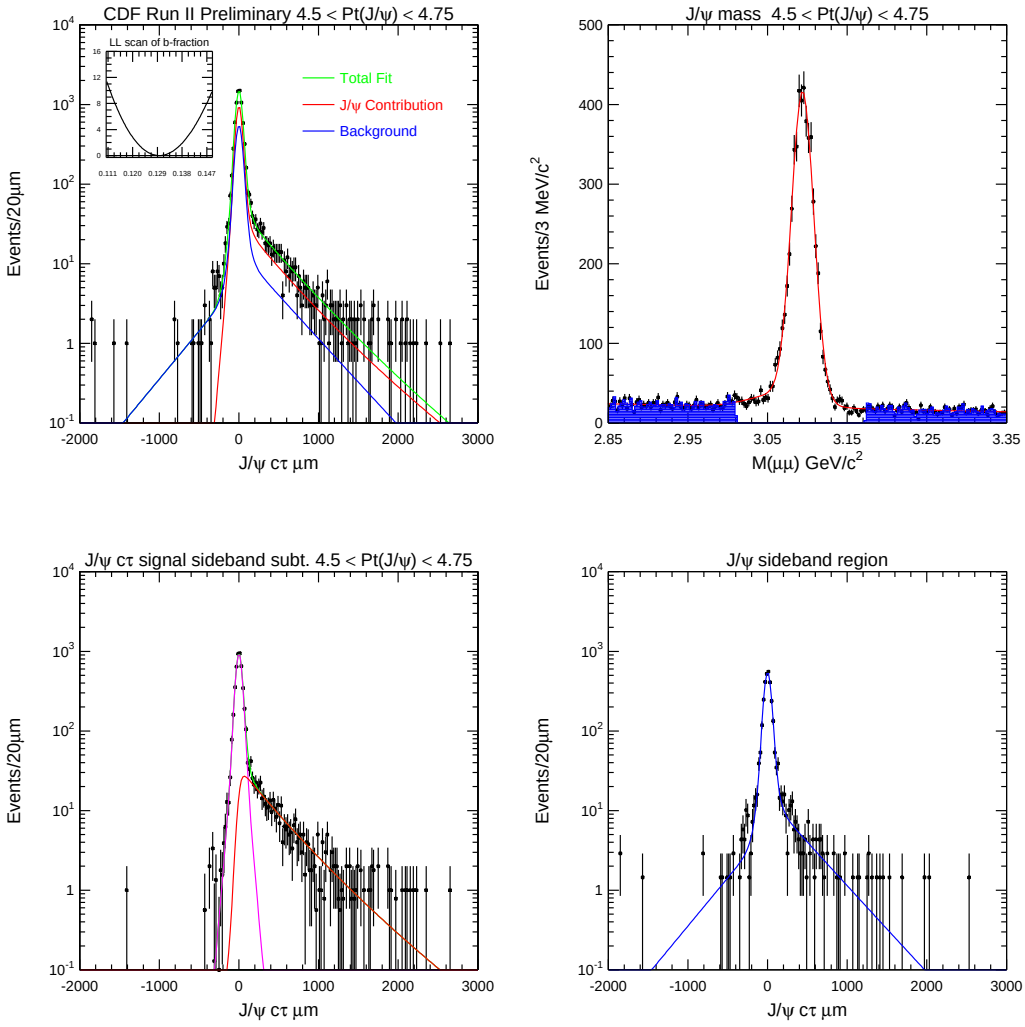

Figure A.11: B lifetime fit results projected onto J/ψ invariant mass and decay length distributions in p_{T} bin 4.5-4.75 GeV/c

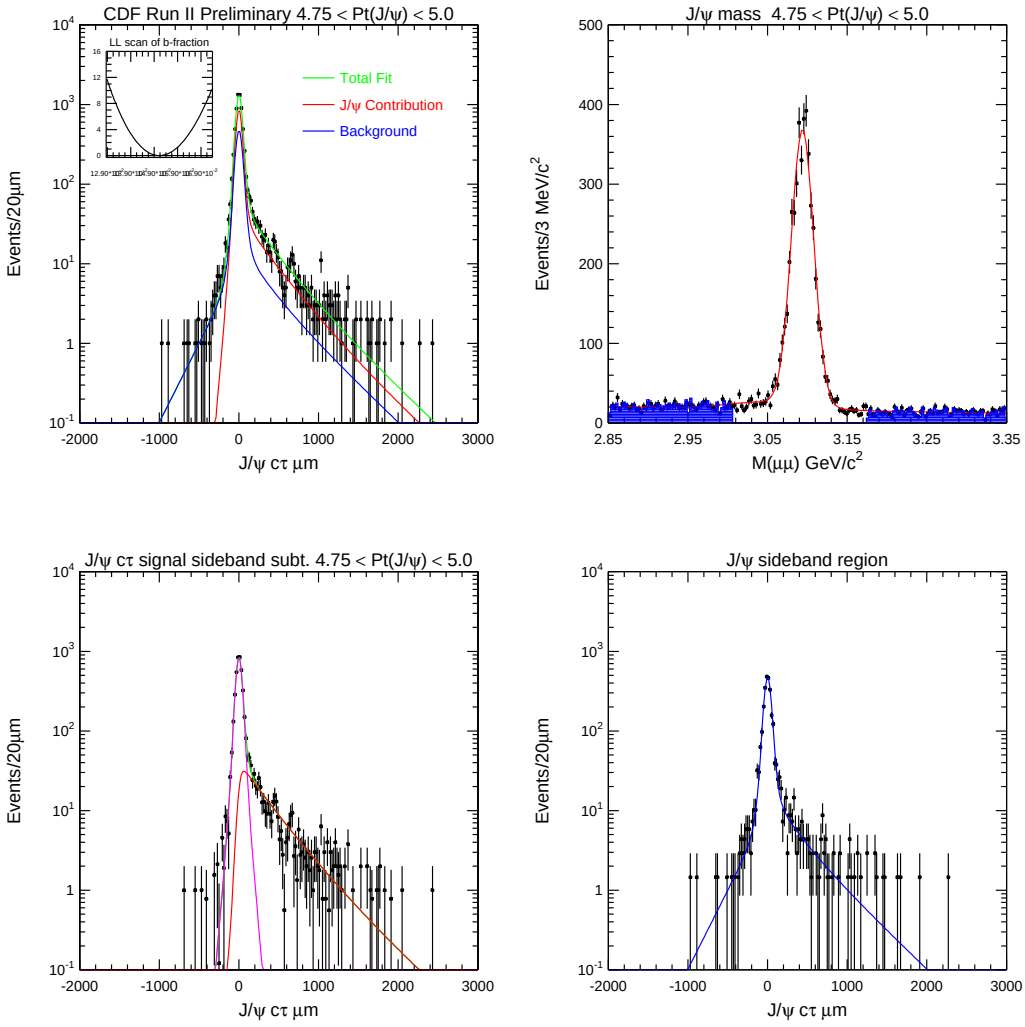

Figure A.12: B lifetime fit results projected onto J/ψ invariant mass and decay length distributions in p_{T} bin 4.75-5.0 GeV/c

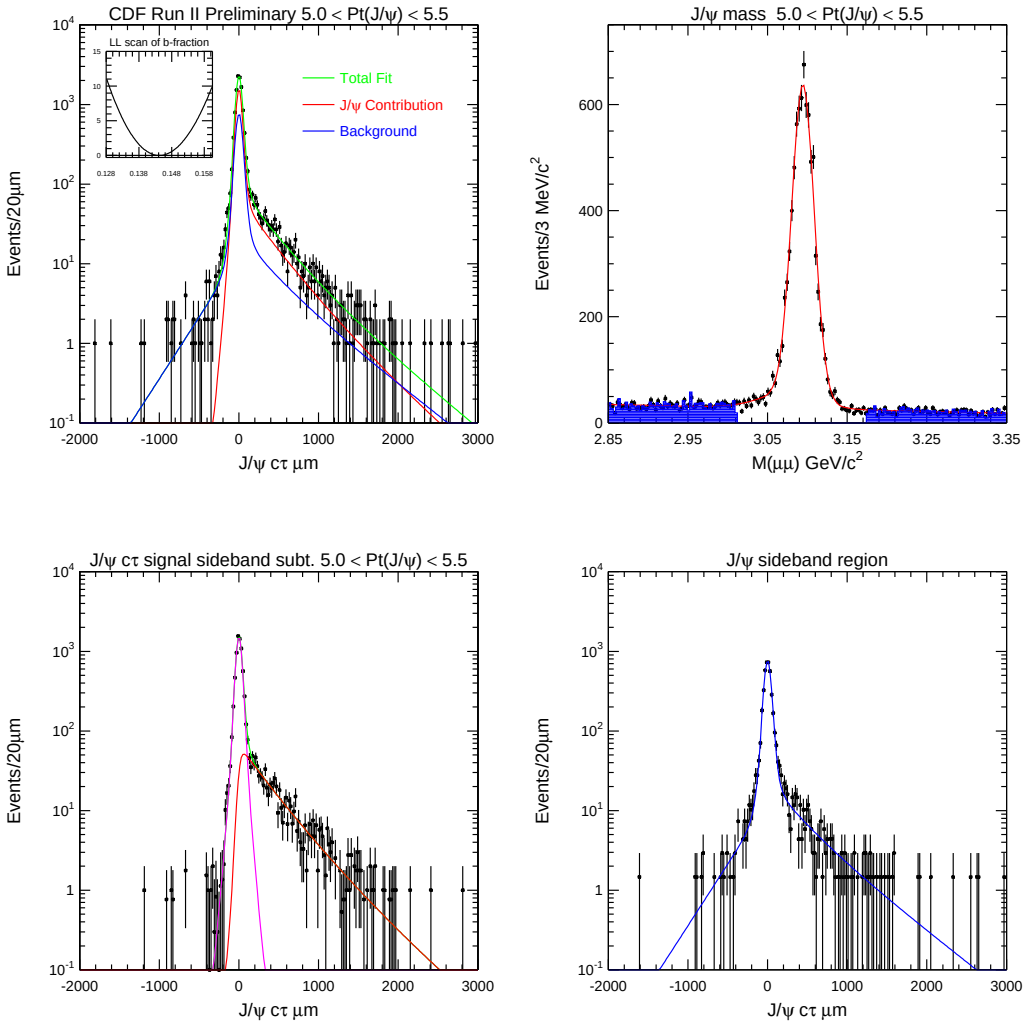

Figure A.13: B lifetime fit results projected onto J/ψ invariant mass and decay length distributions in p_{T} bin 5.0-5.5 GeV/c

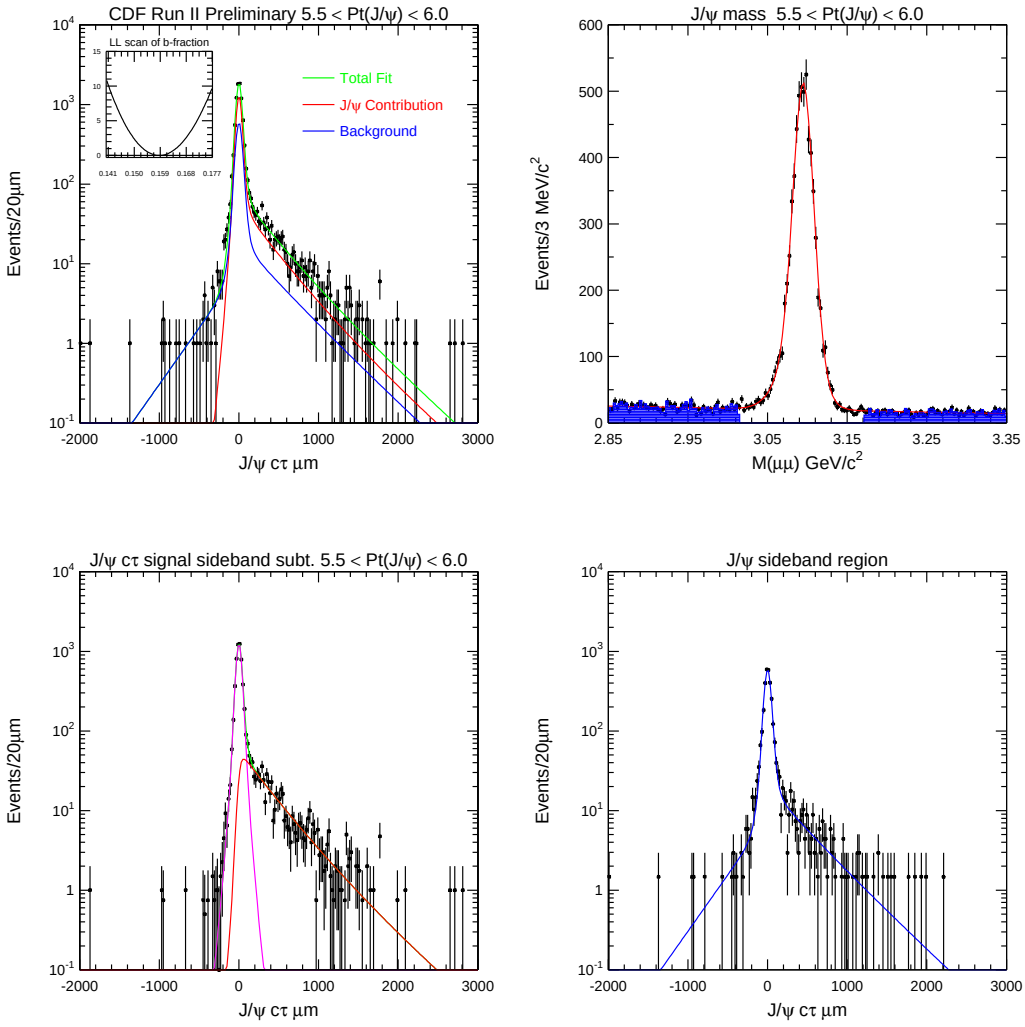

Figure A.14: B lifetime fit results projected onto J/ψ invariant mass and decay length distributions in p_{T} bin 5.5-6.0 GeV/c

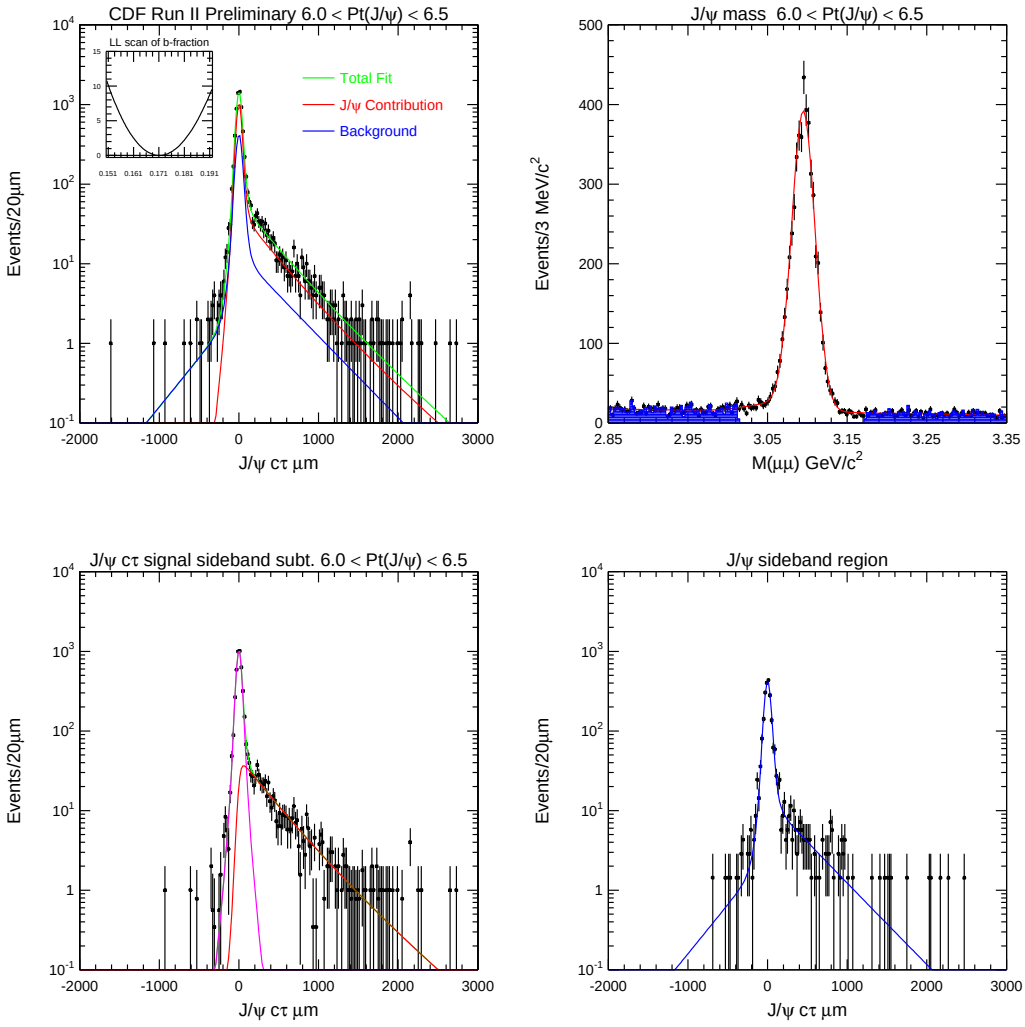

Figure A.15: B lifetime fit results projected onto J/ψ invariant mass and decay length distributions in p_{T} bin 6.0-6.5 GeV/c

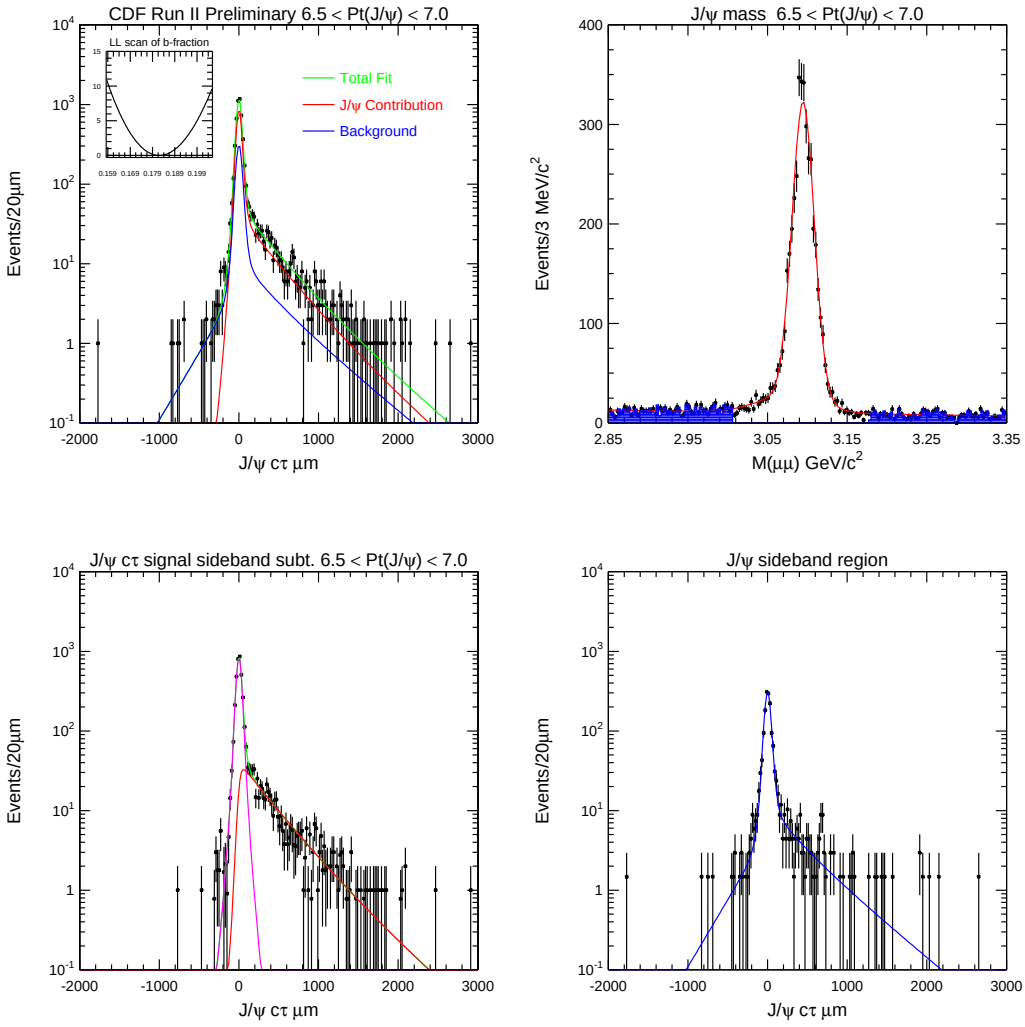

Figure A.16: B lifetime fit results projected onto J/ψ invariant mass and decay length distributions in p_{T} bin 6.5-7.0 GeV/c

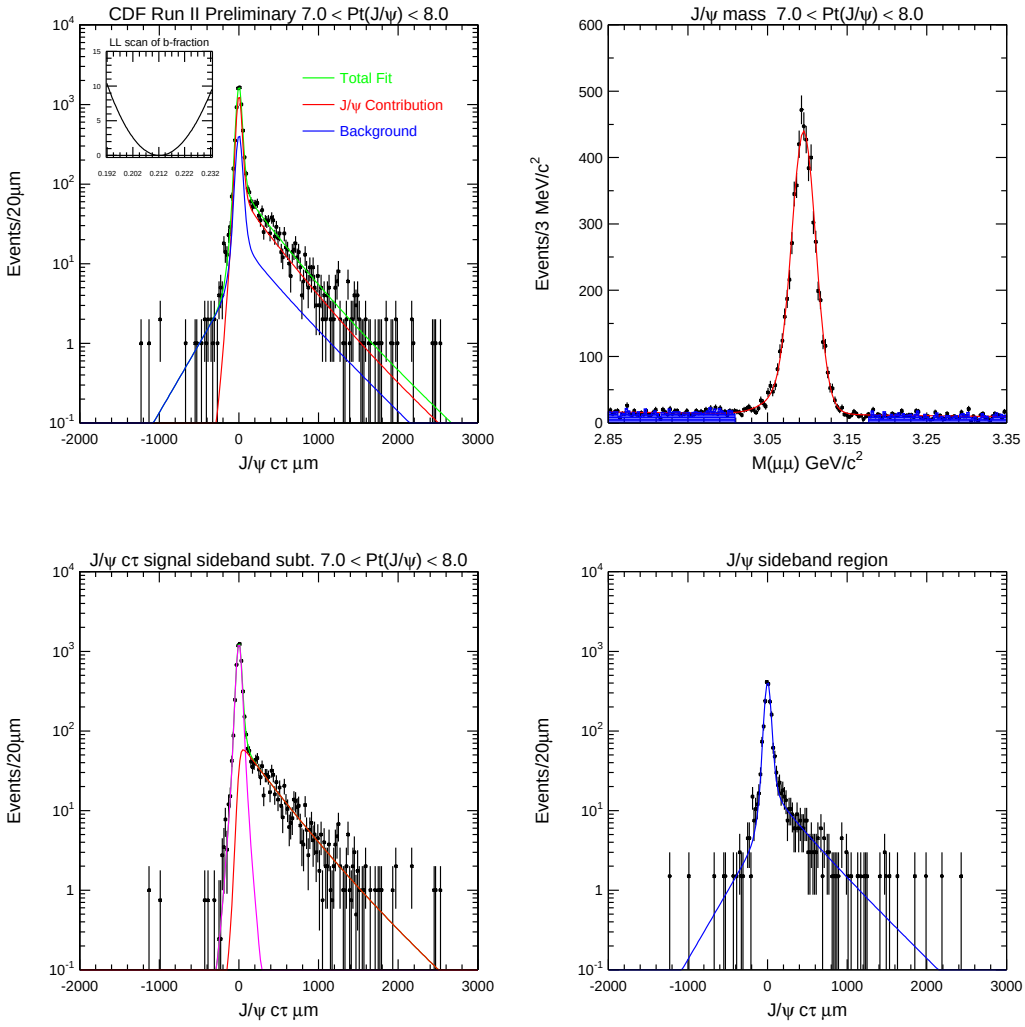

Figure A.17: B lifetime fit results projected onto J/ψ invariant mass and decay length distributions in p_{T} bin 7.0-8.0 GeV/c

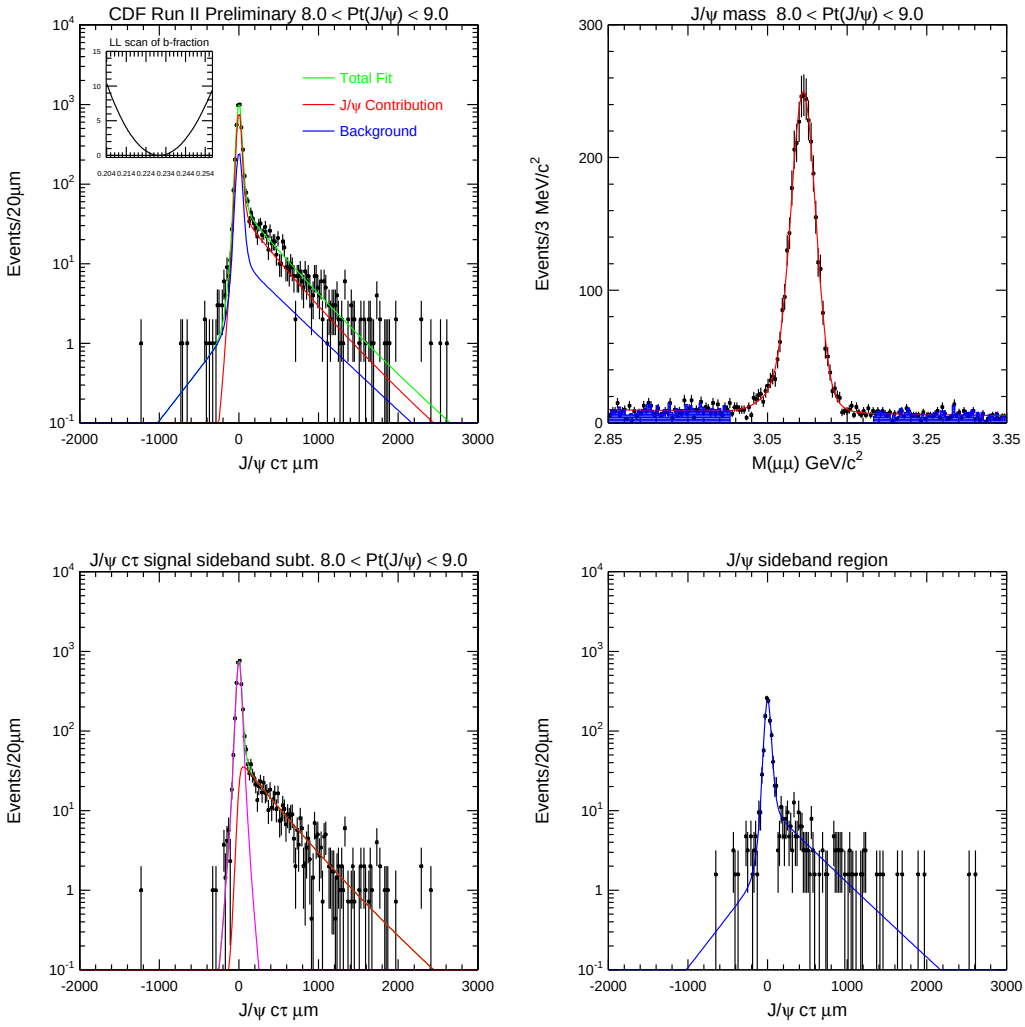

Figure A.18: B lifetime fit results projected onto J/ψ invariant mass and decay length distributions in p_{T} bin 8.0-9.0 GeV/c

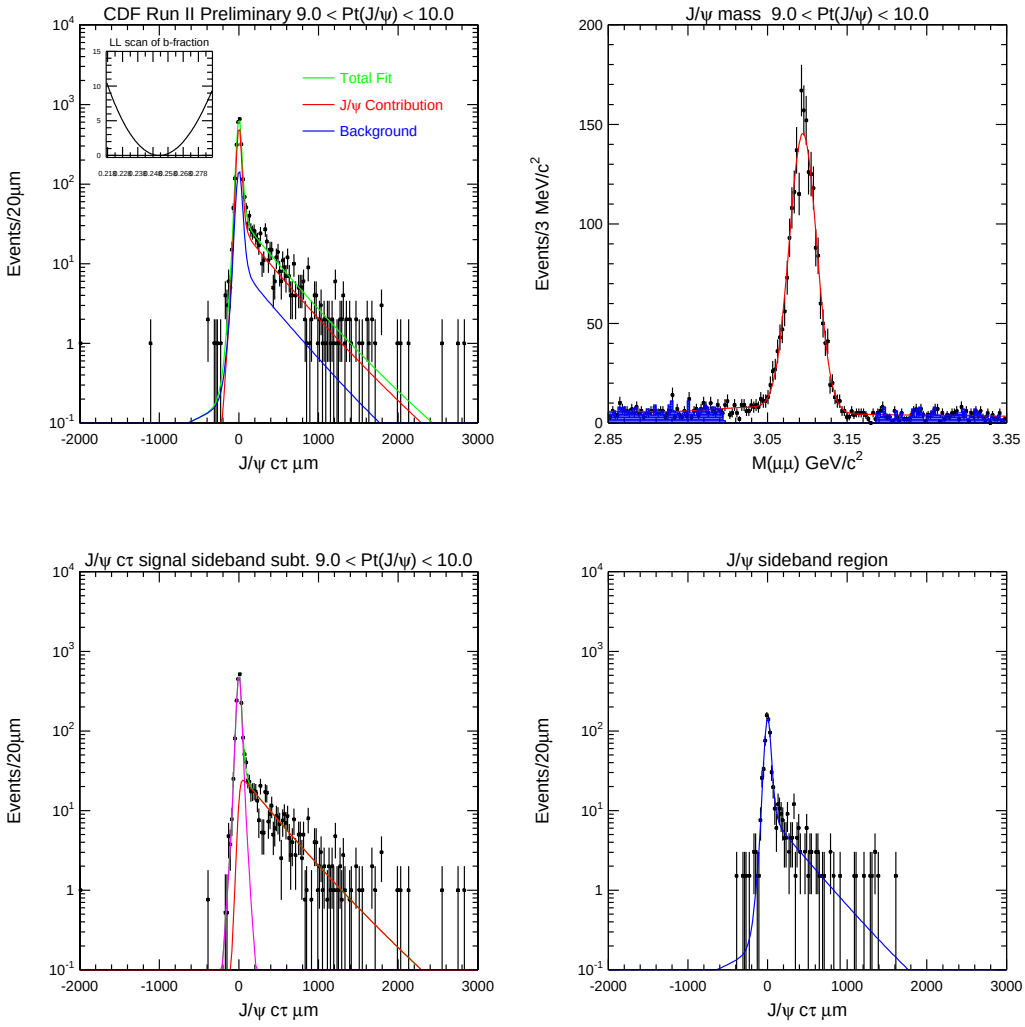

Figure A.19: B lifetime fit results projected onto J/ψ invariant mass and decay length distributions in p_{T} bin 9.0-10.0 GeV/c

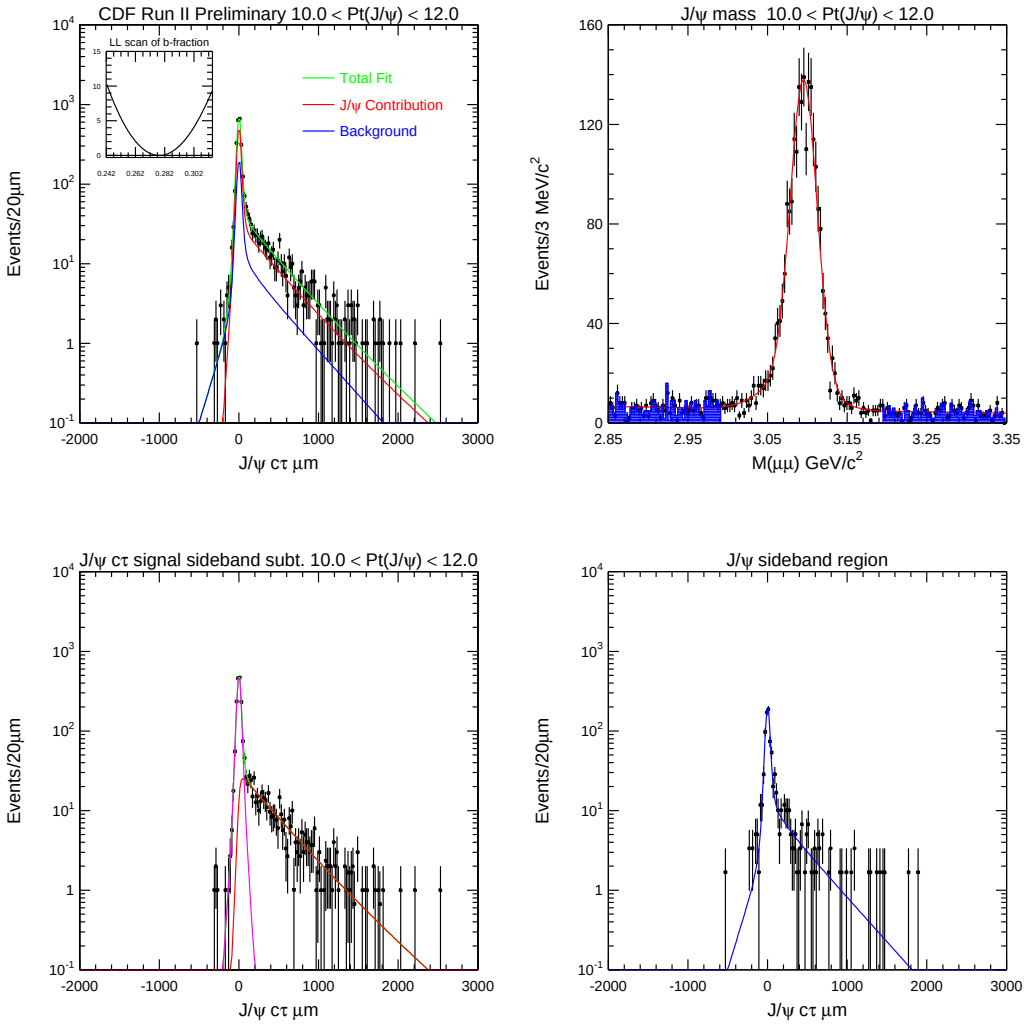

Figure A.20: B lifetime fit results projected onto J/ψ invariant mass and decay length distributions in p_{T} bin 10.0-12.0 GeV/c

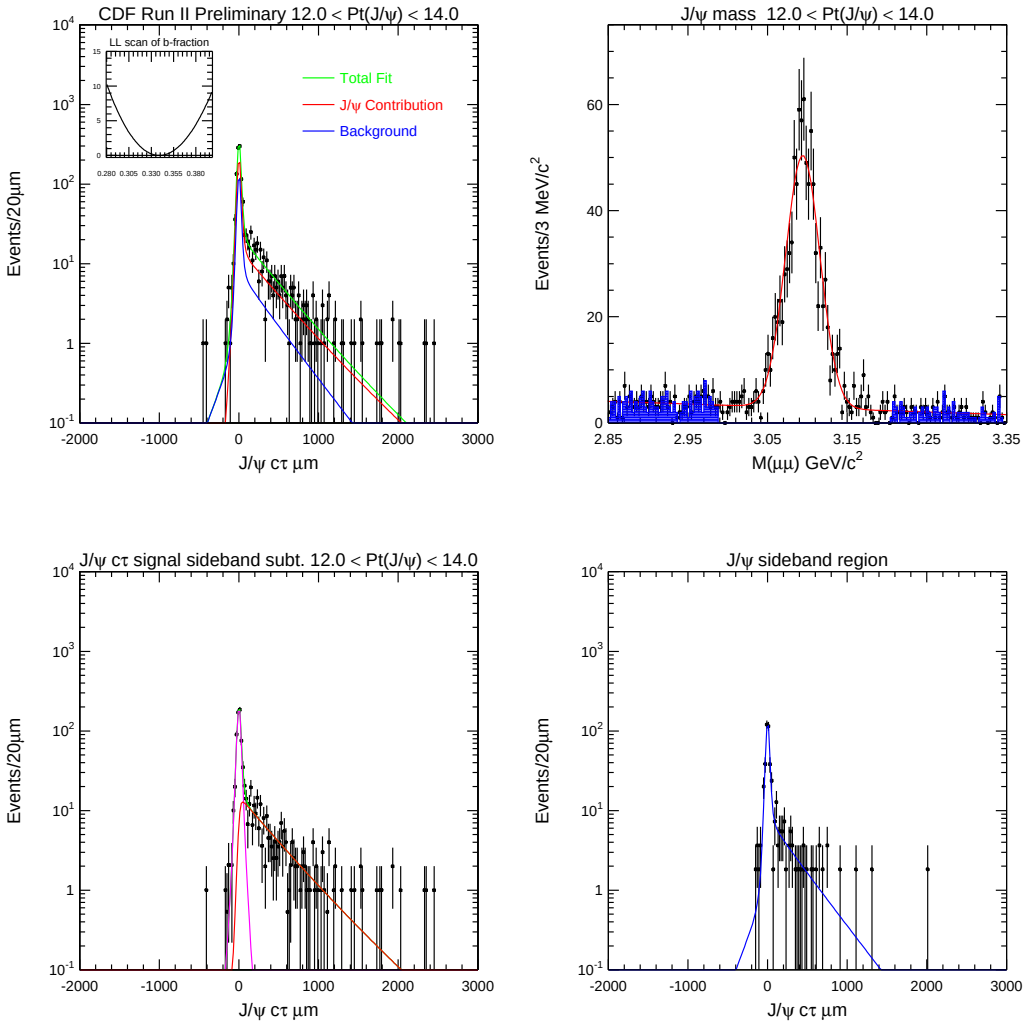

Figure A.21: B lifetime fit results projected onto J/ψ invariant mass and decay length distributions in p_{T} bin 12.0-14.0 GeV/c

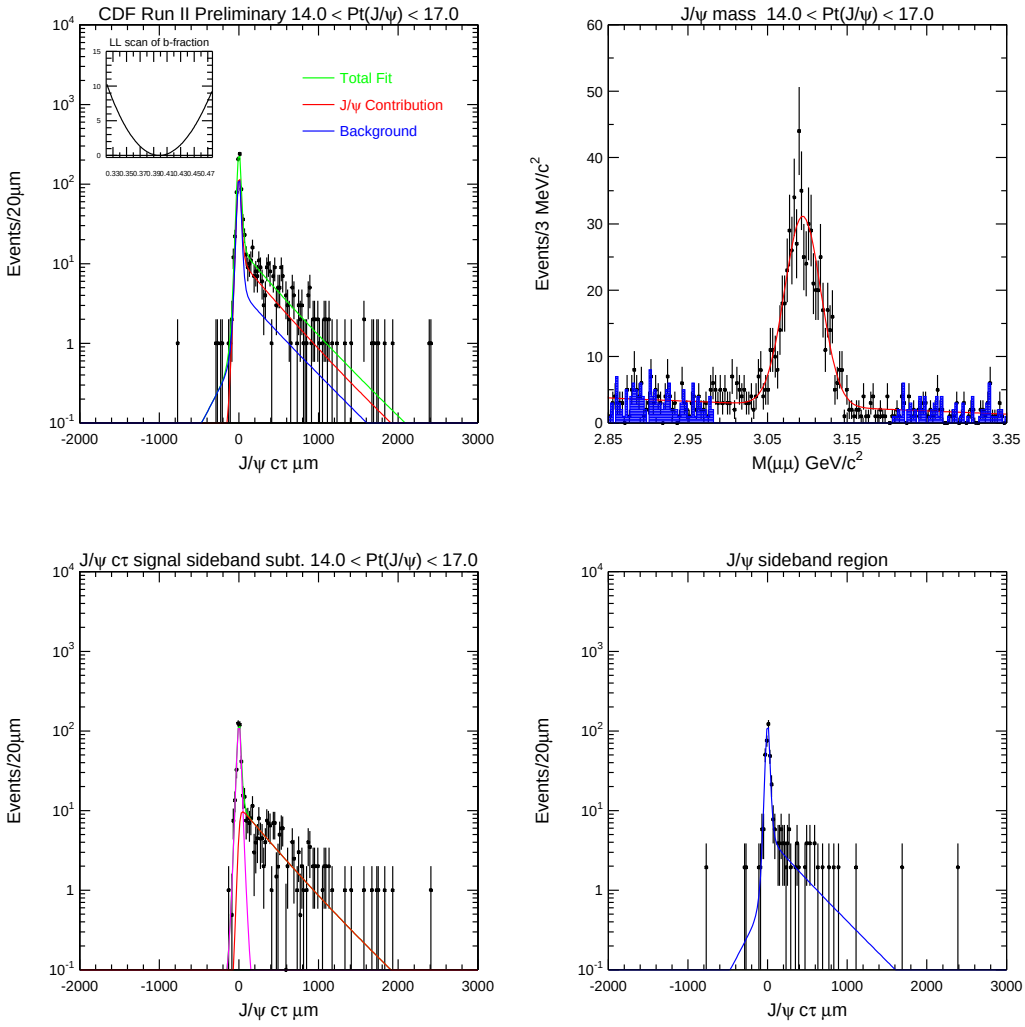

Figure A.22: B lifetime fit results projected onto J/ψ invariant mass and decay length distributions in p_{T} bin 14.0-17.0 GeV/c

Bibliography

[1] F. Abe et al. (CDF Collaboration), *Phys. Rev. Lett.* 74, 2626 (1995)

[2] S. Abachi et al. (D0 Collaboration), *Phys. Rev. Lett.* 74, 2632 (1995)

[3] K. Hagiwara et al., *Review of Particle Physics, Phys. Rev D* 66, 010001 (2002)

[4] K. Kodama et al. (DONUT Collaboration), *Phys. Lett. B* 504, 218 (2001)

[5] P.A.M. Dirac, *Proc. Roy. Soc.* 133, 60 (1931)

[6] S. Glashow, *Nucl. Phys.* 22, 579 (1961)

[7] S. Weinberg, *Phys. Rev. Lett.* 19, 1264 (1967)

[8] S. W. Herb et al. (CFS Collaboration), *Phys. Rev. Lett.* 39, 252 (1977)

[9] K. Anikeev et al., *B Physics at the Tevatron: Run II and Beyond*, Fermilab-Pub-01/197 (2001)

[10] Michelangelo L. Mangano, hep-ph/9711337 (1997)

[11] P. Nason, S. Dawson & R. K. Ellis, *Nucl. Phys. B* 303, 607 (1988)

[12] P. Nason et al., *Nucl. Phys. B* 327, 49 (1989)

[13] P. Nason et al., *Nucl. Phys. B* 335, 260 (1989)

[14] W. Beenakker et al., *Nucl. Phys. B* 351, 507 (1991)

[15] J. Binnewies, Bernd A. Kniehl & G. Kramer, *Phys .Rev. D* 60, 014006 (1999)

[16] Matteo Cacciari and Paolo Nason, *Phys. Rev. Lett.* 89, 122003 (2002)

[17] C. Peterson et al., *Phys. Rev. D* 27, 105 (1983)

[18] S. Brodsky et al., *Phys. Rev. D* 23, 2745 (1981)

[19] J. Aubert et al., *Phys. Rev. Lett.* 33, 1406 (1974)

[20] J. Augustin et al., *Phys. Rev. Lett.* 33, 1404 (1974)

[21] G. Abrams, *Phys. Rev. Lett.* 33, 1452 (1974)

[22] *Fermilab Main Injector Technical Design Handbook* http://www-fmi.fnal.gov/fmiinternal/MI_Technical_Design/index.html

[23] *The Antiproton Source Rookie Book* http://www-bdnew.fnal.gov/pbar/documents/PBAR_Rookie_Book.PDF

[24] *Fermilab Recycler Ring Technical Design Report*, TM-1991, rev. 1.2 (1996)

[25] CDF Collaboration, *The CDF II Detector: Technical Design Report*, Fermilab-PUB-96/390-E (1996)

[26] T.K. Nelson, *Nuclear Instruments and Methods in Physics Research A* 485, 1 (2002)

[27] P. Azzi-Bacchetta et al., *Proposal for a Very Low Mass, Very Small Radius Silicon Layer In the CDF II Upgrade*, CDF Note 4924 (1999)

[28] BaBar Collaboration, *BaBar Technical Design Report*, SLAC-R-457 (1995)

[29] CDF Collaboration, *Proposal for Enhancement of the CDFII Detector: An Inner Silicon Layer and a Time of Flight Detector*, Fermilab-Proposal-909 (1998)

[30] Kevin T. Pitts, *Nuclear Physics B - Proceedings Supplements* 61, 230 (1998)

[31] Ch. Paus et al., *Nuclear Instruments and Methods in Physics Research A* 461, 579 (2001)

[32] L. Balka et al., *The CDF Central Electromagnetic Calorimeter*, Fermilab-Pub-87/172-E (1987)

[33] G. Apollinari et al., *The CDF Central and Endwall Hadron Calorimeter*, Fermilab-Pub-87/174-E (1987)

[34] Ryutaro Oishi et al., *Nuclear Instruments and Methods in Physics Research A* 453, 227 (2000)

[35] G. Ascoli et al., *CDF Central Muon Detector*, Fermilab-Pub-87/179-E (1987)

[36] Tommaso Dorigo, *Nuclear Instruments and Methods in Physics Research A* 461, 560 (2001)

[37] D. A. Smith et al., *Pion Punch-through Probability in the Central Calorimeter*, CDF Note 707 (1988)

[38] W. Ashmanskas et al., *Nuclear Instruments and Methods in Physics Research A* 477, 451 (2002)

[39] T. Zimmerman et al., *Nuclear Instruments and Methods in Physics Research A* 409, 369 (1998)

[40] M. Garcia-Sciveres et al., *Nuclear Instruments and Methods in Physics Research A* 435, 58 (1999)

[41] T. Ohsugi et al., *Nuclear Instruments and Methods in Physics Research A* 383, 116 (1996)

[42] T. Ohsugi et al., *Nuclear Instruments and Methods in Physics Research A* 342, 22 (1994)

[43] *Wedge in a Box for Cable Testing*, http://www-cdf.fnal.gov/internal /people/links/SaverioDAuria/wedgebox.html

[44] A. Affolder et al. *Internal Failures of SVXII Ladders*, CDF Note 5817 (2001)

[45] http://www-cdf.fnal.gov/internal/upgrades/align/alignment.html

[46] W.-M. Yao and K. Bloom, *Outside-In Silicon Tracking at CDF*, CDF Note 5591 (2001)

[47] *Silicon Detector Working Group*, http://www-cdfonline.fnal.gov/∼svxii/detector/detector.html

[48] http://cdfcodebrowser.fnal.gov/CdfCode/source/TrackingSI/TrackingSI /Utils/SiExpected.hh

[49] http://www-cdf.fnal.gov/internal/silicon/SiStudies/minutes /si_021106.html

[50] T. Yamashita et al., *Measurement of the Run II Inclusive* J/ψ *Cross-section*, CDF Note 6288 (2003)

[51] F. Abe et al. (CDF Collaboration), *Phys. Rev. Lett.* 79, 578 (1997)

[52] K. Anikeev et al., *Calibration of Energy Loss and Magnetic Field using* J/ψ *Events in Run II*, CDF Note 5958 (2002)

[53] K. Anikeev et al., *Measurement of B Meson Masses in the Exclusive* J/ψ *Channels*, CDF Note 6022 (2002)

[54] C. Rott, *Track Quality Study*, http://www-cdf.fnal.gov/internal/people/links/CarstenRott/TrackingTalk_September2002.pdf

[55] Y. Gotra et al., *Run II Muon Trigger Efficiency Measurement*, CDF Note 6162 (2003)

[56] P. Sphicas, *A b-bbar Monte Carlo Generator*, CDF Note 2655 (1994)

[57] C. R. Hagen, *Theoretical High Energy Physics: MRST 2000*, AIP Conference Proceedings 541

[58] K. Anikeev et. al., *Description of Bgenerator II*, CDF Note 5092 (1999)

[59] F. Abe et. al. (CDF Collaboration), *Phys.Rev. D* 57, 5382 (1998)

[60] Chakravarti, Laha & Roy, *Handbook of Methods of Applied Statistics*, John Wiley & Sons (1967)